NASA Technical Memorandum 104618 NASA-TM-104618

Differential Absorption Lidars for Remote Sensing of Atmospheric Pressure and Temperature Profiles: Final Report

C. Laurence Korb, Geary K. Schwemmer, Joseph Famiglietti, Harvey Walden, and Coorg Prasad

NOVEMBER 1995

NASA Technical Memorandum 104618

Differential Absorption Lidars for Remote Sensing of Atmospheric Pressure and Temperature Profiles: Final Report

C. Laurence Korb
Geary K. Schwemmer
Joseph Famiglietti
Harvey Walden
Goddard Space Flight Center
Greenbelt, Maryland

Coorg Prasad
Science and Engineering Services, Inc.
Burtonsville, Maryland

National Aeronautics and
Space Administration

Goddard Space Flight Center
Greenbelt, Maryland

1995

This publication is available from the NASA Center for AeroSpace Information,
800 Elkridge Landing Road, Linthicum Heights, MD 21090-2934, (301) 621-0390.

EXECUTIVE SUMMARY

This report describes the development of differential absorption lidar (DIAL) techniques to measure the atmospheric pressure and temperature profiles. Improved measurements of the atmospheric temperature profile are needed both in terms of accuracy and increased vertical (altitude) resolution in modeling atmospheric processes to improve weather and climate forecasting. Pressure and temperature profiles are required for specifying the state of the atmosphere. Passive temperature sensors have fundamental limits in vertical resolution of 5 to 8 km, and no other remote sensing method exists for obtaining pressure profile measurements. The basic premise behind the DIAL measurements is as follows. Spectral absorption lines are pressure broadened in the lower atmosphere, so the absorption lines have a Lorentzian line shape to first order approximation. Oxygen is well mixed in the atmosphere with a constant mixing ratio and the *A* band near 0.76 μm is accessible using near infrared tunable lasers and detectors. With a constant mixing ratio, the absorption at the center of a line is independent of the pressure and varies according to its temperature sensitivity. Temperature is determined using a high *J* line which has a large value of ground state energy along with a nearby reference measurement. On the other hand, pressure is determined using a measurement in the wing of a line where the absorption varies as the square of the pressure, and the temperature sensitivity can be eliminated by choosing the correct location in the band. The pressure-sensitive wing measurement is located in an absorption trough, the region of minimum absorption between two strong oxygen lines, to desensitize the measurement to the effects of laser frequency drifts. The pressure-sensitive measurement is used with a nearby reference measurement. Finding a laser suited to the task of making the measurements has proved to be the most difficult aspect of this research and resulted in more of a technology development component to this program than occurs in most science-funded activities. Under this program, the theory was developed and numerous error analyses carried out. A continuous wave (CW) breadboard experiment was developed and used to prove the feasibility of the method. A two-dye laser DIAL system was developed and upgraded with solid-state alexandrite lasers, which were used to make the first ground-based and airborne pressure profile measurements. Noise-limited precisions of 1.6 to 2 mb were obtained with 37.5 m vertical resolution in the lower atmosphere. The lasers were upgraded and additional airborne pressure data were gathered, as well as ground-based temperature profiles showing noise levels of 1 K with 300 m vertical resolution.

Many chapters in this report are adapted from previous publications or other papers, and have been edited for self-consistency and, in some cases, updated. They are arranged in logical order, starting with the theory of pressure and temperature measurements in Chapters 1 and 2. Chapter 3 describes the theory of the effective frequency technique and is followed by four chapters on technology: the lidar system (Chapter 4), the laser developments (Chapter 5), the detector studies (Chapter 6), and the laser wavemeter development (Chapter 7). This is followed by a design analysis of a Raman channel in Chapter 8. The Raman channel was to be added to the system for determining the aerosol to molecular backscatter ratio, which is needed to correctly analyze the absorption measurements and obtain the greatest accuracy in the derived temperature profiles. Chapters 9 through 12 describe the lidar measurements in chronological order. Chapter 13 is a design study of an advanced automated lidar system that could be used on the NASA ER-2 high altitude research aircraft, and Chapter 14 describes studies of spaceborne systems. The bibliography lists all the publications, reports, and patents that resulted from this research, except for several which remain to be published.

This program has sparked others around the world to pursue our methods of measuring temperature, as well as to use the laser technology we developed for making DIAL temperature measurements. As a result of the technology advances we made, there have been numerous "spin-off" studies, papers, and inventions which are described in this report, all in some way necessary for the successful achievement of atmospheric measurements. The work described in this report is not merely the work of the authors. It has been accomplished through the efforts of many people: those directly associated with the program, those who supported the program with funding or other resources, those who acted in supporting roles, as well as many indirectly involved. We have tried to be complete in acknowledging all who contributed and apologize for any omissions, as sometimes occurs in a work of such large scope as this one.

TABLE OF CONTENTS

CHAPTER 1 THEORY OF LIDAR PRESSURE MEASUREMENTS

INTRODUCTION

This chapter describes the differential absorption lidar technique for measuring the atmospheric pressure profile and surface pressure from both ground- and satellite-based platforms using the trough absorption region between two atmospheric lines. Pressure is one of the basic atmospheric state variables, and a knowledge of the pressure as a function of altitude (pressure profile) is needed in virtually all atmospheric models. For example, the temperature profile can be calculated directly from the pressure profile. Horizontal gradients in the pressure and the Coriolis force are the basic forces acting on an air parcel and are used to derive the balanced wind. Weather patterns are commonly described with contour maps giving the height of constant pressure surfaces. Thus, a knowledge of pressure is essential for weather and climate prediction. We note that the Global Atmospheric Research Program has specified a requirement for the remote measurement of surface pressure to 0.3% (WMO-ICSU, 1973).

Currently, there are no operational remote sensing techniques for measuring pressure, and the pressure field must be deduced from other atmospheric parameters. The pressure profile is generally calculated from the hydrostatic equation using radiosonde or passive satellite radiometer measurements of the temperature profile and barometric measurements of surface pressure, where available. Passive temperature measurements are limited, however, both in vertical resolution (8 km) and accuracy (2 K) (Atlas and Korb, 1981). In addition, *in situ* observations of surface pressure are sparse over large areas of the oceans and in the Southern Hemisphere, and estimates (forecasts) of the surface pressure must be used in these regions. The errors in these parameters limit the accuracy of the calculated pressure profiles.

There has been considerable interest in remotely measuring atmospheric pressure since the 1960's. Early work by Yamamoto and Wark (1961) suggested that cloud-top height could be estimated from satellite measurements of reflected sunlight using absorption by the oxygen *A* band at 0.76 μm. Wark and Mercer (1965) performed a low resolution band analysis of the oxygen absorption near 0.76 μm to evaluate the feasibility of these cloud-top measurements. Singer (1968) considered the feasibility of a lidar measurement of surface pressure using the results of this band analysis. A high spectral resolution lidar technique for measuring the pressure profile and surface pressure using a measurement in the line wing was first described by Korb (1977) and later extended to the use of absorption troughs as outlined by Korb, *et al.* (1979). The use of a measurement in the line wing was also considered by Megie (1980). The average pressure for a 1 km atmospheric path has been measured to a relative accuracy of 0.1% by employing a horizontal path version of this trough technique using scattering from a fixed target (Kalshoven and Korb, 1982). Other techniques which have been considered include an active microwave method for measuring surface pressure over the ocean using a number of frequencies in the 60 GHz oxygen absorption band as described by Peckham and Flower (1981). Gardner (1979) described a lidar technique to measure surface pressure using the time delay between various frequencies caused by the frequency dependence of the atmospheric index of refraction. Russell and Morley (1982) discussed a lidar technique utilizing the backscatter at two widely separated wavelengths to obtain the atmospheric density profile. If the pressure is known at some point on the density profile, the pressure at other altitudes can be extrapolated using the hydrostatic equation. This technique is limited to the upper troposphere and stratosphere.

A high spectral resolution differential ranging lidar measurement of the absorption in the wing of a collision broadened line provides a simple method for measuring pressure. The resultant experiment has limited accuracy, however, since only the absorption in the range-resolved element is used to determine pressure. The measurement is also extremely sensitive to laser frequency jitter, since the absorption in the line wing varies rapidly with frequency. In this chapter, we describe an integrated vertical path technique for measuring the pressure profile which has much higher sensitivity than a differential ranging method. We also discuss the properties of absorption troughs, broad regions of nearly uniform absorption between two strong lines, which can be used to greatly reduce the sensitivity of the pressure measurement to laser frequency shifts.

Oxygen is an excellent candidate for the measurement of pressure, since it is uniformly mixed in the atmosphere and, thus, the mixing ratio of oxygen does not have to be measured independently. The oxygen *A* band near 0.76 μm has strong lines of 1 to 2 cm^{-1} separation with energy and trough absorption suitable for an atmospheric measurement of pressure. In addition, the *A* band region has minimal interference from other species and is easily accessible using tunable lasers. Our laboratory at Goddard Space Flight Center constructed a dual wavelength lidar system for ground-based and aircraft measurements of pressure and temperature.

The following section describes the integrated path differential absorption technique which forms the basis for high accuracy (0.1 to 0.3%) pressure measurements. The theory of pressure measurements (integrated vertical path, differential ranging, and horizontal path) is then given, and methods for correcting for temperature effects are considered. The properties of absorption troughs are described and applied to the pressure measurement. The effects of finite laser bandwidth in a trough region are then considered. This is followed by simulation results and an analysis of the accuracy of the pressure measurements.

THEORY

Integrated Path Differential Absorption Experiment

For a lidar with a coincident transmitter and receiver operating at a single frequency ν with pulse energy E_ν^0, the energy received from an element of the atmosphere at range R with thickness ΔR is given as (Collis, 1969)

$$E_\nu(R) = E_\nu^0\left(\frac{A}{R^2}\right)Q\beta_\nu(R)\Delta R\tau_\nu^c(0,R)\tau_\nu(0,R), \tag{1-1}$$

where A is the area of the lidar receiver, Q is the optical efficiency of the system, $\beta_\nu(R)$ is the sum of the aerosol and Rayleigh backscatter coefficients of the atmosphere per unit solid angle per unit length, $\tau_\nu^c(0,R)$ is the two-way transmission of the atmosphere from range 0 to R due to scattering and continuum absorption effects, and $\tau_\nu(0,R)$ is the two-way transmission of the atmosphere due to resonant absorption.

A two-frequency differential absorption lidar technique forms the basis of the pressure measurement. One frequency is chosen in the distant wing of a collision broadened line in the oxygen *A* band, where the absorption is pressure sensitive. The line is selected so that the resultant measurement will be temperature insensitive. The reference frequency is chosen at a nearby location with minimal resonant absorption but essentially identical backscatter to that at the measurement frequency. For two closely spaced frequencies in the *A* band region, the attenuation due to scattering and continuum absorption processes at the two frequencies is nearly identical (Shettle and Fenn, 1975). Thus, the ratio of the signal returns at the wing and reference frequencies

eliminates the scattering and absorption properties of the atmosphere other than those associated with oxygen absorption. The result is

$$\frac{\tau_w(0,R)}{\tau_r(0,R)} = \frac{E_w(R)/E_w(0)}{E_r(R)/E_r(0)}, \tag{1-2}$$

where $\tau(0,R)$ is the two-way atmospheric transmission of oxygen, and the subscripts w and r denote measurements in the wing and at the reference frequency, respectively. Although a differential ranging technique utilizing the absorption over a single atmospheric layer (Schotland, 1974) could be used for the measurement of the pressure profile, much higher sensitivity can be obtained using an integrated path technique, as will be shown in a later section. For measurements made with finite laser bandwidth, the effects of non-zero absorption at the reference frequency complicate the analysis, since the measured quantity is not directly related to the differential absorption. The analysis of Eq. (1-2) may be simplified if the reference frequency measurement satisfies the following conditions: the absorption is sufficiently weak so that the exponential function can be approximated by a two-term expansion, the absorption over the bandwidth of the measurement can be described by a linear function of frequency, and the laser line shape is symmetric. For these conditions, it follows that Eq. (1-2) can be formulated using an effective frequency technique as

$$\frac{\tau_w(0,R)}{\tau_r(0,R)} = \int_{\nu_1}^{\nu_2} g_w(\nu)\exp\left\{-2\int_0^R \left[K(\nu,x) - K(\bar{\nu}_r,x)\right]dx\right\}d\nu, \tag{1-3}$$

where the measurement in the line wing is made over the spectral interval from ν_1 to ν_2 with a normalized laser line shape $g_w(\nu)$ and $K(\nu,x)$ is the absorption coefficient of oxygen (*i.e.*, the absorption per unit path) at frequency ν. Here, $\bar{\nu}_r$ is an effective frequency at the midpoint of the laser bandpass which gives the absorption at the reference frequency. As shown in Eq. (1-3), the ratio of the transmissions at the two measurement frequencies is directly related to the differential absorption coefficient. In an actual experiment, the measurement conditions of Eq. (1-3) can generally be satisfied.

Theory of Pressure Measurement

The absorption coefficient at frequency ν due to a single line of a linear molecule such as oxygen is given as

$$K(\nu) = C\left(\frac{p}{T^2}\right)\exp\left(-\frac{\varepsilon}{kT}\right)f(\nu-\nu_0), \tag{1-4}$$

where

$$C = q_0(1-q^*)\left(\frac{T_0}{k}\right)S(T_0)\exp\left(\frac{\varepsilon}{kT_0}\right),$$

and q_0 is the volume mixing ratio of oxygen in a dry atmosphere (0.2095), q^* is the volume mixing ratio of water vapor, $S(T_0)$ is the line strength of the transition at standard temperature T_0, p and T are the pressure and temperature of the atmospheric layer, respectively, ε is the ground-state energy of the transition, k is Boltzmann's constant, and $f(\nu - \nu_0)$ is the line shape at frequency ν for a line centered at ν_0.

For the case of atmospheric absorption by the oxygen *A* band, the line shape is significantly influenced by the effects of both collision and Doppler broadening. In fact, the line broadening from these sources is equal at an altitude near 10 km. Thus, the line shape in the *A* band must generally be represented by the Voigt profile, which is a convolution of independent collision-broadened and Doppler profiles. The Voigt profile is a complicated function, however, which is not easily used in analysis. For the far line wing, the Voigt profile can be represented by a power series expansion (Plass and Fivel, 1953) as

$$f(\nu-\nu_0)=\frac{b_c(p,T)}{\pi(\nu-\nu_0)^2}\left[1+d_1\left(\frac{b_c(p,T)}{\nu-\nu_0}\right)^2+d_2\left(\frac{b_c(p,T)}{\nu-\nu_0}\right)^4\right], \tag{1-5}$$

where

$$d_1=\left(\frac{3}{2}\right)a^{-2}-1,$$

and

$$d_2=\left(\frac{15}{4}\right)a^{-4}-5a^{-2}+1.$$

Here the parameter a is defined as

$$a=(\ell n2)^{1/2}\frac{b_c(p,T)}{b_d(T)},$$

where $b_c(p,T)$ is the collision-broadened line halfwidth, and $b_d(T)$ is the Doppler-broadened line halfwidth. These are defined as

$$b_c(p,T)=b_c^0(T)\left(\frac{p}{p_0}\right)=b_c^0(T_0)\left(\frac{p}{p_0}\right)\left(\frac{T_0}{T}\right)^n,$$

and (1-6)

$$b_d(T)=\left(\frac{2kT\ell n2}{M_0c^2}\right)^{1/2}\nu_0,$$

where M_0 is the mass of oxygen, c is the velocity of light, p_0 is standard pressure, and $b_c^0(T)$ is the collision-broadened line half-width at a pressure of 1 atm. Kinetic theory predicts the exponent n of the temperature dependence of the collision-broadened half-width to be one-half. For real molecules, however, it can vary over a significant range. Preliminary measurements for high J lines in the oxygen *A* band give a value of 0.7 (Korb, *et al.*, 1980). For $0.001 \le a \le 1$ and $(\nu-\nu_0) \ge 6b_d(T)$, or for $a \ge 1$ and $(\nu-\nu_0) \ge 5b_c(T)$, Eq. (1-5) has a maximum error of 0.1%. For the case of absorption in the far wings of the strong oxygen lines that will be considered here, $(\nu-\nu_0) > 0.35$ cm^{-1}, and Eq. (1-5) is accurate to better than 0.02% for altitudes above 1.5 km and to better than 0.001% for altitudes above 5 km. We note that the first term in Eq. (1-5) is the line profile in the far wings of a collision-broadened line.

The absorption coefficient in the far line wing is found from Eqs. (1-4) and (1-5) to be

$$K(\nu) = \frac{Cb_c^0(T)}{\pi p_0(\nu-\nu_0)^2}\frac{p^2}{T^2}\exp\left(-\frac{\varepsilon}{kT}\right) \times\left\{1-\frac{1}{(\nu-\nu_0)^2}\left[\left(b_c^0(T)\frac{p}{p_0}\right)^2-\frac{3}{2\,\ell n2}b_d^2(T)\right]\right\}, \tag{1-7}$$

where $b_c^0(T)$ is independent of pressure. Equation (1-7) provides the basic formulation for a horizontal path measurement of pressure and may also be used for a range-resolved pressure measurement. We note that in the far line wing, $(\nu - \nu_0) > 6b_c^0$, and the higher-order terms in Eq. (1-7) contribute < 3%. Thus, the first term is dominant, and the dependence of $K(\nu)$ on temperature is minimized for a line with ground-state energy $\varepsilon = (n + 2)kT$.

As was noted earlier, an integrated path vertical measurement of pressure provides much higher sensitivity than a range-resolved technique. Using the hydrostatic equation with the ideal gas law,

$$dp = -\frac{Mg}{k}\frac{p\,dz}{T}, \tag{1-8}$$

where g is the acceleration due to gravity and M is the average mass of a molecule in the atmosphere, Eq. (1-7) can be integrated over altitude. The resulting extinction for a one-way atmospheric path is

$$\left|\int_{z_1}^{z} K(\nu)dz\right| = \frac{C_1\left|p^2-p_1^2\right|}{(\nu-\nu_0)^2}\left[F_1-\frac{\left[b_c^0(T_0)\right]^2\left(p^2+p_1^2\right)F_2}{2(\nu-\nu_0)^2p_0^2}+\frac{3b_d^2(T_0)F_3}{2\,\ell n2(\nu-\nu_0)^2}\right], \tag{1-9}$$

where

$$C_1 = \frac{CkT_0^n b_c^0(T_0)}{2\pi M p_0},$$

and p_1 and z_1 are located at the laser. The absolute value signs are used in Eq. (1-9) since dz is negative for a downward-looking experiment. The functions F_i account for the effects of temperature on an integrated path measurement for the general case of a non-isothermal atmosphere, and they also account for small variations in g with altitude. They are defined in a mean value sense along the integrated path from p_1 to p as

$$F_1 = \frac{\int_{p_1}^{p}\frac{f(T)}{g}pdp}{\int_{p_1}^{p}pdp}, \tag{1-10a}$$

$$F_2 = \frac{\int_{p_1}^{p} \left(\frac{T_0}{T}\right)^{2n} \frac{f(T)}{g} p^3 dp}{\int_{p_1}^{p} p^3 dp}, \tag{1-10b}$$

and

$$F_3 = \frac{\int_{p_1}^{p} \left(\frac{T}{T_0}\right) \frac{f(T)}{g} p dp}{\int_{p_1}^{p} p dp}, \tag{1-10c}$$

where $f(T) = T^{-(n+1)} \exp(-\varepsilon/kT)$. For a ground-state energy of $\varepsilon = (n+1)k\overline{T}$, the function F_1 [the dominant term in Eq. (1-9)] is temperature independent, and the functions F_2 and F_3 (corresponding to the higher order terms) are only weakly temperature dependent. We note that $\overline{T}$ is an effective temperature defined so that $f(\overline{T}) = \overline{g}F_1$, where $\overline{g}$ is the average value of g in a pressure-weighted sense. Thus, the effects of pressure can be decoupled from those of temperature in Eq. (1-9) to first order by a proper choice of ground-state energy. The residual effects of temperature can be explicitly included in Eq. (1-9) using an estimated or measured temperature profile to evaluate the functions F_i. The temperature profile can also be calculated from the measured lidar pressure profile [with Eq. (1-8)] and then used in an iterative manner to redetermine the pressure profile. The errors due to temperature effects are discussed in a later section.

The extinction, as given by Eq. (1-9), is directly proportional to the difference in the squares of the pressures at the measurement altitude and at the laser, respectively. We note that the higher order terms in Eq. (1-9) contribute only a few percent. Equation (1-9) is thus a quadratic equation in the variable $x = p^2$. It can be solved for pressure versus height using standard algebraic techniques given the pressure at the laser altitude (p_1), which is zero for the case of a satellite measurement.

Trough Technique

The absorption coefficient and extinction in the line wing are not only sensitive to pressure but also have a strong dependence on laser frequency shifts [see Eqs. (1-7) and (1-9)]. The frequency dependence of the pressure measurement may be greatly reduced using a relatively broad absorption trough, the region of minimum absorption, between pairs of strongly absorbed oxygen lines. The basic properties of absorption troughs formed by two lines will be developed in this section. The discussion includes methods for evaluating the trough frequency, the shape of the trough region, and the effects of laser frequency jitter. The perturbation effects of weak isotopic lines in the neighborhood of the troughs will be discussed in the numerical treatment given in the next section.

For the case of two absorption lines at frequencies ν_1 and ν_2 the extinction for a vertical path measurement [Eq. (1-9)] or the absorption coefficient [for either a horizontal or vertical path measurement, Eq. (1-7)] can be represented as

$$K'(\nu) = \frac{A_1}{(\nu-\nu_1)^2} + \frac{A_1 h_1}{(\nu-\nu_1)^4} + \frac{A_2}{(\nu-\nu_2)^2} + \frac{A_2 h_2}{(\nu-\nu_2)^4}. \tag{1-11}$$

Here, $K'(\nu)$ is either the absorption coefficient or the extinction, and A_i and h_i are pressure-dependent functions which can be easily calculated from either Eq. (1-7) or Eq. (1-9), respectively. The trough frequency ν_t, the position of minimum absorption, can be found by setting the derivative of Eq. (1-11) equal to zero and using the Newton-Raphson method. For the case of a trough in the far line wing such that $h_i << (\nu_t - \nu_i)^2/2$, the trough frequency is

$$\nu_t = \frac{\nu_1 + \nu_2 (A_1/A_2)^{1/3}}{1 + (A_1/A_2)^{1/3}}, \tag{1-12}$$

where, for an integrated path vertical measurement,

$$\frac{A_1}{A_2} = \frac{S_1(T_0) b_{c_1}^0(T_0) F_1^{(1)} \exp\left(\frac{\varepsilon_1}{kT_0}\right)}{S_2(T_0) b_{c_2}^0(T_0) F_1^{(2)} \exp\left(\frac{\varepsilon_2}{kT_0}\right)},$$

and the superscripts of F are used to designate the respective line. For troughs formed by lines of nearly equal ground-state energy such as we consider here, A_1/A_2 reduces to the ratio of the strength-width products for the two lines. For the trough regions in the oxygen A band between 13150 and 13154 cm^{-1}, $R(\nu_t - \nu_i)/b_c^0 > 6$ for the primary oxygen lines, and the contribution of the terms involving h_i in Eq. (1-11) is <2% at ground level and decreases rapidly with altitude. Thus Eq. (1-12) provides a reasonable first-order solution for ν_t.

To analyze the frequency dependence of the trough regions, we use a Taylor's series expansion of $K'(\nu)$ about the trough position. That is,

$$K'(\nu) = K'(\nu_t) + \frac{1}{2}\frac{d^2K'(\nu_t)}{d\nu^2}(\nu - \nu_t)^2 + ..., \tag{1-13}$$

where the first order term in $dK'/d\nu$ does not appear since the trough, by definition, is the position of zero slope. For distances from the trough <0.01 cm^{-1} and for $(\nu_t - \nu_i) > 0.5$ cm^{-1}, the quadratic expansion of Eq. (1-13) is accurate to better than 0.03%. The shape of the trough region may be readily evaluated from Eqs. (1-11) and (1-13) as

$$\Delta K'(\nu) = (\nu - \nu_t)^2 \sum_{i=1}^{2} \frac{3A_i}{(\nu_t - \nu_i)^4}\left[1 + \frac{10h_i}{3(\nu_t - \nu_i)^2}\right], \tag{1-14}$$

where $\Delta K'(\nu) = K'(\nu) - K'(\nu_t)$. For the special case of two lines that are well separated and have equal strength - width products, the trough location is equidistant from the two lines by Eq. (1-12), and it follows from Eqs. (1-11) and (1-14) that

$$\frac{\Delta K'(\nu)}{K'(\nu_t)} = \frac{3(\nu - \nu_t)^2}{(\nu_t - \nu_i)^2}. \tag{1-15}$$

Thus, in the region of the trough, the fractional change in extinction for a vertical path [Eq. (1-9)] or the absorption coefficient [Eq. (1-7)] varies as the square of the ratio of the distance from the trough to the distance of the trough from the absorption lines forming the trough. For typical parameters such as laser frequency shifts of 0.005 to 0.01 cm^{-1} and $(\nu_t - \nu_i) \cong 0.5$ cm^{-1}, the corresponding error in extinction or absorption

coefficient is 0.003 to 0.12%. On the other hand, for a measurement in the far wing of a single line, it follows from either Eq. (1-7) or Eq. (1-9) that

$$\frac{dK'(\nu)}{K'(\nu)} = -\frac{2d\nu}{(\nu - \nu_i)}. \tag{1-16}$$

For the same parameters as assumed above, the error in extinction for a measurement in the wing of a single line is seen to be from 2 to 4%. Thus the trough technique reduces the errors due to laser frequency instability by almost two orders of magnitude.

Finite Bandwidth

The use of trough regions for the pressure measurement simplifies the analysis of finite laser bandwidth effects, since the absorption coefficient or extinction in the trough can be represented as a parabola to high accuracy. For a laser with a uniform bandpass which is centered on an absorption feature with a parabolic

frequency dependence (*e.g.*, a trough), the measured transmission can be represented by a monochromatic measurement at the effective frequency

$$\bar{\nu}_e = \nu_t \pm \frac{\Delta\nu}{2\sqrt{3}}, \tag{1-17}$$

where $\Delta\nu$ is the laser bandwidth. For laser bandwidths <0.02 cm^{-1} and $|\nu_t - \nu_i| \geq 0.5$ cm^{-1}, the accuracy of Eq. (1-17) is better than 0.01%. Thus, for finite bandwidth measurements at both the trough and reference frequencies, Eq. (1-3) can be represented by equivalent monochromatic measurements at $\bar{\nu}_e$ and $\bar{\nu}_r$, as

$$\frac{\tau_t(0,R)}{\tau_r(0,R)} = \frac{\tau_{\bar{\nu}_e}(0,R)}{\tau_{\bar{\nu}_r}(0,R)}, \tag{1-18}$$

where τ_t and τ_r are the transmissions at the trough and reference frequencies, respectively. Equation (1-17) may also be used to derive the result for a range-resolved experiment with finite bandwidth. In this case, the measured quantity is determined from the ratio of the signal returns at two adjacent ranges. It follows from Eqs. (1-3) and (1-17) that the resulting measurement on the interval from R_1 to R_2 can be approximated by

$$\frac{\tau_t(R_1,R_2)}{\tau_r(R_1,R_2)} = \frac{\tau_{\bar{\nu}_e}(R_1,R_2)}{\tau_{\bar{\nu}_r}(R_1,R_2)}, \tag{1-19}$$

if ν_t is independent of range from R_1 to R_2. This assumption is valid even for the case of isotopic lines near the trough location, as will be shown in the next section. Thus, for the three different cases considered (vertical integrated path, horizontal path, and differential ranging), the differential absorption at the monochromatic frequencies $\bar{\nu}_e$ and $\bar{\nu}_r$ can be used to represent the results of a finite bandwidth measurement. This result can not only be applied to the analytical models we have used to represent the absorption but can also be used with the numerical models to be described in the following section.

ANALYSIS

The trough regions with appropriate absorption for the pressure measurement occur in the *R* branch of the oxygen *A* band near 13150 cm^{-1} (760 nm). In this section, the spectra of oxygen are calculated using numerical

techniques, and the effects of temperature, frequency stability, humidity, and sensitivity are considered using the analysis methods discussed in prior sections.

Atmospheric Effects

Figures 1-1 and 1-2 show the trough regions in the oxygen *A* band near 760 nm. Figure 1-1 gives the extinction of oxygen for two-way atmospheric paths from space to the surface and to 4 km altitude, respectively, while Figure 1-2 gives the absorption coefficient at the surface. The atmospheric model used for these calculations is a multi-layer one dimensional model with up to 50 layers. The line parameters used are from the AFGL calculations (McClatchey, *et al.*, 1959; Rothman, 1981), where the line strengths and widths have been adjusted to agree with the measurements of Burch and Gryvnak (1969). We note that the troughs in the region from 13150 to 13154 cm^{-1} have ground-state energies appropriate ($\varepsilon \cong 300$ cm^{-1}) for integrated path vertical measurements of pressure, while those from 13156 to 13158 cm^{-1} have energies appropriate ($\varepsilon \cong 500$ cm^{-1}) for horizontal path or range-resolved pressure measurements. The extinction and absorption coefficients in the various trough regions show the p^2 dependence characteristic of absorption in the far line wings. As shown, the positions of the troughs are shifted by the presence of weak isotopic oxygen lines, $O^{16}O^{18}$, which occur in the vicinity of each trough. It is interesting to note that the isotopic lines appear as prominent features in the integrated path vertical case shown in Figure 1-1, whereas they are weak features in Figure 1-2. The relatively strong extinction from the isotopic lines shown in Figure 1-1 occurs primarily in the direct vicinity of these lines. It arises from the absorption of upper atmospheric layers which have narrow line widths and absorb strongly near the line center and only weakly in the line wings (*e.g.*, at the trough location).

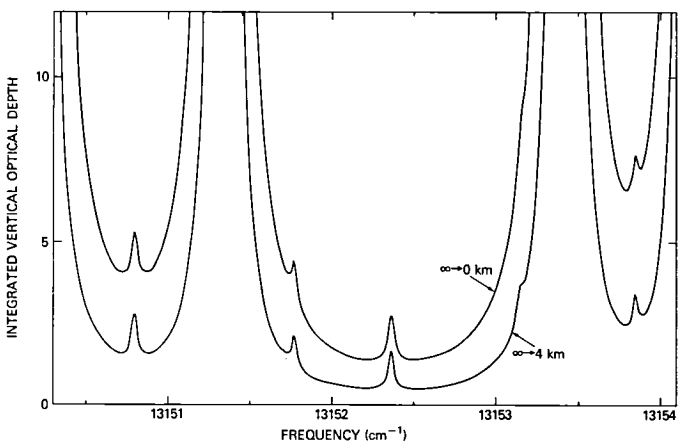

Figure 1-1. The integrated absorption coefficient (extinction) of oxygen in the 13150 cm^{-1} region for two-way atmospheric paths from space to ground level and 4 km altitude, respectively.

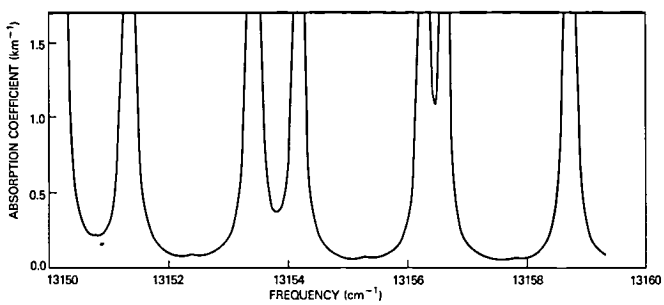

Figure 1-2. The absorption coefficient of oxygen in the 13150 cm^{-1} region at ground level.

Figure 1-3 shows an example of a calculation of the temperature dependent functions F_i for an integrated path measurement, as given by Eq. (1-10). The data are presented as the fractional change in $F_i(z)$ with respect to the value at the surface. The calculations correspond to a high-altitude aircraft or satellite experiment for a standard atmospheric temperature profile using the trough at 13152.49 cm^{-1}. For this trough, the average ground-state energy is close to satisfying the condition for temperature desensitization, *viz.*, $\varepsilon = (n+1)k\overline{T}$. As shown, the function F_1 has little variation with altitude (or, thus, temperature). As expected, the functions F_2 and F_3 corresponding to the higher order terms in Eq. (1-9) have positive and negative altitude dependencies, respectively.

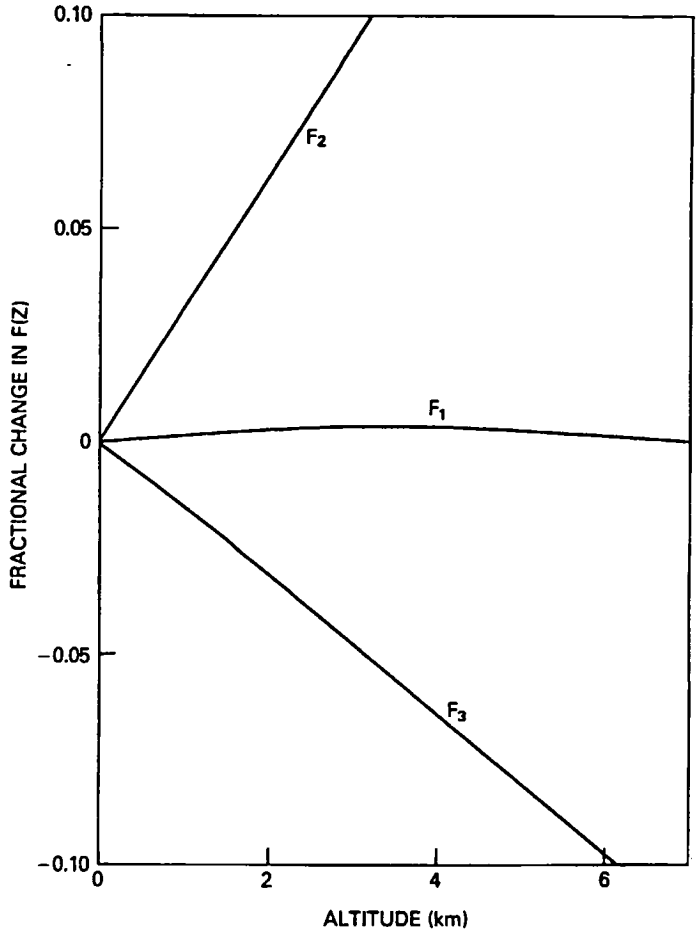

Figure 1-3. The fractional change in the temperature dependent functions F(z) *with respect to their value at ground level for the trough at 13152.49 cm^{-1} (see Eq. 1-10). Results are for a satellite experiment and a standard atmospheric temperature profile.*

Figure 1-4 shows the effect of temperature errors on an integrated path pressure measurement from a high altitude aircraft or satellite for a laser bandwidth of 0.02 cm^{-1}. Simulations were performed at three different troughs by introducing a 2 K bias error in the nominal temperature profile and then calculating the change in pressure necessary to produce the same extinction. As shown, the pressure errors for a 2 K temperature error are generally <0.1% and average ~0.05%. We note that, although the three troughs shown are all located within 3 cm^{-1}, the altitude dependence of the error is quite different. That is, the error is a decreasing function of altitude for the troughs below 13153 cm^{-1} with average ground-state energies <260 cm^{-1}, whereas the error increases with altitude for the troughs beyond 13153 cm^{-1} with energies >300 cm^{-1}.

Figure 1-5 shows an expanded view of the trough near 13152.49 cm^{-1} for an integrated path satellite-based experiment. The data are shown as the fractional change in extinction due to frequency shifts about the trough at 13152.49 cm^{-1}. The presentation of the extinction data in this form allows effects at the 0.1% level to be seen easily. As shown, the trough position for measurements from space to various altitudes exhibits a slight shift to higher frequencies with increasing altitude. This occurs since the nearby isotopic line at 13152.36 cm^{-1} not only causes an overall shift of the trough away from the isotopic line, but also contributes

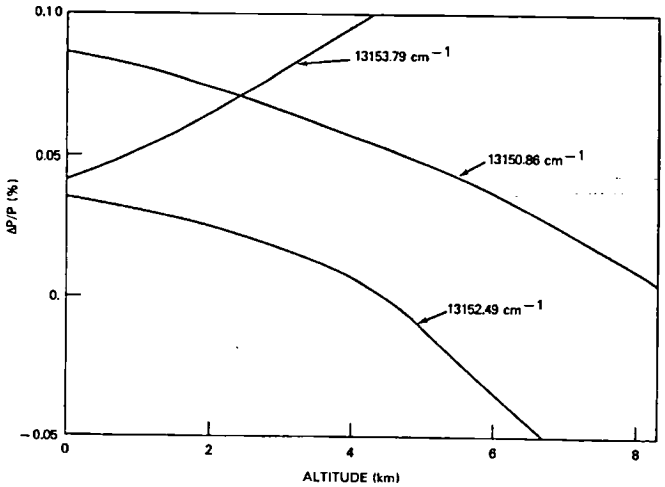

Figure 1-4. The pressure error (in percent) due to a 2 K temperature profile uncertainty for a satellite-based lidar experiment with a 0.02 cm^{-1} laser bandwidth. Results are shown at three trough locations near 13150 cm^{-1}.

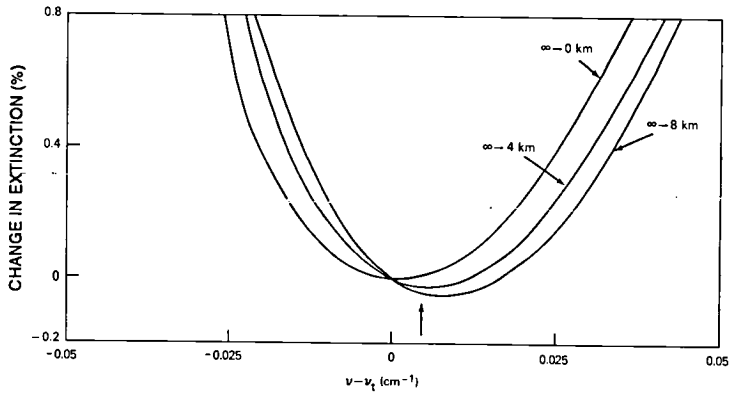

Figure 1-5. The percent change in extinction due to frequency shifts about the trough at 13152.49 cm^{-1} (the infinity to zero trough) for measurements from space to various altitudes.

proportionately more to the total trough extinction at high altitude. The shape of the trough region closely approximates a parabola within 0.01 cm^{-1} of the trough as expected from Eq. (1-14). At larger distances from the trough, the effects of asymmetry introduced by the isotopic line become increasingly important. For this nearby line, the cubic and higher order terms in the Taylor's series expansion of Eq. (1-13) are not negligible, as in the case of the more distant primary oxygen lines. Thus, the strong oxygen lines dominate the absorption in the trough, whereas the weak isotopic lines cause the fine scale effects which are observed.

The data of Figure 1-5 may be used to evaluate the effects of laser frequency stability on a pressure measurement. For optimum accuracy over a given altitude range, the laser frequency should be adjusted to approximately coincide with a trough for the mean measurement altitude. For the case shown in Figure 1-5, the frequency is shifted by ~0.005 cm^{-1} relative to the trough for the space-to-ground level measurement. A laser frequency stability of ±0.01 cm^{-1} then corresponds to fractional errors in extinction <0.14%. Since the extinction varies nearly quadratically with pressure by Eq. (1-9), the corresponding error in pressure is <0.07%.

Water vapor affects the pressure measurement by lowering the mixing ratio of oxygen in the atmosphere, as given by Eq. (1-4). For an integrated path vertical measurement, this effect is partially compensated, since water vapor also lowers the average mass of a molecule in the atmosphere [Eq. (1-9)]. We have calculated the composite of the above effects on a pressure measurement for a standard temperature profile and for an error in the assumed water vapor content of the atmosphere of ±30% of its saturation value. This corresponds to actual values of relative humidity of 20% or 80% as compared with an assumed value of 50%. For a downward-viewing experiment from a satellite or a high-altitude aircraft, the resultant errors in pressure are <0.05% for altitudes above 2 km and <0.1% for measurements extending to ground level.

Discussion of Sensitivity

To evaluate the sensitivity of a pressure measurement, the relationship between the experimental parameters and the pressure measurement error must be determined. We compare here the sensitivity of differential ranging and integrated vertical path measurements for a generalized set of conditions. The following analysis

treats the case of a generalized atmospheric line profile and measurements in a trough region with finite laser bandwidth.

For a finite bandwidth integrated vertical path measurement from a laser at altitude z_0 to altitude z, it follows from Eqs. (1-3) and (1-17) that

$$\frac{d}{dp}\tau_d(z_0,z) = -2\tau_d(z_0,z)\frac{d}{dp}K'_d(z_0,z), \tag{1-20}$$

where τ_d is the ratio of the transmissions at a trough region represented by $\bar{\nu}_e$ and a reference region by $\bar{\nu}_r$, and K'_d is the difference in extinction between these two frequencies for a one-way atmospheric path (*i.e.*, the integrated differential absorption coefficient). From Eq. (1-9), it can be shown that

$$\frac{d}{dp}K'_d(z_0,z) = \frac{d}{dp}K'_d(\infty,z). \tag{1-21}$$

It then follows from Eqs. (1-20) and (1-21) that the fractional error in the pressure measurement is

$$\left|\frac{\Delta p}{p}\right|_z = \frac{1}{\eta(\infty,z)[2K'_d(\infty,z)](S/N)}, \tag{1-22}$$

where the coefficient of pressure sensitivity η is given as

$$\eta(\infty,z) = \frac{dK'_d(\infty,z)/K'_d(\infty,z)}{dp/p},$$

and the composite signal to noise ratio (S/N) for the measurement is related to the fractional error in transmission by $(S/N)^{-1} = d\tau/\tau$. We note that η gives the effective pressure dependence of the extinction through $K'_d \propto p^{\eta}$ and is nearly a constant in the far line wing with a value of 2. For the trough at 13152.49 cm^{-1} the coefficient η varies from 1.98 for downward-viewing measurements, where the end point is near the surface, to a value approaching 2 for measurements where the end point is at high altitude. For a range-resolved or horizontal path finite bandwidth experiment, an analogous expression for the pressure error can be derived from Eqs. (1-3), (1-7), and (1-19) as

$$\left|\frac{\Delta p}{p}\right|_z = \frac{1}{\eta(z)[2K'_d(z)\Delta R](S/N)}, \tag{1-23}$$

where $K'_d(z)$ is the differential absorption coefficient at altitude z and ΔR is the distance over which the pressure measurement is made.

Equations (1-22) and (1-23) give the dependence of the pressure errors on the lidar experimental parameters. In each case, the error in pressure is inversely proportional to the product of the coefficient of pressure sensitivity, the optical depth, and the S/N. For the differential ranging or horizontal path cases given by Eq. (1-23), the optical depth and coefficient η (which is essentially a constant) correspond to the measured path, as expected. This is not the case, however, for the integrated vertical path measurement described by Eq. (1-22). As shown, the optical depth and coefficient η correspond to a path from infinity to altitude z, independent of the actual measured path. Thus, for an upward-looking experiment from z_0 to z the optical path and η in Eq. (1-22) are evaluated on the interval from z to infinity, although this path is not actually traversed in the experiment.

The surprising result from Eq. (1-22) can be better appreciated if one considers the physical basis of an integrated path vertical pressure measurement. That is, the measured quantity is the pressure at altitude z, which is determined from the hydrostatic equation by the total mass of the atmosphere above altitude z, *i.e.*, from z to infinity. Thus, an integrated path measurement of pressure along any vertical path is equivalent physically to a measurement of the mass above altitude z. The properties of the measured path enter Eq. (1-22) through the *S/N*, which corresponds to the actual path.

The relative accuracy R of a vertical pressure measurement using an integrated path method, as compared with a differential ranging method, may be evaluated by taking the ratio of Eq. (1-23) to Eq. (1-22). It follows from Eqs. (1-7) and (1-9) that

$$R \equiv \frac{kT}{Mg}\frac{\sqrt{2}}{2\Delta R}, \tag{1-24}$$

where the total absorption for each measurement is assumed to be equal at the trough appropriate to each measurement. Equation (1-24) also includes the assumption that the *S/N* for the integrated path measurement is higher by a factor of $\sqrt{2}$ than that for the differential ranging method, since only two signal returns are required for the former method, whereas four are required for the latter. We note that the factor kT/Mg in Eq. (1-24) is the pressure scale height of the atmosphere (~8 km). Thus, for a ground- or aircraft-based lidar measurement with a typical resolution of 100 m, an integrated path measurement will have an accuracy more than fifty times better than a corresponding differential ranging measurement. Further, as given by Eq. (1-24), this result is essentially independent of the altitude of the pressure measurement.

Measurement Technique and Simulations

A measurement of pressure requires that the corresponding altitude be accurately determined, since pressure varies at a rate of ~0.1% per 10 m in the lower troposphere. For a target with an impulse response and a laser whose pulse length is small compared to the detection time, the expected error in determining the height of a single measurement is one-quarter the width of the detection range gate. Laser systems with pulse lengths of the order of 10 nsec and range-gated detection systems with 10-bit accuracy, 50 nsec/range bins, and 2000 range bins are currently commercially available. These parameters correspond to an error in height of 1.9 m or to a 0.02% error in pressure for measurements on a single range bin. For measurements of the pressure profile, the results may be averaged both vertically for a number of range bins and temporally for a number of pulses to reduce the effects of random photon fluctuations. We note that averaging further reduces the error in the height determination.

There are a number of weakly absorbing regions which can be used as the reference frequency for the pressure measurement. These include the region between 13168 and 13170 cm^{-1}, which is beyond the head of the A band at 13165 cm^{-1}. This region is free of absorption lines and has a two-way optical depth through the atmosphere of <0.05. Alternatively, the strongly absorbing pressure measurements at 13150.86 or 13153.8 cm^{-1} could use the relatively weak trough absorption at 13152.5, 13155.4, or 13157.5 cm^{-1} for the reference frequency.

Figure 1-6 shows simulations of the error in ground-based upward-viewing measurements of the pressure profile due to photon fluctuations on the return signal, which has both signal and background radiation components and a 10-bit signal processing accuracy per resolution element. The results as calculated from Eq. (1-22) are given for three different troughs in the 13150 cm^{-1} region for an integrated path experiment. The return signals backscattered from the atmosphere were calculated from Eq. (1-1) using parameters similar

to those of our system in 1982 (see Table 1-1). The contributions of daytime sky background radiation are included in the analysis, although the effects are small compared with the relatively large backscattered lidar signals. The analysis includes both Rayleigh and aerosol components (Elterman, 1968) in the atmospheric backscatter. The transmission at each trough, the integrated absorption coefficient for the appropriate path, and the coefficient of pressure sensitivity needed in Eq. (1-22) were calculated using a line-by-line multi-layer atmospheric program, as described in Chapter 2. As shown, the simulations indicate eight shots are sufficient to obtain high accuracy pressure measurements for altitudes up to 4 km. This is a direct consequence of Eq. (1-22). Accurate measurements at higher altitudes can be obtained by increasing the number of shots which are averaged. However, the effects of residual temperature sensitivity and humidity will limit the accuracy of the pressure measurements to 0.1%. The results obtained in Figure 1-6 using Eq. (1-22) were also independently checked by direct numerical analysis. That is, the pressure profile in the atmospheric model was varied by a small increment, and the resultant change in transmitted signal compared to the noise level due to photon fluctuations and the effects of 10-bit signal processing errors.

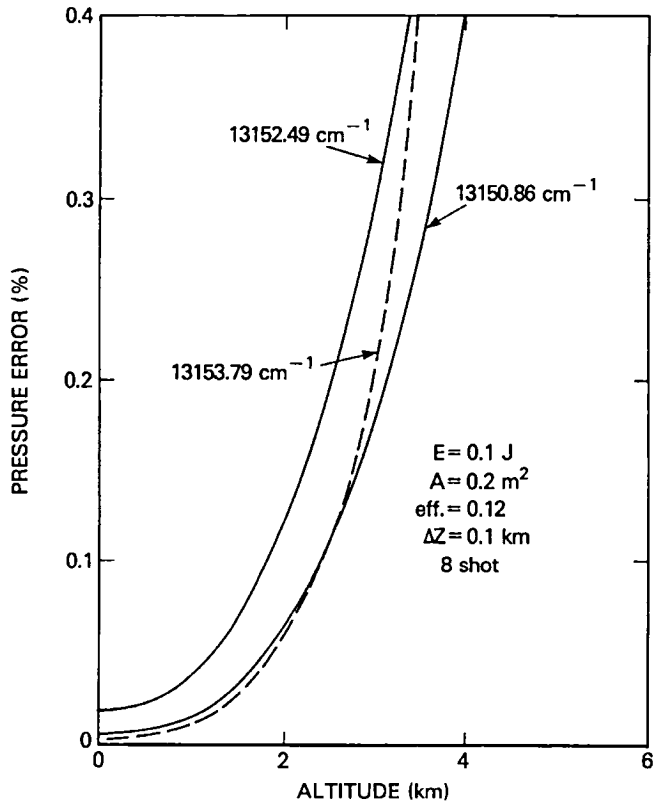

Figure 1-6. Simulated accuracy of pressure profile measurements for a ground-based lidar system using an integrated path technique. Results are shown for a single shot measurement at three trough locations in the 13150 cm^{-1} region (see Table 1-1).

Figure 1-7 shows simulations of the error in the pressure profile and surface pressure due to photon fluctuations for an integrated path measurement from the Space Shuttle at an altitude of 200 km. The analysis is similar to that described for Figure 1-6, and the system parameters are given in Table 1-1. To reduce the effect of solar radiation backscattered from the Earth's surface (an albedo of 0.1) and from the atmosphere to a

sufficiently low level, a receiver field of view of 0.3 mrad is used for the simulation in conjunction with a 0.2 cm^{-1} spectral detection bandwidth. A piezoelectrically scanned Fabry-Perot etalon could be used to perform the relatively narrowband spectral detection (NASA, 1979). Results are given for measurements both of the pressure profile and surface pressure. For the pressure profile, a 175-shot average of the atmospheric backscatter is used, which corresponds to a spatial resolution of 125 km at a laser repetition rate of 10 Hz. The simulations of the pressure profile use 1 km vertical averaging. For surface pressure, a 35 shot average of the backscatter from the surface (50 nsec range bins) is sufficient to provide good accuracy and corresponds to 25 km spatial resolution. As shown, the trough at 13150.86 cm^{-1} provides high accuracy measurement of the pressure profile over the 1 to 6 km altitude range and also allows high accuracy measurement of surface pressure to 0.1%. On the other hand, the trough at 13153.79 cm^{-1} can be used to obtain high accuracy measurements of the pressure profile, particularly above 3 km, while the trough at 13152.49 cm^{-1} yields the highest accuracy measurements of surface pressure.

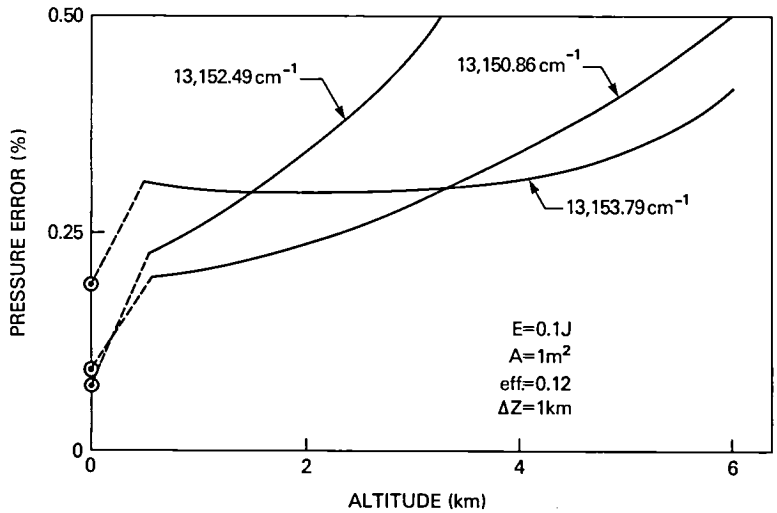

Figure 1-7. Simulated accuracy of a Shuttle-based lidar pressure experiment at 200 km for three tough locations in the 13150 cm^{-1} region. A 175 shot average (125 km horizontal resolution) is used to determine the pressure profile and a 35 shot average (25 km horizontal resolution) is used for surface pressure (see Table 1-1).

Table 1-1. System Parameters Used for Simulated Ground- and Shuttle-Based Pressure Profile (and Surface Pressure) Measurements

Parameter	Ground-based	Shuttle-based (at 200 km)
On-line frequency (cm^{-1})	13150.86, 13152.49, 13153.79	13150.86, 13152.49, 13153.79
Reference frequency (cm^{-1})	13168-13170, 13155.4,[a] 13157.5[a]	13168-13170, 13155.4,[a] 13157.5[a]
Pulse energy (J)	0.1	0.1
Spectral bandwidth (cm^{-1})	0.02	0.02
Repetition rate (Hz)	10	10
Spectral modes	3	3
Pulses averaged	8	175, 35[b]
Horizontal resolution (km)	—	125, 25[b]
Vertical resolution (km)	0.1	1, 0.0075[b]
Telescope area (m^2)	0.2	1
Receiver field of view (mrad)	1	0.3
Optical efficiency	0.5	0.5
Quantum efficiency	0.24	0.24
Detection bandwidth (cm^{-1})	20	0.2
Digitization (bits)	10	10
Range gate (nsec)	50	50

[a] For use with on-line measurement frequencies of 13150.86 or 13153.79 cm^{-1}.
[b] Surface pressure measurement.

The accuracy of lidar pressure profile and surface pressure measurements from a satellite will be only slightly affected by subvisible cirrus or other thin clouds, since the attenuation of the clouds is the same at both the pressure sensitive and reference frequencies and thus is eliminated in the pressure determination. The presence of a cloud in the lidar field of view will be apparent since the backscatter from the cloud greatly enhances the signal in the corresponding range elements. For measurements in the presence of optically thick clouds, the pressure profile could be measured above the cloud, and the cloud-top pressure height could be determined using the signal reflected from the cloud. Simulations of the accuracy of cloud-top pressure height determinations from the Space Shuttle, for the trough at 13153.79 cm^{-1}, show the effects of random noise due to photon fluctuation are <0.2% for altitudes from 0.5 to 8 km for a six shot average, a 50% cloud reflectance, and the parameters of Table 1-1.

The integrated path technique for measuring the pressure profile and surface pressure [Eq. (1-9)] gives the pressure at altitude z with a vertical resolution determined by the laser pulse length and the width of the range gate at altitude z. For an atmosphere in hydrostatic equilibrium, the pressure profile information obtained with the integrated path technique is essentially identical to that which could be obtained using a range-resolved technique [Eq. (1-7)]. The ability to determine a profile from range-gated integrated path absorption information is peculiar to the pressure measurement. As previously discussed, this allows the pressure profile to be determined to much higher accuracy than could be obtained with a differential ranging measurement. This is a critical feature in pressure measurements with an accuracy level of the order of a few tenths of a percent.

As shown in Eq. (1-22), the fractional error in the pressure measurement is inversely proportional to the product of the coefficient of pressure sensitivity (equal to nearly 2), the two-way optical depth from space to altitude z, and the *S/N*. For the trough at 13150.86 cm^{-1} with a two-way optical depth from space to the surface of 4, a 1% measurement of the relative transmission (*i.e.*, a *S/N* of 100) yields a 0.125% measurement of surface pressure, a 0.2% measurement of the pressure profile at an altitude of 2 km, and a 0.3% measurement at 4 km. Thus, relatively large optical depths and a nonlinear relationship of the optical depth to the measurement parameter can be used to significantly enhance the measurement accuracy. There is also experimental evidence to indicate that measurements at this level of accuracy are feasible. We have previously reported temperature measurements over a 1 km horizontal atmospheric path with an average noise level of 0.5% or 0.3 K (a *S/N* of 200) (Kalshoven, *et al.*, 1981). We have also made horizontal path measurements of pressure using the same system with similar *S/N's*, which gave an average noise level in terms of pressure of better than 1 mb (0.1%) (Kalshoven and Korb, 1982).

Other Error Sources

The effects of differential spectral backscatter between the pressure sensitive and reference frequency cause errors in the measurement of the pressure profile (clear air backscatter), while the effects of differential spectral reflectance cause errors in the measurement of surface pressure. The magnitude of these errors is generally proportional to the spectral separation of the two measurement frequencies. We consider the case of a 20 cm^{-1} separation, which corresponds to a worst case analysis. In the case of reflection from terrestrial targets, the maximum differential reflectance error in the *A* band region is 0.01% per wavenumber for a silt loam target, as given by Grant (1982). This corresponds to a 0.2% error in transmission ($d\tau/\tau$) for a 20 cm^{-1} separation. For the 13150.86 cm^{-1} trough with a two-way atmospheric optical depth of 4 and a coefficient of pressure sensitivity η of 2, the error in surface pressure, as given by Eq. (1-22), is 0.125 times the error in transmission or 0.025%. In the case of backscatter from the atmosphere, the error due to differential spectral backscatter effects arises from two sources: the wavelength dependence of the aerosol backscatter and the relative contribution of backscatter from aerosol and molecular components, which are not known precisely. We note that the attenuation and scattering of aerosols are given by a smoothly changing function of wavelength in the *A* band region, as given by Shettle and Fenn (1975). If first-order corrections are made for these effects, the residual error in transmission is 0.07% for an error in the spectral dependence of the aerosol backscatter of $\lambda^{-1/2}$ and for a 20% error in the magnitude of the relative contributions of aerosol and molecular backscatter. For a measurement of the pressure profile at an altitude of 5 km using the trough at 13150.86 cm^{-1}, the corresponding error in pressure, from Eq. (1-22), is 0.035%.

The return signals backscattered from the atmosphere (or the Earth's surface) at the pressure sensitive and reference frequencies can be separated and detected with high efficiency with a single detector by introducing a small time delay between the two outgoing laser pulses. A time delay introduces two different error sources into the differential absorption measurement. In the case of measurements of the atmospheric pressure profile, turbulence and advection cause the aerosol composition within a given volume element of the atmosphere to change over relatively short time scales. We have calculated the separation time between the two pulses (the advective time scale) as 0.5 msec for a 0.1% measurement of transmission ($d\tau/\tau$), using the analysis given by Schotland (1974) for the following parameters: an upward viewing ground-based measurement at an altitude of 2 km, a receiver field of view of 1 mrad, an aerosol velocity of 10 m/sec, and a 20% variation in backscatter between adjacent atmospheric elements. The resultant error in the pressure profile at 2 km altitude using the trough at 13150.86 cm^{-1} is 0.02% [see Eq. (1-22)] for a single pulse measurement. We also note that a time delay as short as 0.1 msec between the two measurement frequencies is feasible, which would reduce the error in pressure to 0.004% (Schwemmer, *et al.*, 1982).

In the case of a downward viewing Shuttle-based experiment, the Shuttle motion during the time delay between the pressure sensitive and reference pulses causes each laser beam to be backscattered from a slightly different field of view. A 0.2 msec delay allows temporal separation of the two frequencies and corresponds to a 2.5% change in field of view for the parameters of Table 1-1 and a Shuttle orbit. The resulting error in a measurement of the pressure profile at 5 km altitude for the 13150.86 cm^{-1} line is 0.02% for a change in backscatter for the differential change in field of view of $\Delta\beta/\beta = 0.2$ and a 175 pulse average. We assume that the change in backscatter between different pulse pairs for the differential field of view is uncorrelated, as is expected. In the case of a surface pressure measurement, the error is 0.05% for the 13150.86 cm^{-1} line for a change in surface reflectance for the differential field of view of $\Delta\rho/\rho = 1.0$ and a 35 pulse average.

Speckle affects the measurement of pressure, since the lidar signal returns are backscattered from the atmosphere or from the Earth's surface, which can be considered as rough targets. The speckle variance is inversely proportional to the product of the number of independent spatial and temporal cells observed, the number of laser spectral modes, and the number of pulses used for a measurement (Goodman, 1965). For measurements at the relatively short wavelengths of the oxygen *A* band, the effects of speckle are small. For upward looking pressure profile measurements (see Table 1-1) with 100 m vertical resolution, 3 laser spectral modes, and an 8 pulse average, the total number of independent cells is $>10^8$. For a downward viewing measurement of the pressure profile with 1 km vertical resolution and a 175 pulse average or surface pressure with a 35 pulse average, the number of independent cells is $>10^{10}$ or 3×10^7, respectively. For the trough at 13150.86 cm^{-1}, the corresponding error is <0.01% for an upward or downward viewing measurement of the pressure profile at 5 km altitude, as well as for a measurement of surface pressure.

Table 1-2 gives a summary of the various error sources affecting the pressure measurement. As shown, shot noise is generally the dominant error source for pressure measurements. For ground-based upward viewing profile measurements and Shuttle-based surface pressure determinations, the effects of temperature, humidity, and laser frequency stability are also important contributors to the total noise.

Table 1-2. Summary of Error Sources for Pressure Profile and Surface Pressure Measurements Using the Absorption Trough at 13150.86 cm^{-1}, a Reference Frequency at 13168 cm^{-1}, and the System Parameters of Table 1-1.

		Pressure error (%)		
Error source	Specification	Ground-based (<5 km)[a]	Shuttle-based (<5 km)[b]	Shuttle-based surface pressure[c]
Shot noise	Table 1-1	0.01-0.4	0.2-0.4	0.1
Temperature[d]	2 K	<0.1	<0.1	<0.1
Humidity[d]	±30% of saturation value	<0.1[e]	<0.05	<0.1
Frequency stability (on-line)[d]	0.005 cm^{-1}	0.07	0.07	0.07
Altitude	50 nsec range bins	<0.01	<0.01	<0.01
Digitization	10 bit	<0.02	<0.005	0.002
Differential spectral backscatter[d]	20 cm^{-1}	0.035	0.035	0.025
Temporal effects				
Advection	0.2 msec	<0.01	<0.01	———
Shuttle motion	0.2 msec	———	0.02	0.05
Speckle	Table 1-1	<0.01	<0.01	<0.01
Total (rms)		0.16-0.43	0.24-0.42	0.2

[a]8 pulse average.
[b]175 pulse average.
[c]35 pulse average.
[d]On-line laser and pulse averaging was not used.
[e]±20% of saturation value for ground-based upward viewing measurement.

SUMMARY AND CONCLUSIONS

A two-wavelength differential absorption lidar technique for measuring the atmospheric pressure profile to high accuracy has been described. A measurement in the distant wing of a line in the oxygen *A* band is used, with a measurement at a nearby reference frequency to determine pressure. For a range-resolved or horizontal path experiment, the average pressure of a layer is determined from the absorption coefficient, which is, to first order, proportional to p^2. The pressure profile may be determined with higher accuracy, however, using an integrated path experiment, where the measured extinction is proportional to the difference in the squares of the pressures at the end points of the measurement. In the former case, the approximate condition for temperature desensitization of the pressure measurement is $\varepsilon = (n+2)kT$, whereas in the latter case the condition is $\varepsilon = (n+1)kT$, where ε is the ground state energy of the absorption line, and n is the exponent of the temperature dependence of the collision broadened half-width. The formulation of integrated path pressure measurements also includes a method for correcting for residual temperature effects.

The properties of absorption troughs, regions of minimum absorption between pairs of strongly absorbed oxygen lines, have been described, and the frequency dependence of the trough region was shown to be a parabola in the vicinity of the trough. Use of a trough technique was shown to produce up to two orders of magnitude in error reduction due to laser frequency stability effects. The problem of measurement with finite laser bandwidth at a trough location was considered, and it was shown that the measured transmission can be represented using an equivalent monochromatic frequency $\bar{\nu}_e$. For a rectangular bandpass, $\bar{\nu}_e = \nu_t \pm \Delta\nu/(2\sqrt{3})$, where ν_t is the trough frequency, and $\Delta\nu$ is the laser bandwidth. A finite bandwidth measurement at a reference frequency with weak absorption can be represented by an equivalent monochromatic measurement at the midpoint of the bandpass for a fairly general set of conditions.

Results of various simulations have been presented. We showed that weak isotopic lines occur in the vicinity of the troughs, which shift the trough location and introduce a slight altitude dependence to the trough frequency. The effect of a 2 K bias error in the temperature profile was investigated at three trough locations and found to produce pressure errors of ~0.05%. Laser frequency jitter was also investigated, and a jitter of ± 0.01 cm^{-1} was found to produce pressure errors <0.1%. We also found that water vapor affects the pressure determination, and that residual errors, due to ±30% uncertainties in the relative humidity, are <0.1% in the boundary layer and <0.05% above 2 km.

Analysis of the sensitivity of an integrated path vertical pressure measurement from a laser to altitude z shows that the measurement accuracy depends on the optical depth from infinity to z for any laser location. We also found that an integrated path vertical pressure measurement is more accurate than a range-resolved measurement by the ratio of the pressure scale height of the atmosphere to $\sqrt{2}$ times the thickness of the range-resolved layer. For typical 100 m vertical resolution, this yields accuracy improvement by more than a factor of 50 for an integrated path experiment. Simulations of the accuracy of integrated path ground-based pressure profile measurements using realistic parameters show that high accuracy can be achieved for an 8-shot average. Simulations of the accuracy of Shuttle-based experiments showed that the surface pressure can be measured to 0.2% accuracy with 25 km spatial resolution, and the pressure profile can be obtained to 0.3% accuracy with spatial resolution of 125 km.

We conclude that an integrated vertical path technique significantly increases the accuracy of lidar atmospheric pressure measurements, and also that an absorption trough technique can be used to greatly decrease the sensitivity of the experiment to the effects of laser frequency instability. These techniques allow measurements of the pressure profile and surface pressure to be made with high accuracy.

CHAPTER 2 THEORY OF LIDAR TEMPERATURE MEASUREMENTS

INTRODUCTION

This chapter describes the theory of a two-wavelength lidar technique with differential ranging for measuring the atmospheric temperature profile from both ground- and satellite-based platforms. Temperature is one of the basic atmospheric parameters, and global measurements are required in essentially all weather and climate prediction models. An extensive radiosonde network has been established to meet this need. Measurements are sparse, however, over ocean areas and in the Southern Hemisphere. Passive temperature sounding techniques have been used from satellite-based platforms to provide information in these data sparse regions. The vertical resolution of current sounders, the full width of the weighting functions at half-height, is limited to 5 to 10 km with consequential limitations in temperature accuracy to ~2 K (Kaplan, *et al.*, 1977; Atlas and Korb, 1981). Significant improvements in both vertical resolution and accuracy, of the order of 2 km and 1 K, are required to meet the needs of improved forecasting techniques (WMO-ICSU, 1973).

A number of lidar techniques have been investigated to obtain improved measurements of temperature. The method we will describe is a two-wavelength differential absorption lidar technique for measuring the vertical temperature profile. With this technique, a high *J* line in the oxygen *A* band is used with an associated reference measurement, as was first outlined by Korb and Weng (1979). Horizontal path versions of this technique, using scattering from fixed targets, have been successfully applied to path-averaged temperature measurements using the oxygen *A* band with 1 km paths (Kalshoven, *et al.*, 1981); a similar experiment was performed by Murray, *et al.* (1980) using the 10.6 μm CO_2 region with 5 km paths. The extension of the latter work to vertical profile measurements would, however, be limited by the weak CO_2 absorption in the 10.6 μm region, which requires the use of very large range gates, as well as by the weak backscatter and wavelength-dependent aerosol absorption at these long wavelengths (Petheram, 1981). Mason (1975) described a three-wavelength differential absorption lidar technique for measuring temperature, using two resonant absorption lines of oxygen and an off-line reference. Simulations of the performance of this method by Schwemmer and Wilkerson (1979) show that the accuracy of this approach is extremely limited for satellite remote sensing. Horizontal path-averaged temperature measurements with a fixed target have been reported using a variation of this three-wavelength technique in the 1.9 μm water vapor band (Endemann and Byer, 1980). The highly non-uniform mixing and large vertical gradient of water vapor in the atmosphere would, however, limit the accuracy and altitude range of temperature profile measurements using a water vapor based technique. Measurements using the Raman scattering technique for remote temperature measurements in the lower troposphere have also been reported (Gill, *et al.*, 1979). The low value of the Raman scattering cross section limits the extension of these measurements to the low signal cases associated with high altitude aircraft or satellite experiments.

The two-wavelength lidar technique, which we will describe, is experimentally simpler than the three-wavelength technique, since it requires only one, rather than two, frequencies to be precisely positioned about the center of an absorption line. Even more importantly, the conditions for a highly temperature sensitive measurement can be easily met with the two-wavelength technique using a single temperature sensitive line with adequate absorption. On the other hand, the three-wavelength method requires that two absorption lines of the same species be found with nearly identical absorption intensities, but with low and high values of ground state quantum energy. These latter conditions cannot be satisfied for most molecules, since absorption depends strongly on ground state energy. As a result, the two-wavelength technique has greater sensitivity by up to an order of magnitude compared to the three-wavelength technique, as we will show. The analysis for the two-wavelength technique presented here is more complex than that given for the three-wavelength method. This complexity arises from explicit accounting for the temperature and pressure

dependence of absorption by lines with a generalized Voigt line profile. Previous analyses of the three-wavelength technique have generally been limited to the case of a purely collision broadened line profile which simplifies the analysis, but provides only a first-order result.

In this work, oxygen is used for measurement, since it is uniformly mixed in the atmosphere and, thus, the mixing ratio does not have to be measured independently. Also, the *A* band region from 0.76 to 0.77 μm has lines of appropriate strength and energy with minimal interference from other species and is easily accessible by tunable lasers.

A detailed presentation of the two-wavelength technique for high accuracy measurements of the vertical temperature profile follows. The next section considers the case of lines broadened by combined collision and Doppler effects near line center and includes corrections for the effects of pressure and humidity. The following section extends this analysis to the case of broadband laser emission encountered in actual experiments and gives a generalized method for determining the temperature profile. Various simulation results are then presented for the case of broadband laser emission.

THEORY

For a lidar with a coincident transmitter and receiver operating at a single frequency ν with pulse energy E^0, the energy received from an element of the atmosphere at range R with thickness ΔR can be derived from Collis (1969) as

$$E_\nu(R) = E^0 A Q \beta_\nu(R) \left(\frac{\Delta R}{R^2}\right) \exp\left\{-2\int_0^R [\alpha(\nu) + K(\nu)]dx\right\}, \tag{2-1}$$

where A is the area of the lidar receiver, Q is the optical efficiency of the system, $\beta_\nu(R)$ is the sum of the aerosol and Rayleigh backscatter coefficients of the atmosphere per unit solid angle per unit length, $\alpha(\nu)$ is the attenuation coefficient of the atmosphere due to scattering and continuum absorption effects, and $K(\nu)$ is the absorption coefficient of the atmosphere due to resonant absorption. Equation (2-1) is valid for monochromatic laser emission and elastic scattering and for lidar pulse lengths $c\Delta t << \Delta R$.

A two-frequency differential absorption technique is used for the lidar temperature measurement. One frequency is selected about the center of a temperature-sensitive line in the oxygen *A* band. A second nearby frequency having minimal resonant absorption, but with nearly identical total attenuation due to scattering and continuum absorption processes, is used as the reference. Shettle and Fenn (1975) have shown that the aerosol absorption and scattering are smoothly varying functions of wavelength in the *A* band region, and the above condition is well satisfied. We note that this condition is generally not well satisfied in the 10 μm region, as discussed by Petheram (1981). The ratio of the signal returns from range R at the on-line and reference frequencies eliminates the scattering and absorption properties of the atmosphere, other than those associated with the resonant absorption effect to be studied. That is,

$$\frac{E_l(R)}{E_r(R)} = \frac{E_l^0}{E_r^0} \exp\left\{-2\int_0^R [K(\nu_l) - K(\nu_r)]dx\right\}, \tag{2-2}$$

where the subscripts l and r refer to the on-line and reference frequency measurements, respectively, and $K(\nu_l)$ - $K(\nu_r)$ is the differential absorption coefficient due to resonant absorption. For measurements in the

low frequency branch of the oxygen *A* band, the separation between the on-line and reference frequencies may be chosen to be of the order of 1.0 to 1.5 cm^{-1}. The ratio of the resonant absorption coefficient at the reference frequency to that at the on-line frequency is then $<10^{-3}$. Thus, the differential absorption may be approximated by the absorption at ν_l with good accuracy.

The logarithm of the ratio of two successive measurements of the signal ratio in Eq. (2-2) for the ranges R and $R+\Delta R$ then yields the average value of the differential absorption coefficient $\overline{K}$ as (Schotland, 1974)

$$\overline{K} = \frac{1}{2\Delta R} \ell n \left[\frac{E_l(R)/E_r(R)}{E_l(R+\Delta R)/E_r(R+\Delta R)} \right]. \tag{2-3}$$

Equation (2-3) is valid for elastic scattering provided that the atmospheric backscatter is uniform and the absorption is linear over the width of a range gate. A method of analysis for finding K for the case of nonhomogeneous scattering and nonlinear absorption has been reported (Korb and Weng, 1980). Equation (2-3) is also limited to the use of a monochromatic laser at the on-line frequency. The next section of this chapter considers a more generalized formulation of this problem for the case of broadband laser emission.

The absorption coefficient $K(\nu)$ of a gas species in the atmosphere at frequency ν is given as

$$K(\nu) = qnS(T)f(\nu - \nu_0), \tag{2-4}$$

where q is the molecular mixing ratio of the species, n is the number density at pressure p and temperature T, $S(T)$ is the line strength, and $f(\nu - \nu_0)$ is the line shape at frequency ν for a line centered at ν_0. Oxygen is uniformly mixed in the atmosphere except for small variations introduced by atmospheric water vapor. This may be accounted for as

$$q = q_0(1 - q^*), \tag{2-5}$$

where q_0 is the molecular mixing ratio of O_2 in the dry atmosphere (0.2095) and q^* is the molecular mixing ratio of water vapor. The effects of water vapor will be considered later in this section. The temperature dependence of the line strength is given as the ratio of the Boltzmann factor to the rotational partition function. For linear molecules such as oxygen, the partition function is directly proportional to temperature and, thus,

$$S(T) = S(T_0)\left(\frac{T_0}{T}\right)\exp\left\{-\left(\frac{\varepsilon}{k}\right)\left(\frac{1}{T} - \frac{1}{T_0}\right)\right\}, \tag{2-6}$$

where ε is the ground state energy of the transition including rotational and vibrational terms, k is Boltzmann's constant, and T_0 is standard temperature.

For atmospheric measurements in the oxygen *A* band, the effects of both collision and Doppler broadening contribute significantly to the line shape. The line shape is given by the Voigt profile, which is a convolution of independent Lorentz and Doppler profiles, as (Penner and Kavanagh, 1953)

$$f(\nu - \nu_0) = \frac{f'a}{\pi} \int_{-\infty}^{\infty} \frac{\exp(-y^2)dy}{a^2 + (\xi - y)^2}, \tag{2-7}$$

where

$$f' = \left(\frac{\ell n 2}{\pi}\right)^{1/2}\left(\frac{1}{b_d}\right),$$

$$a = (\ell n 2)^{1/2}\left(\frac{b_c}{b_d}\right),$$

and

$$\xi = (\ell n 2)^{1/2}\left(\frac{\nu - \nu_0}{b_d}\right),$$

where b_c is the collision broadened line half-width, and b_d is the Doppler broadened line half-width. These are defined as

$$b_c = b_c^0\left(\frac{p}{p_0}\right)\left(\frac{T_0}{T}\right)^m \tag{2-8a}$$

and

$$b_d = \left(\frac{2kT\ell n 2}{M_0 c^2}\right)^{1/2}\nu_0, \tag{2-8b}$$

where M_0 is the mass of the oxygen molecule, c is the velocity of light, p_0 is standard pressure, and b_c^0 is the collision broadened line half-width at standard temperature and pressure (STP). From kinetic theory, the exponent m of the temperature dependence of the collision broadened half-width is predicted to be one-half. For real molecules, however, m can vary over a significant range.

A general form for the absorption coefficient is obtained from Eqs. (2-4) to (2-6) as

$$K(\nu) = Cq_0(1 - q^*)\left(\frac{p}{T^2}\right)\exp\left(-\frac{\varepsilon}{kT}\right)f(\nu - \nu_0), \tag{2-9}$$

with

$$C = \left(\frac{T_0}{k}\right)S(T_0)\exp\left(\frac{\varepsilon}{kT_0}\right),$$

where the line profile depends on both temperature and pressure. We note that at line center, for the limiting case of very high pressure, the line profile is given as $f(0) = p_0/[\pi b_c^0(T)p]$ (Penner, 1959), and the absorption coefficient is independent of pressure. In the case of very low pressure, the line profile is given as $f(0) = f'$, and the absorption coefficient is directly proportional to pressure. Thus, for the case of high or low pressure, lidar measurements of differential absorption determine either the mixing ratio or species density which can be found directly from Eq. (2-9), if the temperature is known. Alternatively, if the mixing ratio is known *a priori*, as in the case of oxygen, and if the pressure can be estimated, then Eq. (2-9) can be used to determine the temperature.

Given the absorption coefficient $\overline{K}$ for a monochromatic measurement at line center, the temperature may be found from Eq. (2-9) using graphical or iterative methods. For a laser with a uniform bandpass and a sufficiently narrow spectral bandwidth $\Delta\nu$ which is centered on an atmospheric absorption line at ν_0 with a Voigt line profile, it can be shown (Korb and Weng, 1982), that the absorption coefficient can be approximated by that at a monochromatic frequency

$$\nu_e = \nu_0 \pm \frac{\Delta\nu}{2\sqrt{3}}.$$

For laser spectral bandwidths <0.01 cm^{-1}, the accuracy of this approximation is better than 0.3%. We note that in the Doppler limit, this corresponds to a ratio of laser linewidth to Doppler half-width as large as 0.7. An iterative solution for the temperature is then found from Eq. (2-9) as

$$T_{i+1} = \frac{\varepsilon / k}{\ell n\left[Cqf_i(\nu_e - \nu_0)\right] - \ell n\left[\overline{K}T_i^2 / p\right]}, \tag{2-10}$$

where T_{i+1} is the iterated temperature value calculated from T_i and the Voigt line shape f_i is an implicit function of the temperature T_i. For highly temperature sensitive lines as are considered here, Eq. (2-10) converges very rapidly. For an initial temperature estimate of 200 K, seven iterations are sufficient for an accuracy of 0.01 K at line center.

In order to analyze the dependence of the absorption coefficient on temperature and pressure, we consider the form of the absorption coefficient at line center. For this case, the Voigt profile is given as (Penner, 1959)

$$f(0) = 2f'\pi^{-1/2}\exp(a^2)\int_a^\infty \exp(-y^2)dy. \tag{2-11}$$

The dependence of the absorption coefficient on temperature may be determined from its derivative with respect to temperature, where the absorption coefficient and Voigt line profile are given by Eqs. (2-9) and (2-11), respectively. The result is

$$\frac{dK(\nu_0)}{K(\nu_0)} = \left[\frac{\varepsilon}{kT} - \frac{5}{2} - 2a^2\left(m+\frac{1}{2}\right) + \frac{a\left(m+\frac{1}{2}\right)}{\exp(a^2)\int_a^\infty \exp(-y^2)dy}\right]\frac{dT}{T}. \tag{2-12}$$

Detailed measurements of the temperature dependence of the collision broadened line half-width have not been reported for oxygen. Preliminary measurements for the $^{P}P27$ line,[1] however, give a value of 0.7 (Korb, *et al.*, 1980). For the kinetic theory case of $m = 0.5$, the limiting forms of Eq. (2-12) are found by series expansion of Eq. (2-12) as

[1] The oxygen *A* band has four branches. The notation $^{P}P27$ refers to the *P* branch transition, $\Delta J = -1$, from the ground quantum state with total angular quantum number $J = 27$, and the *P* superscript refers to the change in rotational quantum number, $\Delta K = -1$ (Miller, *et al.*, 1969).

$$\frac{dK(\nu_0)}{K(\nu_0)} = \begin{cases} \left[\frac{\varepsilon}{kT} - \frac{5}{2}\right]\frac{dT}{T} & \text{for} \quad a = 0, \\ \left[\frac{\varepsilon}{kT} - \frac{3}{2}\right]\frac{dT}{T} & \text{for} \quad a = \infty. \end{cases} \tag{2-13}$$

We note that the limiting forms given above agree with those independently derived from Eq. (2-9) for the Doppler and Lorentz line profiles. From Eq. (2-13), it is seen that measurements of absorption will be highly temperature sensitive for transitions for which $\varepsilon/(kT)$ is large. This will occur for ground state transitions with large values of the total angular quantum number J, since $\varepsilon \approx BJ(J+1)$, where B is the rotational constant. It will also occur in hot band transitions which originate from excited vibrational states. In the case of absorption by the oxygen A band, the ^{P}P29 line at 12999.95 cm^{-1} with $J = 29$ and the ^{P}P27 line at 13010.81 cm^{-1} with $J = 27$ have good absorption for measurement in the atmosphere. The values of $\varepsilon/(kT_0)$ are 6.57 and 5.71, respectively, for these lines (Burch and Gryvnak, 1969). For the ^{P}P29 line, it follows from Eq. (2-13) that a 1% change in temperature at T_0 will cause a 4 to 5% change in the measured absorption coefficient. The conditions for which a measurement of concentration can be made temperature insensitive can be found from Eq. (2-12). This, for example, would apply to the measurement of the concentration of various species such as water vapor or carbon dioxide. For the Lorentz case given by Eq. (2-13), the value of ε which allows for a temperature insensitive measurement of the mixing ratio is $(3/2)kT$.

For a measurement made using the Voigt line profile, the absorption is pressure dependent even at line center. This dependence must be analyzed and taken into account in order to obtain an accurate determination of temperature. The sensitivity of the absorption coefficient to pressure changes may be evaluated from Eqs. (2-9) and (2-11). The result is

$$\frac{dK(\nu_0)}{K(\nu_0)} = \left[1 + 2a^2 - \frac{a}{\exp(a^2)\int_a^\infty \exp(-y^2)dy}\right]\frac{dp}{p}. \tag{2-14}$$

Series expansion shows that the bracketed term in Eq. (2-14) has a value of unity for the Doppler profile ($a = 0$) and a value of zero for the Lorentz profile ($a = \infty$), as expected. Evaluation of the bracketed term in Eq. (2-14) for oxygen at sea level and at a height of 5 km yields values of 0.1 and 0.3, respectively.

At sea level, the atmospheric pressure is known to an accuracy of the order of 1% from climatic information. It follows from Eq. (2-14) that the fractional error in absorption coefficient due to this error source is only 0.1%, which corresponds to a temperature error of 0.06 K for the ^{P}P29 line of oxygen. The uncertainty in the pressure data increases rapidly with increasing altitude, and is of the order of 10% at 10 km, which corresponds to a temperature error of several kelvin.

The magnitude of the errors introduced by the pressure dependence of the absorption coefficient can be greatly reduced using measured temperature profile information. From the hydrostatic equation and the ideal gas law, it follows that the pressure at height Z_{i+1} is related to the pressure at height Z_i by

$$p(Z_{i+1}) = p(Z_i)\exp\left[-\left(\frac{Mg_i}{k}\right)\left(\frac{\Delta Z_i}{T_i}\right)\right], \tag{2-15}$$

where M is the average mass of air molecules, ΔZ_i is the thickness of the layer, T_i is the temperature of the layer as derived from the lidar measurement, and g_i is the acceleration due to gravity for that layer. It follows that, if Eq. (2-15) is used to construct the pressure profile from the temperature profile, the fractional error in the pressure at height Z_n is given as

$$\frac{\Delta p(Z_n)}{p(Z_n)} = \frac{\Delta p_0}{p(Z_0)} + \left[\sum_{i=1}^{n}\left(\frac{Mg_i\Delta Z_i}{kT_i}\right)^2\left(\frac{\Delta T_i}{T_i}\right)^2\right]^{1/2}, \tag{2-16}$$

where Δp_0 is the error in pressure at a reference level at height Z_0, and ΔT_i is the error in the lidar temperature measurement for layers in the region Z_0 to Z_n The derivation of Eq. (2-16) assumes the temperature errors are randomly distributed. The error buildup in pressure, as given by the second term of Eq. (2-16), is only 0.18% at 10 km altitude for a lidar temperature accuracy of 1 K and a resolution ΔZ of 2 km. Thus, for a ground-based experiment for which the surface pressure is measured to an accuracy of 0.1%, the total pressure error at 10 km would be <0.3%. On the other hand, for an aircraft or satellite measurement for which the estimated surface pressure is known to only 1% accuracy, the total pressure error will remain essentially constant (near 1%) with altitude. As will be shown in the next section, the temperature error corresponding to a 1% pressure error is <0.3 K. Thus, the effects of pressure uncertainties can be greatly reduced by a one-step iteration procedure using Eq. (2-15).

The only effect of humidity on the temperature determination is to change the mixing ratio of oxygen in the atmosphere, as given by Eq. (2-5). We have calculated the effect on temperature due to an error in the assumed water vapor content of the atmosphere of ±30% of its saturation value. This, for example, would correspond to actual values of humidity of 20% or 80% of their saturation values versus an assumed value of 50%. Results show a temperature error of 0.3 K for measurements in the boundary layer with a mean temperature of 290 K, and errors < 0.1 K for altitudes > 2.5 km with temperatures <270 K. We note that the saturation water vapor content of the boundary layer at 290 K is nearly 2% of the atmospheric composition of this layer by volume.

ANALYSIS AND SIMULATION

In order to conduct high accuracy lidar temperature experiments, procedures for evaluating and correcting for the effects of systematic error sources are required. In this section, we will consider the effects of broadband laser emission, laser frequency shifts, and the effects of uncertainties in atmospheric pressure. Procedures to reduce errors from these sources will be developed. The accuracy of simulated ground-based and Shuttle-based experiments will also be evaluated for realistic system parameters.

Finite Bandwidth

Errors in the lidar measurement of differential absorption due to finite laser bandwidth effects were investigated by Cahen and Megie (1981). They evaluated the errors which would result from measurements made in low pressure atmospheres where the Doppler line shape pertains. They did not, however, consider the possibility that data could be corrected for the effects of finite bandwidth. In this section, we will develop a solution to this problem for generalized line shape.

For the case of finite spectral bandwidth, the transmission of the atmosphere $\overline{\tau(Z_0,Z)}$ along the two-way vertical path from the laser at heights Z_0 to Z is given as

$$\overline{\tau(Z_0,Z)} = \frac{\int_{\nu_1}^{\nu_2} h(\nu)\exp\left[-2\int_{Z_0}^{Z} K(\nu,z)dz\right]d\nu}{\int_{\nu_1}^{\nu_2} h(\nu)d\nu}, \tag{2-17}$$

where $h(\nu)$ is the laser spectral line shape which has finite contribution between ν_1 and ν_2 We assume that $h(\nu)$ is uniform on this interval and the numerical integration is performed with a spectral spacing of 10^{-3} cm^{-1}. The absorption coefficient for each layer $K(\nu,z)$ is calculated from Eq. (2-9), where the Voigt profile (2-7) is evaluated using numerical techniques (Armstrong, 1967). The absorption parameters for oxygen are taken from Burch and Gryvnak (1969) and Miller, *et al.* (1969). The atmospheric model used for evaluation of Eq. (2-17) is a multi-layer one-dimensional model with up to 50 homogeneous layers. The layer thickness is chosen as one-half the vertical resolution of the lidar experiment.

We now describe a general method for determining temperature for a lidar differential absorption experiment with finite bandwidth. For this case, the parameter which can be determined from the ratio of the four backscattered lidar signals is $\overline{K}_m$, as opposed to the absorption coefficient $\overline{K}$ of Eq. (2-3), which was previously found for a single frequency experiment. Since the ratio of the normalized lidar signal returns at the on-line and reference frequencies is the atmospheric transmission as given in Eq. (2-17), it follows from Eq. (2-3) that the observed absorption coefficient for the atmospheric layer from Z_1 to Z_2 is

$$\overline{K}_m = -0.5\frac{\ell n\left[\overline{\tau(Z_0,Z_2)}/\overline{\tau(Z_0,Z_1)}\right]}{|Z_2 - Z_1|}, \tag{2-18}$$

where the resonant absorption at the reference frequency is assumed to be negligible compared to that at the on-line frequency. $\overline{K}_m$ depends primarily on a spectrally weighted value of the transmission of the particular layer in question, *i.e.*, from Z_1 to Z_2. As a result of the finite bandwidth, however, $\overline{K}_m$ also has a residual dependence on the transmission properties of the intervening layers between the laser and the measured layer, *i.e.*, from Z_0 to Z_1.

The problem may be solved as follows. Figure 2-1 shows the variation of absorption coefficient with temperature for the ^{P}P29 line of oxygen. The absorption coefficient for each layer was calculated from Eqs. (2-17) and (2-18) using an estimated atmospheric temperature profile to account for the effects of the intervening layers between the laser and the measured layer. These results are for a two-way path satellite-based experiment with 2 km resolution and a bandwidth of 0.02 cm^{-1}. We note that the values of absorption coefficient calculated for this 0.02 cm^{-1} bandwidth are as much as 10% smaller than the values at line center. Since the absorption coefficient and the height are experimentally measured quantities, the temperature corresponding to a given measurement can be read directly from Figure 2-1. This solution for the temperature profile is, however, only correct to first order, since an assumed temperature profile was used to account for the effects of the intervening layers. This first-order solution provides a good estimate of the temperature profile and can be used to recalculate the curves of Figure 2-1 with subsequent redetermination of the temperature profile. In practice, only a small portion of the curve for each altitude needs to be recalculated for each iteration. This iteration procedure is repeated until convergence is obtained.

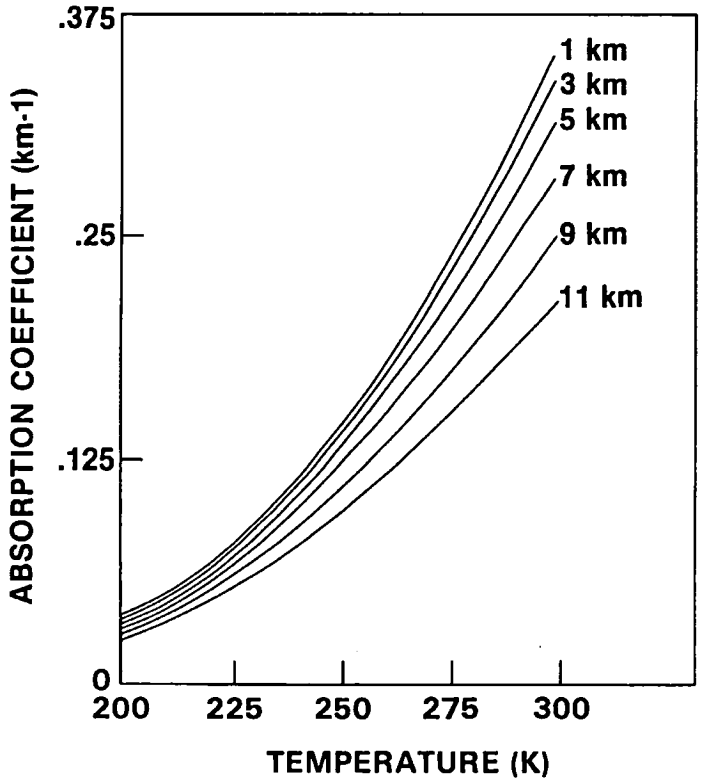

Figure 2-1. The dependence of the absorption coefficient at various altitudes on temperature for a satellite-based lidar measurement using the $^{P}P29$ line of oxygen with a 0.02 cm^{-1} laser spectral bandwidth.

For the assumed 0.02 cm^{-1} laser bandwidth, the effect of the intervening layers produces maximum errors of only 0.3 K. For an experimental measurement accuracy of 1 K, a one-step iteration procedure is sufficient to reduce this error source below the 0.01 K level. However, the effects of finite laser bandwidth increase rapidly with increasing bandwidth, since a larger portion of the atmospheric line profile is observed. For a laser bandwidth of 0.04 cm^{-1}, the values of absorption coefficient are as much as 50% smaller than the line center values, and the intervening layers produce errors as large as 1.5 K. The iteration procedure outlined above would reduce this error to < 0.05 K. A detailed treatment of the general method for treating the finite bandwidth problem will be given in Chapter 3.

Effects of Pressure, Frequency Stability, and Temperature Dependence

The pressure profile may be constructed from the temperature profile using a reference pressure level and Eq. (2-15) with resultant errors in the pressure profile of ~1%, as discussed in the previous section. The effect on temperature of a 1% uncertainty in pressure was calculated from Eqs. (2-17) and (2-18) using a variational analysis technique. It is given in Figure 2-2 as a function of laser bandwidth for various atmospheric layers. As shown, the error increases with increasing altitude and bandwidth. For bandwidths <0.025 cm^{-1}, the temperature error is <0.3 K. Thus, if pressure is derived from the lidar temperature measurement and used to redetermine temperature in an iterative manner, the effects of pressure on temperature determination can be reduced to the range of 0.05 to 0.3 K.

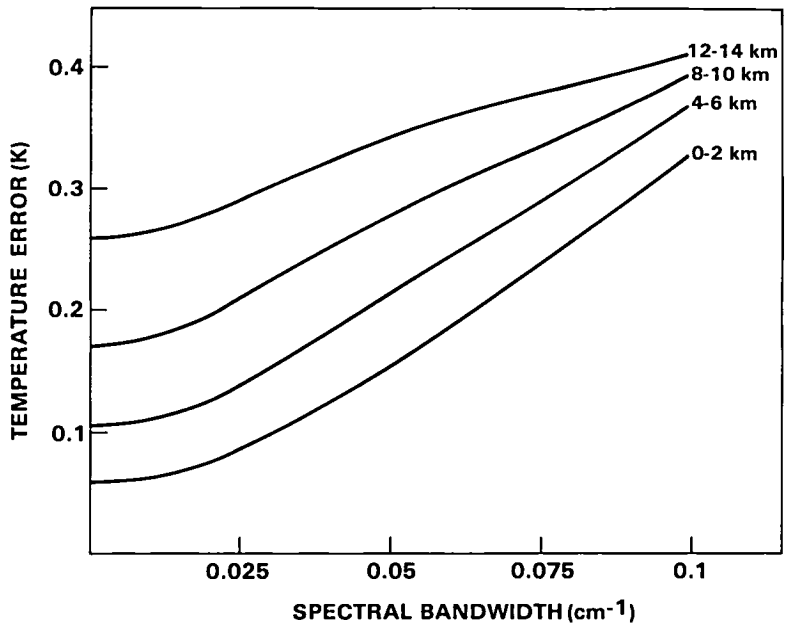

Figure 2-2. The temperature error for various atmospheric layers due to a 1% uncertainty in the atmospheric pressure profile as a function of laser spectral bandwidth for a satellite-based lidar measurement of the $^{P}P29$ line of oxygen.

A primary source of error in a differential absorption lidar experiment is the laser frequency stability. Figure 2-3 shows the error in temperature measurement for the $^{P}P29$ line of oxygen as a function of the laser frequency shift for a downward-looking experiment with a bandwidth of 0.02 cm^{-1}. As shown, the temperature error is a strong function of laser frequency stability. A stability of the order of 0.005 cm^{-1} is required to obtain errors of the order of 1 K on a per pulse basis. If the laser jitter were random, these errors could be reduced by averaging a suitable number of pulse returns. For non-random laser frequency shifts, the errors can be greatly reduced by monitoring the laser frequency on a per pulse basis and applying corrections to the data. We have also found that the results given in Figure 2-3 change relatively little for lidar bandwidths in the range of 0 to 0.05 cm^{-1}, and are relatively insensitive to the lidar vertical resolution and viewing direction.

The accuracy of the temperature measurement is directly related to the coefficient of temperature dependence

$$\eta = \frac{d\overline{K}_m / \overline{K}_m}{dT/T},$$

where $\overline{K}_m$ is defined by Eq. (2-18). Figure 2-4 shows η for the $^{P}P29$ line of oxygen for a satellite-based experiment with a 0.02 cm^{-1} bandwidth. Lorentz and Doppler limits [see Eq. (2-13)] are also given for comparison. The temperature dependence of the absorption coefficient, as given, varies from $\sim T^4$ to T^7 over the range of atmospheric temperatures. As shown in Figure 2-4, the temperature error is inversely proportional to η.

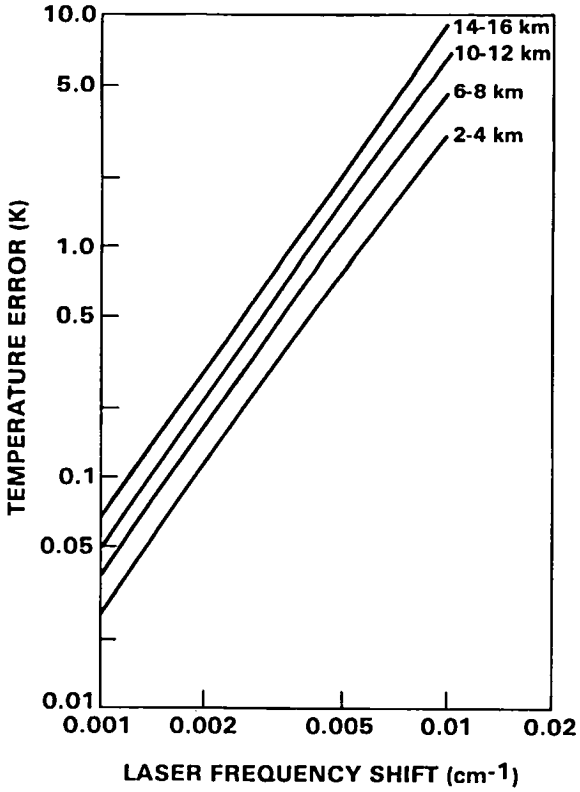

Figure 2-3. The temperature error for various atmospheric layers as a function of laser frequency shift for a single pulse satellite-based lidar measurement of the $^{P}P29$ line of oxygen with a 0.02 cm^{-1} spectral bandwidth.

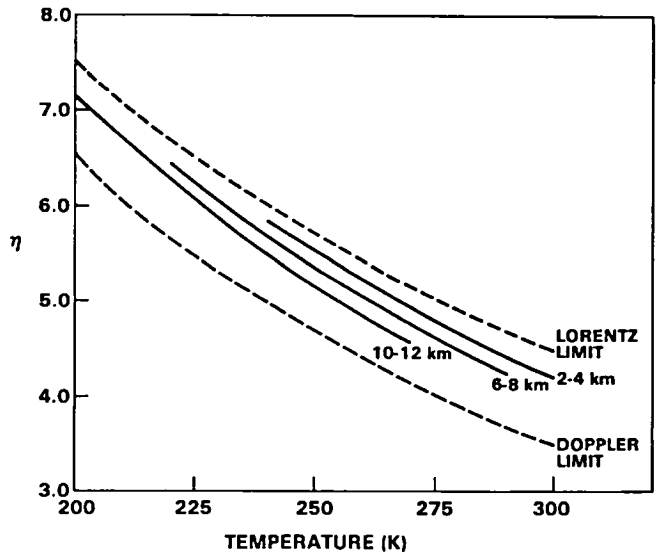

Figure 2-4. The coefficient of temperature dependence of the absorption coefficient,

$$\eta = \frac{d\overline{K}_m/\overline{K}_m}{dT/T},$$

for various atmospheric layers as a function of temperature for a satellite-based lidar measurement of the $^{P}P29$ line of oxygen with a 0.02 cm^{-1} spectral bandwidth. Limiting cases of Lorentz and Doppler line profiles are also shown.

Analysis of Measurement Capability

The sensitivity of this technique has been evaluated for simulated ground- and Shuttle-based experiments. The relationship between the temperature error and the experimental parameters for a finite bandwidth experiment can be found by taking the derivative of Eq. (2-18) with respect to temperature over the incremental measurement layer from Z_1 to Z_2. From the definition of η given on the previous page, the result is

$$\Delta T = \frac{T}{(2\eta\overline{K}_m\Delta Z)(S/N)}, \tag{2-19}$$

where (S/N) is the composite signal-to-noise ratio for the four signals needed to define a measurement for a single layer and $2\overline{K}_m\Delta Z$ is the optical depth of the layer. Thus, the coefficient of temperature dependence η and the optical depth of the measured layer have the same relationship to the temperature error as the signal-to-noise ratio. The lidar parameters used for analysis are for state-of-the-art systems (see Table 2-1). The atmospheric backscatter coefficient used for the simulations included both Rayleigh and aerosol components. The aerosol model used was that given by Elterman (1968).

Table 2-1. System parameters used for simulated ground- and Shuttle-based temperature measurements.

Parameter	Ground-based	Shuttle-based at 200 km
A band line	$^{P}P27$	$^{P}P29$, $^{P}P27$
Frequency (cm^{-1})	13010.81	12999.95, 13010.81
Pulse energy (J)	0.1	0.1
Spectral bandwidth (cm^{-1})	0.02	0.02
Repetition rate (Hz)	10	10
Pulses averaged	150	350
Horizontal resolution (km)	—	250
Vertical resolution (km)	0.1-0.5	2
Telescope area (m^2)	1	1
Receiver field of view (mrad)	0.3	0.3
Optical efficiency (%)	0.5	0.5
Quantum efficiency (%)	0.24	0.24
Detection bandwidth (cm^{-1})	20	20

Figure 2-5 gives the results for a ground-based system using the $^{P}P27$ line of oxygen at 13010.81 cm^{-1}. The noise sources considered were those due to photon statistics, daytime background levels, and a 1% signal processing error for each layer. The results shown are for a 150 shot average, which corresponds to a measurement time of ~15 sec. The effects of signal processing are dominant at short ranges. For large ranges, the temperature error, which is primarily due to photon noise, varies as $(\Delta R)^{-3/2}$, where ΔR is the lidar vertical resolution. As shown, accuracies generally better than 1 K can be obtained with 200 and 500 m vertical resolution. It should be noted that the measurement accuracy can be improved for altitudes >4 km using the weaker absorption associated with the $^{P}P29$ oxygen line.

The results for a Shuttle-based system at an altitude of 200 km are shown in Figure 2-6. The parameters are similar to those used for the ground-based system, with the exception of the lines used for measurement and the lidar vertical resolution (see Table 2-1). For measurements in the troposphere, the $^{P}P29$ line of oxygen is used with a 2 km vertical resolution, while for measurements extending into the lower stratosphere, the $^{P}P27$ line of oxygen is shown with both 2 and 3 km vertical resolution. The results are given for a 350 shot average, which corresponds to a 250 km horizontal resolution at a laser pulse repetition rate of 10 Hz. The results for the lower troposphere show accuracies approaching 0.4 K. We note that the boundary layer measurement uses a combination of surface reflection and atmospheric backscatter, which gives improved accuracy. The results for the $^{P}P27$ line show accuracies of ~1 K over the altitude range from 5 to 16 km. The loss in accuracy at the low altitude portion of this curve results from the loss in return signal due to very strong absorption. The increase in the measurement error at the high altitude end of each curve results from weak absorption in the respective range elements. The effects of signal processing errors are negligible for these downward-looking Shuttle measurements.

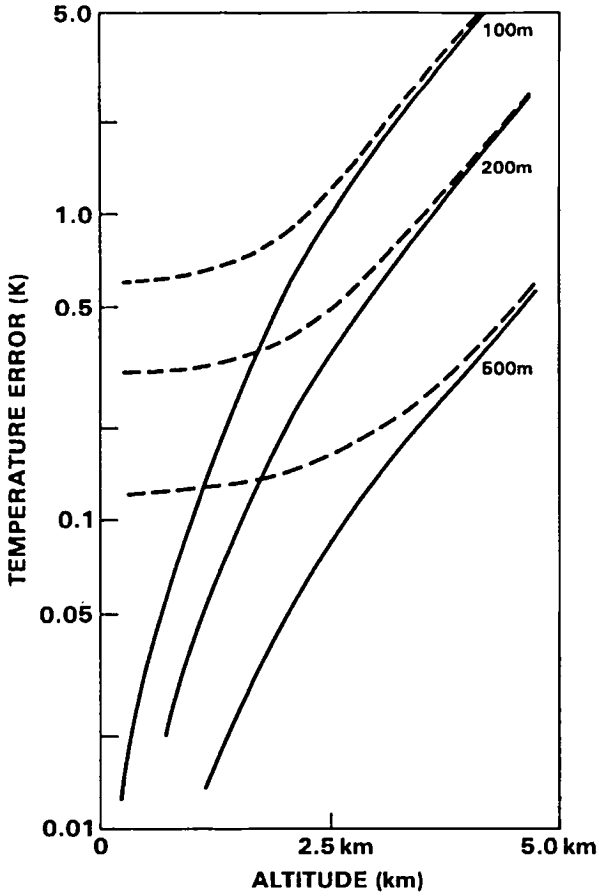

Figure 2-5. Simulated accuracy for a ground-based lidar system with a vertical resolution of 100, 200, and 500 m as a function of altitude for the $^{P}P27$ line of oxygen at 13010.81 cm^{-1} with a 0.02 cm^{-1} spectral bandwidth. Solid lines show errors due to photon statistics and daytime background level, while dashed lines also include effects of 1% signal processing errors. Results are shown for a laser energy of 0.1 J per shot, a 1 m^2 telescope, efficiency of 0.12, and a 150 shot average.

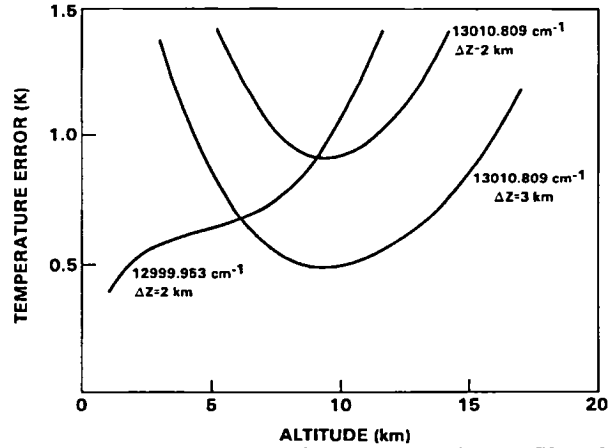

Figure 2-6. Simulated accuracy for a Shuttle-based lidar experiment at 200 km as a function of altitude for the $^{P}P27$ and $^{P}P29$ lines of oxygen with spectral bandwidths of 0.02 cm^{-1}. Results are for an efficiency of 0.12, and a 350 shot average which gives a 250 km horizontal resolution.

An estimate of the sensitivity of the two-wavelength technique versus the three-wavelength technique can be obtained by a comparison of the results obtained here with those given by Schwemmer and Wilkerson (1979). For the case of Shuttle measurements in the troposphere, our results show more than an order of magnitude increased accuracy for the same measurement conditions. We believe the higher accuracy associated with the two-wavelength technique results from two factors. First is the ability to select a much more highly temperature sensitive line for the measurement, the $J = 29$ line in our work versus the $J = 1, 17$ line pair in Schwemmer and Wilkerson (1979). The second factor is the ability to optimize the absorption for any given altitude range by selecting slightly different values of J. For the three-wavelength technique, the choice of the high J line is constrained by the need to approximately match the absorption of the high J line to that of the low J line. This limits the temperature sensitivity coefficient η and thus the accuracy [see Eq. (2-19)]. The amount of absorption is then dictated by that of the low J line and may be far from optimum.

SUMMARY

A two-wavelength differential absorption lidar technique for measuring the atmospheric temperature profile to high accuracy has been described. A high J line in the oxygen A band is used with a nearby reference measurement to obtain a sensitive temperature determination. The theory of differential absorption lidar measurements for lines with Voigt profile has been given for the general case of absorption by linear molecules. It can be easily adapted for a nonlinear molecule by using the appropriate temperature dependence of the partition function for that molecule. An iteration procedure for calculating the temperature has been given for the case of narrow laser bandwidths assuming elastic scattering. For bandwidths <0.01 cm^{-1}, the accuracy is better than 0.2 K from ground level to 20 km.

General expressions for the temperature and pressure dependence of lines with Voigt profile have been formulated at line center. The expressions for the temperature dependence can be used both to find and describe temperature sensitive lines, and to determine the conditions for a temperature-insensitive measurement of species mixing ratio. Uncertainties in atmospheric pressure were shown to affect the accuracy of lidar differential absorption measurements. In order to correct for these effects, an iteration procedure using the measured temperature profile to determine the pressure was described. We also found that moisture affects the temperature determination, and that residual errors from this effect are of the order of 0.3 K in the boundary layer and <0.1 K above 2.5 km.

The theory of the differential absorption technique with differential ranging for elastic scattering and monochromatic lidar measurements has been briefly reviewed. A procedure for extending this technique to include the effects of finite laser bandwidth was described. It was shown that the combined effects of spectral averaging and of intervening layers are separable to good accuracy, with residual errors <0.05 K for bandwidths as large as 0.04 cm^{-1}.

The effects of pressure errors were obtained from numerical simulations as a function of laser bandwidth. The expected residual errors from this source are typically from 0.05 to 0.3 K. Studies show that laser frequency stability is a critical parameter for differential absorption lidar measurements and that either stability or knowledge of the laser frequency is needed to within 0.005 cm^{-1} accuracy to obtain temperature accuracy of 1 K for a single pulse measurement. The sensitivity of the technique has been evaluated for both ground- and Shuttle-based measurements using typical system parameters. The results show that accuracies are generally better than 1 K.

Current theoretical areas of investigation include the effects of non-homogeneous media and nonelastic scattering processes. Both of these effects are important for high accuracy measurements of differential absorption. A discussion of the formalism for treating non-homogeneous effects and a general method of solution has been given (Korb and Weng, 1980). The problem of nonelastic scattering in differential absorption measurements requires further investigation.

CHAPTER 3 EFFECTIVE FREQUENCY TECHNIQUE

INTRODUCTION

The effects of finite bandwidth distort a spectral measurement by broadening the line and decreasing the apparent absorption at line center. This can produce large errors in the measured spectrum (Kostkowski and Bass, 1956). For laboratory measurements, deconvolution techniques may be used to recover the true spectrum (Jansson, 1970). The analysis of range resolved lidar measurements of differential absorption in the atmosphere is more complex, since the spectral line shape changes with altitude, and the intervening atmosphere affects the measured differential absorption at the end point of the measurement (Cahen and Megie, 1981). A method of solving for the differential absorption has been briefly discussed using a complex iteration procedure (Chapter 2; Korb and Weng, 1982).

In this chapter, we will describe a fundamentally new approach to analyze the problem of instrumental distortion. We will show that an equivalent monochromatic frequency may be used to represent the effects of finite bandwidth. In the vicinity of line center, the equivalent frequency can be expressed by a simple analytical form that depends on the characteristics of the instrumental distortion function rather than the nature of the spectral line profile and the particular characteristics of the path being used. The technique is applicable to radiative transfer calculations as well as to a large class of active and passive spectroscopic experiments in both the laboratory and the atmosphere. An equivalent frequency not only greatly simplifies the computation of finite bandwidth effects for forward problems in radiative transfer but also allows the inverse problem of the remote measurement of species concentration and atmospheric properties to be solved using simplified monochromatic methods.

An integrated form of the mean value theorem provides the theoretical basis for this technique. It can be shown for a finite bandwidth measurement that an equivalent frequency exists at some point within the instrumental bandwidth if the instrumental line profile is a continuous function and does not change sign (Buck and Buck, 1965). However, the location of the equivalent frequency is not defined. In this chapter, we present general methods for calculating the equivalent frequency and show that the results are applicable to the whole range of spectroscopic and atmospheric line profiles.

THEORY

For the case of finite bandwidth, the transmission of the atmosphere is related to the absorption coefficient $K(\nu,x)$, the absorption per unit path, as (Chapter 2)

$$\bar{\tau}_\nu(0,R) = \int_{-\infty}^{\infty} h(\nu)\exp\left\{-2\int_0^R K(\nu,x)dx\right\}d\nu, \tag{3-1}$$

where the integral of the instrumental line shape $h(\nu)$ is normalized to have unit value. In the vicinity of an absorption line centered at ν_0, the absorption coefficient may be expanded as

$$K(\nu,x) = a_1(x) - a_2(x)(\nu-\nu_0)^2 + O\left[(\nu-\nu_0)^4\right], \tag{3-2}$$

where we explicitly allow for a dependence of the absorption coefficient on distance as, for example, would be encountered in the atmosphere. The quadratic expression of Eq. (3-2) is valid, in general, since a Taylor's series expansion of any function about a maximum or minimum yields an equation of this functional form, whereas $dK/d\nu|_{\nu_0} = 0$, and the linear term in the expansion is zero. Equation (3-2) provides a good approximation to the absorption coefficient for bandwidths that are small compared to the absorption line width. For a collision-broadened or Doppler profile, Eq. (3-2) gives the absorption coefficient to accuracies better than 1% for distances up to 0.3 half-widths from the line center. Since Eq. (3-2) is general, it can be used to represent the absorption coefficient near line center for the Voigt line profile, or even for a complex line shape such as results from integrating Voigt profiles over an atmospheric path with varying pressure and temperature. Equation (3-2) can also be used to represent the absorption in trough regions of minimum absorption between two absorption lines (Chapter 1).

To evaluate the transmission for a measurement centered on an absorption line, an explicit form for the observational line shape is required. We consider first the case of a Gaussian profile,

$$h(\nu) = \frac{2}{\Delta\nu}\left(\frac{\ell n 2}{\pi}\right)^{1/2} \exp\left\{-\ell n 2\left[\frac{\nu-\nu_0}{\Delta\nu/2}\right]^2\right\}. \tag{3-3}$$

It follows from Eqs. (3-1), (3-2), and (3-3) that the transmission is given as

$$\bar{\tau}_\nu(0,R) = \sqrt{\frac{b}{\pi}} \exp\left\{-2\int_0^R a_1(x)dx\right\} \int_{-\infty}^{\infty} \exp\left\{-(\nu-\nu_0)^2\left[b - 2\int_0^R a_2(x)dx\right]\right\} d\nu, \tag{3-4}$$

where $b = 4\ \ell n 2/(\Delta\nu)^2$. Equation (3-4) can be integrated, and for

$$(2b)^{-1}\int_0^R a_2(x)dx << 1, \tag{3-5}$$

the result can be expressed as

$$\bar{\tau}_\nu(0,R) = \exp\left\{-2\int_0^R\left[a_1(x) - \frac{a_2(x)}{2b}\left(1 + b^{-1}\int_0^R a_2(x)dx\right)\right]dx\right\}. \tag{3-6}$$

Equation (3-5) is equivalent to the condition that the change in the optical depth between the center and half-width point of the measurement bandpass is small with respect to $\ell n 2$. It then follows from Eqs. (3-1) and (3-2) that

$$\bar{\tau}_\nu(0,R) = \exp\left\{-2\int_0^R K(\bar{\nu}_e,x)dx\right\},$$

where

$$\bar{\nu}_e = \nu_0 \pm \frac{\Delta\nu}{2\sqrt{2\,\ell n\,2}}\left(1 + \frac{(\Delta\nu)^2}{8\ell n 2}\int_0^R a_2(x)dx\right). \tag{3-7}$$

Thus, the transmission for a measurement centered on an atmospheric line or in a trough region can be represented by an equivalent monochromatic measurement at the frequency $\bar{\nu}_e$ for bandwidths that are small compared to the atmospheric line width. We note that the first order term for the equivalent frequency depends only on the characteristics of the instrumental distortion function.

An effective frequency can also be used to analyze finite bandwidth effects for a measurement with a rectangular line shape. In this case, the line shape is

$$h(\nu)=\begin{cases}\dfrac{1}{\Delta\nu}, & \text{for} \quad |\nu-\nu_0|\le\dfrac{\Delta\nu}{2},\\ 0, & \text{for} \quad |\nu-\nu_0|>\dfrac{\Delta\nu}{2},\end{cases} \tag{3-8}$$

and

$$\bar{\tau}_\nu(0,R)=\int_{-\Delta\nu/2}^{\Delta\nu/2}\exp\left\{-2\int_0^R\left[a_1(x)-a_2(x)(\nu-\nu_0)^2\right]dx\right\}d\nu.$$

We note that a rectangular line shape provides a first order approximation to the average spectral output of a multimode laser with a frequency jitter of the order of the mode separation. From Eqs. (3-1), (3-2), (3-8), and an analysis similar to that given for Eqs. (3-4) to (3-7), it can be shown that, for a rectangular line shape,

$$\bar{\nu}_e=\nu_0\pm\frac{\Delta\nu}{2\sqrt{3}}. \tag{3-9}$$

Equations (3-7) and (3-9) show that for a Gaussian or rectangular instrumental line shape, the transmission over the atmospheric path from range 0 to R can be represented simply by the transmission at the effective frequency $\bar{\nu}_e$. We note that Eqs. (3-7) and (3-9) are valid for any atmospheric path.

We can also utilize the equivalent frequency technique for an analysis of finite bandwidth effects at a reference frequency. Since a reference frequency is generally chosen either in the far wing of a line or on the edge of an absorption band where the absorption changes slowly with frequency, the absorption coefficient may be represented as a linear function of frequency for a moderately narrow bandwidth. That is,

$$K(\nu,x)=a(x)+b(x)(\nu-\nu_r). \tag{3-10}$$

When the variation in the atmospheric optical depth is small over the line shape, *i.e.*,

$$2(\nu-\nu_r)\int_0^R b(x)dx<<1, \tag{3-11}$$

it follows that the corresponding term in the transmission in Eq. (3-1) can be expanded, yielding

$$\bar{\tau}_r(0,R)=\exp\left\{-2\int_0^R a(x)dx\right\}\int_{-\infty}^{\infty}h_\nu\left[1-2(\nu-\nu_r)\int_0^R b(x)dx\right]d\nu. \tag{3-12}$$

For a line shape which is symmetric about ν_r, it is seen that $h(\nu)(\nu - \nu_r)$ is an odd function with zero integral, and Eq. (12) reduces to

$$\bar{\tau}_r(0,R) = \exp\left\{-2\int_0^R K(\nu_r,x)dx\right\}, \tag{3-13}$$

and

$$\bar{\nu}_e = \nu_r.$$

Thus, the transmission in the region of the reference frequency can be represented by an equivalent monochromatic measurement at the center of the bandpass, if the absorption coefficient is a linear function of frequency and if the instrumental line shape is symmetric.

APPLICATION TO DIFFERENTIAL ABSORPTION

Consider a two-frequency lidar measurement of the resonant absorption for an atmospheric species (*e.g.*, CO_2 or H_2O) or property (*e.g.*, temperature or pressure) where the measurement at each frequency is made with a finite bandwidth laser. The measurement frequency ν is typically centered on an absorption line of the desired atmospheric species. A reference frequency ν_r is then selected at a nearby location where the resonant absorption is weak compared to that at the measurement frequency. The two frequencies are chosen sufficiently close, however, so that the atmospheric backscatter and the attenuation due to both scattering and continuum absorption processes is essentially identical at the two frequencies. The ratio of the signal returns backscattered from the atmosphere at two adjacent frequencies at ranges R_1 and R_2 eliminates the scattering and absorption properties of the atmosphere, except for those of the resonant absorption effect to be measured. For elastic and homogeneous scattering and absorption over a range gate of width ΔR, it follows from the lidar equation (Collis, 1969) that

$$\frac{\bar{\tau}_\nu(0,R_2)/\bar{\tau}_r(0,R_2)}{\bar{\tau}_\nu(0,R_1)/\bar{\tau}_r(0,R_1)} = \frac{E_\nu(R_2)/E_r(R_2)}{E_\nu(R_1)/E_r(R_1)}, \tag{3-14}$$

where $\bar{\tau}_\nu(0,R)$ and $\bar{\tau}_r(0,R)$ are the transmissions due to resonant absorption along the two-way path from 0 to R for laser bandwidths centered at frequencies ν and ν_r, respectively, and $E(R)$ is the energy received from an element of the atmosphere at range R with thickness ΔR and $R_2 = R_1 + \Delta R$.

The inclusion of finite laser bandwidth effects and non-zero resonant absorption at the reference frequency complicates the analysis of Eq. (3-14) considerably, since the differential absorption coefficient, $K(\nu) - K(\nu_r)$, is not a directly measured or easily derived quantity. In addition, the differential ranging measurement given by Eq. (3-14) not only has absorption information in the desired range element of width ΔR centered at $R = (R_1 + R_2)/2$, but also contains absorption information from the region 0 to R_1.

If an effective frequency is used to represent the absorption at the reference frequency, Eq. (3-13), it follows that a differential absorption measurement with differential ranging and finite bandwidth at both the on-line and reference frequencies can be represented as

$$\frac{\bar{\tau}_\nu(0,R_2)/\bar{\tau}_r(0,R_2)}{\bar{\tau}_\nu(0,R_1)/\bar{\tau}_r(0,R_1)} = \frac{\int_{-\infty}^{\infty} h(\nu)\exp\left\{-2\int_0^{R_2}\left[K(\nu,x)-K(\nu_r,x)\right]dx\right\}d\nu}{\int_{-\infty}^{\infty} h(\nu)\exp\left\{-2\int_0^{R_1}\left[K(\nu,x)-K(\nu_r,x)\right]dx\right\}d\nu}, \tag{3-15}$$

where $h(\nu)$ is the laser line shape for the on-line measurement. Equation (3-15) has the form of a differential absorption measurement. We note that Eq. (3-15) is valid even for the case of strong absorption in the region of ν_r, since no assumptions on the overall level of absorption were made.

An effective frequency can also be used to greatly simplify the analysis of finite bandwidth measurements at the on-line frequency. It follows from Eq. (3-15) that a differential absorption measurement with differential ranging and finite bandwidth can be expressed in terms of the effective frequencies $\bar{\nu}_e$ and ν_r as

$$\frac{\bar{\tau}_\nu(0,R_2)/\bar{\tau}_r(0,R_2)}{\bar{\tau}_\nu(0,R_1)/\bar{\tau}_r(0,R_1)} = \exp\left\{-2\int_{R_1}^{R_2}\left[K(\bar{\nu}_e,x)-K(\nu_r,x)\right]dx\right\}. \tag{3-16}$$

COMPARISON WITH SIMULATION

To evaluate the application of the effective frequency technique, we consider the case of generalized absorption in the atmosphere. The absorption coefficient of a gas species in the atmosphere at frequency ν is (Chapter 2)

$$K(\nu) = qnS(T)f(\nu-\nu_0), \tag{3-17}$$

where q is the molecular mixing ratio of the species, n is the number density at pressure p and temperature T, $S(T)$ is the line strength, and $f(\nu - \nu_0)$ is the line shape at frequency ν for a line centered at ν_0. For atmospheric measurements where the effects of both collision and Doppler broadening contribute significantly to the absorption, the line shape is given by the Voigt profile (Penner and Kavanaugh, 1953), which is a convolution of independent Lorentz and Doppler profiles. It is given as

$$f(\nu-\nu_0) = \frac{f'a}{\pi}\int_{-\infty}^{\infty}\frac{\exp(-y^2)dy}{a^2+(\xi-y)^2}, \tag{3-18}$$

where

$$f' = \left(\frac{\ell n2}{\pi}\right)^{1/2}\frac{1}{b_d}, \tag{3-19a}$$

$$a = (\ell n2)^{1/2}\frac{b_c}{b_d}, \tag{3-19b}$$

and

$$\xi = (\ell n 2)^{1/2} \frac{(\nu - \nu_0)}{b_d}, \tag{3-19c}$$

where b_c and b_d are the collision broadened and Doppler broadened line half-widths at half-height, respectively, and are defined as,

$$b_c(p,T) = b_c^0(T_0)\left(\frac{p}{p_0}\right)\left(\frac{T_0}{T}\right)^m,$$

and (3-20)

$$b_d(T) = \left[\frac{2kT\ell n 2}{M_o c^2}\right]^{1/2} \nu_0,$$

where M_o is the mass of oxygen, c is the velocity of light, p_0 is standard pressure, $b_c^0(T)$ is the collision-broadened line half-width at a pressure of 1 atm and the exponent of the temperature dependence of the collision-broadened half-width m is predicted to be one-half from kinetic theory.

To evaluate the error in the determination of the differential absorption coefficient using an effective frequency, Eq. (3-15) was evaluated numerically for rectangular and Gaussian laser line shapes of various widths using Eqs. (3-17) and (3-18). The atmospheric model used for evaluating Eq. (3-17) is a multilayer, one-dimensional model with up to 50 homogeneous layers. The calculations simulated measurements for a two-way atmospheric path from infinity to various altitudes for a total optical depth of 2 at line center. The altitude of the end point of the measurement is represented by the pressure at that altitude, as given by the parameter a proportional to pressure. Thus, the calculations begin with a Doppler profile at high altitude, $a = 0$ and include all values of a for the Voigt line profile up to and including the value of a at the end point of the measurement.

Figures 3-1a and 3-1b give the errors between this detailed evaluation of the differential absorption coefficient and the simplified analysis using a monochromatic calculation at an effective frequency for the cases of Gaussian and rectangular laser line shapes, respectively. The errors are shown as a function of the ratio of the laser bandwidth, the full width at half height, to the half-width at half-height of the Voigt line profile at the end point of the measurement, b_v (Olivero and Longbothum, 1977). In general, the error increases with increasing values of $\Delta\nu/b_v$ and a. For values of $\Delta\nu/b_v < 0.5$, the error in using an effective frequency is $< 0.5\%$ for a rectangular line shape, and $< 1\%$ for a Gaussian line shape. Accuracy at the 0.1% level can be obtained for values of $\Delta\nu/b_v < 0.2$.

We also evaluated the error in the determination of the differential absorption coefficient for horizontal paths using an effective frequency. In this case, the ratio of the transmissions, Eq. (3-1), at the on-line and reference measurements was evaluated numerically for rectangular and Gaussian laser line shapes of various widths, using Eqs. (3-17) and (3-18), as before. The calculations included the range of Voigt parameter a from near Doppler (small a) to near Lorentz (large a) profiles.

Figures 3-2 and 3-3 give the error between the detailed numerical integration of the Voigt profile to find the absorption coefficient and the simplified monochromatic calculation, using the effective frequency for an optical depth of 2 at line center. As shown in Figure 3-2 for the case of a rectangular laser line shape, the

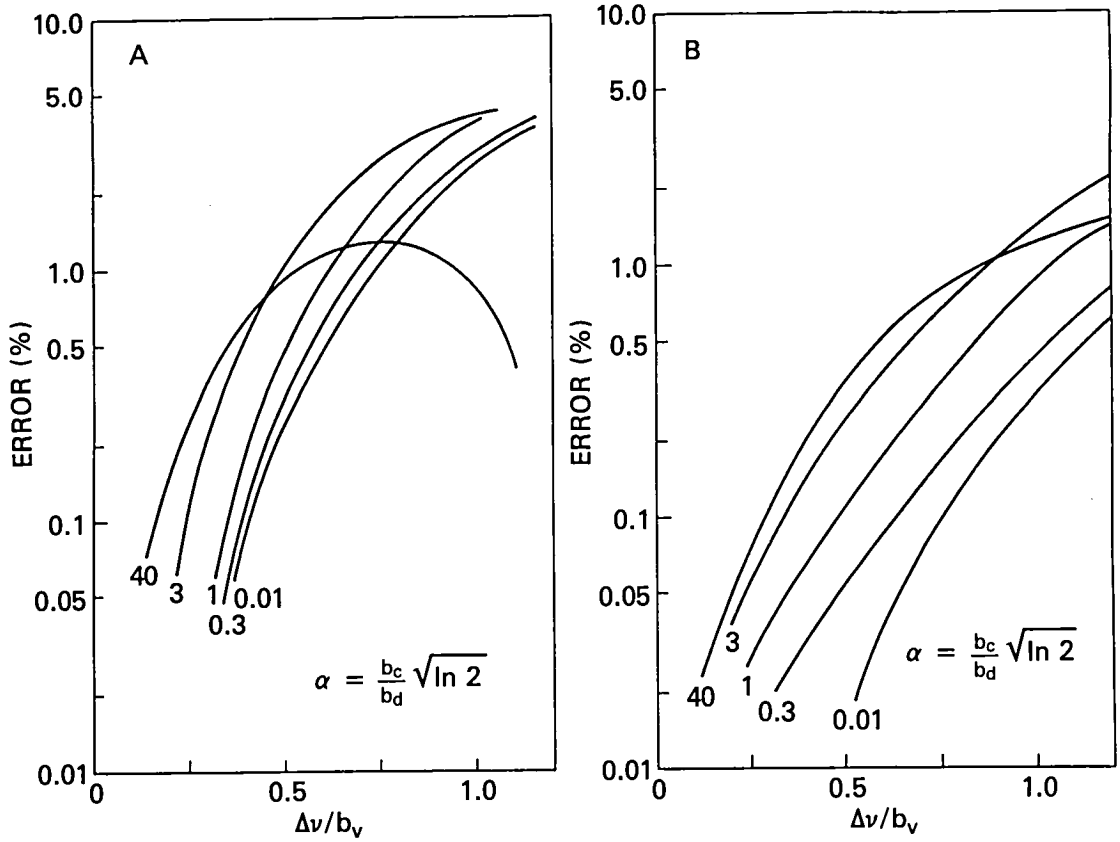

Figure 3-1a and -1b. The percentage error in the differential absorption coefficient, as a function of the laser bandwidth to the half-width at half-height of the Voigt line profile, using a monochromatic calculation at an effective frequency to represent the effects of finite laser bandwidth. Figures 3-1a and -1b are for the cases of Gaussian and rectangular laser line shapes, respectively, for a downward viewing experiment from space to an altitude (pressure) in the atmosphere defined by the Voigt parameter $a = \left(b_c^0 p / b_d\right)\sqrt{\ell n 2}$.

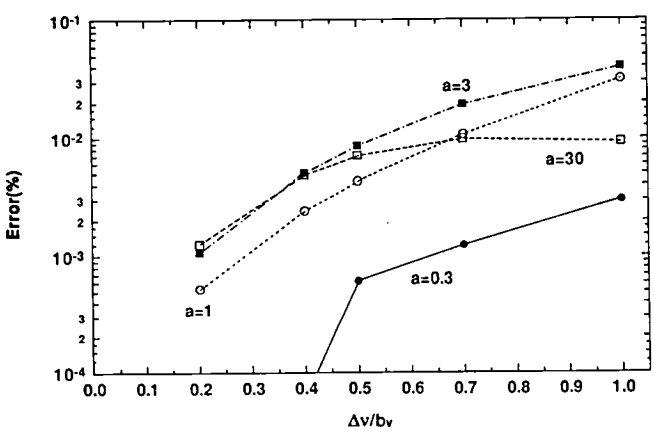

Figure 3-2. As Figure 3-1, but for a horizontal air path with an optical depth of two and a rectangular laser line shape.

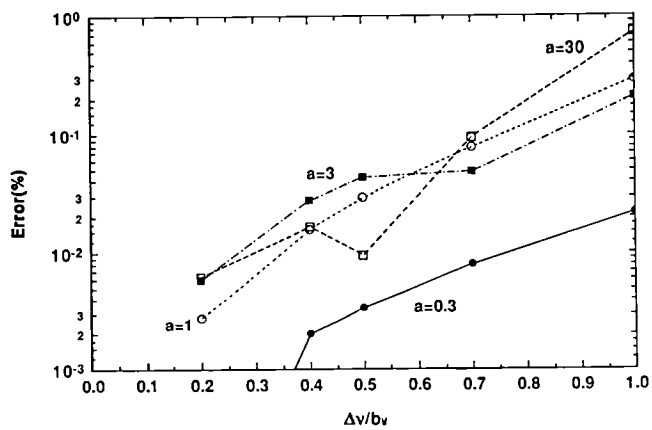

Figure 3-3. As Figure 3-2, but for a Gaussian laser line shape.

errors are < 0.01% for values of $\Delta\nu/b_v$ up to 0.5. Figure 3-3 shows that for a Gaussian laser line shape, the errors are < 0.1% for $\Delta\nu/b_v$ up to 0.7.

CONCLUSION

We have shown that an effective monochromatic frequency can be used to represent the effects of finite instrumental bandwidth for spectral measurements centered on an absorption line, a trough region, or a slowly varying spectral feature. The technique is applicable to both integrated path and differential ranging experiments, and the resulting frequency is independent of the atmospheric line shape and path, to first order. The application of the effective frequency technique greatly simplifies the analysis for a large number of spectroscopic problems. Analyses similar to those we have presented for Gaussian and rectangular line shapes can be used to derive the effective frequency for other instrumental line shapes. Complex line shapes, including multimode structure, can also be represented by a set of effective frequencies which correspond to a superposition of elementary forms.

CHAPTER 4 DIFFERENTIAL ABSORPTION LIDAR SYSTEM

INTRODUCTION

This chapter describes the design and operation of the differential absorption lidar (DIAL) system developed to remotely measure atmospheric pressure and temperature fields. In addition, results of system tests and calibrations are discussed, including the first detailed measurements of alexandrite laser spectral properties.

The lidar system is designed to remotely measure atmospheric pressure and temperature profiles from the ground looking up and from an aircraft looking down to the surface. Major parts of the system are used in both configurations; only the supportive framework and telescope are not shared. The lidar system consists of three major subsystems (Figure 4-1): a transmitter subsystem containing the lasers with their power supplies and cooling systems, beam steering optics, and laser output monitoring instruments; a receiver subsystem comprised of a telescope, gated photomultiplier, and optical and electronic filters; and the control and data acquisition subsystem consisting of electronic modules for digitizing the transmitted and received signals, system clocks and timing circuitry, a microprocessor controller, data handling and storage devices, and a video terminal for operator interface. Figure 4-2 is a photograph of the lidar system configured on a 1.5 by 3.6 m optical table. The power supply for one of the alexandrite lasers appears in the foreground. The laser heads are mounted on the near edge of the table. The telescope is centered behind the table, and the detector package is mounted on the small elevated table on the right side of the picture.

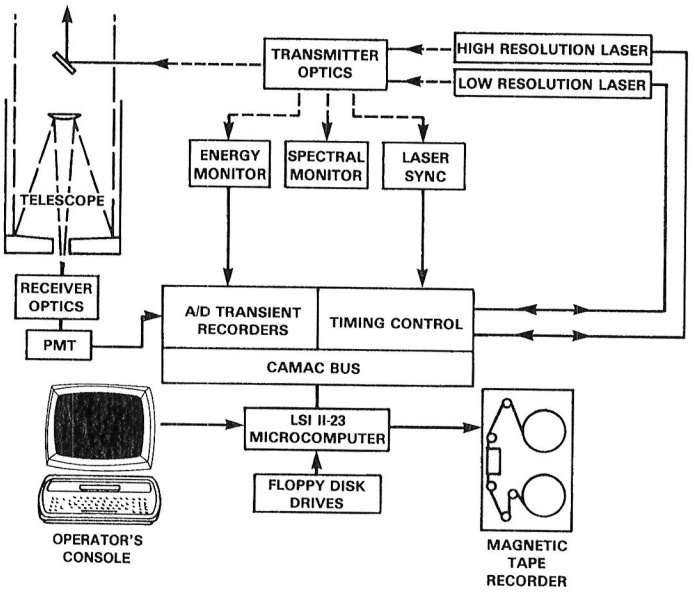

Figure 4-1. Block diagram of the lidar system with the original data system. Dashed arrows indicate optical paths and solid arrows indicate electrical paths.

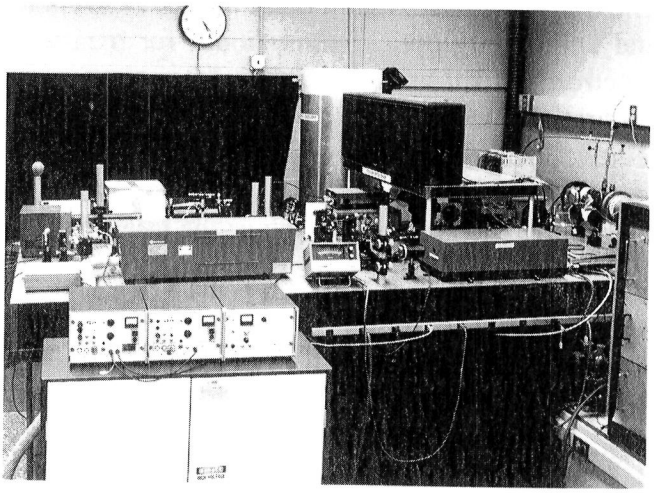

Figure 4-2. Photograph of the laboratory lidar system as it first appeared with two alexandrite lasers in 1983.

Figure 4-3 shows the major system components as they are configured in the NASA Lockheed Electra aircraft. The transmitter and receiver optical tables are mounted to a single rigid aluminum framework which in turn is shock-mounted to the aircraft floor tracks. The telescope is also attached to this framework and can be oriented pointing down as well as up.

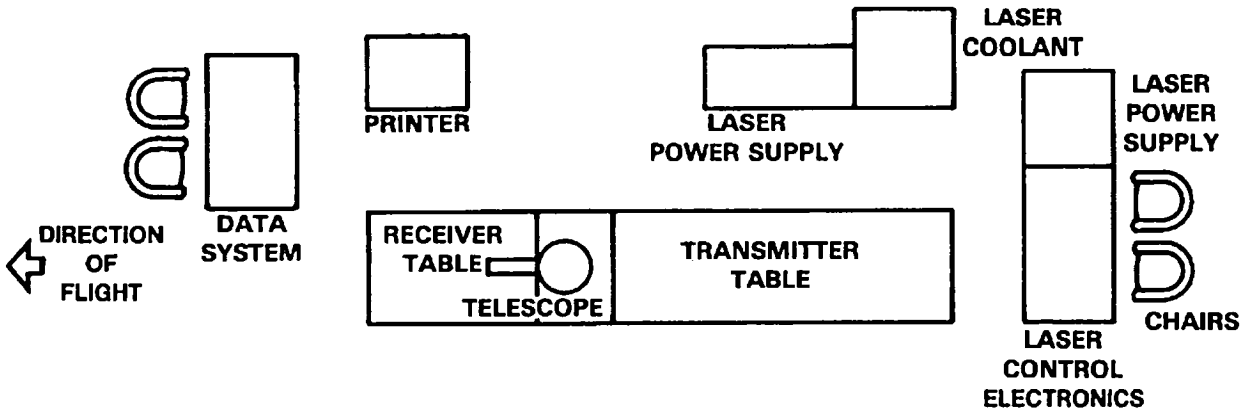

Figure 4-3. Top view of lidar system components inside the NASA Lockheed Electra aircraft. A 40 cm window in the aircraft's belly lies directly below the telescope and is located along the plane's centerline.

TRANSMITTER

The transmitter subsystem is comprised of two narrow band tunable pulsed alexandrite lasers, beam steering and collimating optics, photodiodes for measuring laser energy and marking time, a 0.5-m focal length spectrometer for an approximate determination of laser wavelength, and a multipass gas cell for spectral calibrations and diagnostics. Figure 4-4 is a block diagram of the transmitter optical bench showing the relative location of the components. Not shown is the gas cell, which is attached to a shelf underneath the transmitter optics. Figure 4-5 is a photograph of the aircraft optical bench looking forward in the aircraft, and Figure 4-6 is a photograph of the laser control electronics, power supply, and cooling systems.

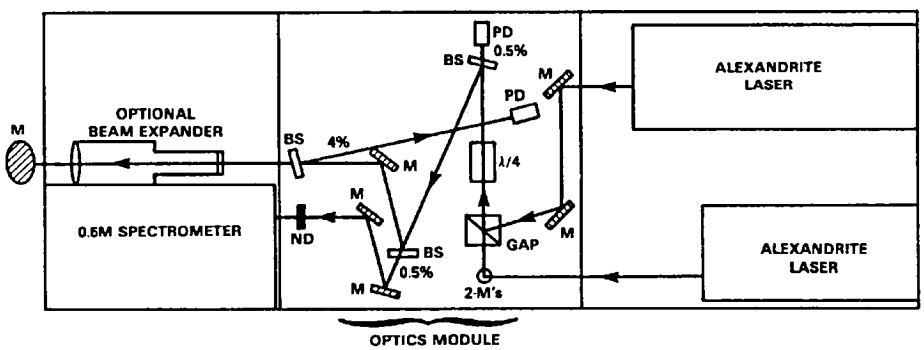

Figure 4-4. Transmitter schematic diagram showing relative location of components which are mounted to an 84 by 244 cm optical bench. Key: M-mirror, GAP-Glan Air prism, λ/4-quarter-wave circular polarizer, BS-beam splitter, PD-photodiode, and ND-neutral density filter.

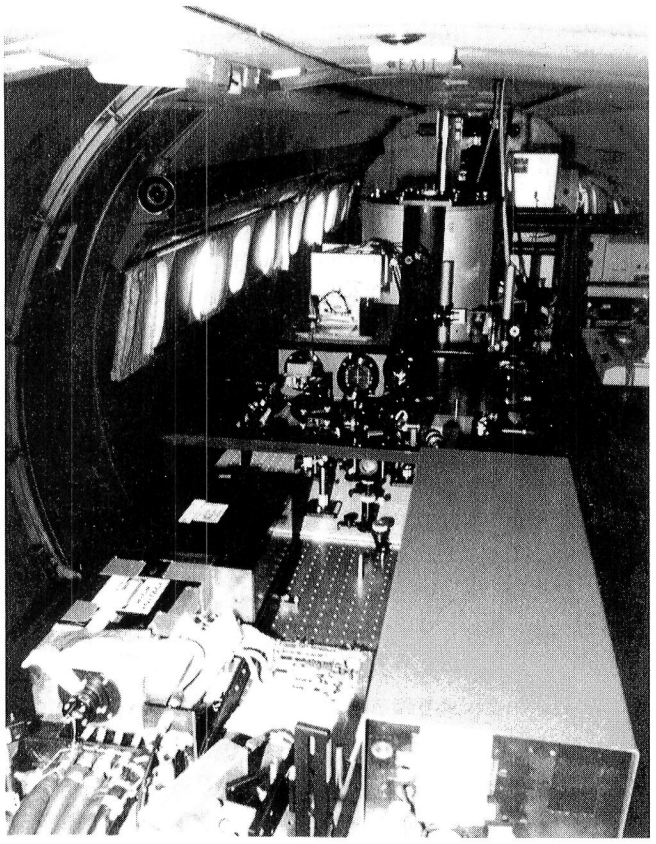

Figure 4-5. Photograph of the airborne system transmitter optical bench, showing the two alexandrite laser heads in the foreground and the receiver telescope in the background.

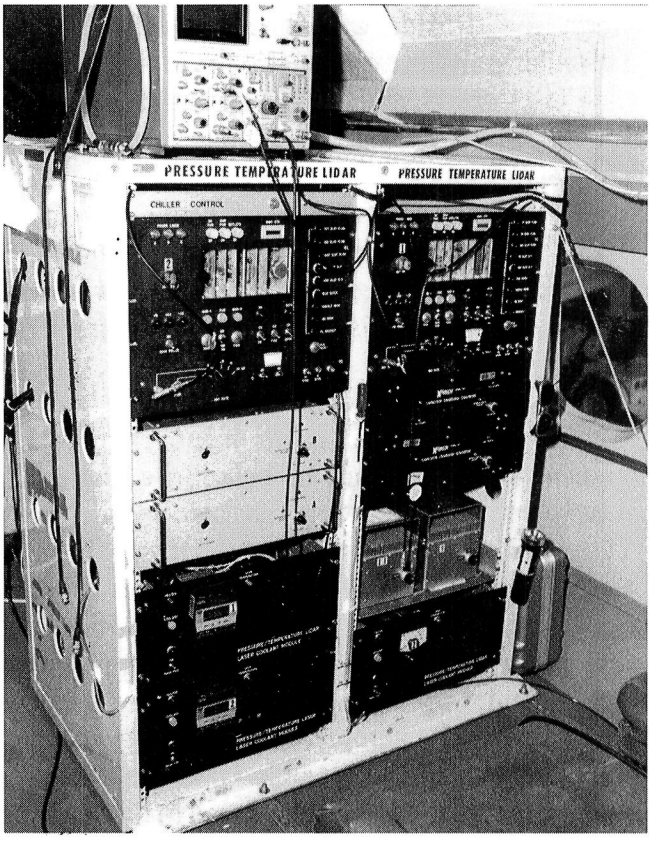

Figure 4-6. Photograph of the alexandrite laser control electronics, power supplies and cooling systems.

The lidar system utilizes two solid-state alexandrite lasers, referred to as "Alex I" and "Alex II". Ruby-pumped liquid dye lasers were initially used in the transmitter (Korb, *et al.*, 1983) and, at that time, were the only commercially available tunable high-resolution lasers for this spectral region. A single alexandrite laser (Alex I) and ruby-pumped dye laser were used to make the first remote measurements of the atmospheric pressure profile (Korb, *et al.*, 1985). The repetition rate of the ruby-pumped dye laser system was limited to 0.5 Hz, whereas with two alexandrite lasers, the system repetition rate was 5 Hz, limited by the data system. With improvements to the data system, we were able to increase the rate to 10 Hz. Each alexandrite laser is tunable from approximately 725 to 780 nm. To obtain sufficient measurement accuracy, the spectral bandwidth (FWHM) of the on-line laser needs to be no greater than 0.02 cm^{-1} with a line-center frequency stability of ± 0.002 cm^{-1} during the course of a set of measurements (typically, 30 sec to 30 min). The spectral specifications for the off-line laser are less stringent, namely, 0.2 to 2.0 cm^{-1} FWHM and ± 0.05 cm^{-1} stability, depending on the exact wavelength chosen. The development of solid-state tunable alexandrite lasers (Walling, *et al.*, 1980) has resulted in a more compact and efficient system and holds promise for developing a space-qualified lidar system capable of carrying out measurements of atmospheric temperature and pressure from satellites.

Because the alexandrite laser development has been the most challenging aspect of this research, Chapter 5 describes it in detail.

The two laser beams are combined onto a single axis using a Glan-Air prism (see Figure 4-4). The beams are orthogonally polarized, so that one will be transmitted straight through the prism while the other, entering the

prism from the side, will be nearly totally reflected at the Brewster cut in the prism. A Pockels cell is used as a circular polarizer on the two orthogonally polarized beams, producing equal polarization components in each laser wavelength. This is to minimize any systematic discrepancies in the measurements of outgoing energy or backscattered signal due to preferential reflection of either polarization in any of the other optics. The beam splitter that samples the outgoing beam for the energy monitor is placed near normal incidence to further minimize preferential reflection of either laser wavelength. The voltage on the Pockels cell is adjusted so that the ratio of the two laser energies transmitted by the system, as measured by an independent photodiode placed in the outgoing beam, equals the ratio measured by the energy monitor. This effectively calibrates the energy monitor, and is validated by exchanging detectors and digitizers.

The two lasers are tuned to within 0.5 cm^{-1} of the desired frequencies by monitoring their wavelengths with a 0.5 m Czerny-Turner spectrometer. This instrument has an X-Y cathode ray tube (CRT) display of its focal plane array detector output, including a cursor with wavelength readout. The laser outputs are directed to the atmosphere or to a multipass gas cell, and a real-time plot of atmospheric (or gas cell) transmission is displayed on the system console terminal (Figure 4-7). At the terminal, we select the altitude and the number of range bins and laser pulses to be averaged for the transmission display calculations. The on-line laser is then electronically tuned with a constant scan rate while the display is continuously updated, generating an absorption spectrum which is displayed on the terminal screen. Figure 4-8 includes a laser frequency scan of the transmission through a multipass gas cell showing the low-pressure oxygen lines at 13153.4 and 13154.2 cm^{-1}. By comparing the absorption line spacings and relative strengths with laboratory data on these line parameters, the laser etalon position is calibrated to the known oxygen absorption line frequencies. The on-line laser is then manually tuned to the desired absorption feature, either an absorption trough for pressure measurements or an absorption peak for temperature measurements. The measurements of laser signal backscattered from the atmosphere versus altitude for the on-line and off-line frequencies are then recorded on digital magnetic tape for post-measurement analysis.

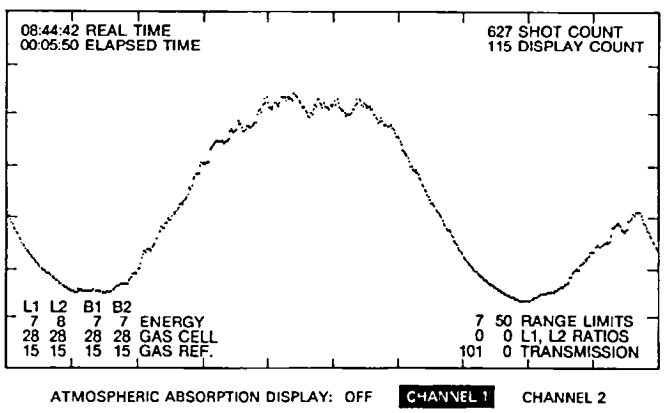

Figure 4-7. Console monitor display showing real-time plot of atmospheric absorption as the laser frequency is scanned across the two oxygen lines near 13154 cm^{-1}. This is the two-way transmission across an 850 m horizontal path near the ground to a hard target. The numerals indicate photodiode readings and housekeeping information.

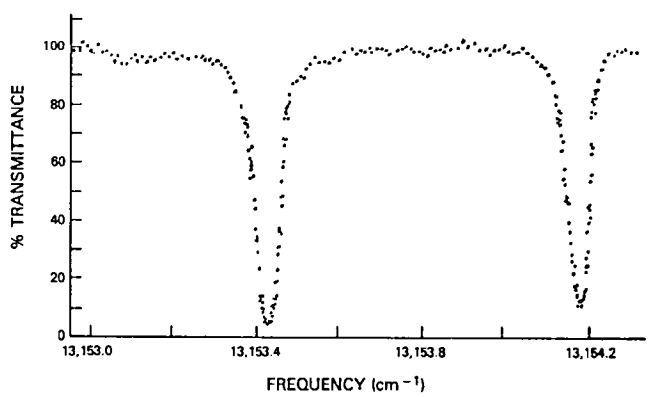

Figure 4-8. Playback of previously recorded gas cell transmission measured as the laser frequency was scanned across the two oxygen lines near 13154 cm^{-1}. The O_2 pressure in the cell was 48 torr and total path length was 149 m.

A silicon photodiode is used to monitor the output energy of each laser to normalize the lidar return signals for shot-to-shot energy variations and for the ratio of the on-line and off-line laser energies needed for measuring pressure. A small portion of the outgoing beam is directed to the energy monitor. An opal glass diffuser in front of the energy monitor eliminates effects due to spatial nonuniformities in the laser beam and the detector surface. Neutral density filters are used to attenuate the laser radiation, and a 10 nm interference filter reduces background and flash-lamp radiation. This signal is fed to a 9-bit gated charge digitizer. Each laser pulse energy is digitized and recorded on tape with the lidar return signals.

The system includes a lidar return simulator which can be used to perform system tests without actually transmitting any laser energy into the atmosphere. It consists of a light-emitting diode (LED) placed in front of the receiver field stop, and pulsed with an exponentially decaying current to simulate actual laser radiation scattered off the atmosphere. It simulates the different atmospheric absorptions for the on-line and off-line laser frequencies by pulsing the LED twice, with different decay time constants to represent the two different laser return signals.

RECEIVER

The major components of the receiver are a telescope, focal plane optics, photomultipliers, optical and electrical filters, power supplies, amplifiers, and gating electronics.

The telescope used for aircraft measurements is a 40 cm diameter *f*/12 Cassegrain with aluminum-coated optics and a Nasmyth focus. The ground-based system telescope is a 44 cm diameter *f*/4.5 Newtonian with a gold-coated primary and aluminum-coated secondary mirror. This telescope rests on the floor and is directed to the zenith through a hatch in the roof. The aircraft system telescope can be directed toward the zenith as well as the nadir, through either of a pair of 40 cm windows in the aircraft. The windows are mounted at a 7.5° angle with respect to the optical bed and floor of the aircraft to prevent reflections of the transmitted laser beam from entering the receiver. The laser beams are transmitted coaxially to the telescope, reflected off a dielectric mirror mounted behind the telescope's secondary mirror. Baffle tubes enclose the beams from the transmitter optical table to the aircraft window in order to prevent stray light or reflections from entering the receiver. For daytime measurements, we use a collimating lens and narrowband (1.0 to 2.0 nm) interference filter to reduce background light. A low-pass optical filter with a 720 nm cutoff was used for night measurements. However, subsequently we have used 1 nm bandwidth filters for nighttime measurements because the rotational Raman scattering contaminated the measurements (see Chapter 8). The photomultiplier detector is electronically gated on for about 100 μs, starting several microseconds after the laser fires by switching the voltage on the second dynode. When looking down from the aircraft, ground and ocean surface reflections produce a very strong transient in the signal. We notch out this transient by gating the tube off for several microseconds while the ground reflection occurs. This greatly reduces a small bias in the tube's output following such a strong transient. Background measurements are made on each shot about 50 μsec after the ground reflection. The photomultiplier tube (PMT) output is amplified with a low-noise transimpedance amplifier and is then filtered at the Nyquist bandwidth with a single pole passive LC filter before input to a 12-bit digitizer. The digitized record of the on-line and off-line return signals is transferred from the digitizer memory to magnetic tape after each pulse pair, along with data from the system clock, counters, and energy monitor. The system was built with two receiver channels for using two detectors, one with high gain and one with low gain, to increase receiver dynamic range. For aircraft measurements, one channel is converted to an altimeter to give precise aircraft altitude information.

CONTROLLER AND DATA ACQUISITION

The data acquisition system converts the analog electrical signals to digital information and records that information on magnetic tape. The same microprocessor that controls the lasers also controls the data acquisition equipment. The CAMAC Standard (ANSI/IEEE 583-1975) was chosen as the format for the data acquisition equipment. The modularity helps reduce the system cost by tailoring the system to meet only necessary or desired functions and reduces obsolescence (*i.e.*, improvements to any one function require replacing only that one module). Each module plugs into a crate containing power supplies and a backplane for the data bus (CAMAC data-way). Referring to Figure 4-9, the crate contains a controller, two transient digitizers, two programmable clocks, a charge digitizer, and the lidar control module, which contains circuits to control timing functions, such as the firing of the lasers and the gating of the photomultipliers and transient digitizers. An 80 MHz master clock was later added to drive the two digitizers and other timing functions. The microprocessor used for system control and the coordination of all input/output (I/O) is an LSI-11/23. The computer system includes a dual floppy disk drive, a video graphics terminal, a graphics printer, and a 2-inch nine-track digital tape drive. The computer has floating point hardware and 2 Mbytes of random access memory (RAM). All operator information is input via the video terminal, and all data are stored on the nine-track magnetic tape. Figure 4-10 is a photograph of the LSI-11/23-based lidar data acquisition system. The nine-track tape recorder is mounted behind the data system rack. The CAMAC crate controller connects directly to the LSI Q-Bus and makes all the CAMAC modules appear as individually addressable peripherals to the microprocessor. A 12-bit 10 MHz CAMAC transient digitizer (Transiac model 2012) is used to digitize the output of the PMT. Typically, less than 500 samples per laser shot are taken. The digital samples are read out by the computer after each pair of shots. The digitizer has an oscilloscope display output which drives an X-Y CRT display monitor. A programmable three-speed clock generator is used to control the sampling speed of the transient digitizer during a measurement cycle, as discussed in detail below. The clock module contains counters which we use to record the on-line and off-line laser pulse separation and the number of samples digitized.

The altitude registry on the return signals is provided by triggering a clock and counter circuit with the leading edge of a saturated signal from a photodiode which detects when each laser pulse was transmitted (laser synchronization). The clock pulses are used to trigger the receiver signal digitizer, and the counter ticks off a preset delay which determines when digitizing commences relative to the laser output. The maximum clock rate to the digitizer is 20 MHz, which is derived from an 80 MHz oscillator. Each laser synchronization signal is used to restart the delay counters. A problem occurred during the data analysis when we took the ratio between the on- and off-line return signals, due to inadequate accuracy in the altitude registry between the two signals. Since the laser pulse can occur randomly anywhere within the digitizer clock period, the average error in the clock phase (relative to the laser pulse) is one-half or one-quarter of the clock period. Structure in the return signals due to inhomogeneities in the atmospheric aerosols produced a ringing effect in the ratio of the return signals, particularly where large, rapid changes in the signals occur at aerosol layer boundaries. The data were adjusted computationally to correct for the relative error in altitude registry between on-line and off-line returns. It was found that the ratio was sensitive to misregistries as small as one-tenth of a clock period, even though the signal was bandwidth limited to less than half the clock frequency. Subsequently, the clock electronics were redesigned so that the 80 MHz oscillator is now rephased to each laser pulse with a residual error of a few hundred picoseconds. In addition, it was determined that fluctuations in the laser output energy caused the leading edge detector to undergo significant (tens of nanoseconds) jitter with respect to the laser energy pulse peak. The leading edge detection electronics were replaced with a constant fraction discriminator, and the photodiode operated in the linear region. These have been tested and the residual jitter due to this effect is a few hundred picoseconds.

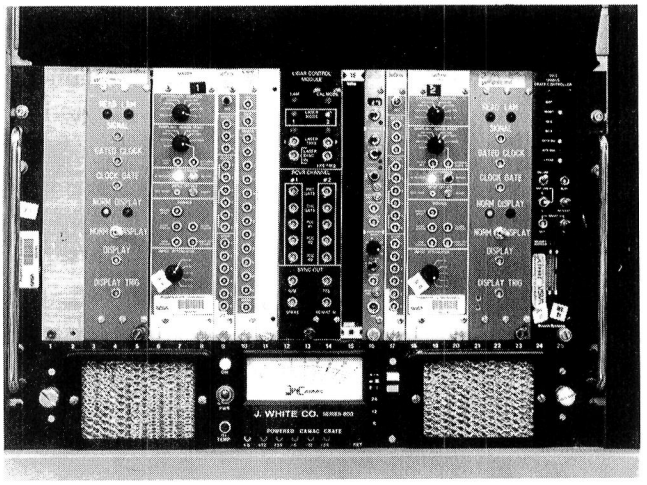

Figure 4-9. Photograph of the CAMAC data acquisition instruments with the cabling removed.

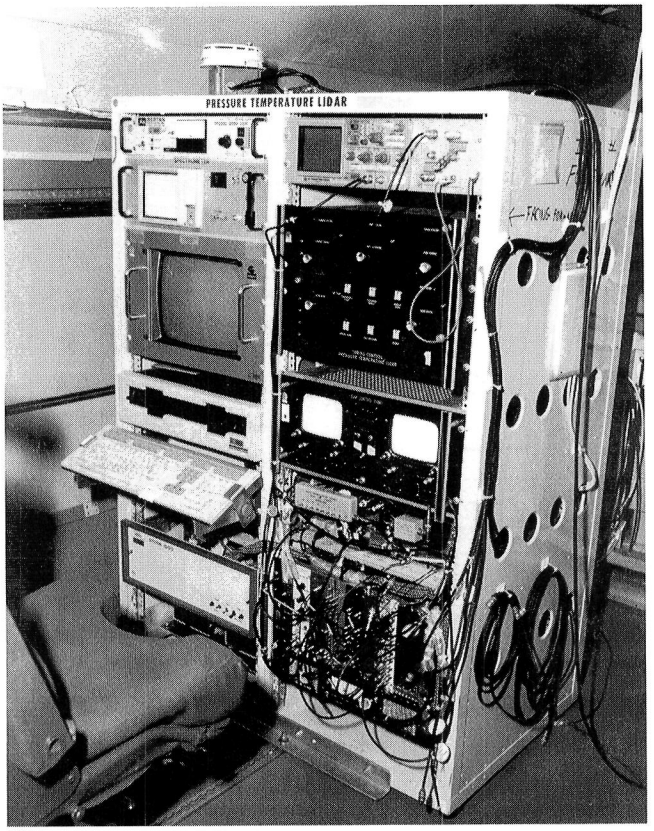

Figure 4-10. Photograph of the LSI-11/23-based data system, except for the tape recorder.

The lidar control module (LCM) is the interface between various parts of the lidar system (Figure 4-11). It provides trigger pulses to the lasers, gating signals to the photomultipliers, a gate to the laser energy digitizer, and timing control pulses to the programmable clocks based on the PMT gate pulse settings. Figure 4-12 illustrates the timing sequence for a laser pulse pair data acquisition sequence. The following describes each of the LCM functions in detail. A "fire" command to the LCM, initiated via a computer instruction or a manual pushbutton, causes the laser timing circuit to initiate a firing sequence. A separate trigger is generated for each of the two lasers, and each laser emits a pulse about 100 μsec later. The lasers are triggered in sequence with a time separation determined by a thumbwheel switch on the control panel.

In order to suppress ground loop currents and noise on the laser control lines from entering the data system and lidar signal cables, optically isolated logic interfaces have been installed on the laser trigger lines. The logical "or" of both trigger pulses can be sent to the lidar return simulator (LRS). However, either the lasers or the LRS is in operation at any given time, as determined by a toggle switch on the control panel. One or both lasers can be fired, depending on the state of a programmable flip-flop. A toggle switch on the control panel can be used to interrupt automatic (computer) operation of the system to allow manual firing of the lasers. The laser and LRS triggers are suppressed when the system is programmed into the calibration mode, which allows background readings to be taken on all detectors. Thumbwheel switches on the display module front panel are used to set each PMT gating delay and width. The delay is measured from the detection of the laser output by the synchronization photodiode until the PMT is gated on. Each digitizer is clocked at a high rate (5, 10, or 20 MHz) while the PMT is gated on. The clock is slowed to 100 kHz between the end of the PMT gate for the first lidar return and the beginning of the gate for the second lidar return. The clock then resumes its previous high rate for digitizing the waveform from the second lidar return.

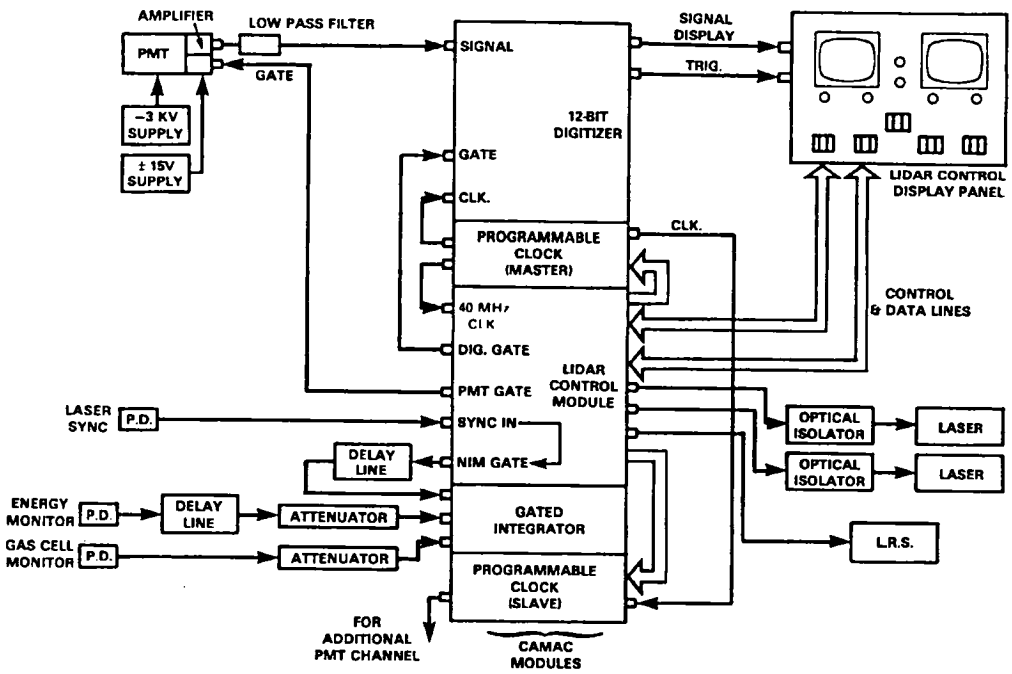

Figure 4-11. Data acquisition electronics diagram in its initial configuration. Only one receiver channel is shown for clarity. A rephasable 80 MHz clock and discriminator were added later to eliminate timing jitter between successive laser pulses and the return signals.

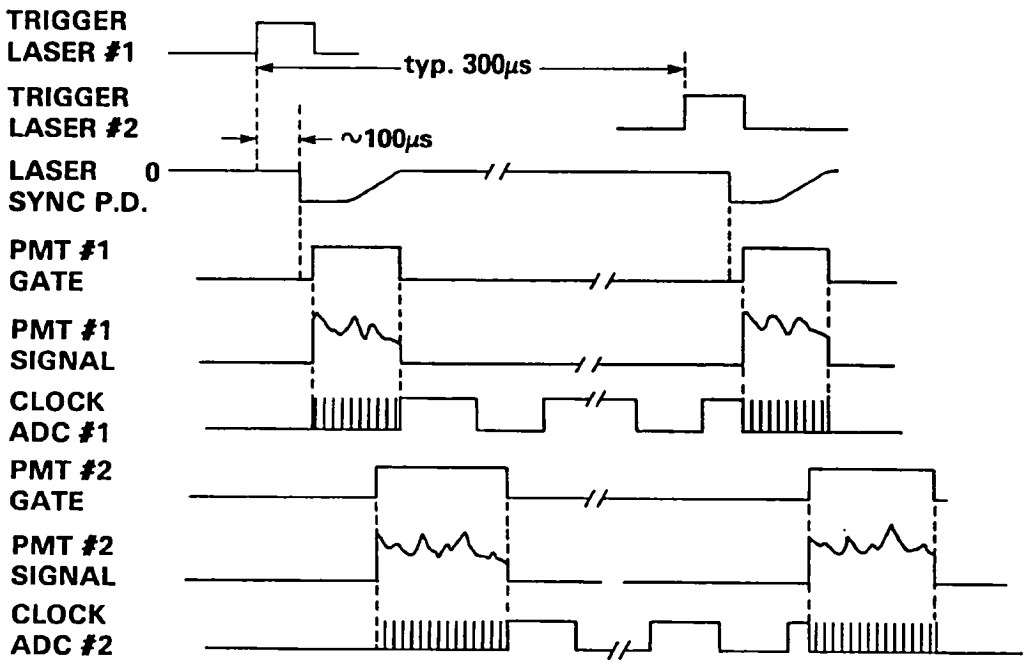

Figure 4-12. Timing diagram illustrating the data acquisition sequence. Two lasers are triggered sequentially and a photodiode detects the laser pulses in order to synchronize the gating and digitizing of two photomultipliers, each of which measures part of the atmospheric backscatter signal from each laser pulse.

The system repetition rate is determined by a pulse generator used to trigger the laser flashlamps. The computer data acquisition is then slaved to the laser output pulses using what is essentially a software phase-locked loop.

SYSTEM SOFTWARE AND OPERATION

The lidar system is controlled by the system microprocessor with operator input via the console keyboard. There is a separate control panel to adjust the detector gating parameters and laser separation, and a laser tuning control panel to operate the on-line laser. All data system functions are controlled by the system software with the console keyboard acting as a control panel.

The software is interactive and provides real-time displays on the video terminal to assist the operator. System operation begins with the display of a menu of adjustable system parameters on the screen (see Table 4-1). The operator may select from among the following options: one or two laser transmissions, active (laser firing) or passive (calibration) modes, one or two receiver channels (and, if one, which channel), output to be displayed on the screen only or also recorded onto tape, digitizer sampling rates of 5, 10, or 20 MHz, automatic background subtraction mode enabled or not, and an upper limit on the number of shots, if desired.

For each parameter, the default value is highlighted on the screen, and, to change the current value, a unique single code letter (generally, the initial letter of the parameter name, as indicated by underscoring on the screen) is input on the operator console. A command interpreter in the software is used to toggle between the permitted options for each parameter. When the choice of parameter values is completed, an exit code is pressed on the console to begin laser operation, and the selected parameter values will remain invariant

throughout the laser firing session. The lidar control module then triggers the lasers, and the program acquires and records data, if this option was selected. A real-time parameter menu appears on the terminal screen containing interactive options, which may be modified during the firing of the lasers (see Table 4-2). Assuming lidar data are being recorded, input of the appropriate code from the console will cause data recording on the magnetic tape to pause until the code is pressed again, thereby resuming recording. A different code allows the opening or closing of a new file for storing data on the tape. Another parameter code is used to choose the method for laser frequency control, *viz.*, either open loop tuning or locking to the wavemeter. Two additional codes permit real-time displays on the terminal screen (replacing the parameter menu) of either gas cell absorption or atmospheric absorption, as described below. Repeating the display codes returns the parameter menu to the screen with all current options indicated. When data taking is completed, an exit code input from the console terminates the lidar data acquisition program.

Table 4-1. Lidar data acquisition system menu of parameters available for selection prior to data acquisition. The system operator toggles between options by pressing the corresponding code letter on the console keyboard.

Parameter name	Code letter	Options (default value underscored)
Transmitter	T	One laser, Two lasers
Mode	M	Active (laser firing), Passive (calibrate)
Receiver	R	Channel 1, Channel 2, Both channels
Output	O	Display, Record on tape
Sample rate/lidar range	S	20 MHz, 10 MHz, 5 MHz
Background subtraction	B	No, Yes
Number of shots	N	0, Enter value*
Exit from menu	E	

*A non-zero positive integer (less than 32 K).

Table 4-2. Lidar data acquisition real-time parameter menu. Options are selected by pressing the corresponding code letter on the console keyboard while data acquisition is in progress.

Parameter name	Code Letter	Options (default value underscored)
File	F	Close current file, Open new file
Tape	T	Pause (leave file open), Continue
Gas cell absorption display	G	On, Off
Atmospheric absorption display	A	Off, Channel 1, Channel 2
Laser frequency control	L	Open loop tuning, Lock to wavemeter
Exit from program	E	

The gas cell or atmospheric transmission display (see Figure 4-7) shows the real-time transmission for each laser shot versus the shot number. Up to 512 shots can be displayed across the screen. A linear recursive digital filter with adjustable weighting is used for averaging transmission data. Inputting the numeral n on the console keypad will produce the weighting coefficient $(1 - 2^{-n})$to be associated with the previous averaged

value and the weighting coefficient 2^{-n} to be associated with the current parameter value, where n is in the range 0 to 9. The digital filter used for averaging is of the form:

$$y_{k+1} = \left(1 - \frac{1}{2^n}\right) y_k + \left(\frac{1}{2^n}\right) x_{k+1} \tag{4-1}$$

for $n = 0,1,2,...,9$, where y are the averages and x the current data values. Thus, higher values of n result in more "smoothing" of the graph.

Various diagnostic and informational data are also shown and updated on the screen in real time. The current time and the elapsed time from the initiation of measurements are given, as well as the total number of shots fired in the session, and the number of shots currently displayed on the screen, which is refreshed after every 512 shots. The designations, "L1", "L2", "B1", and "B2" refer to the respective channel of laser (L) and background (B) data from the energy monitor. Average values of the energy monitor, the gas cell monitor, and the gas cell reference photodiode signals are displayed using the same recursive filter as for the transmission graph. The range limits indicate the range elements over which the on-line and off-line signals are averaged for the purpose of plotting atmospheric (rather than gas cell) transmission. These limits, nominally 1 to 50 range bins, can be adjusted using the cursor control arrow keys on the terminal console. Also computed are the gas cell output to input ratio for each laser, and the final transmission values in percent. The information on the display may be recorded onto hardcopy by the terminal printer at any time by pressing the code letter "P" on the console.

HORIZONTAL PATH

The ground-based lidar system is also used in a horizontal measurement configuration, which facilitates laser alignment and divergence measurements. This allows horizontal path absorption measurements to be made using the large signal scattered from a hard target. The horizontal hardware consists of two major parts. One part is a flat 30 cm square mirror mounted on a small tower, which can be placed over the roof hatch to direct the transmitted laser beam horizontally. It also directs backscattered laser light into the telescope. The other part is a 13 m tower with a 1.5 m square target covered with retro-reflective encapsulated glass bead sheeting. The target tower is located 850 m from the laboratory, and the laser beam traverses a level horizontal path about 7.5 m above the highest ground along the path. A television camera with a small l-m focal length telescope is used to boresight the target and facilitates alignment of both laser beams and the receiver telescope. Preliminary alignment of the two laser beams through the system is made by steering He-Ne laser beams, prealigned with each pulsed laser, through two iris apertures centered on the system optical axis. The combined beams are then aligned to the telescope optical axis using a large corner cube temporarily placed on top of the receiver telescope. An aluminum disk, with cross hairs scribed on its surface and painted white, is placed in the telescope focal plane. The corner cube is used to direct the laser beams into the telescope parallel to the direction of transmission. Beam steering mirrors following the beam expander in Figure 4-4 are then used to steer the combined laser beams onto the telescope optical axis. This is done by centering the beam on the cross hairs scribed on the target disk placed at the telescope focus. This apparatus facilitates alignment of the laser beams to within 0.25 mrad of the telescope optical axis. Even finer alignment is achieved using the horizontal targeting system by observing the pulsed laser beam spots on the outdoor horizontal target with the system boresight camera. This procedure allows alignment of the beams to within 50 to 100 μrad of each other and the telescope optical axis.

PERSONAL COMPUTER BASED DATA ACQUISITION

In 1992 and 1993, our system was reconfigured with a new computer rewritable optical disk storage as illustrated in Figure 4-13. The new configuration merges the lidar and wavemeter data streams, incorporates more real-time analysis, and provides a 2- to 6-hr continuous recording capability (depending on the number of receiver channels in operation). For ground-based measurements, the altimeter PMT is replaced with a high sensitivity (20% quantum efficiency) GaAs PMT for extending the dynamic range of the signal acquisition using photon counting. An 80486 personal computer controls system functions, monitors the operator inputs, displays real-time system status and data, and records the raw data on a 1 Gbyte magnetic disk drive. A removable rewritable optical disk drive is used to archive the data. A second 80486 computer, collecting the wavemeter data, is interfaced to the lidar data computer via a fiber optic serial communications link. The spectrum of each laser pulse is transferred to the lidar computer and attached to the lidar return signal data for that shot. In addition, the system repetition rate is set by a 10 Hz oscillator in the on-line laser frequency stabilization system, which triggers a multi-channel delay generator to trigger the off-line laser, wavemeter, and data acquisition system computers.

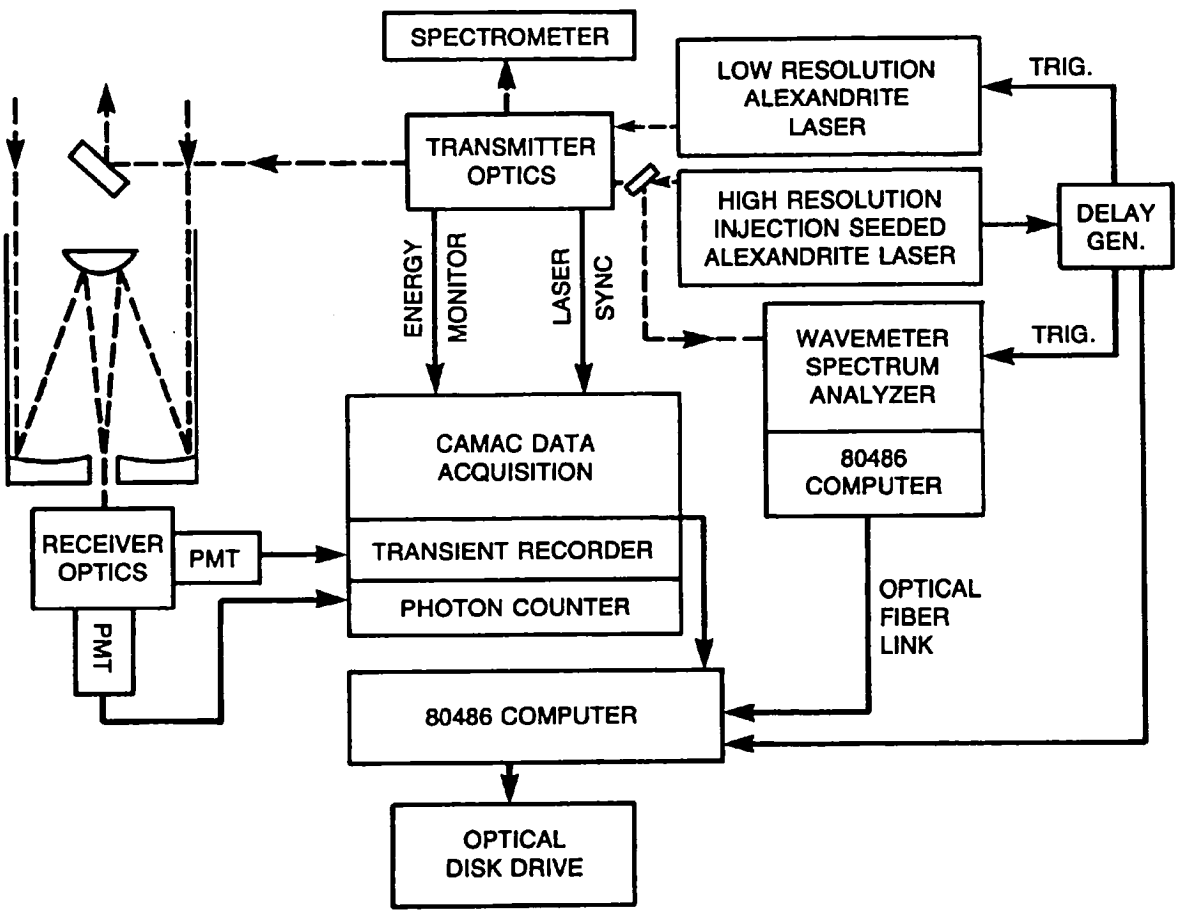

Figure 4-13. Updated data system using 80486 computers to control the lidar and wavemeter data acquisition. The wavemeter data are transferred via optical fiber to the lidar data acquisition computer on every laser pulse.

CHAPTER 5 ALEXANDRITE LASER DEVELOPMENT

The initial experiments using CW krypton laser pumped dye lasers were carried out while we considered the design of a pulsed dye laser to carry out lidar measurement that would yield vertical profiling. During that period, a company in France began marketing a pulsed dye laser that met our spectral linewidth criterion. They modified one of their Nd:YAG pumped lasers to work with a ruby laser pump so that we could reach the oxygen *A* band with reasonable conversion efficiency. By the time CW experiments were completed, another company had also developed a narrowband pulsed dye laser. We purchased one and then had the two lasers necessary to take lidar measurements. We had great difficulty in keeping either one of the dye lasers in working order. The fluorescent dye solution had to be changed every day, and over the course of a few hours, its absorption coefficient changed sufficiently to require realignment of the laser optics. The output would shift from about 90% narrowband output to about 50% narrowband, 50% amplified spontaneous emission (ASE) as a result of the deteriorating dye and subsequent misalignment.

With our dye lasers experience and the announcement of the discovery of tunable laser radiation in alexandrite, we contracted for a narrowband alexandrite laser. A flashlamp pumped solid state laser has obvious advantages over a liquid dye laser, especially as far as increased lifetime and decreased maintenance, both of which are important for eventual spaceborne use. The overall efficiency is also better, and the size and complexity are reduced. The following year we ordered a second alexandrite laser with increased pulse energy and electronic tuning controls.

ETALON NARROWED LASER

What follows is a brief history of each of the Pressure-Temperature Lidar alexandrite lasers, referred to as Alex I and Alex II. Alex I (Figure 5-1) was delivered to Goddard in March 1981. It contains a 5 mm diameter by 75 mm long crystal in a close coupled, diffuse ceramic flooded pump chamber with twin flashlamps fired by separate pulse forming networks (PFN's). The coolant is a solution of sodium nitrite and sodium hydroxide in deionized water. The chemicals serve to absorb ultraviolet radiation, and must be replaced annually. (Its absorption cutoff gradually shifts toward the visible.) The power supply and Pockel's cell controller were from a JK Nd:YAG laser. The laser was specified as 100 mJ and10 Hz, and passed all acceptance tests but one. After-pulsing occurred about 1 msec after the Q- switched pulse. The electro-optic Q-switch was replaced with an acousto-optic Q-switch that had the ability to respoil the cavity immediately following the main output pulse. The tuning optics (Figure 5-2) consist of a three-plate birefringent filter (BRF) (thickness ratio 1-4-16), a 0.5 mm, 20% *R* solid etalon, and a 4.3 mm, 20% *R* solid etalon. The 60% *R* flat output coupler and 5 m center of curvature high reflector are spaced about 50 cm apart. For off-line operation, only the BRF is used in the cavity, which gives a special linewidth of 1.5 cm^{-1} or, with the addition of the 1 mm etalon, a linewdith of 0.08 cm^{-1}. With all three tuning elements installed, the spectral linewidth is about 0.026 cm^{-1}. All optics are mounted on three parallel invar rods. The tuning elements are manually controlled except for the thick etalon, which is temperature tuned. This arrangement proved to be impractical for scanning through absorption lines to locate line centers and troughs. However, we were sufficiently pleased with the performance to order a second laser to replace the remaining ruby pumped dye laser, which was difficult to maintain and operate.

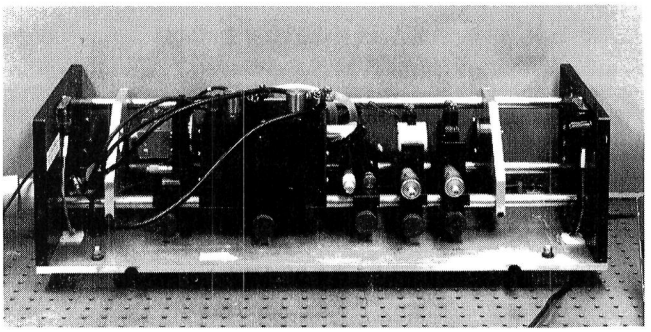

Figure 5-1. Photograph of Alex I laser head with the cover removed to show the layout of optical components. From left to right: end mirror (located on end plate), acousto-optic Q-switch, pump chamber, 3-plate birefringent filter, oven stabilized and tilt tuned thick solid etalon, tilt tuned thin solid etalon, and output coupler. The thick etalon could also be temperature tuned, but the thermal response was too slow to make this practical. The original Q-switch was an electro-optic Pockels cell which was replaced by the acousto-optic cell so that the cavity could be spoiled shortly after the output pulse in order to prevent "after-pulsing."

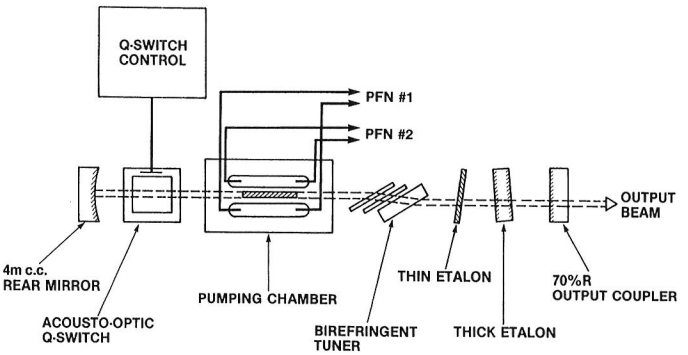

Figure 5-2. Alexandrite laser optical resonator cavity configuration. The cavity has an optical path length of about 55 cm. (Figure, courtesy R. Sam, Allied Corporation.)

With the experience gained from using Alex I for several months, we wanted the second laser to have ganged tuning optics, which, once aligned, could be continuously tuned over a reasonable frequency range that would encompass two or more oxygen lines. Alex II (Figure 5-3) was delivered in July 1983, a year late. For the most part, the problems with this laser, particularly the PFN's and the tuning electronics, could be attributed to poor engineering and workmanship. We experienced many difficulties with this laser until all of the electronics (except the capacitor charging supplies, which were standard commercial units), the fluid handling systems, and certain mechanical components in the tuning optics were redesigned and rebuilt. This was all accomplished by a very capable Experimental Instrumentation Branch in GSFC. Identical power supply and cooling modules were made also for Alex I, and the new modules installed in both lasers in July - August 1987.

The laser head was built in an invar box (Figure 5-2) containing three compartments to aid in thermal control of the tuning optics. The flooded pump chamber consists of a stainless block with slide-in double ellipse reflectors. The reflectors are stainless with electro-plated silver coatings. The 5 mm diameter by 100 mm alexandrite crystal is surrounded by a pyrex flow tube to absorb ultraviolet radiation and to separate the hot water, which heats the rod to 80°C, from the flashlamp water, which floods the pump chamber. The laser output pulse energy rating is 150 mJ and 10 Hz. The Q-switch is acousto-optic, and the flashlamps are fired by independent PFN's. We gained a fair amount of experience with the PFN and simmer circuits, having designed them after trying numerous commercial units and designs. The flat, 70% R output coupler is separated from the 5 m center of curvature high reflector by about 55 cm. The five-plate BRF, thin etalon (0.73 mm, 20% R) and thick etalon (1.0 cm air gap, 20% R) are all contained in one temperature controlled chamber in the head. The five-plate BRF is controlled with a DC torque motor and uses an optical encoder

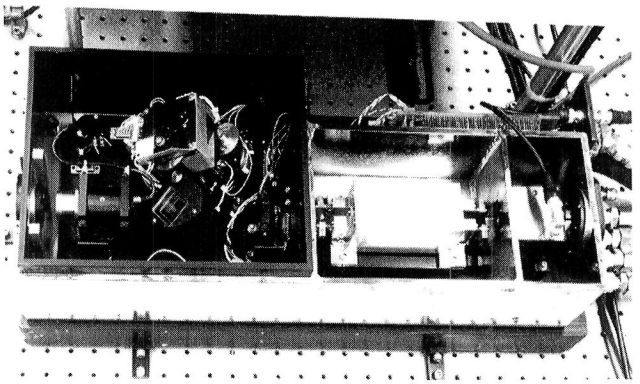

Figure 5-3. Photograph of Alex II laser head with the inner and outer covers removed. The head is divided into three chambers. From left to right: the PZT tuned thick (air-gap) etalon, 5-plate birefringent tuner with optical encoder, and tilt tuned thin solid etalon are all contained in a temperature stabilized chamber, pump chamber, and acousto-optic Q-switch. The open design of the optical encoder on the BRF subjected it to erroneous signals from laser light scattered inside the head which caused it to jump around and impart frequency jitter to the laser output.

for position feedback. The thin etalon is 0.74 mm thick and is tilt tuned, also using a DC motor. The high-resolution etalon is a piezoelectrically scanned, 1 cm air space Fabry-Perot etalon. The laser spectral linewidth with all three elements installed is about 0.018 cm^{-1}. The continuous tuning range without etalon order jumping is 3.0 cm^{-1}. For a larger change in frequency, the thin etalon and BRF must be set to a different order number of the thick etalon before another 3.0 cm^{-1} scan is possible. In this manner, piecewise continuous tuning over the entire fluorescence band of the laser (725-780 nm) is possible without any gaps.

Because Alex II has the electronically driven and servo tuning optics, it has been used exclusively as the on-line laser. However, due to problems with the thick etalon, we were often not able to run the laser in a high resolution mode. The mechanical alignment stability of this etalon is very poor if it undergoes any kind of temperature cycling. The dielectric reflective coatings on the optic plates are easily damaged. We have used a variety of vendors for coating these plates, with mixed results.

Laser Spectral Requirements

Atmospheric pressure is obtained by measuring the absorption of the on-line laser in a broad trough region between strong absorption lines in the 760 nm band, whereas atmospheric temperature is obtained by measuring the absorption of the on-line laser centered on a narrow absorption line. Thus, for temperature measurements, the laser bandwidth and frequency jitter must be sufficiently small to prevent large errors caused by some or all of the laser radiation occurring far enough from the line center to produce lower than predicted absorption. The width (FWHM) of these lines at sea level atmospheric pressure is ~0.1 cm^{-1}. With increasing altitude (decreasing pressure), the linewidth decreases until it approaches the Doppler limit of 0.03 cm^{-1} FWHM at zero pressure. Thus, for ground-based and low altitude measurements, the laser bandwidth should be small

with respect to the linewidth, *e.g.*, ~0.02 cm^{-1}, and the frequency stability must be approximately 10 times smaller than the FWHM, *e.g.*, ~0.003 to 0.005 cm^{-1}. For higher altitude measurements, the requirements are even more stringent. In addition, measurements with strong absorption are extremely sensitive to any laser radiation outside the nominal laser bandwidth (*e.g.*, due to amplified spontaneous emission), since this radiation would not be absorbed by the oxygen line. For example, if 1% of the laser energy is broadband, the actual backscattered signal would be twice the expected backscatter signal (100% error) for a measurement altitude for which 99% of the narrowband energy has been absorbed by the oxygen absorption feature. Because of the potentially large errors caused by the spectral properties of the lasers (Cahen and Megie, 1981; Megie, 1980), we performed a series of measurements to characterize their spectral structure. We made precise measurements of the spectral purity, linewidth, line shape, and shot-to-shot frequency jitter of the lasers, using a high-resolution Fizeau interferometer and a long path multipass absorption gas cell (Schwemmer, *et al.*, 1987). Measurements of laser linewidth and frequency stability after 1987 were made with the wavemeter described in Chapter 7 of this report.

The Alex I laser has a three-mode output with a 0.027 cm^{-1} spacing between the two outermost modes; however, the modes are not equally spaced. This is probably due to higher-order transverse modes associated with one or more of the longitudinal modes. We found a number of problems inherent in making good quantitative measurements. The most serious problem is spatial inhomogeneities in the laser beam, due to the multiple transverse modes of the alexandrite laser. This causes a misrepresentation of the relative energy in each laser mode as seen by the detector, and, in some cases, could even cause a mode to be absent in one of the interferometer orders. It is also suspected that various parts of the beam cross section will have a diverse mix of frequencies if a different set of transverse modes is associated with each longitudinal mode. A way is needed to uniformly scramble the transverse laser modes and to present a uniform intensity distribution to the interferometer. Modifying the laser to produce a single transverse or longitudinal mode output reduces the laser efficiency prohibitively. Spatially filtering the input to the interferometer using a pinhole would undoubtedly alter the spectrum of the light being sampled. Chapter 7 describes a successfully implemented solution to this problem.

We measured the spectral purity of the on-line laser by using a very strong but narrow oxygen-absorption feature as an extremely narrowband notch filter. This was done in our laboratory using a multipass confocal cavity gas cell constructed by the University of Maryland and specifically designed for use with lasers. The cell has a 1 m base path length. The beam enters through a small hole in one mirror and exits through a slit which bisects the second mirror. The number of passes is determined by the angle of incidence of the input beam and an angular adjustment of the bisected mirror. We were able to achieve up to 149 passes in the cell. This 149 m path length was verified by a light pulse propagation time measurement. The transmission of the radiation through the cell was measured using two photodiodes, one monitoring the input beam by way of a beam splitter, and the other monitoring the cell output. We made measurements on the strong oxygen absorption line at 13142.57 cm^{-1} at oxygen partial pressures from 305 to 620 torr. We scanned the laser through the oxygen line, then centered the laser frequency on the line, and increased the amplifier gain on the oscilloscope with which we measured signals from the two photodiodes. At the higher oxygen pressures, the absorption line strongly attenuates the narrowband radiation while allowing any broadband component to be transmitted relatively unattenuated. There may be some broadband radiation from the laser that is not well collimated. However, this uncollimated radiation is of little consequence in the lidar application where the field of view of the receiver is narrow. We have found that a large portion of the ASE from multi-amplifier dye lasers can be highly collimated. Dye lasers have also exhibited broad band spectral pedestals when careful design is used to suppress ASE (Ehret, *et al.*, 1993; Theopold and Bosenberg, 1993).

In Table 5-1, a comparison of measured values of gas cell transmission with calculated values is given for various pressures of oxygen with the cell adjusted for a 149 m path length. At the highest pressure, the measured transmission implies a maximum possible value for the total broadband energy which may be transmitted through the gas cell. The calculated transmission at that pressure is less than 0.01% over a bandwidth of 0.027 cm^{-1} about line center. From this we conclude that the total laser emission outside of the three longitudinal modes observed with the spectrum analyzer is less than 0.01% of the total laser output energy. At low pressures, shot-to-shot instabilities of the mean frequency of the laser contribute to values of transmission which are larger than the calculated values, because the absorption linewidth of 0.034 cm^{-1} (FWHM) is comparable to the laser linewidth.

Table 5-1. Measurements of Alex II spectral impurity inferred from measured transmission through a 149 m path in a multipass gas cell at a frequency of 13142.57 cm^{-1}, compared with calculated values.

Pressure (torr)		Transmission (%)	
O_2	N_2	Measured	Calculated
305	120	0.1	0.042
340	120	0.05	0.030
380	120	0.033	0.022
500	120	0.013	0.010
620	120	0.007	0.0063

Laser frequency stability was accurately measured by positioning the laser frequency on the steep side of a Doppler broadened oxygen line and measuring gas cell transmission as described above. Any frequency modulation on the side of an absorption line will result in a modulation of the transmission. The frequency stability was determined to have a short-term noise or random component with a standard deviation of 0.005 cm^{-1}. Frequency drifts of much larger magnitudes were observed over periods of many minutes due to drift in the high-resolution intracavity etalon. This etalon is not stabilized for temperature, mechanical drift, piezoelectric creep, or drift in the piezo drive signal, which is used to tune the laser. Much of the short-term jitter is due to noise observed on the drive voltage. We redesigned the laser electronics to correct this problem and to reduce the long-term drift so that longer measurement periods could be utilized to accurately observe changes in the atmospheric temperature or pressure profile. The following section describes the redesigned electronic tuning and scanning electronics.

ELECTRONIC TUNING AND SCANNING

A digitally controlled tuning and scanning control servo system simultaneously positions all three optical elements to provide continuous high resolution laser spectral tuning. The user may select manual, single, or continuous modes of automated scanning of ranges up to 3.00 cm^{-1} and at scan rates up to 3.85 cm^{-1}/min. Scanning over an extended range of up to 9.999 cm^{-1} may be achieved if the thick etalon is removed from the system. The control system is also capable of being remotely operated by another computer or controller via a standard RS-232 serial data link. We have also incorporated many features that provide improved system noise immunity, sensitivity, and operational flexibility.

Background

The alexandrite laser output is spectrally narrowed and tuned by the use of three optical elements located within a temperature controlled tuning chamber (Figure 5-4) stabilized at 35.0 ±0.1°C. The three elements

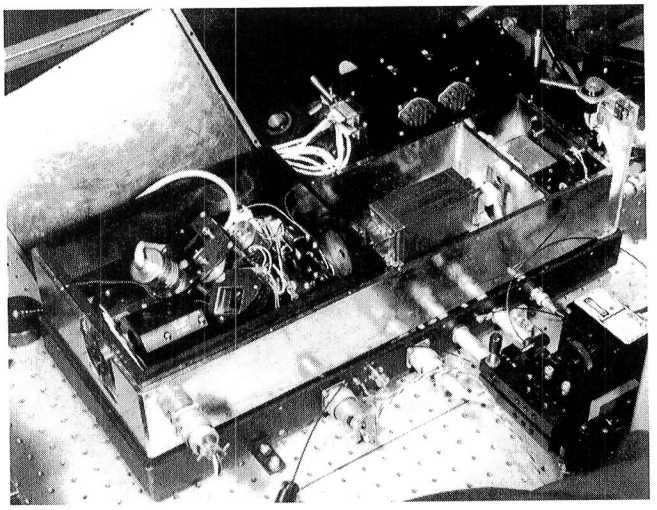

Figure 5-4. Photograph of the Alex II head after reengineering the lasers. The optical encoder has been replaced with a sealed unit, better temperature control has been instituted by increasing the heater wattage, and the PZT etalon has been encased in its own oven with a large thermal mass kept a few degrees above the rest of the tuning chamber. Critical tuning electronics have been shielded in the black box behind the pump chamber. In the foreground is a diode laser head which was later used to injection seed the alexandrite laser, eliminating the need for the two etalons.

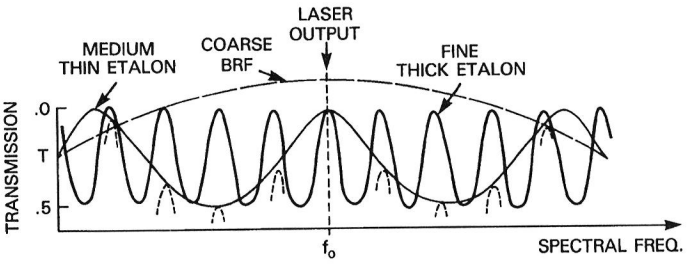

Figure 5-5. Spectral transmission curves of the three optical tuning elements. Laser action occurs where peaks of all three elements coincide to give maximum transmission, and hence, lowest intracavity losses.

are a BRF, a thin etalon, and a thick etalon. Each successive element provides a higher degree of spectral resolution. The BRF is used as a broad bandpass filter to narrow spectrally the laser to 1.5 cm^{-1} (90 pm). This filter can be tuned from 725 to 785 nm by rotating it about an axis normal to the plane of the filter plates (which is at Brewster's angle with respect to the laser optical axis). The medium resolution element is a solid quartz etalon of 0.7 mm thickness with 20% reflective dielectric coatings. This etalon acts as a "comb" filter having many transmission peaks within the gain curve of the laser. The laser output is confined to a single transmission peak of the thin etalon by centering the BRF passband over that peak (Figure 5-5). This reduces the laser bandwidth to about 0.08 cm^{-1} (5 pm). The etalon is tuned by tilting it with respect to the optical axis ("tilt tuned"), thus shifting the entire family of transmission peaks toward the shorter wavelengths as the tilt angle increases. While tuning the etalon, the BRF must occasionally be tuned to keep its bandpass peak centered over that peak. The final tuning element is a 1 cm air gap etalon that is tuned with piezoelectric transducers (PZT) that change the plate spacing of the etalon as a function of applied voltage. The thick etalon transmission peaks are about ten times closer together than those of the thin etalon, and it narrows the laser output to about 0.02 cm^{-1} (1.2 pm). Narrowband operation is obtained by superimposing a transmission peak of the thick etalon with one from the thin etalon. Laser tuning is accomplished by tracking the desired transmission peaks of the etalons and the BRF.

System Concept

The overall system design incorporates a user interactive scheme providing digitally adjusted inputs (digital pots) and computer driven analog control servos. Each individual optical element is driven with its own closed-loop servo positioning system. These servo loops require only the new desired position information as input. These input data are provided in a 12-bit word format which is then compared to the 12-bit digital representation of the actual position. Appropriate analog and digital feedback are then generated to effect a new optical element position. The servo will continue to provide corrective feedback and drive the element's position until a zero error state exists, *i.e.*, the actual servo position data match the input position information. The combination of digital input position data and self-contained servo control relieves the main computer from being burdened with the responsibilities of providing the necessary closed-loop control functions. The simultaneous positioning of all three optical elements, in addition to keeping track of user inputs, would be very cumbersome and software intensive, possibly requiring multi-tasked dedicated controllers. A simple one-chip microcomputer control or "director" approach is preferred. This streamlined technique works very reliably and efficiently by reducing the difficulties often associated with multi-tasking programming, integration, and implementation. The system architecture offers the best of analog and digital features by simplifying the control program software and providing system function modules capable of being designed, developed, tested, debugged, and repaired individually with minimal impact on operation schedule and resources.

System Operation

The tuning control system is divided into three modules: front panel tuning control (Figures 5-6 and 5-7), composite PZT drive and scan control (Figure 5-8), and BRF and thin etalon drive controls (Figure 5-9).

The front panel tuning control block diagram consists of the following six control functions: tuning control board, main computer control board, scanning control board, tuning position display board, PZT and motor drive board, and auxillary computer interface board.

The tuning control board allows the user to adjust each optical filter position individually and to set the system scanning parameters (scan rate and scan width). These five adjustments utilize the outputs of digital incremental encoders (256 pulses/rev. two-phase quadrature). Each knob (digital pot) has its own hardware digital storage register which keeps track of the current digital output count as the knob is adjusted (Smith, 1988a). This digital information corresponds to the appropriate value for each individual parameter. The total digital adjustment range is 0 to 4095 counts (12 bits), which are made to correspond to the adjustment range of each optical element. Hardware logic provisions have been provided to prevent overflow and underflow conditions from occurring while adjusting these registers. Once the maximum count has been reached (by turning the knob clockwise), the storage register is inhibited from rolling over to an all zeroes state (overflow). Conversely, when the minimum count of zero is reached (by turning the knob counter-clockwise), the storage register is again inhibited from rolling over to the all ones state (underflow). Exit from either of these two inhibited states occurs by simply turning the adjusting knob in the opposite direction. The data in each of these five digital storage registers (coarse, medium, fine, scan rate, and scan width) are multiplexed onto a common 4-bit data bus and accessed by the main computer control board via standard 4-bit I/O expander bus interface circuitry.

The main computer control board consists of an Intel 38749 series microcomputer operating at 11 MHz, a Mostek MK48Z02B non-volatile random access memory (RAM), an Intel 8231 arithmetic logic unit (ALU) running with a 4 MHz oscillator, interrupt service registers, and a standard Intel 4-bit 8243 I/O expander bus

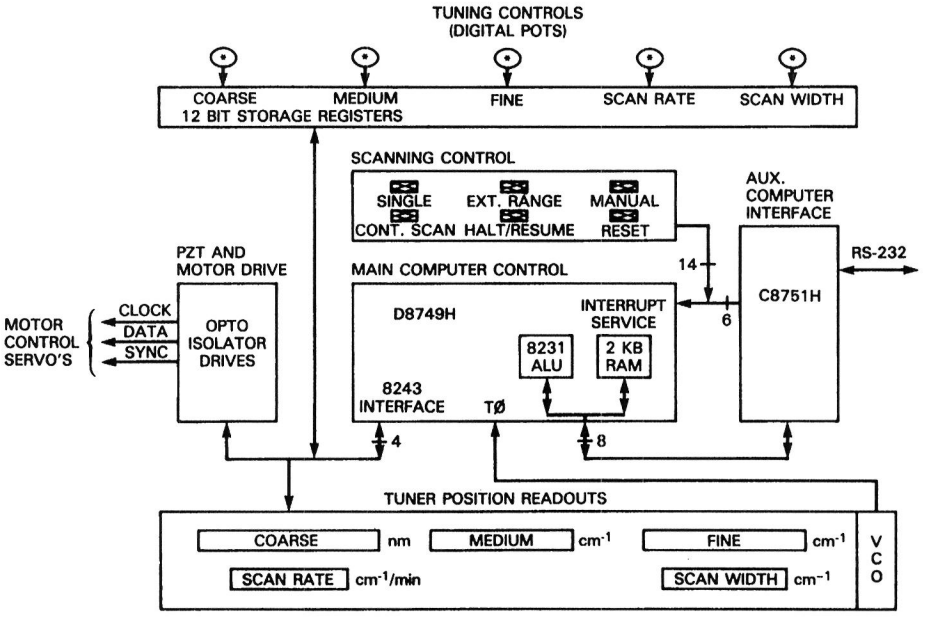

Figure 5-6. Front panel tuning control block diagram, where each block represents a circuit board. Not shown are the PZT and motor drive circuitry, which are located at the laser head (Figures 5-7 and 5-8).

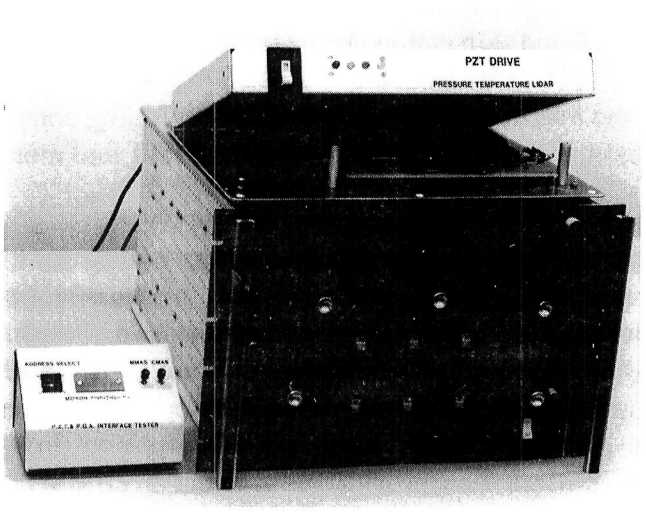

Figure 5-7. Photograph of the tuning control panel. All controls are read by the microprocessor; hence, their functions are programmable. The PZT drive electronics, which are the most sensitive to noise, reside in the shielded enclosure on top of the control panel. This unit drives a high voltage DC amplifier circuit (not shown).

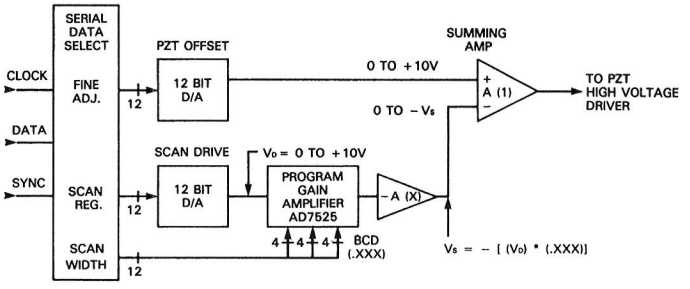

Figure 5-8. PZT drive circuitry. A positive offset and a scan drive (V_s) are summed to provide position drive data.

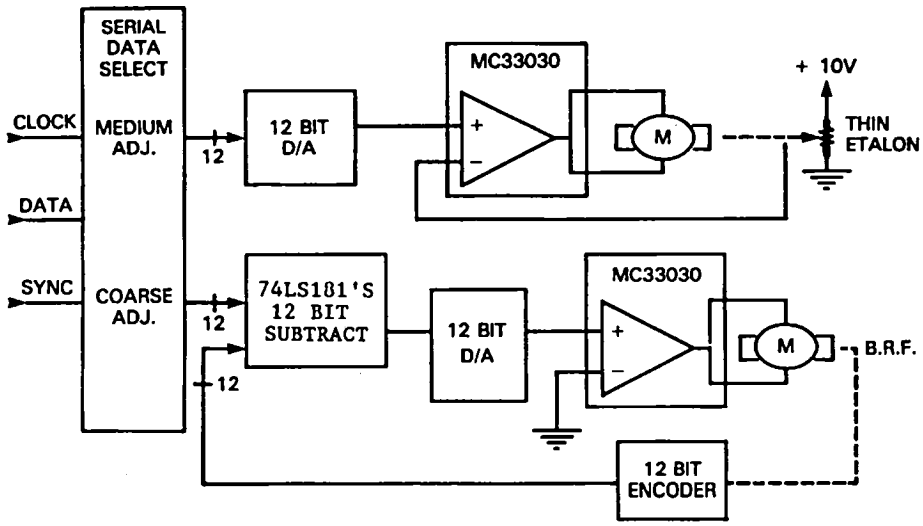

Figure 5-9. Birefringent filter and thin etalon motor servo-control block diagram.

interface system for data communication between all the system peripherals. This 4-bit bus is the main interface that handles all the data associated with the user inputs (digital pots), motor controls, scan parameters, and LED display information. The microcomputer's internal 8-bit data-bus is used exclusively for data transfers involving the ALU, RAM, and auxillary computer control. The main computer control acts as the central hub and director for all the data. The data from the tuning control board are collected, properly scaled using the ALU, and then sent to the motor drive and LED display boards. The ALU converts and scales the digital information into a convenient "user-friendly" LED display formatted and labeled with the physical units of nanometers (nm) and wavenumbers (cm^{-1}).

The tuning position display board receives the multiplexed data from the computer control board and sequences the data to the proper LED readout display. The BRF adjustment is scaled for a display format range of 685.35 to 850.00 nm. The BRF employs a 12-bit positional optical encoder (Figure 5-9) with the output being a linear function of the wavelength displayed. The thin etalon input data register is also scaled linearly for a 0.000 to 9.999 cm^{-1} display. The positional feedback element used here is a precision linear slide potentiometer whose range of movement corresponds to a 10 deg filter tilt that results in a 0 to +10 volt position feedback signal. There is a square root functional relationship between the digital input register contents and the desired motor drive data of the form:

$$\text{MOTOR DRIVE DATA} = (\text{INPUT DATA REGISTER})^{1/2} + \text{CONSTANT.}$$

This is due to the sine-drive nature of the positioning mechanism. The fine tuning element (thick etalon) is formatted for a display of 0 to 3.0000 cm^{-1} and responds linearly to a 0 to +10 volt drive signal. The signal is derived from a digital to analogue (D/A) output with its input data provided by the value of the fine tuning digital input register. There is no positional feedback data available due to the nature of the transducer system. To provide for stable etalon operation, it is enclosed within a thermally regulated (±0.1°C) aluminum mounting block kept at 40°C (Figure 5-4). The scan rate range encompasses 0 to 3.85 cm^{-1}/min and is linearly scaled with its digital input storage register. The scan rate register provides the inputs for a D/A driven, voltage controlled oscillator (VCO). The output of this VCO establishes the system timing for the automated scanning modes. The scan width display is also linearly scaled with the input data register and has a display range of 0 to 3.00 cm^{-1}.

The PZT and motor drive board act as the conduit for transmitting and updating the PZT drive, motor position, scanning register, and programmable gain amplifier (PGA) information. Due to the remote location (approximately 10 m) of the PZT and motor positioning circuitry, the outputs are configured to drive opto-isolators. The data transmission scheme utilizes a serial three-wire distribution arrangement (Smith, 1988b). The 12-bit data are transmitted in a 16-bit serial format to all potential receivers (5 total: Figures 5-8 and 5-9) with the first four data bits being the destination address code and the remaining 12 bits the data.

The auxillary computer control board utilizes an Intel 8751 series microcomputer that may be programmed to communicate with an external computer via a standard RS-232 data link. The data received are then transferred to the main computer over the internal 8-bit data bus. The data and commands sent dictate the action taken by the main controller. The realm of possible external command requests is limited to those that can be done manually on-site at the control panel itself. This feature allows the control system to be operated remotely and perhaps to be totally automated.

The scanning control board provides a pushbutton user interface to select the system operating mode. There are three fundamental operating modes: uncoupled adjustment, manual scan, and automated scanning. The selected mode is passed to the main computer control via the interrupt service registers, which identify the button being pressed. The pushbutton which is pressed is identified to the user by illumination of the LED within the button. Resetting the system interrupt flags and LED pushbutton displays is also accomplished through the interrupt service registers.

Operational Modes

The uncoupled adjusting mode is entered at power up, so that the transmission peaks of the optical elements can be checked for alignment. While in this mode, each optical element may be adjusted independently from other elements. The scan rate and scan width may also be adjusted. However, software restrictions and correcting routines are applied to ensure that a sum total PZT offset and scan width value remain within the 3.00 cm^{-1} range of the thick etalon.

During the manual scan mode, the movements of all three optical elements are coupled, causing the transmission peaks to track each other and allowing "mode-hop free" laser tuning to occur. When the manual scan mode is selected, the fine tuning adjust knob provides the "manual adjust" input for this scan mode. The value in the fine tuning register provides the initial value of the PZT offset voltage. This register is then zeroed and becomes the input digital storage register for the manual scan adjustment. Thus, the scan width resolution becomes one part in 12 bits, providing for the maxium tuning precision for all scan widths. The scan register is the "counter" for these incremental steps and is indexed once each cycle of the digital pot output of the fine tune adjust knob. Since all scans are divided equally into 4095 increments, the full scale output of the scan register D/A must be scaled (Figure 5-8). The PGA attenuates this full scale D/A output (V_d) to provide the proper voltage range (V_s) for the selected scan width. The signal voltage V_s is then summed with the initial PZT offset position voltage to provide the composite PZT scan drive signal. The 0 to +10 volt output of this summing amplifier drives the input of a high-voltage 100x amplifier to drive the PZT. The range of adjustment while in the manual mode is determined by the scan width value selected prior to entering the manual scan mode. The scan width adjustment is inhibited while in the manual scan mode. This is necessary because the PGA and scan register weighting factors must be held constant to maintain correct tracking of all three optical elements. The automated scanning mode operation is functionally the same as the manual scan mode with the exception that the scan register is incremented automatically as opposed to being manually adjusted. Both the single and continuous automated scanning modes utilize the

"TO" input pin on the main computer control board, which is tested by the scanning control software. The scan register is zeroed at the commencement of automated scan modes. The scan register is then incremented once for every input cycle of the TO input pin. The VCO output is applied to this pin and establishes the scan rate. The VCO output is linearly scaled to provide a maximum frequency output (~90 Hz) over the digital input range of 0 to 4095 counts. The single iteration loop timing during the automated scanning modes requires a minimum of 11 msec to complete. This translates to a maximum 4.00 cm^{-1}/min scan rate. The maximum allowable system scan rate has been set at 3.85 cm^{-1}/min to allow for an adequate safety margin. If a continuous scan mode is selected, the scan register will be zeroed after the maximum count (4095) is reached, and the process will start over again. It should be noted that the actual repetition of the scan process commences only when all the optical elements return to their initial positions. That is, during continuous scanning operation, the program software monitors the motor drive of each element and waits for each drive to "back-track" to the start of scan position before initiating another scan process. If a single scan mode was requested, the scan register will be allowed to reach its maximum count only once. It will then be re-zeroed and the initial settings recalled from non-volatile RAM storage and loaded back into the position registers. The system then returns to the uncoupled power-up condition.

The extended range mode is essentially a manual scan mode that couples only the thin etalon and the BRF movements, allowing the laser spectral output to track over the entire range of the thin etalon. The scan register scheme mentioned above is in no way utilized here. Scanning is accomplished by manually adjusting the thin etalon control knob (medium tuning). The limits of this scan mode become the adjustment limits of the thin etalon. It is assumed that the PZT etalon has been removed from the system prior to entering the extended range mode.

Software

The system program control software (Figure 5-10) is written in assembly language and resides totally within the microcomputer's 2 kilobyte EPROM. Most of the computer's 128 bytes of RAM are used to store the 32-bit floating point conversion factors that are used with the ALU in scaling the LED display formats and motor drive data. There are an additional 2 kilobytes of non-volatile RAM storage that are used to store the system's digital storage register contents continually. These data are recalled at power up, and the system is initialized with this information to provide the same system parameters and filter positions that existed at power down.

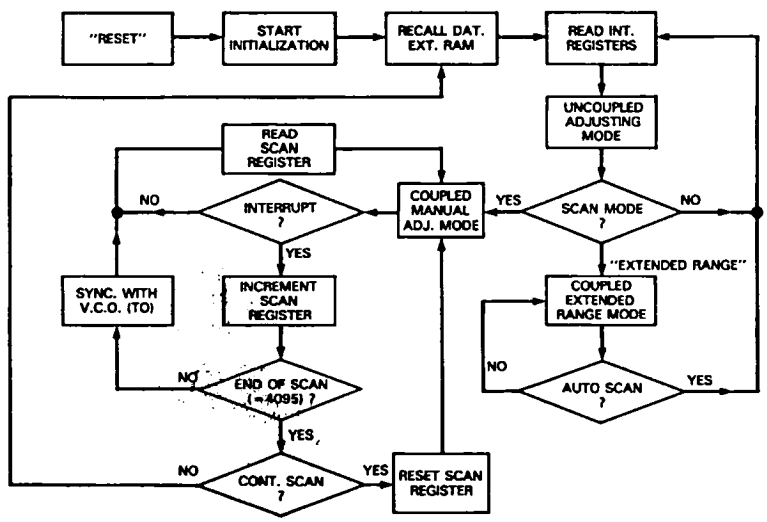

Figure 5-10. Flow chart of laser tuning control program.

THERMAL STABILIZATION

To obtain accurate temperature measurements, a line center frequency stability and accuracy of ± 0.002 cm^{-1} are required over an extended period of time, typically ~30 min, which corresponds to a set of measurements. In addition, the spectral bandwidth of the on-line laser should be less than 0.02 cm^{-1}. A series of measurements of the on-line alexandrite laser frequency was performed using the wavemeter, incorporating the technique we developed to reduce the effect of speckle (see Chapter 7). These measurements showed the presence of both short- and long-term variations. The short-term instability was found to be a shot to shot frequency jitter, whereas the long-term variation was a drift. To examine this, the temperature of each of the optical elements of the laser was monitored using thermocouples and a data logger. It was found that the temperature of the tuning elements housed in the optical enclosure tended to increase by as much as 1 to 2°C/hr during continuous operation of the laser, which contributed to the long-term frequency drift. The optics enclosure of the high resolution on-line alexandrite laser is of invar construction and is insulated on the inside to reduce transfer of heat from the pump chamber. Electric heaters controlled by a temperature regulator should maintain a constant elevated temperature in the optics enclosure. Since our investigations showed that the temperature regulation was not adequate, the thermal behavior of the enclosure was analyzed and modified.

To improve the thermal stability of the optics enclosure, various modifications were made (Figure 5-4). The thermal mass of the enclosure was increased significantly by the addition of copper blocks, the insulation was improved, and convection of hot air from the laser head was prevented. Cooling jackets (not shown) were attached to the pump chamber housing to reduce heat transfer to the optics enclosure, and a more effective temperature regulator was used. Also, the nitrogen purge gas (needed to displace the oxygen from the optical path in the laser) was preheated to the temperature of the optical enclosure and admitted into the enclosure. The preheated gas then flows across the optical elements and exits from the optics enclosure to the pump chamber and the rest of the laser head. Significant temperature gradients can exist between the etalons and the enclosure, since the optical mounts and the etalons have a high thermal resistance. The purge gas flow reduces these gradients and also effectively limits the convective flow of gases from the pump chamber into the enclosure, which can cause significant perturbations. These modifications were incorporated into the laser before the aircraft flights of the Pressure - Temperature Lidar in May - June 1989 for measurements of the atmospheric pressure field. For these flights, the etalon temperature was maintained constant to within ± 0.1°C over entire flights (~2 hr). The frequency stability required for pressure measurements is less severe than for temperature, since the laser frequency is tuned to the trough between two absorption lines, where the absorption does not vary rapidly (see Chapter 1). For the pressure measurements, only the birefringent filter and thin etalon were used, which yield a frequency bandwidth of 0.08 cm^{-1}. The passive stability of the laser with the above modifications was found to be adequate for the pressure measurements.

OPTICAL DAMAGE CONTROL

The following is an analysis[2] of alexandrite failures based on experience with the two alexandrite lasers, especially the optical components. We have kept extensive logs of these lasers since their delivery, and a summary of the failure rates of the mechanisms for each laser follows.

[2] Memo to the LASE Project Team (February 1, 1990).

Regarding optical damage, we instituted a regimen which was followed closely. First, the laser covers are on at all times unless we have to get into the head. Second, whenever any new optics are installed, we put the laser through an annealing process, running the laser long pulse at a low energy (~20 mJ) for 15 min, then 50 mJ for 15 min, then 100 mJ for 15 min, then Q-switched at 20 mJ for 15 min, and finally 50 mJ for 15 min before running at the rated energy. In addition, each time the laser is started, it is operated for ~1 min with the cavity spoiled, before turning on the Q-switch, to allow the rod to reach a new thermal equilibrium. The same procedure is followed even if the pump energy is to be changed. At the first sign of optical damage, *i.e.*, a sudden drop in energy (10% or more) or an unstable output energy (fluctuations of 10% or more), we shut off the laser and inspect all the optical surfaces, replacing any blemished optics. Because of the frequency of this problem, and the cost and lead time for new optics, we have installed offset optical mounts on some of the optics, so they can be rotated or translated to a fresh portion of the surface without the need to replace that optic each time it is damaged.

The following is a summary of failures for Alex I, which has logged over 16.18×10^6 shots (over 449 hrs) since May 1981, 9.14×10^6 shots over 71 months on the original equipment, and 7.04×10^6 shots over 29 months on the new equipment.

Flashlamps: Average loading of 55 J per lamp. Three explosions, one of which was attributable to a coolant failure. A total of 7.33×10^6 shots was logged on lamp pairs in which one lamp of each pair expired naturally. A calculated mean time between failures (MTBF) of 2.44×10^6 shots is misleading, since the lamps were always replaced in pairs. The lamps were also likely to break during disassembly and reassembly of the pump chamber to change the rod, which happened three times over the 16.18×10^6 shots on this laser.

Alexandrite rods: No bulk damage.

Anti-reflection (AR) coatings: 16 failures, MTBF 1.01×10^6 shots.

Thin etalon coatings: Damaged at least five times; however, an MTBF is hard to calculate since this optic is not always used.

Thick etalon coatings: Burned once, but this optic is not often used.

Q-switch: Burned AR coatings once. Overheated once (a failure in the RF drive caused CW RF to be delivered to the crystal, which is not cooled), leaving the crystal with permanent stress induced birefringence.

Other optics: 3 burned mirrors, MTBF 5.39×10^6 shots.

Total optical damage (counting multiple simultaneous burns as one): MTBF 0.81×10^6 shots.

Power supply and other electronics:

Under the old J-K supply: 3 failures in 9.14×10^6 shots (MTBF 3.05×10^6 shots).

With new system: 1 failure in 7.04×10^6 shots - a pitted lamp electrode and connector were arcing.

Cooling system (including related electronics):

Old system: 8 failures (MTBF 1.14×10^6 shots, or 32 hrs).

New system: 1 failure, a flow switch (MTBF 7.04×10^6 shots, or 196+ hrs).

Total:

Old system: 22 failures (MTBF 0.42×10^6 shots).

New system: 15 failures (MTBF 0.47×10^6 shots).

The following is a summary of failures for Alex II, which has logged over 23.14×10^6 shots (over 643 hrs) since July 1983, 8.48×10^6 shots over 51 months on the original equipment, and 14.66×10^6 shots over 27 months on the new equipment.

Flashlamps: Average loading of 52 J per lamp. One expired naturally (failed to simmer), and one was accidentally broken. Lamps were replaced eight times because of water contaminant deposits or because simmering problems were suspected, which were the old simmer circuits or redesigned and commercial simmers. We finally perfected a design which has not yet failed.

Pump reflectors (needing either polishing or replacement): 15 servicings; however, much of this is due to experimenting with different reflectors, including vacuum silver coatings with SiO overcoats, electroplated copper, CVI second surface silver coated pyrex, MACOR ceramic, and several versions of pressed and sintered Teflon reflectors. Those that have worked best are electroplated silver over stainless substrates, which need repolishing about every 1 to 2 x 10^6 shots, depending on lamp loading level. Solid silver reflectors are no more expensive than any others we have tried. They must be polished, but not replaced as often.

Alexandrite rod AR coatings: MTBF 1.78 x 10^6 shots.

Thin etalon coatings: MTBF 5.78 x 10^6 shots.

Thick etalon coatings: Damaged four times; however, laser not always used with thick etalon.

Q-switch: AR coatings damaged once; gold wire in crystal assembly broke once.

Other optics: MTBF 5.78 x 10^6 shots.

Total optical damage (counting multiple simultaneous burns as one): MTBF 1.16 x 10^6 shots.

Power supply and related electronics:

Old system: MTBF 0.39 x 10^6 shots.

New system: One failure in 14.66 x 10^6 shots.

Tuning electronics and electro-mechanical components:

Old system: MTBF 0.94 x 10^6 shots (reliability not as much of a problem as performance).

New system: MTBF 3.66 x 10^6 shots.

Cooling system (including related electronics):

Old system: MTBF 2.12 x 10^6 shots (59+ hrs).

New system: MTBF 3.66 x 10^6 shots (102+ hrs).

Total:

Old system: 44 failures, MTBF 0.19 x 10^6 shots.

New system: 35 failures, MTBF 0.42 x 10^6 shots.

Note: Multiple simultaneous failures counted as one failure, because they are usually related, especially when burned optics is the failure.

Optical damage is obviously the greatest reliability problem. Damage to the coated surfaces of optical components, such as the laser rod, the mirrors, and the etalons, can occur at high optical fluence levels prevalent in high energy short pulse Q-switched solid-state lasers. In tunable alexandrite lasers such as the ones used in the Pressure-Temperature Lidar, optical damage to the laser rod surface was found to occur frequently, even when the fluence level ($\leq$35%) was much below the specified damage threshold (10 J/cm^2) for the hard anti-reflection coating. A detailed examination of the causes of optical damage revealed that damage tended to be nucleated at residue sites of solvent cleaners. Damage was also found at sites where microscopic leaks of the coolant occurred, leading to build-up of salts or other residues on the anti-reflection coated surfaces of the rod. The rod seals were improved, and a new cleaning procedure for the rod was initiated. As a result of these steps, optical damage to the laser rods has been virtually eliminated, and more than 10^7 shots have been accumulated without rod surface damage. Before the new cleaning procedure was developed, only ~10^6 shots occurred between failures due to laser rod damage.

In the flash lamp pumped tunable alexandrite lasers used in the Pressure-Temperature Lidar, optical damage to the anti-reflection coated laser rod surface was found to occur frequently (0.5 to 1.0 x 10^6 shots). Damage to other intracavity optical components, such as the coated surfaces of the thin etalon, the high (>99%) reflectivity mirror, and the output coupler, also occurred, although less frequently. The normal operating conditions for the laser are: output energy per pulse, 100 mJ; pulse duration, 150 to 200 nsec; beam diameter, 2 to 3 mm; rod temperature, 70 to 80°C; average fluence level, ~3.2 J/cm^2. Several steps were taken to alleviate the problem, such as careful inspection of the rod surfaces with a 20x loupe and cleaning with spectroscopic grade methanol prior to installation, annealing of the laser rod by gradually increasing the pump level from near the threshold over ~3 x 10^4 shots to the operational level, changing the vendor for the anti-reflection coating, and maintaining a higher cleanliness level in the laser and working area. None of these steps resulted in any significant improvement.

MECHANISMS FOR LASER ROD OPTICAL DAMAGE

A systematic study was undertaken to discover the causes of the optical damage. Since alexandrite is a low gain laser medium compared to Nd:YAG, it requires a higher pumping energy and a higher level of intracavity fluence with a higher reflectivity output coupler. Furthermore, the rod is maintained at an elevated temperature (80°C), which causes additional difficulty in terms of thermomechanical stability of the laser cavity, and the thermal cycle of laser turn-on and -off can cause moisture condensation on the rod surface exposed to the air. In spite of all these factors, there seem to be no intrinsic characteristics of the alexandrite rod which should result in a considerably different damage threshold from that of other solid-state laser materials such as Nd:YAG.

The damaged alexandrite laser rod faces were inspected under a high magnification optical microscope to characterize the nature of the damage and to search for any patterns in the damage spots. Figure 5-11 shows typical rod surface damage characterized by a group of damage spots with sizes ranging from 1 mm to a few tens of microns. Some of the larger damage spots exhibit a crater-like structure of considerable depth. The material sputtered from these craters appears to be deposited in the surrounding area, which may in turn develop into new damage spots.

The damage pattern does not show any resemblance to the beam profile or the laser mode shape. These spots do not appear to be caused by dust particles from the air, considering the large number of damage spots as well as their nonuniform distribution. Therefore, it is assumed that this kind of damage originates either from bad anti-reflection coatings or from unsatisfactory laser rod cleaning.

The normal procedure prior to laser rod installation in the pump chamber consists of inspection and cleaning of the rod faces in the laboratory, after the rod is received from the coating plant. High spectral purity methanol (Fisher Optima grade) is used to wet a lens tissue placed flat on the rod surface and then dragged, without exerting any pressure on the rod surface. High spectral purity acetone is used in the same fashion if any stubborn spots remain after cleaning with methanol. On some occasions, a drop of collodion is applied to the rod and peeled after it dries. Sometimes this is followed by cleaning with methanol, or vice versa. After cleaning, the rod surface is again inspected using a low magnification lens (<5x) and a 20x loupe to ensure that the surface is clean and that there are no streaks or other deposits left by the methanol. Although this inspection ensures the absence of large dust particles and large blemishes or streaks on the rod surface, small particles (less than a few millimeters) or relatively clear marks on the surface cannot be detected by the magnifier or the loupe.

To characterize the rod surface after cleaning by the conventional method, the rod surface is examined under a high magnification (up to 500x) microscope. In this study, a new laser rod surface is utilized and cleaned several times with lens tissues wetted with acetone and then with methanol. As long as liquid methanol drops are left on the rod surface, blemish spots are observed on the surface after the drops dry, even when fresh high-grade methanol is used. In fact, when the cleaning is done very carefully using little solvent, the typical spot sizes are somewhat reduced, and thus the surface appears to be free of blemishes under a 20x loupe. Even with the highest grade methanol with very low water content, similar results are obtained. Figure 5-11 shows the rod surface after cleaning, and it appears to be contaminated by residue from the methanol cleaning. The shape and size distribution of the methanol residue spots are remarkably similar to the optical damage pattern. Repeated cleanings with methanol, acetone, and even collodion reduced only the residue contrast, indicating that the new rod surface was contaminated when received from the supplier.

Based on these observations, one may conclude that the optical damage originates from inappropriate cleaning procedures which leave residual spots or blemishes on the rod surface. The residue spots then become centers for absorption of the high intensity intra-cavity laser flux, causing local heating and eventual local damage (melting or ablation) of the laser coating material. Alexandrite is somewhat different from other solid-state laser materials, in that it has strong temperature dependence of terminal state absorption leading to a runaway thermal heating, which further increases the absorption initiated from the absorption center (Walling, 1987). This mechanism lowers the surface damage threshold fluence to about 1.5 GW/cm^2, in contrast to a bulk damage threshold of 30 GW/cm^2. The local damage spreads by the splattering of the molten material from deep craters, which then become new absorption centers, and eventually the damage propagates over a large area on the laser rod surface. Such optical damage can be avoided by preventing the buildup of the runaway hot spots on the rod surface. This can be accomplished by ensuring that the rod surface is scrupulously clean. The

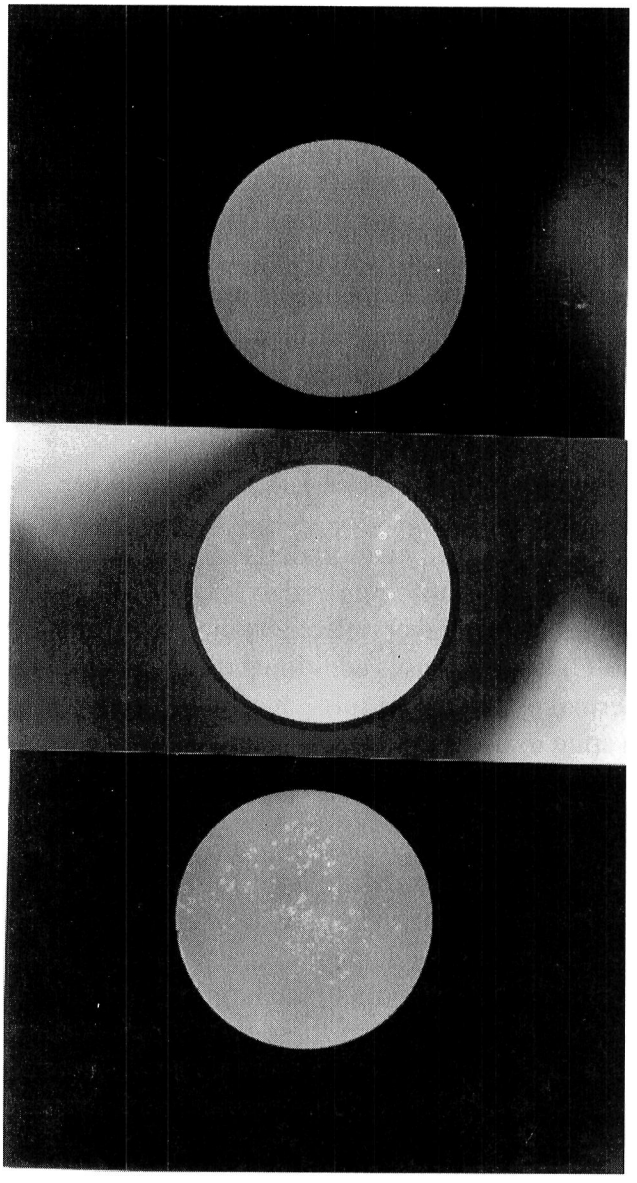

Figure 5-11. Photograph of alexandrite rod end faces: cleaned using the new method we developed (top), as cleaned using conventional techniques (center), and after conventional cleaning and subsequent use and damage in a laser (bottom).

new cleaning procedure (as described below) appears to be quite successful, since the laser rod cleaned using this technique has already logged more than 10^7 shots without damage.

CLEANING PROCEDURE FOR LASER RODS AND COMPONENTS

The rod is first washed with distilled and deionized water and then washed in methanol. This ensures the removal of particles or debris left on the rod from the polishing or coating process. Spectroscopic grade hexane is used to remove any oil or grease from the rod surfaces and barrel. After washing with acetone and methanol, the rod is transferred to a clean bench. Collodion is then applied to the coated rod face and peeled after it dries. Repeated applications of collodion are adequate to remove all traces of residue from the solvents. With stubborn residues, it may be necessary to scrub the rod face with lens tissue. Several lens tissues are liberally wetted with solvent (acetone or methanol) and moved vigorously across the rod face. After each step, the rod face is inspected under the microscope with at least 70x magnification. After the laser rod face is cleaned with solvents, it is repeatedly cleaned with collodion until no visible blemishes are apparent under a 70x to 200x magnification microscope.

After thorough cleaning, care must be taken to maintain the surface cleanliness during installation in the pump chamber. Fresh O-rings are thoroughly degreased and cleaned before installing them on the laser rod. The rod is again inspected after installing the O-rings, and collodion is used to clean the face, if residue from the O-ring is present.

The same procedure is followed in the cleaning of other optical components, such as mirrors, used in the laser. Optical coatings are to be handled with great care. While hard coatings can withstand vigorous rubbing, soft coatings can be easily scratched, and, in such situations, only gentle dragging with wetted tissue is possible. Also, some coatings may not withstand peeling with collodion. Hence, the above procedure is applicable only when the coatings are hard and have good adhesion to the substrate. With all components, inspection under a 70x microscope is the essential first step in revealing flaws or blemishes.

OTHER MEANS TO PREVENT OPTICAL DAMAGE

Absorption centers on the laser rod surface can also be created by other mechanisms during laser operation. A leak of the rod coolant through failure of the O-ring seal can lead to the formation of residue deposits on the rod face from the dissolved salts in the coolant. Such spots are very strong absorption centers and lead to severe rod damage. Even a small seepage will result in such damage. To prevent this, high performance seals are required which assure no leaks even with continuous temperature cycling. A double O-ring seal with an intermediate spacer has been utilized for sealing the laser rod in the pump chamber (Figure 5-12).

Condensation of water on the rod faces or other optics is another possible source of damage. Condensation can occur in the alexandrite laser head especially during laser shut down, when the laser pump chamber cools from its normal operational temperature (80°C) to ambient temperature (20°C). The condensate evaporates slowly, leaving residues that can serve as nuclei for damage. Condensation is prevented by maintaining a purge of dry nitrogen during the cool down cycle of the laser.

Sapphire apertures are utilized to prevent walk-off beams from the etalons from hitting the O-rings or edges of the pump chamber end walls surrounding the rod ends. Without these apertures, material is ablated onto the rod ends when a walk-off beam hits either the O-ring or the edge of the pump chamber.

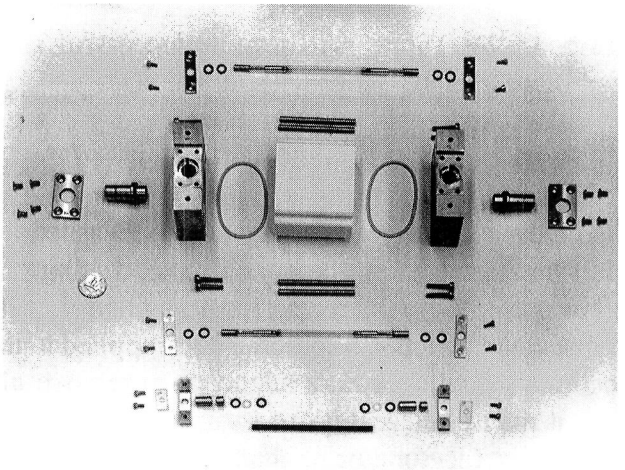

Figure 5-12. Exploded view of the pump chamber for Alex I. Coolant micro-leaks were sealed by the use of double O-rings on the rod (bottom) and flashlamp ends. Sapphire apertures were added to prevent rod-end contamination by ablation of the O-ring compression plates by stray radiation.

DIODE LASER INJECTION SEEDING

As a parallel effort to eliminate optical damage in etalons and to eliminate a frequency jitter remaining despite the digital timing controls, we developed diode laser injection seeding of alexandrite. We present here a method of spectrally narrowing and frequency stabilizing an alexandrite laser suitable for making atmospheric temperature, pressure, and water vapor measurements. A CW AlGaAs laser is utilized (Figure 5-13) to injection seed the alexandrite laser. Then we describe a technique for frequency stabilizing the diode laser to a molecular absorption line center, using frequency modulation and a photoacoustic generated

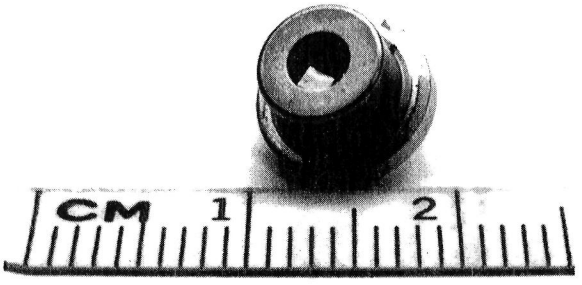

Figure 5-13. Photograph of an AlGaAs diode laser used for injection seeding alexandrite. It was the development of these small single mode lasers that made injection seeding of alexandrite lasers for flight use practical. Prior to these, the only alternative was to use a dye laser pumped by either a Nd:YAG or a Krypton ion laser.

feedback signal. Frequency stability of the diode laser is inferred from measurements of the feedback error signal. The pulsed alexandrite frequency stability is measured using a Fizeau interferometer, which simultaneously records a high resolution spectrum of the laser output; the measurements are described in Chapter 7 of this report.

Spectrally narrowing and tuning the alexandrite lasers using a combination of intracavity birefringent tuners and etalons are inherently complex, unstable, and unreliable. Each tuning element must be tuned so as to achieve a single narrow bandpass output, and all must be tuned synchronously in order to achieve continuous scanning. Each of the tuning elements is subject to temperature and mechanical drift. In addition, intracavity etalons are particularly lossy, increasing the circulating energy densities for a given output energy and frequently incurring optical damage. Injection seeding obviates the need for etalons and offers other advantages as well. The injection seeded laser achieves narrowband operation without sacrificing efficiency. If the seed laser has CW output, it is more readily frequency stabilized using active feedback techniques, thus facilitating frequency stable operation of a high power slave laser.

Injection seeded alexandrite laser

We distinguish injection seeding from injection locking, using the definition of Siegman (1986). In injection seeding, the injected or slave laser is not necessarily mode matched to the injection or seed laser, *i.e.*, the longitudinal modes are not spectrally aligned with each other. The frequency of the seed laser will typically fall on the wing of one of the slave laser cavity transmission modes. As the slave laser pulse builds up from the seed frequency, the peak frequency of the pulse gradually shifts over to the peak of the nearest slave cavity mode. If the seed laser output is broad enough or is far enough from the nearest slave cavity mode, then two or more slave cavity modes may appear in the output. Injection locking is a specialized case of injection seeding in which the two laser cavities are longitudinally as well as transversely mode matched. If the seed laser frequency is close enough to a slave cavity mode, it will pull the output frequency of the slave laser to match that of the seed laser.

Referring to Figure 5-14, the collimated output of an AlGaAs diode laser is focused into a photoacoustic cell filled with oxygen at 760 torr, recollimated, and then injected through the output coupler of a pulsed alexandrite laser, after passing through three optical isolators. The diode output is approximately 80% polarized along the axis of minimum beam divergence, which is aligned vertically (after being rotated by the optical isolators) to correspond to the polarization vector of the slave laser. The optical isolators are necessary to separate the alexandrite output beam from the diode beam, and to prevent the alexandrite from seeding, or worse, destroying the diode. We have utilized diode powers ranging from 3 mW to 100 mW, with about 1 mW entering the cavity from a 30 mW laser in the final configuration.

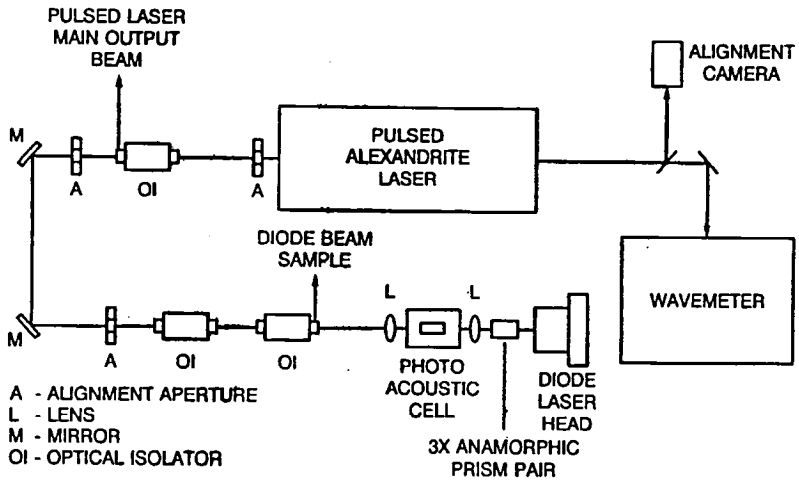

Figure 5-14. Optical layout of the injection seeded standing wave alexandrite laser. Apertures are used not only to facilitate optical alignment, but also to reduce forward scattered light from decreasing the effective optical isolation of the diode seed laser from the pulsed alexandrite laser.

Seed laser characteristics

The diode is selected for a room temperature wavelength about 5 nm greater than the wavelength of the oxygen absorption line to which we wish to lock. We then cool the diode to between 0 and -40°C using Peltier coolers to bring the wavelength within range of the desired line and adjust the diode current to fine tune it to the final wavelength. By cooling the diode laser, we achieve a narrower spectral bandwidth, increased lifetime, higher output power for a given current, and the ability to use higher currents without affecting the reliability of the laser. The wavelength tuning sensitivity of this type of diode laser was measured across the 760 to 770 nm spectral range (Schwemmer, 1988). The diodes we used have a tuning sensitivity of between -1 and -5 cm^{-1}/K for a fixed current, and -1.5 cm^{-1}/mA for a fixed temperature. The tuning sensitivity of any given mode, however, is considerably lower, ~ -1.0 cm^{-1}/K and -0.2 cm^{-1}/mA. The disparity in tuning coefficients for the cavity mode and the peak of the gain curve causes these lasers to mode hop, leaving gaps in their tuning curves. They also exhibit hysteresis, hopping through one set of modes while tuning in one direction and hopping through a different set of modes when tuning back. For this reason, one may have to try a few different diodes to find one that operates exactly at a particular wavelength.

A small portion of the diode output is directed to the wavemeter to make high resolution measurements of the diode laser spectrum. The measured diode laser bandwidth is 0.008 cm^{-1} FWHM, or 242 MHz. We note that, in this measurement, the signal is integrated for a few seconds, and no particular caution is taken to stabilize the current or temperature of the diode during this period. The wavemeter optical resolution at these wavelengths is 0.0035 cm^{-1} (100 MHz) and has less than 0.004 cm^{-1}/hr drift. Therefore, assuming Gaussian line shapes, the actual bandwidth of the diode laser is approximately 0.0072 cm^{-1} or 220 MHz.

Diagnostic systems

A 0.5 m focal length spectrometer with 0.25 cm^{-1} resolution is used to monitor the wavelengths of the seeder and the alexandrite simultaneously (Figure 5-15). The output beam of the alexandrite laser is tapped by a beam splitter at the exit port of the second isolator and sent to the wavemeter for a high resolution spectral characterization. The output of the wavemeter is connected to a digital oscilloscope for recording and plotting. Combining the spectrometer and wavemeter diagnosis, the output spectrum can be characterized in terms of the absolute wavelength and spectral shape of the laser pulse, clearly resolving the longitudinal mode structures (Figure 5-16).

A high speed photo-diode is used to measure the laser pulse temporal shape. The output of the detector is displayed on an oscilloscope which is triggered by the leading edge of the Q-switch pulse. Thus, the laser pulse build-up time (BUT) from the leading edge of the Q-switch pulse can be measured by the temporal location of the laser pulse on the oscilloscope. For a given injection seed intensity and pump energy level, the BUT will reach a minimum when optimal seeding occurs. This reduction of the BUT is a powerful diagnostic parameter that is extensively used in this experiment as a measure of the quality of the seeding. The BUT has also been used as the feedback parameter of an injection locked single mode YAG laser to control the cavity length (Rahn, 1985).

Mode matching

There are generally four sources of mode mismatch: mode size, wave front curvature, spatial displacement, and angular tilt. The latter two sources are related to the alignment of the slave beam and the seeder beam and can be controlled to be negligible in our setup. The first two sources of error are related to the match in the beam waist sizes and the relative position of the waists. For simplicity, the fundamental spatial mode, TEM_{00}, is considered in this discussion. Referring to the experimental setup, the fraction of power coupled from the seeder to the slave laser cavity is estimated to be better than 70% (Kogelnik, 1964).

Birefringent tuner

In the present configuration, the birefringent tuner (BRT) is the only passive component which tunes the laser frequency. The three-plate BRT used in the slave laser defines the lasing band as 1.2 cm^{-1} FWHM, as shown in Figure 5-15A. As long as the seeder frequency is within the half width of the BRT band, the alexandrite output exhibits a narrow spectrum within the resolution of the spectrometer, when seeded as shown in Figure 5-15B. The high resolution wavemeter data of Figure 5-16 show two longitudinal modes spaced by 0.007 cm^{-1}. A 1 cm^{-1} range of tuning is possible for a fixed BRT position. It is important to maintain the BRT band shape as smooth as possible without any extra peaks. When the BRT band shape is not smooth due to misalignment of the BRT plates, the slave alexandrite laser has output not only at the main seeder mode, but also at other wavelengths within the BRT bandpass.

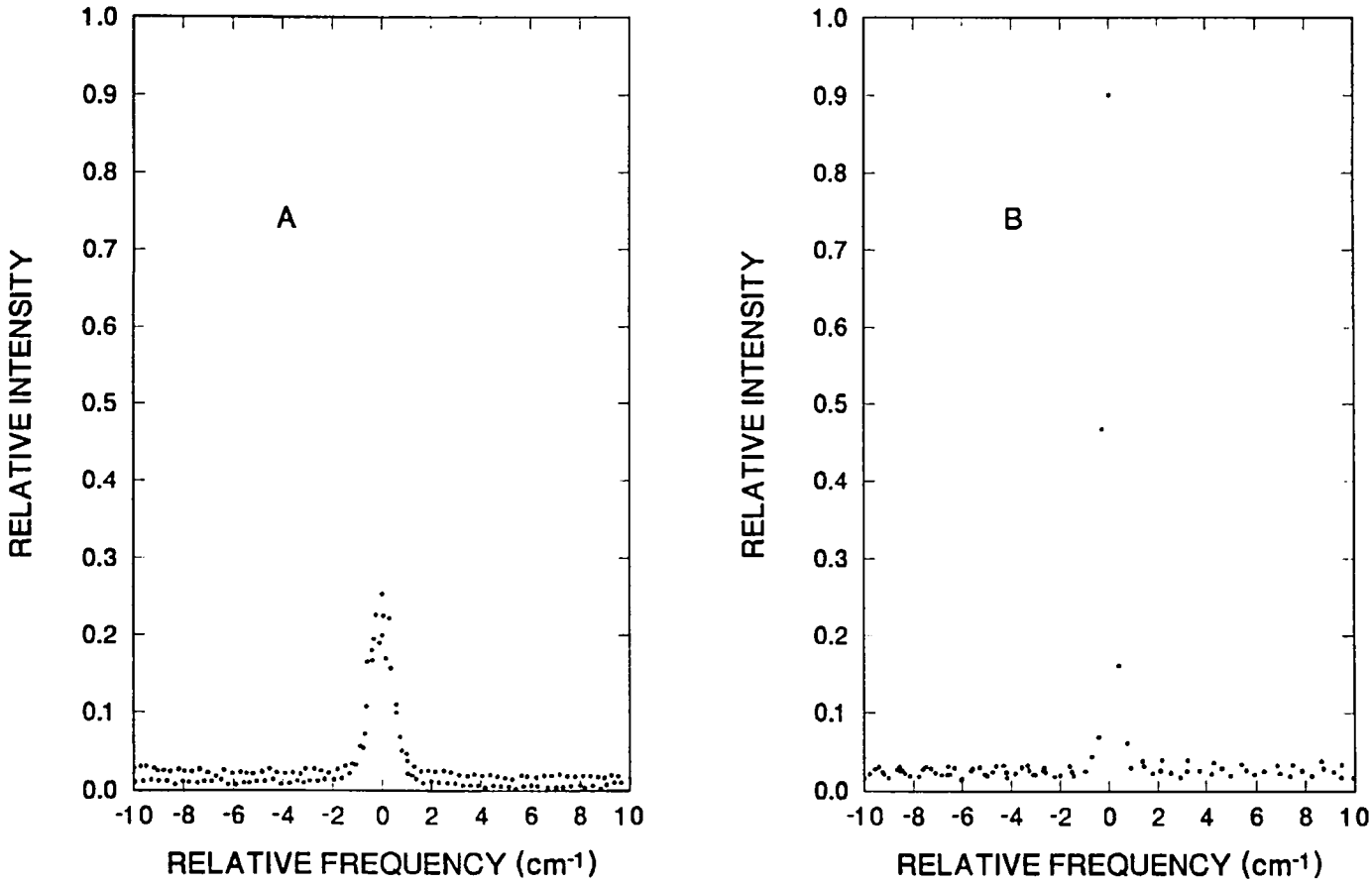

Figure 5-15. Spectrometer measured output spectrum of the unseeded alexandrite laser (A), and of the injection seeded alexandrite laser (B).

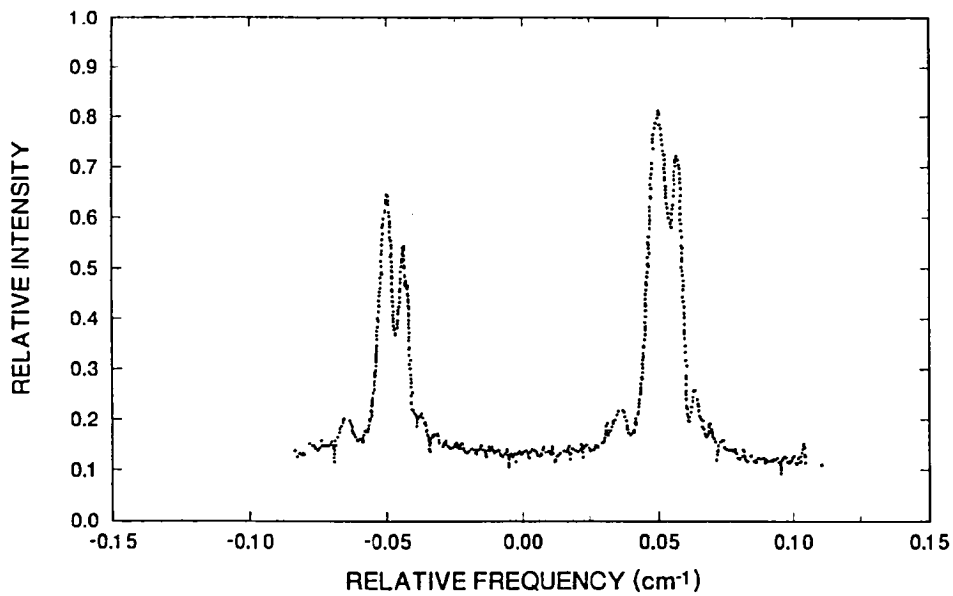

Figure 5-16. Fizeau interferometer measurement of a single pulse of the seeded alexandrite output spectrum. The free spectral range of the interferometer is 0.1 cm^{-1}.

DIODE LASER FREQUENCY STABILIZATION

The diode laser used for injection seeding the alexandrite laser is frequency stabilized to an oxygen absorption line center used for atmospheric temperature measurements. For pressure measurements, the diode can be frequency stabilized to the trough between two closely spaced absorption lines. Water vapor measurements require locking the diode to a water vapor absorption line center. In each case, the diode laser current is dithered a small amount, causing the diode wavelength to oscillate. A non-resonant photoacoustic cell, housed inside a gas cell, is used to generate a feedback signal controlling the laser current. Similar techniques employing gas transmission cells have been used to lock AlGaAs diode lasers to Cs-D_2 (Hori, *et al.*, 1983), Rb-D_2 (Tsuchida, *et al.*, 1982), and H_2O (Pevtschin and Ezekiel, 1987).

Frequency stabilization system

Figure 5-17 is a block diagram of the apparatus used for the active frequency stabilization. The laser output is focused into the photoacoustic cell, a 4 mm diameter by 6 cm long glass cylinder with Brewster windows and enclosed by a larger gas cell containing 1 atm of oxygen. The acoustic cell has a microphone affixed to a hole in the side wall of the glass cylinder, and there is another opening to maintain equilibrium pressure with the outer cell. The diode laser frequency is determined by the applied bias current and the diode junction temperature. These are set so as to tune the laser to the desired absorption frequency. The DC current is stable to 1 μA, and the temperature is stable to 0.1 K. These will generate frequency instabilities of a given laser mode of about 10^{-4} cm^{-1} (3 MHz) and 0.1 cm^{-1}, respectively. A 1 mA peak to peak 10 Hz sinusoidal dither current is added to the bias supply current to cause the laser output frequency to sweep back and forth across the full width of the absorption line (Figure 5-18). As the diode sweeps in frequency, the change in absorption causes local temperature changes in the gas inside the acoustic cell. The local pressure fluctuates correspondingly and is detected as an acoustic signal by the microphone. When the diode frequency is centered over the absorption line, the acoustic frequency will correspond to twice the dither frequency, and there will be no acoustic energy at the fundamental frequency. The microphone signal is input to a lock-in amplifier, which generates an output voltage proportional to the magnitude of the acoustic signal at the

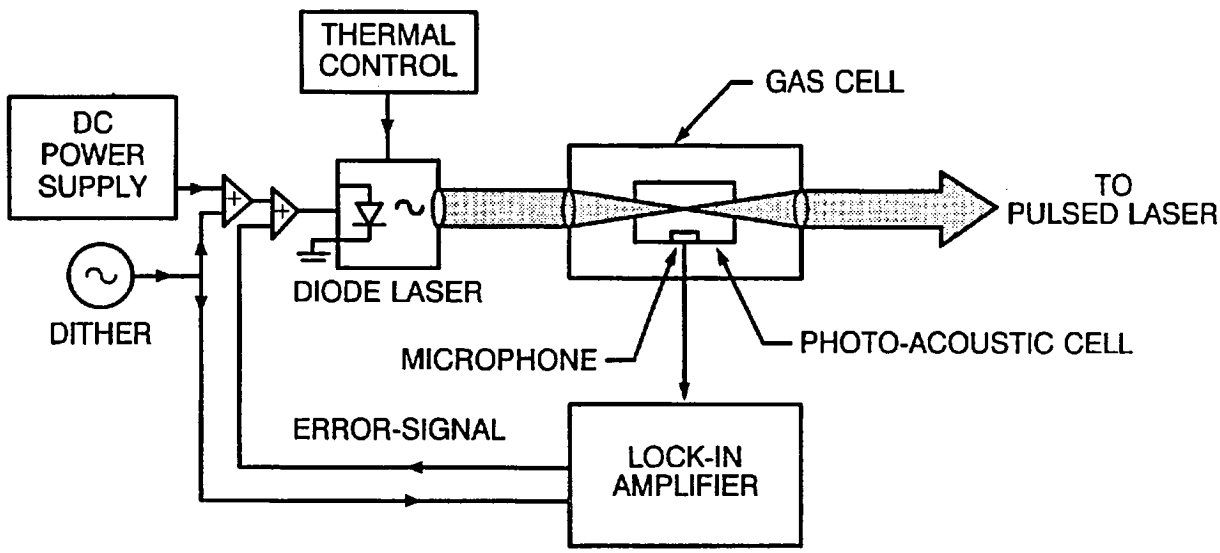

Figure 5-17. Block diagram of the active frequency stabilization system used on the diode seed laser.

fundamental frequency. The lock-in output corresponds to a derivative spectrum if the dithering laser frequency is slowly scanned across the oxygen line by adjusting the bias current or the junction temperature while the feedback is disconnected. There is a small offset in the derivative spectral line center due to amplitude modulation of the diode output as the current is dithered (Walls, 1987). This offset may be compensated by a phase offset in the lock-in amplifier. The lock-in output is summed with the diode bias supply current, providing a negative feedback signal to the laser, keeping it centered on the absorption line. Thus, the current tuning property of the diode laser is used to counter wavelength drift due to imprecise temperature control. We have locked the diode to two different oxygen lines of different strengths. First, we locked the laser to the strongly absorbing oxygen line at 13078.22 cm^{-1}, having a line strength of 5.66×10^{-24} $cm^{-1}/molec/cm^2$ (Ritter and Wilkerson, 1987). To first order, the error signal is linearly proportional to the amount of frequency drift of the diode laser while under frequency locked conditions. The frequency of the laser was held to within 500 kHz (1.7×10^{-5} cm^{-1}) of the absorption line center over a period of 4 hrs using a servo-loop gain of 300 and a 4 sec time constant (Figure 5-19). In the second test, we chose a line weaker by a factor of 26, the 13010.81 cm^{-1} line that is used to make atmospheric temperature measurements. In this case, the laser was held to within 15 MHz (5×10^{-4} cm^{-1}) of line center for a period of 15 hrs using a loop gain of 30 with a 4 sec time constant (Figure 5-20).

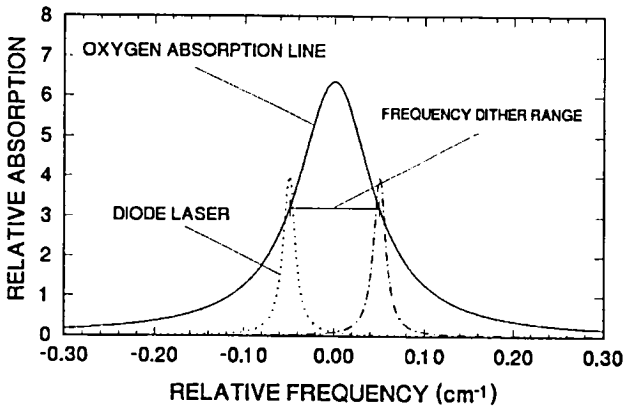

Figure 5-18. Spectral absorption line of oxygen with the diode laser output superimposed at the extrema of its frequency dither range.

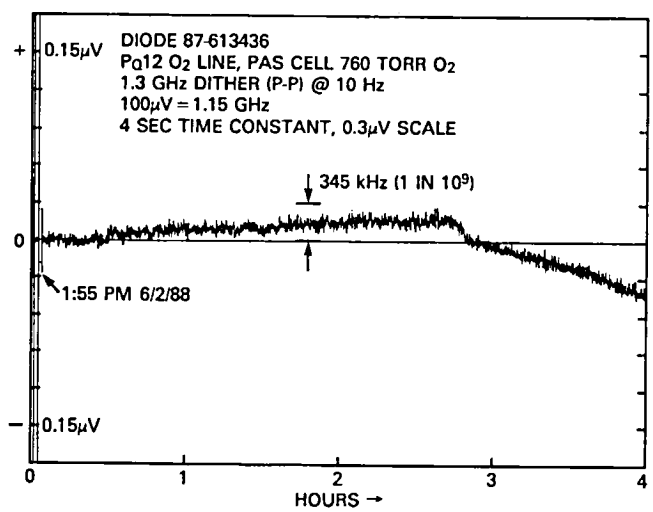

Figure 5-19. Error signal of the frequency dither stabilized diode laser locked to the strong 13078.22 cm^{-1} absorption line of oxygen.

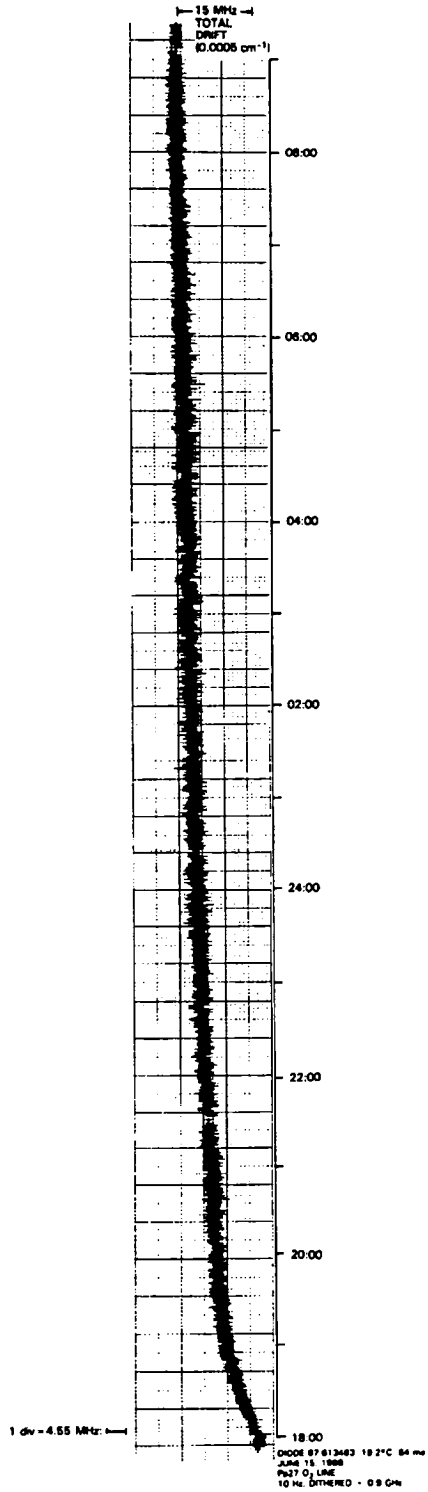

Figure 5-20. Error signal of the frequency dither stabilized diode laser locked to the weak 13010.81 cm^{-1} absorption line of oxygen.

Pulsed laser synchronization

The pulsed alexandrite laser is synchronized to the dithering diode laser by using a trigger derived from the dither oscillator. Thus, the alexandrite fires once in each dither cycle as the diode frequency crosses the absorption line center (Figure 5-21). The trigger signal fires the flashlamps that pump the alexandrite, and the Q-switch is delayed a fixed amount. A flashlamp trigger delay may be adjusted with respect to the dither sinusoid to allow the alexandrite to sweep in frequency or fire at any position on the absorption line. This is equivalent to a phase adjustment in the lock-in amplifier phase-lock loop and may also be used to compensate for the asymmetry in the derivative spectrum, as mentioned previously. The frequency stability of the pulsed alexandrite laser when injection seeded is discussed in Chapter 7.

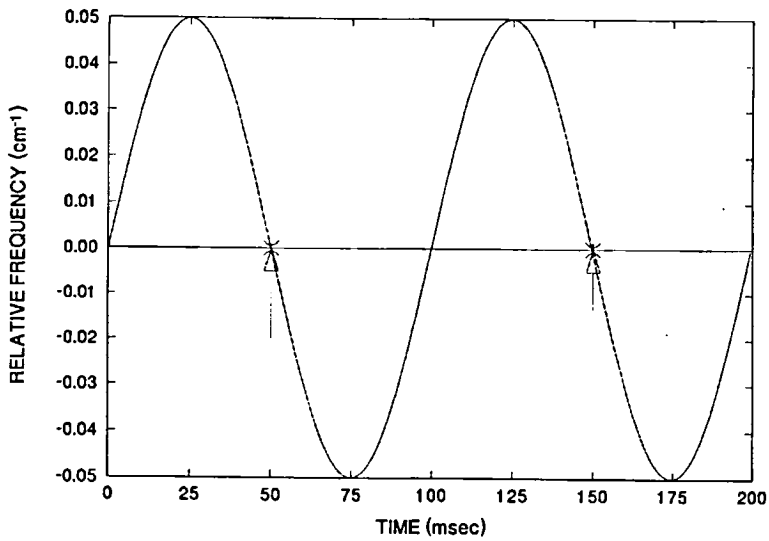

Figure 5-21. Diode laser instantaneous frequency versus time showing the triggering times (arrows) for the pulsed slave alexandrite laser.

RING LASER

Advanced development of laser technology for remote sensing of pressure and temperature has been pursued by NASA over the last several years. An effort was made to advance the performance of solid-state tunable lasers, in particular, to improve on the encouraging results of the injection seeded alexandrite laser work. The results[3] of the development of a single mode tunable alexandrite laser are summarized in what follows.

Table 5-2 lists the operating parameters of the alexandrite ring laser system. This system features the ring laser resonator, laser rod pump chamber, flash lamp high voltage power supply operated at 10 Hz, and coolant recirculator to maintain pump chamber temperature. The ring laser (shown in Figure 5-22) is seeded by an AlGaAs diode laser coupled through beam shaping optics and optical isolators. The system also includes a microcomputer, PZT controller, and a seed diode laser resonance detector for active alexandrite cavity length control.

[3] "Development of Systems for Continuous Tuning and Single Mode Operation of Solid-State Lasers," Science and Engineering Services, Inc., Burtonsville, MD, Small Business Innovation Research (SBIR) Phase II Report.

Table 5-2. Alexandrite ring laser parameters.

Parameter	Dimensions
Laser rod diameter	5 mm
Laser rod length	120 mm
Cr^{3+} doping	0.17 atomic %
Coolant temperature	70°C
Fluorescence bandwidth	1800 cm^{-1}
Fluorescence lifetime	250 μsec
Flash lamp pump pulse	100 μsec
Output coupler reflectivity	70%
Q-switched lasing threshold	35 J
Ring optical path length	108 cm
Beam divergence	0.85 mrad
Laser wavelength:	
Free running	753.1 nm
With birefringent tuner	740-775 nm
Output energy	100 mJ
Pulse width	200 nsec
Laser bandwidth:	
With 3-plate birefringent tuner	2.5 cm^{-1}
Injection seeded	<0.01 cm^{-1}

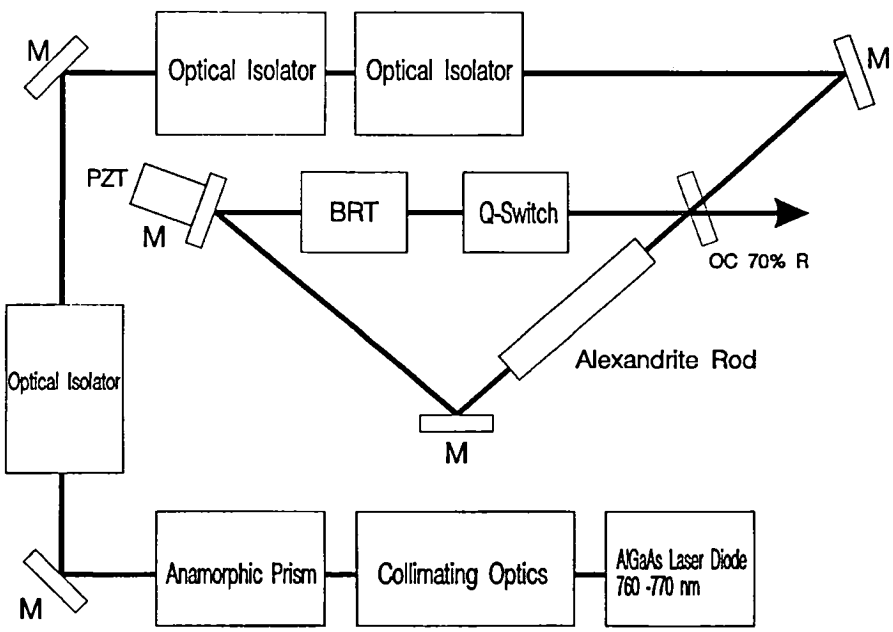

Figure 5-22. Optical configuration of the injection seeded, Q-switched, ring alexandrite laser.

The alexandrite laser resonator consists of three laser mirrors, arranged so the optical path is a triangle with bilateral symmetry. The angles of incidence of the beam path at each mirror are 20°, 20°, and 50°. The sides of the triangular path are 30 cm, 30 cm, and 48 cm, giving a total round trip optical path of 108 cm. The alexandrite rod and pump chamber are placed along one of the shorter sides. The output coupler is placed at one of the 20° corners. As the longer side was aligned parallel to the longer dimension of the breadboard, this arrangement allows the forward traveling output to exit the laser in a convenient direction, parallel to the longer dimension. The seed beam is injected through the output coupler directly into the shorter leg of the resonator, where the pump chamber is located. The forward traveling mode inside the laser resonator is then defined as that traveling wave in the direction of the injected seed laser radiation. In the longer leg of the resonator are placed the birefringent tuner (BRT), and the Q-switch crystal (Q-SW), where at different times, both a Pockels cell with KD*P for electro-optic Q-switching, and an acousto-optically activated quartz crystal have been used. The laser mirror at the 20° angle opposite the output coupler is mounted on a piezoelectric translator (PZT) in order to match an alexandrite resonator cavity longitudinal mode with the seed laser frequency. Both mirrors at the 20° positions have focal lengths of 10 m, while the third mirror at the 50° position is a flat. The resonator is designed as a stable cavity with low dioptic power in order to achieve improved performance with thermal lensing from the alexandrite laser rod.

The seed laser radiation is injected into the alexandrite laser resonator using optical isolators that prevent the reverse traveling output of the alexandrite from destroying the seed laser. The optical isolators consist of Faraday rotators, which rotate the input polarization in the same direction for inputs of both directions, and polarizers, which pass the radiation from one direction but attenuate the radiation from the opposite direction. The diode laser is collimated by a short focal length lens, and passes through a Galilean telescope composed of two 2.5 cm diameter lenses. The beam is circularized by an anamorphic prism pair. The telescope reduces the diameter of the seed beam, which facilitates directing it through the isolators and also imparts a near collimated beam divergence for transverse mode matching with the alexandrite laser.

During this study, the choice of possible resonator candidates was narrowed in four steps. First, it was found that the triangular resonator is preferable to the rectangular resonator. Second, it was recognized that the performance of a cavity improves as the length is shortened. Third, the power of the mirrors in the cavity was optimized, and fourth, the shape of the cavity was found not to be crucial in the performance, allowing the design of the cavity to conform to other system requirements. To judge the stability of a particular resonator design, we computed the number of rays (out of a baseline of 100) that would complete 19 transits of the cavity and compared it to the corresponding number of rays for a 70 cm triangular resonator using three plane mirrors and a thermal lensing focal length of 2 m. The goodness parameter is defined as the percentage of rays completing the 19 transits compared to this baseline cavity. A triangular resonator was shown to have greater tolerance for rotational alignment than a rectangular resonator of the same length. A comparison of 70 and 140 cm resonators showed improved performance of the cavities for decreased length.

Choosing the optimum mirror power required a trade-off between a high goodness parameter and a beam radius large enough to avoid damage to optic surfaces. Based on the goodness parameter alone, a resonator with three 2.5 m focal length mirrors would present the optimum choice. However, considering the power density at the beam waist, it is clear that the mirrors in such a resonator would be susceptible to damage from focused beams. The range of the anticipated thermal focusing in alexandrite is large, *viz.*, 50 to 200 cm focal length (Driedger, *et al.*, 1986). The possibility of strong focusing of the rod requires careful consideration of the addition of more focusing from the cavity mirrors. Of the aligned resonators, only those with low power (or flat) mirrors meet the requirement of <1.5 GW/cm^2 power density at the beam waist, for thermal lensing of 50 to 200 cm focal length. Therefore, when using curved mirrors, their combined focal length should be greater than 5 m.

There is no substantial advantage in any one shape for a given resonator length. Various arrangements of optics for a given shape are roughly equivalent in terms of stability. The results indicate that beam focusing is not excessive for mirror focal lengths of 5 m or greater in the range of expected thermal lensing of the rod.

With the basic limit on mirror power delineated, other aspects of the laser system design can be considered in the resonator layout. For example, it is desirable to minimize the angle at the output coupler to enable both the seed and output beams to pass through unobstructed by the mount. This sets an upper limit of 40° to 45° for this angle. Also, the preferred shape of the resonator is an isosceles triangle for symmetry advantages. It is also preferred to have some curvature on at least two of the mirrors in order to reduce their susceptibility to rotational misalignment. The mirror at the large angle of ~100° should be a flat to minimize aberrations. The chosen arrangement has two mirrors of 10 m focal length and one flat, arranged in an isosceles triangular shape of ~108 cm perimeter length.

Cavity Control System

The efficiency of injection seeding a Ti:S laser has been evaluated by measuring the relative intensity of the backward to forward wave output. When seeded in an optimum fashion, the forward to backward intensity ratio was seen to be on the order of 1000:1 (Raymond and Smith, 1991). In order to achieve optimum seeding for single longitudinal mode output, the seed frequency may be expected to coincide with the slave resonator mode to within approximately 1/8 the slave mode spacing (Raymond and Smith, 1991; LaChambre, *et al.*, 1976). Therefore, the desirability of controlling the cavity length to match the two frequencies is evident. Two possible feedback techniques are to minimize the intensity of the backward traveling wave at 10 Hz, or to monitor the seed beam intensity in the laser cavity to detect the resonant condition. The possibility of using 10 Hz information as feedback for the cavity control system has been evaluated. It was found to be unfeasible due to higher frequency (>10 Hz) changes in the cavity length. Also, coupling of the forward to the reverse traveling component (due to scattering or reflection from the rod faces) results in mode competition between both components, where a substantial percentage of the reverse energy is narrow band, thereby reducing its utility as an indicator of overall spectral purity. To date, a control system has not been implemented.

Stability Measurement

After the laser was assembled, an experiment was performed to test the stability of the cavity length. The seed diode was injected into the laser resonator and aligned so that multipass interference was observed behind one of the cavity mirrors. This leakage was directed to a photomultipier tube (PMT), after passing through a spatial filter and a 10 nm interference filter. The PMT output was examined on an oscilloscope. Figure 5-23 shows the cavity passing through the resonant condition (inverted signal: negative peaked at maximum intensity) at 500 Hz or less. A fast Fourier transform (FFT) of this signal shows the spectral power peaked at DC with the remainder in a plateau of -90 dB below 500 Hz. This observation confirmed that forecasting the resonant condition based on the state of the previous laser pulse would not be feasible.

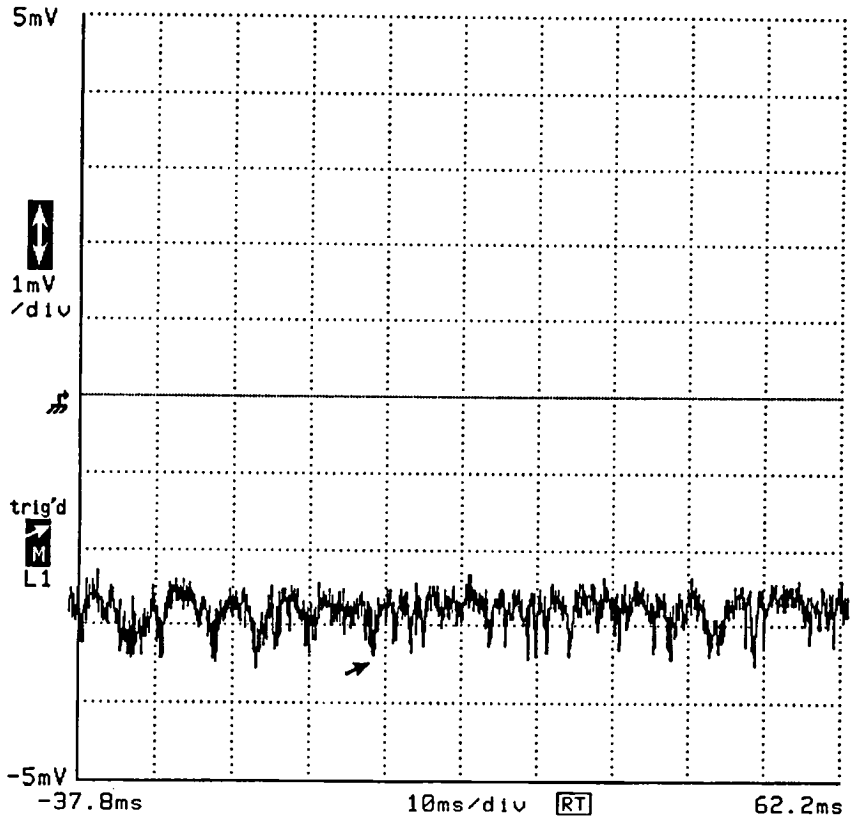

Figure 5-23. Signal level of laser diode at PMT (1 mV vertical scale, inverted) showing cavity passing through resonance with laser diode.

Laser Performance

The following parameters were studied for their effect on laser performance, particularly on spectral purity of the alexandrite laser output: spatial mode, diode laser spectral purity, diode laser beam divergence, and linewidth. Apertures were placed in the alexandrite laser cavity, although it is not clear that it was operating on a TEM_{00} mode. Etalons were placed in the diode laser beam to filter out extraneous modes and broadband radiation that otherwise contributed as much as 10% to the diode laser output. Care was taken to match the beam waist and divergence of the seed laser and the alexandrite output. Measurements of spectral purity were made using a multipass gas cell having a 56 m total optical path, and also over an outdoor atmospheric path of 1.7 km. The best spectral purity measurements were made with the white cell (96%), and with the target board (98%). It is noted that the white cell is more susceptible to scattered light contaminating the measurements, so the measurement with the target board is believed to be more accurate.

THE FUTURE

The high accuracy and high vertical resolution that lidar techniques offer can increase our understanding of atmospheric processes and improve numerical weather forecasting, especially if spaceborne lidar instruments capable of global coverage can be realized. The main technology drivers to get lidar systems into space are currently the size, weight, and power requirements of the laser systems in order to achieve the optical output powers neccessary to obtain sufficient signal to noise for good measurements. The one factor which has the largest impact on size, weight, and power is the overall, or "wall-plug", efficiency of the laser. The overall

efficiency is simply the usable optical power output divided by the total electrical power input to the laser. If the recent developments of diode pumped Nd:YAG lasers and visible red diode laser arrays, capable of pumping tunable chromium doped lasers like alexandrite, are an indicator of what may be possible in the near future, than DIAL systems capable of making temperature, pressure, and water vapor measurements are a distinct possibility.

Other important performance features of any laser used for these measurements are the spectral properties of the laser output. These include, in particular: 1) narrowband Q-switched operation (for temperature measurements, which have the most stringent requirements, a bandwidth of 0.01 to 0.005 cm^{-1} or less); 2) the ability to tune precisely to molecular resonant absorption features to an accuracy of 0.001 cm^{-1} or better and to remain there with that accuracy; and 3) the spectral purity of the output, defined as the complement of that fraction of the laser output that falls outside of the spectral absorption line used to make the measurement. In addition, for satellite applications, the laser must be capable of continuous tuning in order to keep the frequency tuned to the Doppler-shifted absorption feature. If one envisions a conically scanning lidar, the Doppler shift incurred will change from plus to minus several gigahertz as the laser scans from fore to aft of the satellite direction of motion. The transmitter must be tuned to compensate for the shifted molecular absorption line, and the receiver must be tuned on the opposite side of the line to account for the twice shifted backscattered signal (Schwemmer, 1993). In addition, smaller corrections will have to be made to account for the Earth's rotation, as a function of latitude.

Previously, laser pumped dye lasers were utilized to generate the tunable near-infrared short pulses required to make these measurements. Presently, solid-state flashlamp-pumped alexandrite lasers are utilized, because they have significant maintenance, lifetime, and efficiency advantages over liquid dye lasers. Nd:YAG laser-pumped Ti:sapphire lasers are also being developed for these applications. Their advantage over chromium doped lasers is that their high gain enables good energy extraction from a single transverse mode. However, a disadvantage is that the upper state lifetime is only about 2 μsec, which precludes them from being pumped with available semiconductor lasers, thereby limiting the expected overall efficiency to about 1%. A chromium doped laser, such as alexandrite, can be directly pumped by visible red wavelength diode lasers and could be expected to achieve up to 10% wall-plug efficiency. The high power short wavelength lasers required to pump chromium lasers are just now becoming available. A scanning lidar system built on an approach that uses a few kilowatts of spacecraft power could achieve nearly global coverage (see Chapter 14). Alexandrite has strong absorption at 630 nm on only one crystal axis, limiting useful pump geometries to the end-on configuration. The search for better materials continues. One promising material is chromium-doped LiCaLF, which has somewhat higher gain than alexandrite, and better short wavelength absorption on all crystal axes (Payne, *et al.*, 1988). An alternative approach is to use the output of diode lasers directly, which can have wall-plug efficiencies of 30% or more. However, their peak power output is limited to only about twice their average power output. This limits their use to CW and quasi-CW systems. While there are CW lidar techniques (Nagasawa, *et al.*, 1990; Takeuchi, *et al.*, 1983), it is expected that they will only be useful for nighttime measurements in the near future because of the high daytime background levels present when looking down at the Earth from space. The solar spectral irradiance at the top of the atmosphere at *A* band wavelengths is over 1 watt/m^2/nm. Considering that spot sizes from low Earth-orbiting lidar systems will cover several hundred square meters, in order to maintain an eye-safe energy density, daytime measurements will only be possible with systems that can produce multiple kilowatts of single mode radiation. This technology still needs considerable work before it becomes feasible. For the near term, a diode laser pumped tunable solid state laser appears to be the best candidate for the realization of spaceborne DIAL remote sensing systems.

CHAPTER 6 PHOTOMULTIPLIER RESPONSE CHARACTERISTICS

Numerous efforts have been made over the years to calibrate the photomultiplier tubes (PMT) used in the lidar system. Linearity and after-pulsing are two well known effects that may introduce errors into measurements made with these devices. To quantify these effects for the specific detectors used in lidar temperature and pressure measurements, a careful and systematic study was made of the characteristics of detector responses to understand the cause of various systematic biases and to minimize these undesirable effects in measurements of transient signals having a large dynamic range. We quantitatively evaluated signal induced bias, gain variation, and the linearity of commonly used gated photomultipliers in the current integrating mode. Analysis of the results indicates that impurity ions inside the photomultiplier tube are the source of the signal induced bias and gain variation. The signal induced biases of two different photomultiplier tubes used in this study show a significant variation in the magnitude of the bias and decay behavior. It can be minimized by using an external amplifier to reduce PMT gain, and by applying a low potential between cathode and first dynode. The linearity of a photomultiplier tube was also studied over a large dynamic range of input intensities employing a new technique which does not require an absolute calibration. The result of this study shows that the photomultiplier response is linear only for a limited input intensity range below a certain anode current.

INTRODUCTION

In optical measurements, a detector is used to convert light intensity to a measurable electrical signal. The PMT is a sensitive, widely used detector in which the photons falling on the cathode surface generate photoelectrons. This photoelectron flux is amplified inside the tube by means of a dynode chain to produce a current at the anode.

The output electrical signal of a detector, *e.g.*, the anode current of a PMT, is generally assumed to be linearly proportional to the input light intensity. It is also assumed that the output electrical signal is zero when there is no light input. However, the detector response is nonlinear for very large input intensities due to the saturation effect (Fenster, *et al.*, 1973; Hartman, 1978; Hunt and Poultney, 1975; Keen, 1963; Land, 1971; Lush, 1965; Pitz, 1979; Sanders, 1972). If a PMT is subjected to a high intensity light pulse, the PMT output exhibits after-pulsing, a non-zero residual signal which lasts over tens of microseconds (Coates, 1973a, 1973b; Riley and Wright, 1977; Yamashita, *et al.*, 1982). This corrupts the measurement of low intensity signals in the tail of the high intensity impulse even if the initial transient is gated "off" by switching the cathode or first dynode voltage. This is a problem in many measurements, including DIAL, because the magnitude of weak signals cannot be determined against an unknown baseline. This long lasting residual signal known as signal induced noise has been observed previously (Hunt and Poultney, 1975; Jones and Kent, 1974; Yamashita, *et al.*, 1982). In this report, we refer to it as "signal induced bias" (SIB) due to the long lasting and non-oscillatory nature of this noise. Previous work, however, considers only brief measurements over a very limited range of operating parameters. We report this effect with regard to light intensity, dynode voltage distribution, design, and also gating time. The short term stability of the detector gain is also an important aspect in DIAL measurements. A variation in the gain (Akopdzhanov, *et al.*, 1979) results in a distortion of the output pulse shape, which, in turn, introduces false information in the retrieved parameters. The gain stability effects and others have been enumerated in reviews relative to photon counting (Candy, 1985; Mead, 1981).

The objective of this work is to study quantitatively the characteristics of fast response gated PMT detectors to light impulses comparable to those encountered in atmospheric lidar systems. In the next section, we give a brief discussion of the effects of detector response on DIAL measurements and its importance in improving

the accuracy of DIAL measurements. The experimental setup used is discussed, including the optical setup, the electronic system, and the data acquisition system. The method of generating a light pulse with a rapid decay and the verification of the assumed decay profile are also discussed in detail. Care was taken to eliminate possible contaminating light sources to ensure that we were truly observing the detector response and not a light source characteristic or optical material fluorescence. We present the measurements and analysis of the results of signal induced bias, gain stability, and linearity for selected PMT's and a microchannel plate. Physical interpretations of the results based on the dynamics of the PMT operation and an optimum configuration of the gated PMT in DIAL measurements are also discussed.

EFFECTS OF THE DETECTOR RESPONSE ON LIDAR MEASUREMENTS

Three different aspects of detector response to transient light signals are discussed: signal induced bias, short-term gain stability, and response linearity. Each of these can cause systematic errors in the determination of the relative strength of backscattered light signals. Because lidar signals typically have a large dynamic range, a small bias will be comparable in magnitude to a low level signal and hence create a large measurement error. When a strong backscattered signal is received from the near field (*i.e.*, a cloud, or the ground return in nadir-pointing systems), the signal amplitude is very high, as shown in Figure 6-1, and a large SIB effect can be created. As a result, the data immediately after the peak may be contaminated and the signal baseline may be ambiguous.

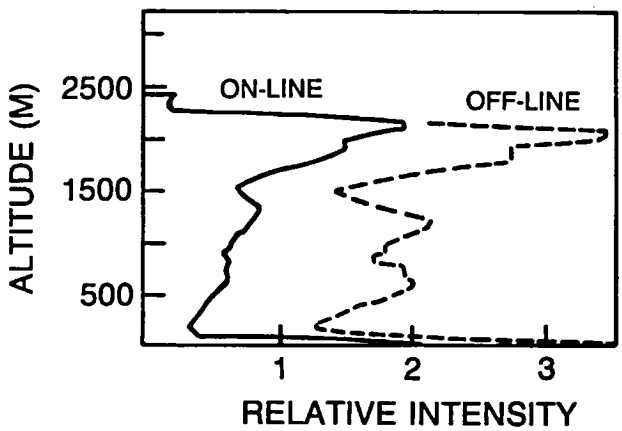

Figure 6-1. Typical example of airborne lidar signals from the on-line and off-line laser pulses. Notice the strong ground return signal.

Short-term gain stability can have an effect similar to SIB, particularly if background light signals are present which must be subtracted from the measurements to derive the laser backscattered signal. One would like to assume that the background level is constant over the duration of the lidar return signal (on the order of tens to hundreds of microseconds).

The linearity of the PMT response is important because of the large dynamic range in DIAL signals. The PMT response becomes highly nonlinear for intensities substantially larger than the threshold value. In addition, the response below this threshold is not necessarily strictly linear. We found that responsivity may change by a few percent over 3 to 4 decades of intensity. For some applications, even this small nonlinearity may be important. One way to overcome this problem is by use of more than one PMT to cover a large dynamic range. Then all PMT responses must be inter-calibrated to assure consistency of the data set.

EXPERIMENTAL SETUP

Since the objective is to characterize the detector response, one needs to design an experiment with a well defined optical signal. This requires generating optical signals whose characteristics are defined based on first principles and which do not require measurements using the detector itself to characterize the light source. The validity of the assumption should also be verified, if possible. The experiments should be designed so that they do not depend critically on the absolute intensity of the light pulse to avoid the requirement of absolute calibration. They should be accurate enough to study small effects.

To satisfy these requirements, we designed an experimental setup consisting of the generation of the optical signal, the detector to be tested, and the digital data acquisition and analysis system. The experimental setup for the SIB measurements also forms the baseline for the linearity and gain variation experiments. In the following section, we discuss the main features of the setup in detail, and setup modifications for the other studies will be described as applicable.

Light Pulse Generation

A short light pulse with a well defined period is generated by chopping a stable CW He-Ne laser using a high speed rotating chopper, as shown in the schematic of the optical setup, Figure 6-2. Judicious use of baffling ensures that no stray light from the source can reach the detector when the chopper blocks the beam. This arrangement eliminates any unknown light sources possibly associated with fluorescence or other residual light when an electrically generated light pulse is used as the source (Jones and Kent, 1974). Further care was taken to eliminate fluorescence from the neutral density filter by employing partially aluminized filters. Using relay optics and a very small aperture on the rotating chopper wheel on which the laser beam is focused, we generate a short (500 nsec FWHM) optical pulse of near trapezoidal temporal profile. Although the width of this pulse is somewhat longer than the actual laser pulse (100 nsec FWHM) of our lidar system, the pulse width is suitable for all aspects of this study.

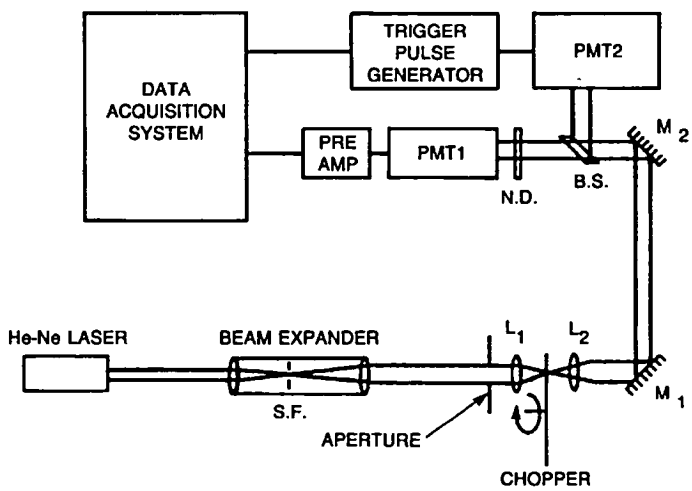

Figure 6-2. Schematics of experimental setup - SF: spatial filter, L_1 & L_2: lens 1 & 2, ND: neutral density filter, BS: beam splitter, M_1 & M_2: mirror 1 & 2, PMT_1: test photomultiplier, PMT_2: trigger photomultiplier.

Since the spatial profile of the laser beam is displayed temporally, the beam intensity profile should be symmetrical and decay rapidly in the direction of the chopper rotation to prevent confusing low intensity wings as SIB. The Gaussian profile of the laser TEM_{00} mode serves well for this requirement. To produce a specklefree beam profile, the output laser beam is spatially filtered with a 50 μm pinhole at the focal point of the beam expander. This filtered output beam is then refocused onto the chopper wheel using a fast lens.

The maximum chopper rotational speed is 40 Hz. However, the rotational speed stability is not sufficient to use the internal trigger signal generated by a detector located on the chopper 180 deg from our aperture. We require better than 50 nsec stability in order to exceed the data acquisition time resolution. To attain this stability, we use a double aperture mask mounted on the chopper. The first aperture consists of a narrow slit (10 μm width) with 5 mm height. The second aperture consists of a 14 μm diameter pinhole. The pinhole is darkened by hot flame oxidization in order to minimize laser beam scattering by the pinhole. Thus, light leaks are reduced when the focused laser beam spot falls near the boundary of the pinhole. The first aperture is used for the trigger pulse to start the data acquisition, and the second aperture is used to generate the optical signal for the test measurements.

The radial location of the pinhole from the chopper wheel axis is 85 mm, and the axial distance between the two apertures is 2 mm. Therefore, the temporal separation between the trigger pulse and the sample pulse is 94 μsec, and the resulting jitter in the temporal location of the sample pulse is approximately 50 nsec, which is half the sampling rate of the digitizer. With this jitter and a 500 nsec trapezoidal pulse shape, we expect the effect of the jitter will be minimized. Statistical averaging of 100 data sets further reduces any residual effect.

To generate a short pulse of a few hundred nanoseconds duration with high light rejection both before and after the pulse requires a careful opto-mechanical design. Since the chopper speed at the radius of the aperture is 23.8 m/sec, the pinhole diameter must be limited to about 12 μm to generate a pulse width of 500 nsec or less. In addition, the laser beam waist at the pinhole should be small compared to 12 μm so that the rise and decay times of the pulse will be extremely short. Also, the scattered light level should be negligible compared with the amplitude of the SIB we are studying.

The extremely small pinhole size, however, poses problems due to the mechanical vibration of the chopper. The location of the pinhole relative to the focused beam spot must be controlled extremely accurately to assure pulse amplitude stability. One may solve this problem by making the focused laser beam waist size much smaller than the size of the pinhole. Thus, we employ a 14 μm diameter pinhole, which corresponds to a 588 nsec pulse, whereas the focused laser beam diameter is 3.5 μm. (We note that a pinhole specified to be 20 μm diameter by the manufacturer has been blackened in our laboratory by the flame oxidization method. The actual pinhole size is determined from the measured pulse shape.) In this way, the pulse peak amplitude is maintained constant even in the presence of small jitter. Any residual effect is further reduced by statistical averaging . Another way of doing the alignment is to use a narrow slit in place of the pinhole. This method provides good stability in the pulse peak amplitude and pulse width. However, a substantial amount of scattered light leaks through after the pulse and, thus, this method was found to be unsuitable for this study.

The rise and decay time of the pulse is determined by the focused beam waist size and the chopper speed. In order to obtain the minimum beam waist size, one needs to employ a low *f*/number lens with small spherical aberration. Ordinary optical quality lenses show large aberrations when a large portion of the lens aperture is used, thereby introducing significant light intensity in the wing of the pulse profile. We limit the collimated beam to half of the lens aperture to minimize the effect of aberrations. We use a fast microscope objective lens with a focal length of 18 mm and an aperture of 20 mm.

The diffraction limited Gaussian beam waist size at the focal point is given (Siegman, 1986) as

$$W = \frac{f\lambda}{\pi W_0}, \tag{6-1}$$

where W is the HWHM of the focused beam, f is the focal length of the lens, W_0 is the HWHM of the collimated beam in front of the focusing lens, and λ is the laser wavelength (632.8 nm). The collimated laser beam profile in front of the focusing lens is accurately measured using a linear detector array of 1024 elements with a total length of 2.5 cm. The measured beam shows a Gaussian profile with a 2.3 mm beam radius (HWHM). With this collimated beam radius we calculate a 1.58 μm beam radius (HWHM) at the focal point based on Eq. (6-1).

Another important aspect of the optical setup is the depth of field of the focusing lens relative to chopper vibration in the direction of the optical axis. The depth of field of the lens is sufficiently large that the beam radius 20 μm away from the focal point increases to about 6 μm. The chopper vibration is considerably smaller than a few microns, and the depth of field is large enough to accommodate the vibration.

The light pulse generated, as discussed above, is characterized by a fast rise and decay profile with a flat plateau at the pulse center. The rise and decay time is characterized by the focused laser beam radius of 1.58 μm (HWHM) and the chopper speed of 23.8 m/sec. One way to quantitatively characterize the rise time is to measure the time the chopper takes to scan between the half-power points of the Gaussian beam profile at the focus. Based on a Gaussian profile of the focused laser beam and the chopper speed, we calculate this time as 133 nsec. The two half-height points correspond to 12% and 88% of the peak intensity because the measurement yields the convolution of the Gaussian function with a square pulse. In Figure 6-3, we show the measured pulse profile with a 1% neutral density filter in front of the PMT. From this, we measure a 130 nsec rise time between the two points corresponding to 12% and 88% of the peak, confirming the calculated rise time of 133 nsec. The details of the intensity in the far wing of the pulse are also confirmed by repeating the measurement without the neutral density filter, thereby saturating the center of the pulse.

Based on the above observations and analysis, we confirmed that the rise time profile of the light pulse was characterized by a convolution of a Gaussian function with a square pulse function. The decay profile of the light pulse cannot be measured due to the effect of the SIB itself which is being investigated in this study. However, the symmetry of the geometry can be applied to argue that the decay behavior of the light pulse should be the same as the rise profile with a 130 nsec decay time (time between the points corresponding to 88% and 12% of the peak) and a Gaussian profile. With this profile, the decay time is sufficiently short that we do not need to compensate for the residual light intensity level in the analysis. The duration of the plateau is directly related to the size of the pinhole mounted on the chopper. The measured time of 588 nsec corresponds to a 14 μm pinhole size, which is smaller than the manufacturer's specification. The actual pinhole size might have been affected by the pinhole darkening process discussed earlier.

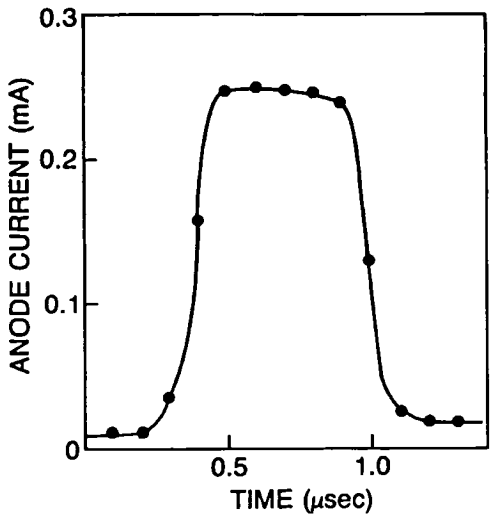

Figure 6-3. Measured pulse profile at low output signal level.

Detectors

In this study, we are interested in the analog or current integrating application of fast response detectors for time resolved DIAL measurements. The maximum time resolution of the measurement is 200 nsec based on the 10 MHz sampling rate of the analog to digital converter. The lidar measurement involves profiling atmospheric pressure and temperature, and the intensity variation covers a few decades of dynamic range for each data set. In particular, the atmospheric backscattered laser pulse intensity near the receiver system is large so that we gate out this portion of the return signal. An electronic gating circuit that switches the first dynode potential is used for this purpose. The laser wavelength used here is tunable from 725 to 780 nm. This near infrared wavelength requires a special low work function photocathode material.

Based on these requirements, we chose multi-alkali (NaKSbCs) head-on type gated PMT's in this study. The PMT's studied here are an RCA 8852 and a Hamamatsu R1017, hereinafter referred to as PMT-A and PMT-B respectively.[4] The manufacturer's specifications are listed in Table 6-1, and both PMT's are used in the experimental setup. The physical dimensions and the cathode material of these two PMT's are the same, but there are two distinctive differences between them. PMT-A employs a linear focused type electron multiplier, while PMT-B uses a box and grid type electron multiplier. PMT-A also has a gallium phosphide first dynode for high gain.

In addition to these PMT's, we also investigated a microchannel plate (MCP) detector used in some laser ranging systems. The MCP features the same photocathode, but it differs from the PMT in the configuration of the electron multiplier. We did not attempt to gate the MCP in our experiments.

The PMT dynode potential distribution and the gate circuit are shown in Figure 6-4. A negative high voltage potential is applied between the cathode and ground. The anode is grounded through a 50 ohm resistor which works as the output load of the PMT. The last four stages of the dynodes are connected by parallel capacitors to increase the available peak current in pulse mode operations. Referring to Figure 6-4, the tube

[4] Commercial names and models are used for identification purposes only; no endorsement of any product is intended.

Table 6-1. PMT characteristics.

Parameter	PMT-A	PMT-B
Window material	Pyrex	Borosilicate
Cathode material	NaKSbCs	NaKSbCs
Cathode sensitivity (@ 633 nm)	33 mA/W	30 mA/W
Current amplification (@ 1000V)	8.0×10^3	4.3×10^5
Dark noise (@ 1000 V, 25°C)	10 nA	15 nA
Dynode type	Linear Focus	Box and Grid
Dynode material	GaP (1st), BeO	Unknown
No. of stages	12	12
Voltage distribution	660 V, 1, 1.4, 1, ...,1	300 V, 1, 1.4, 1, ...,1
Maximum voltage (K-P)	2500 V	1500 V

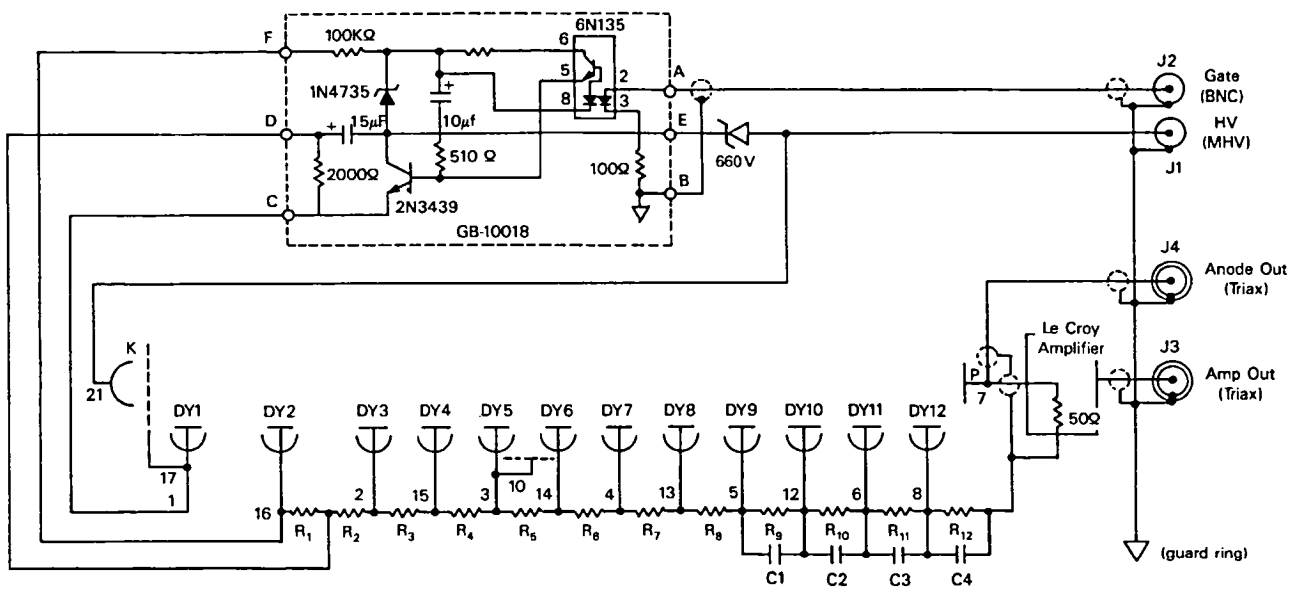

R_1: 81 KΩ, ½W, 5%
R_2: 68 KΩ, ½ W, 5%
R_3-R_{12}: 100KΩ, 1W 5%

C1: 0.02μf, 600VOC
C2: 0.05μf, 600 VOC
C3: 0.10μf, 600VOC
C4: 0.20μf, 600VOC

Figure 6-4. Test photomultiplier base circuit diagram.

is normally off when the first dynode is held at a potential between that of dynode 2 and dynode 3. Gating is realized by switching the potential of the first dynode to a fixed value relative to the cathode, determined by a Zener diode in series with the high voltage supply. The gating time is controlled by the gate signal input.

Data Acquisition and Processing System

The PMT anode current is measured across the 50 ohm load resistor, and this signal is fed to a trans-impedance preamplifier (Analog Modules model LNCA-30 MHz) with a gain of 3.3 KV/A. The preamplifier is AC coupled with a very low-frequency cutoff, and thus the output pulse shape is well preserved for a signal duration of a few hundred microseconds. The bandwidth of the preamplifier and successive buffer amplifier is about 30 MHz. A 12 bit, 10 MHz CAMAC transient digitizer (Transiac model 2012) is used to digitize the final amplifier output signal. The digitizer output is then recorded onto magnetic tape. For each experimental parameter, 100 to 200 data sets are acquired and processed using the lidar data system.

The amplifier chain impulse response has been independently measured by applying an electrical pulse from a pulse generator (Hewlett Packard 8012B pulse generator) to the input of the preamplifier. A square input pulse of 0.5 μsec duration and 0.5 V peak amplitude was monitored, together with the 5 V peak amplitude output pulse, on a Tektronix oscilloscope with a differential amplifier module model 7A22. The PMT output peak amplitude is saturated by as much as a factor of 6 in this experiment. The baseline of the output after the pulse peak was monitored with a 1 MHz bandwidth and better than a 0.5 mV resolution for a duration of 20 μsec. The measurement shows less than a 0.5 mV after-pulse amplitude at 1.0 μsec after the pulse peak. No significant ringing or base line shift was observed following the pulse with a resolution of 0.5 mV. For the amplification factor of 66 and the 50 ohm anode resistance, the 0.5 mV after-pulse amplitude corresponds to 0.15 μA which is far less than any SIB discussed in this chapter.

MEASUREMENTS AND DATA ANALYSIS

In this section, we will discuss the three different aspects of our results characterizing detector performance: signal induced bias, gain stability, and linearity of the response.

Signal Induced Bias

When an intense light pulse falls on a detector, the peak of the pulse may saturate the detector. A non-zero slowly decaying bias signal has been observed (Yamashita, *et al.*, 1982) for PMT's after such an intense pulse. This bias is significant in a time resolved DIAL measurement both because of its magnitude as well as its long duration. The SIB amplitude is largest immediately after the pulse peak and begins with the first after-pulse associated with the He^+ ion often discussed in the literature (Coates, 1973b). The amplitude of the SIB decays slowly and persists after a few tens and even hundreds of microseconds, obscuring the base line of the signal, thereby introducing uncertainties in the measurements.

The time reference trigger signal for the data acquisition is generated by the signal from PMT-B (Figure 6-2) due to the light pulse from the first slit on the chopper. This pulse is about 400 nsec wide and falls on the PMT under test as well. The gate pulse to turn on PMT-A is generated 45 μsec after the trigger signal, to avoid contamination by the SIB from the first light pulse or by scattered light leaking past the slit. The data acquisition starts from the beginning of the gate pulse and lasts the entire duration of the gate pulse, which is normally 100 to 200 μsec. In this way, the digitizer captures the peak of the pulse from the second aperture (pinhole) in the middle of the data array. The front portion of the data array before the pulse peak provides the baseline which is then subtracted from the signal after the pulse peak. The experimental parameters

are the peak power of the light pulse, the PMT dynode voltage, and various parameters of the PMT dynode circuit. The light intensity is varied as much as two decades by placing a neutral density filter in front of the PMT. The PMT dynode voltage is varied from a low value, for which the peak signal is not saturated, to the highest operational voltage. The combination of these two parameters covers the entire operational conditions of the DIAL measurement.

PMT-A

The measured light pulse profiles using PMT-A at various overall dynode voltages are shown in Figure 6-5 for 100-shot averages and a peak light pulse intensity of 3 mW. Note that 3 mW is the baseline light pulse intensity used for all measurements, unless otherwise stated. This light intensity level corresponds to the intensity of ocean surface reflections observed by our lidar system when flown at an altitude of about 2800 m. Scattering from clouds can also cause signals at this level. It is apparent that the measured pulse profile is not symmetric. The rising portion of the pulse is characterized by a fast rise, and the decay of the pulse is characterized by a few large after-pulses and a long-lasting bias. The amplitude of this bias increases as the PMT voltage increases. For a high PMT voltage, the after-pulse itself is saturated, and the pulse width appears to be broadened. However, the location of the pulse peak does not change significantly, which again verifies the assumed characteristics of the light pulse profile. The after-pulses are not related to the oscillations that normally occur in a wide bandwidth electronic circuit, but are related to the impurity gases in the tube. Detailed analysis of these after-pulses will be discussed later in this chapter.

The SIB is measured from this data set as a function of time for each PMT voltage and light intensity level. The time is measured from the center of the pulse peak, and the bias is measured from the signal baseline determined by the signal level before the pulse. In Figure 6-6, the SIB is plotted as a function of the PMT voltage for various times. As shown, the SIB is a very strong function of the PMT voltage. In this and the following figures, the standard deviation of the signal is negligible within the resolution of the 12 bit digitizer; thus, error bars are generally omitted from the figures. In Figure 6-7, the SIB is shown as a function of the idealized pulse peak signal. The idealized peak current is the expected peak current for a given PMT gain (dynode voltage) and light intensity level in the absence of saturation effects. Therefore, in such absence, this parameter is proportional to the small signal gain. The result shows that the SIB increases super-linearly as a function of the pulse peak current. The SIB also appears to be dependent on the pulse peak light intensity, with decreasing magnitude at lower intensities. This indicates that the origin of the SIB is closely coupled with the electron/ion dynamics in the tube near the cathode and first dynode locations, as opposed to being a function of the anode pulse current. In this experiment, the lower intensity light pulse is amplified by increasing the overall dynode voltage in order to get the same idealized anode signal as with the higher intensity light pulse. If the SIB amplitude is a linear function of the light pulse intensity, then we expect no dependency of the SIB on intensity variation.

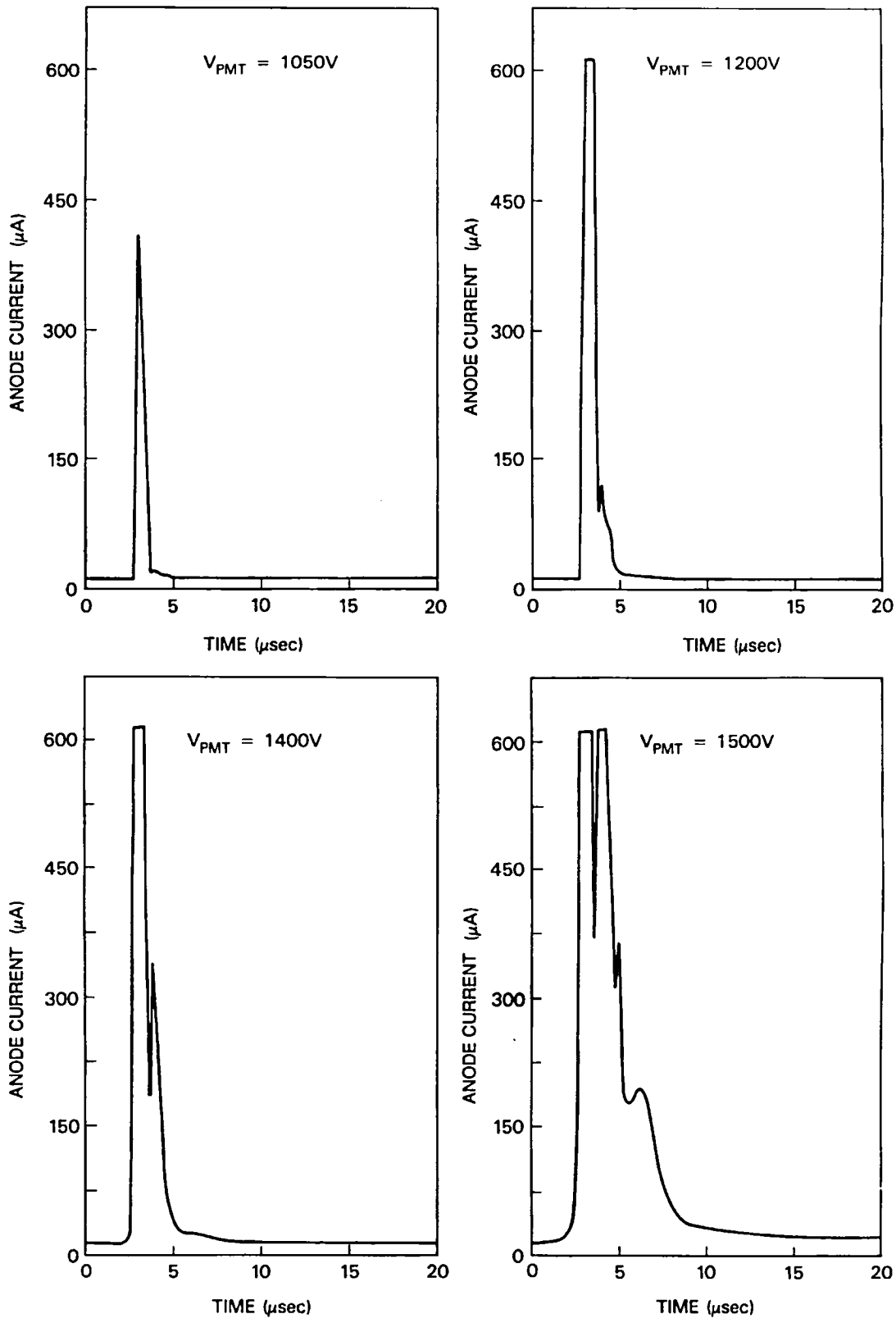

Figure 6-5. PMT-A output signal amplitude vs. time for various PMT dynode voltages (V_{PMT}), for a 3 mW light intensity.

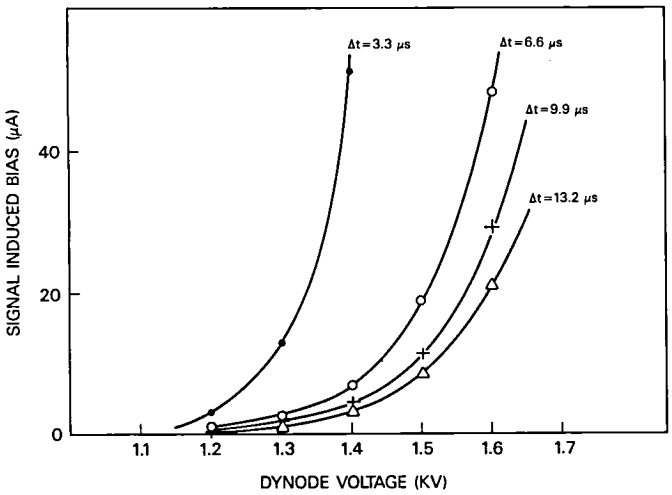

Figure 6-6. PMT-A signal induced bias vs. PMT dynode voltage at various times (Δt) after the pulse peak for a pulse peak intensity of 3 mW. The signal induced current is large immediately (3.3 μsec delay) following the signal pulse and decays rapidly after that. It also increases with PMT gain, and hence the PMT current.

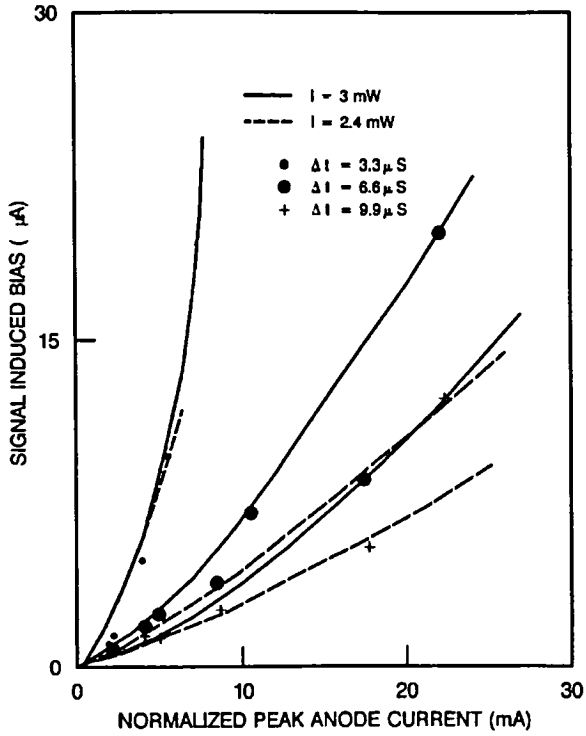

Figure 6-7. PMT-A signal induced bias vs. idealized peak anode current for 2 intensity levels and 3 delay times. The solid line is for a peak intensity of 3 mW and the dotted line is for 2.4 mW.

The above observations suggest that the SIB amplitude increases faster than the amplification factor of the electron multiplication channel. Thus, the SIB effect may be minimized by setting the PMT voltage at a lower value and using an external amplifier to obtain the necessary gain.

One way of characterizing electron/ion dynamics is to measure the decay processes of a certain parameter. In Figure 6-8a, we plot the decay of the SIB amplitude for the dynode circuit with the original configuration depicted in Figure 6-4, while in Figure 6-8b we show the result for a capacitance (C4 in Figure 6-4) of one-half the original value. As shown, the decay behavior is quite similar in both cases. This clearly shows that the SIB has no direct relationship with the dynode saturation phenomenon. We note here that the relative ratio of these two intensities is not very well calibrated due to long term mechanical drift of the experimental setup, because the two sets of experiments were separated by about six months in time. The changeover of the fast decay process at the beginning to a rather slow power function decay also suggests that the SIB results from more than one process. The SIB amplitude at high PMT voltages is still high even after a few tens of microseconds and is as much as a few percent of the normal 1 mA signal amplitude range.

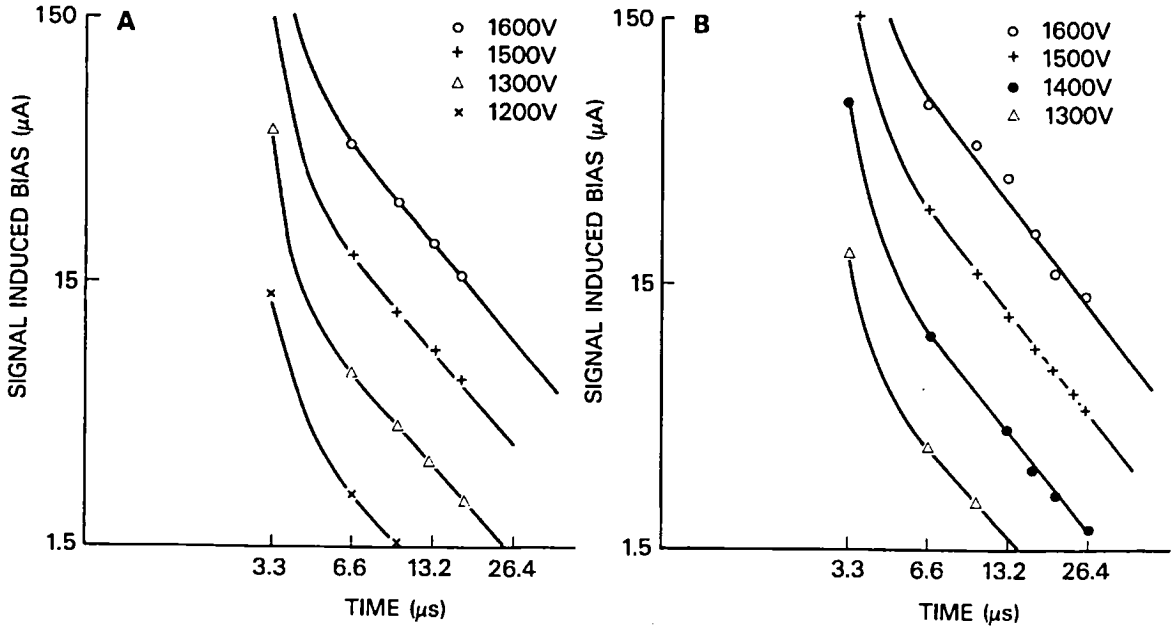

Figure 6-8. PMT-A signal induced bias decay profiles for two different dynode capacitor values- A: original capacitor values shown in Figure 6-4, B: one half of the original capacitor values.

PMT-B

The suggested dynode potential distribution for PMT-B is slightly different from that of PMT-A. A potential drop of 300 V between the cathode and the first dynode is used in this study, compared to 600 V for PMT-A. We believe this may be an important factor for improving the SIB effect of a PMT. Figure 6-9 shows the pulse shapes measured by using PMT-B for two voltage settings for the same peak intensity of 3 mW used with PMT-A. As shown, the magnitude of the SIB increases as the PMT voltage increases. Note that the overall responsivity (anode sensitivity) of PMT-B is considerably higher than that of PMT-A. The anode sensitivity of PMT-B at 600 V is equal to that of PMT-A at 1100 V, with almost the same slope of the sensitivity curve on a log-log plot. The prominent after-pulse peaks observed with PMT-A, however, are somewhat suppressed and the magnitude of the SIB is substantially reduced.

Figure 6-10 shows a plot of the SIB versus PMT voltage for PMT-B. This figure is equivalent to Figure 6-6 for PMT-A. Comparing Figures 6-6 and 6-10, one sees that the functional behavior of the SIB in terms of the PMT voltage is similar for both PMT's. One may compare Figures 6-7 and 6-11 to notice the significant reduction of the SIB amplitude in Figure 6-11 for the various ranges of peak signal and time. This reduction is quite dramatic, especially for data long after the pulse, *e.g.*, as much as a factor of 10 reduction at 13.2 μsec after the pulse peak. The SIB amplitude of PMT-B appears to be almost linearly proportional to the calibrated peak signal amplitude for all times. We attribute the improved SIB characteristic of PMT-B to the lower impurity gas density as evidenced by the smaller after-pulse amplitude, to the design of the dynode structure, and perhaps to the lower first dynode potential.

The clear reduction of the SIB amplitude for the lower optical signal shown in Figure 6-11 indicates again that the origin of the SIB is near the cathode area. The absolute magnitude of the SIB amplitude becomes small only a short time after the pulse (0.1 percent of the normal PMT signal amplitude).

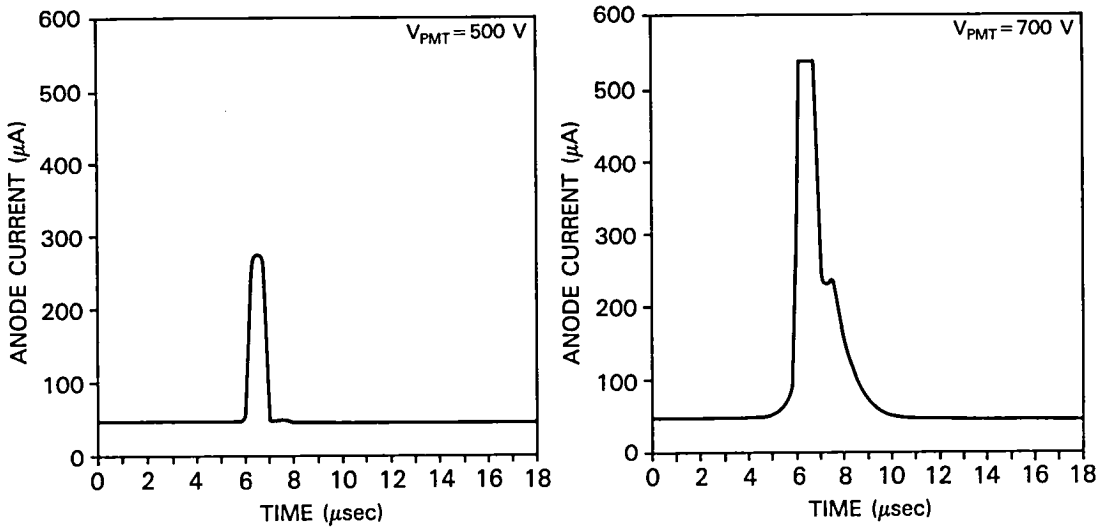

Figure 6-9. PMT-B output signal amplitude vs. time for two PMT dynode voltages where the pulse peak intensity is 3 mW.

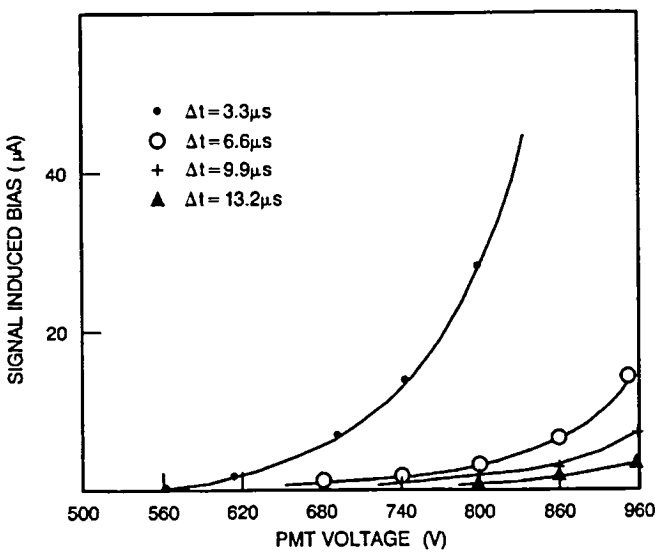

Figure 6-10. PMT-B signal induced bias vs. PMT dynode voltage at various times (Δt) after the pulse peak (pulse peak intensity is 3 mW).

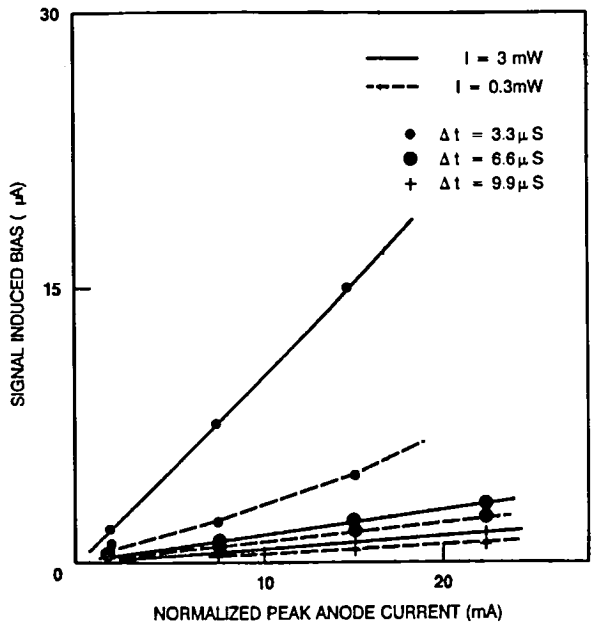

Figure 6-11. PMT-B signal induced bias vs. idealized peak anode current at various delay times and 2 intensity levels. The solid line is for a peak intensity of 3 mW and the dotted line is for 0.3 mW.

As shown in Figure 6-12, the decay behavior of the tail of the SIB long after the pulse reveals a fast exponential function with a 7 μsec decay constant, which is not like the case of PMT-A. The exponential decay for PMT-B continues for 26 μsec from the pulse peak, and, after that, the signal to noise ratio of the data set becomes too low for a quantitative analysis. The decay behavior of the SIB amplitude for lower light intensities shows little difference from the high intensity results.

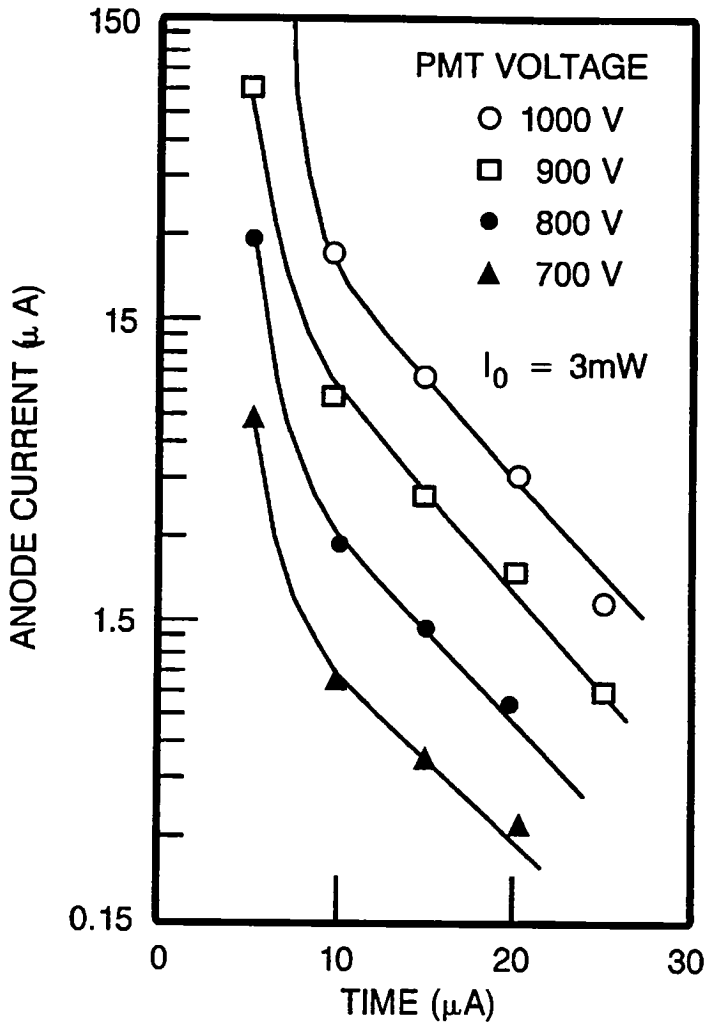

Figure 6-12. PMT-B signal induced bias decay profiles for various PMT voltages.

Microchannel Plate

The pulse profile measured using the MCP is characterized by a significantly depleted baseline level immediately after the pulse peak, followed by a moderately positive SIB amplitude. The magnitude and duration of the depletion of the baseline level are substantial for a large pulse peak amplitude. This phenomenon originates from the so-called dead time effect of the microchannel. This results from positive charge accumulation on the MCP after the electron avalanche due to the slow charging rate of the microchannel, thereby suppressing further electron multiplication. The SIB amplitude following the depletion is, therefore, strongly influenced by the dead time effect. For a very high peak output amplitude, the dead time effect is more important than SIB, as illustrated in Figure 6-13. Although these two effects cancel each other due to their opposite signs, which reduces the SIB amplitude for a long time, the MCP is not very useful for DIAL measurements because of this dead time effect. In fact, the SIB amplitude at intermediate peak signals appears to be the same magnitude as that of the PMT-A.

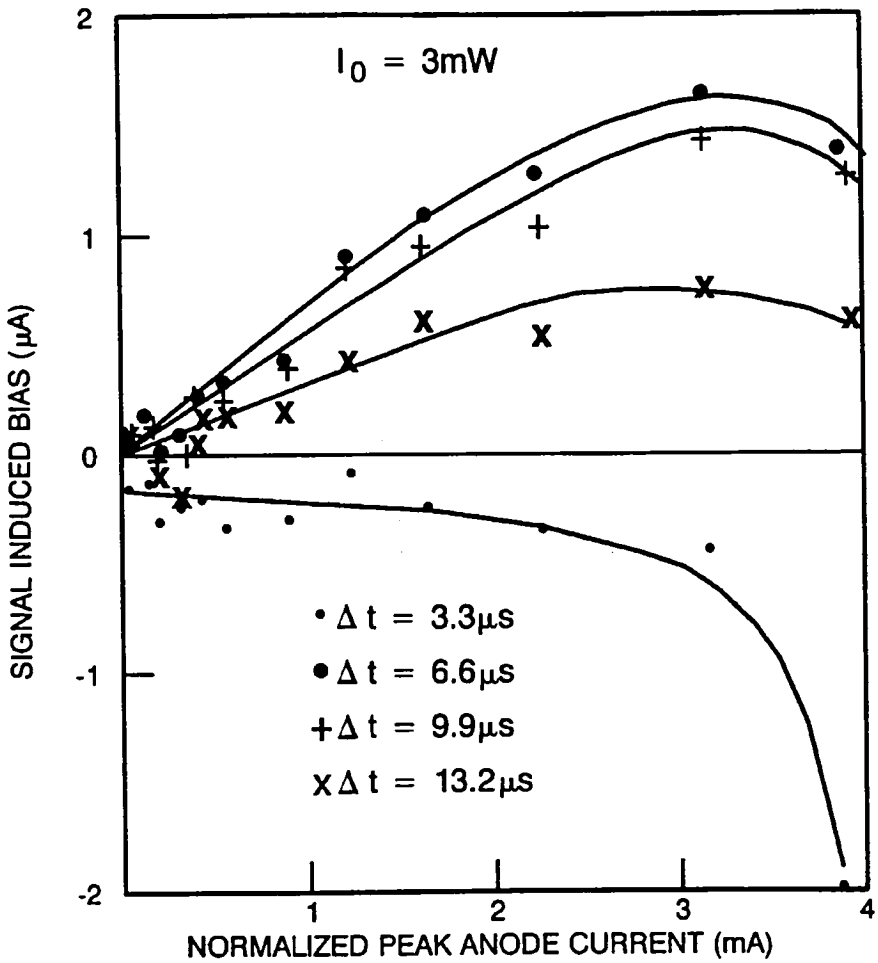

Figure 6-13. Hamamatsu microchannel plate signal induced bias vs. idealized peak anode current at various times after the pulse peak.

Dynamics of Charged Particles Inside the Photomultiplier Tube

It is important to understand the dynamics of charged particles inside the PMT in order to interpret the above observations, *viz.*, the SIB effect, gain variation, and linearity. The electron multiplication process is well understood (Lush, 1965) and does not need further discussion here. However, impurity ion dynamics need to be addressed to understand various aspects of non-ideal PMT responses.

When impurity gases are present in the tube, the photoelectrons from the cathode will ionize these gases through inelastic collision processes. The electron kinetic energy of a few hundred electron volts near the first dynode provides a large cross section for these processes (Massey and Burhop, 1969; Zeldovich and Raizer, 1966). The positive ions formed near the first dynode area are then accelerated back to the cathode and impinge on its surface with a kinetic energy of a few hundred electron volts, releasing electrons from the cathode which are then accelerated toward the first dynode by the electric field. This process generates the after-pulses in PMT's.

This process decays slowly because the ion (*e.g.*, He^+) transit time across the dynode and cathode space is a few microseconds. The 7 μsec decay time of the PMT-B SIB which was discussed earlier strongly suggests

that these impurity ions may be the source of the SIB effect. Note that the decay behavior of PMT-A is quite different from an exponential function for large times. But the decay rate of the SIB in the earlier portion of the tail is comparable to that of PMT-B, indicating that the major source of the SIB for PMT-A may also be related to the impurity ions. However, the slow power function decay cannot be explained entirely by impurity ions.

Gain Stability

A basic assumption in detector operation is that of constant gain during the measurement, which is not quite valid in high accuracy time resolved measurements (Barrick, 1986). In pulsed operation mode, the PMT gain changes due to the disturbance of the dynode electric potential by the signal current and, perhaps, by voltage changes due to the gating circuitry.

In order to study the change in the PMT gain, we designed an experiment in which the input intensity to the PMT is maintained constant by using an LED light source driven by a precision battery. The PMT is gated by a pair of pulses characterized by 50 μsec duration and 100 μsec separation. This pair of pulses is then repeated after 100 msec to simulate the operation of a lidar system at 10 Hz (see Figure 6-14). The experimental parameters varied are the light intensity and the PMT voltage.

The gain variation (in units of μA/μsec) over a single pulse is plotted in Figure 6-15 as a function of the PMT voltage for various intensity levels. The anode current for this data set ranges from 0.01 to 0.5 mA depending on the PMT voltage setting and the intensity level. The results plotted in Figure 6-15 show that gain variation increases rapidly as a function of the PMT voltage for each light intensity level. For clarity of presentation, the curves are discontinued at high voltage levels. We note that the curve actually decreases after a peak value, as illustrated in Figure 6-16, due to anode saturation; the divider network is incapable of continuously supplying the requisite current for such high signals.

In order to simplify the results and to highlight the physics involved, Figure 6-17 indicates the percentage gain variation per microsecond versus the anode current. This plot shows that the percentage gain variation is a function only of the anode current (the intensity dependency is eliminated) and decreases with anode current. In fact, this behavior continues for large negative anode current values which correspond to saturation. The gain variation phenomenon appears to be related to positive impurity gas ions which are produced in the vicinity of the first dynode, and the regeneration of electrons from the cathode by the impinging ions. It is a positive feedback process, and, therefore, the time slope of the gain is positive. As the signal magnitude increases, the space charge effect increases, and the feedback mechanism becomes less efficient due to ion-electron recombination. As the dynode current increases, later stages of the dynode chain are subjected to saturation, which reduces the efficiency of the electron multiplication. The best gain stability is attained when these two effects cancel, which is near 1 mA anode current.

The absolute magnitude of the gain variation in normal lidar operation can be as high as 2% across a 3 km range on each return signal pulse. However, the net effect of the gain variation in DIAL measurements occurs in the ratio between the absorption (on-line) and reference (off-line) signals. This effect may be substantially smaller if the on- and off-line intensities are of similar magnitude.

The gain variation may be understood qualitatively in terms of the impurity ions. The impurity ion induced electron flux is a positive feedback mechanism with a time lag of a few microseconds. When a constant light intensity is fed onto the cathode for an extended period, this feedback process will generate a photoelectron flux which increases in time. The feedback time constant and efficiency determine the slope of the gain

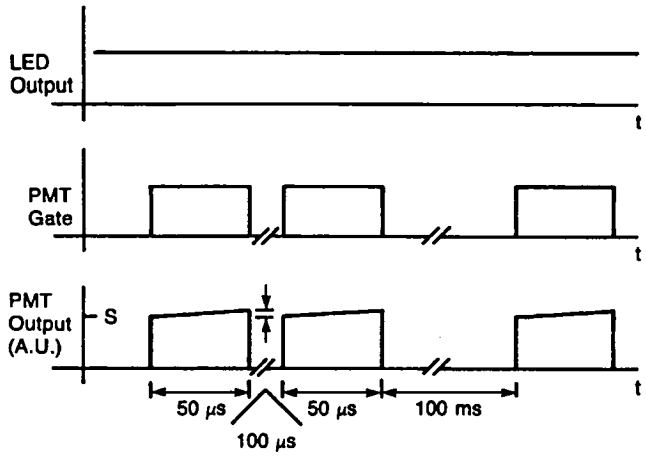

Figure 6-14. Timing diagram for the gain stability experiment.

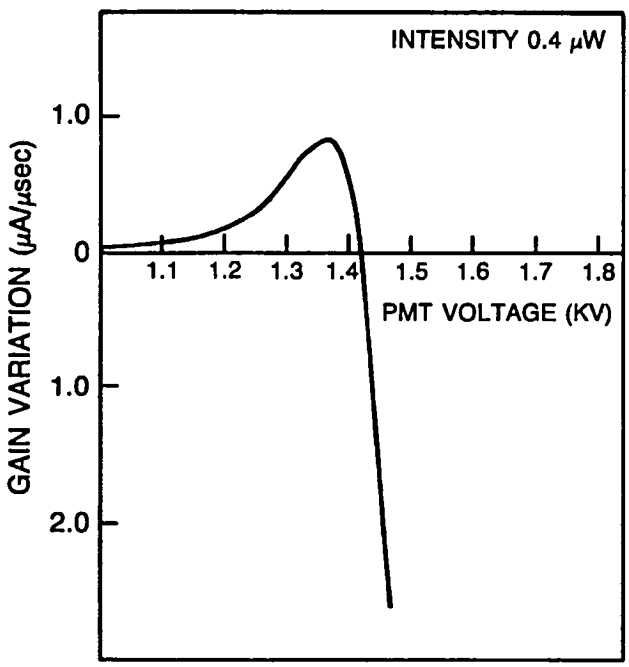

Figure 6-16. PMT-A saturation behavior: PMT gain variation vs. PMT voltage.

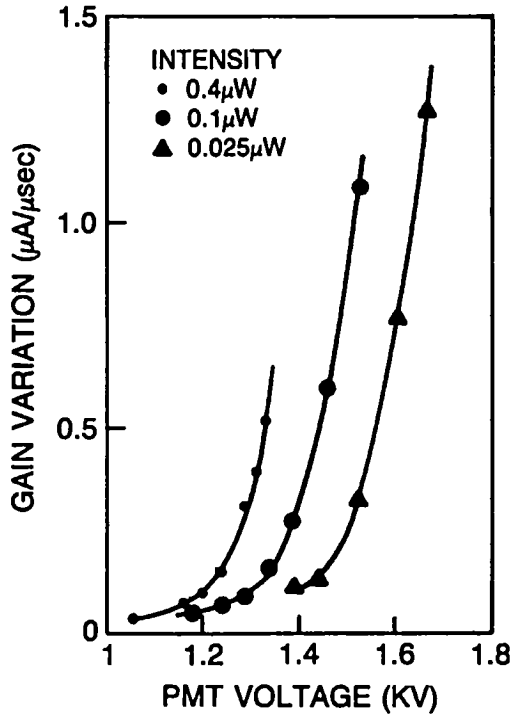

Figure 6-15. PMT gain variation vs. PMT voltage at various intensity levels.

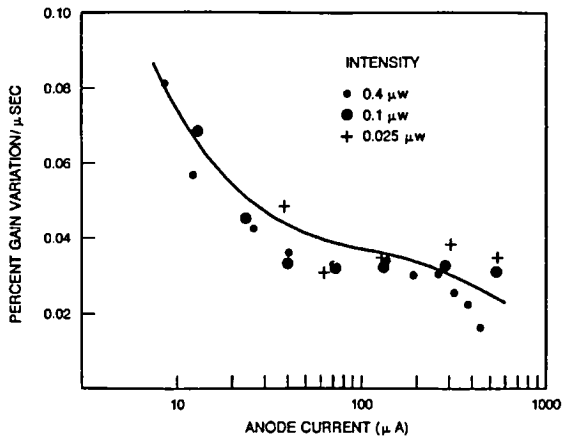

Figure 6-17. Percent gain variation vs. anode current at various intensity levels.

variation. Therefore, we expect less gain variation when there is less impurity gas available for the generation of ions. Note that the SIB amplitude will also be reduced for the low impurity ion flux, as evidenced by the much lower after-pulse amplitude of PMT-B when compared to PMT-A.

Detector Response Linearity

Since the signal intensity in a lidar measurement can cover several decades of dynamic range, it is important to operate the detector in the linear region. We have made a study of the linearity of PMT-B over a large dynamic range, employing a new technique described below.

The experimental technique used in this study consists of alternately introducing a neutral density filter into a light beam to produce two different intensity levels. The data are analyzed by taking the ratios of the PMT output signals for these two intensities. The data should have a fixed ratio for a linear system, as the source intensity level as well as the PMT voltages are varied. Therefore, deviations from a linear response will indicate a change in the measured PMT output ratio as the source intensity and the PMT voltage are varied.

The experimental setup shown in Figure 6-2 is used with different apertures on the chopper wheel. For this experiment, the apertures are enlarged to 1 mm width and 1 mm separation, and a nominal 50% neutral density filter is mounted on one of the apertures. As the chopper rotates, we generate two square pulses with two different intensities of 100 μsec duration and separation. Since the time between the pulse separation is short, this minimizes the low frequency noise components and improves the precision of the measurement. Any SIB from the first pulse is down to a negligible level by the second pulse. The source intensity is varied over six decades of dynamic range by inserting various neutral density filters in the common portion of the optical beam. In order to measure signals over such a large intensity variation with a 12 bit digitizer, we vary the PMT voltage. We measure the signal intensity as the average signal over the pulse duration, thereby averaging the gain variation discussed in the previous section.

For a linear PMT response, the ratio of the signals from the two apertures should be constant as the source intensity is varied. Indeed, the nonlinearity of the PMT response may be quantitatively characterized by measuring the deviation of this ratio from the value corresponding to low intensity and a low dynode voltage. The absolute calibration of the neutral density filter is not necessary in this technique.

In Figure 6-18, we plot the signal ratio as a function of the relative source intensity, which is determined from the optical density of the filters used to vary the source intensity. For a given source intensity value, the PMT dynode potential is also varied to study the effect of the anode current magnitude. The results for two different ranges of anode currents are depicted in Figure 6-18 by different symbols. This result clearly shows that the linearity of the PMT response is not only related to the input intensity, but also to the magnitude of the anode current. Linearity vanishes when the intensity exceeds a certain threshold, and the threshold is also a function of the anode current. The threshold intensity is high for a relatively low anode current (0.1 mW at 0.1 mA anode current). We note that the linear region is never reached for very large anode current (1 mA anode current, not shown in Figure 6-18). We ascribe any nonlinearity of the detector system to the PMT, since the anode current, which is the input signal to the preamp, is kept the same for the entire range of the light intensity variation.

Another important point to note in Figure 6-18 is the gradual increase in the ratio as the intensity decreases. The variation amounts to as much as 4% across three decades of intensity variation below 30 μW for the low anode current case. This calls for special attention when one deals with measurements over a large dynamic range. For many DIAL applications, measurements of 1% relative accuracy are desired. Figure 6-18 indicates that in order to achieve this, the PMT anode current should be kept below 0.4 mA over the two decades of intensity variation below 0.3 μW. Three or four decades of intensity variation below 30 μW can be accurately measured by keeping the anode current below 0.1 mA. For near-infrared wavelengths at intensities of 0.3 nW and below, photon counting techniques are advantageous due to the small signal.

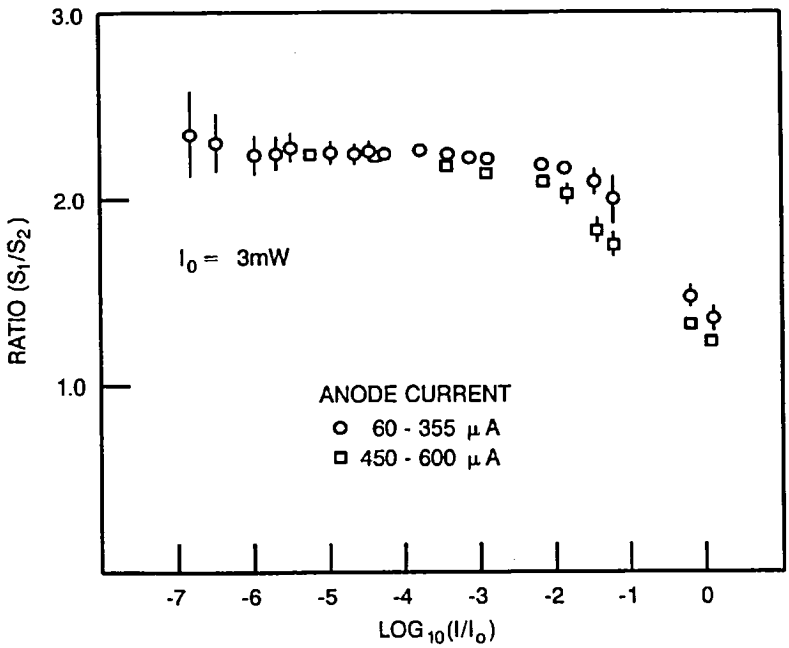

Figure 6-18. Ratio of two output signals corresponding to input intensities of I (S_1) and I/2 (S_2) as a function of input intensity, where full scale I_0 value is 3 mW.

SUMMARY

In this chapter, we have described the experimental setup and the results of a detector characterization study for the application of gated photomultiplier tubes used in a current integrating mode in DIAL measurements. A possible source of signal induced bias and gain variation is identified, and selection of an appropriate PMT configuration for minimizing the effect was made. The PMT linearity across six decades of input light intensity variation has been studied employing a new method which requires no absolute calibration. The peak light level and the anode current for linear operation of the PMT were established for lidar measurements.

It is concluded that the major portion of the signal induced bias and gain variation originate from impurity ions accelerated toward the cathode and subsequent electron emission from the cathode. These effects can be minimized by using a PMT with low impurity gas density in the tube and minimizing the voltage at the first dynode. A specific dynode configuration (box and grid type) may also be helpful in minimizing this effect due to the structural configuration of the dynode channel whereby the ion feedback may be decreased. A microchannel plate has also been studied in terms of SIB and linearity, and found not suitable for our application due to the dead time effect.

CHAPTER 7 PULSED LASER WAVEMETER DEVELOPMENT AND ALEXANDRITE LASER SPECTRAL CHARACTERISTICS

INTRODUCTION

The requirements for the spectral characteristics of the high resolution alexandrite laser used as the on-line laser in the P-T lidar have already been specified in the earlier chapters. The line width of the on-line laser is to be less than 0.001 cm^{-1}, the frequency stability is to be better than 0.0005 cm^{-1} over the duration of the experiment, and the spectral purity of the laser is to be greater than 99.9%. The requirements for pressure measurements, where the absorption is measured in the trough between two strong lines, are far less critical, and can be relaxed by a factor of 10 or more. When the laser contains multiple longitudinal and transverse modes, it is necessary that the detailed shape of the spectrum, *i.e.*, the mode locations and intensities, be known in order to derive a weighted centroid frequency. Hence a high resolution spectrum that is resolved sufficiently to show the detailed longitudinal and transverse mode structure of the laser output is required.

Spectroscopic measurements of the on-line pulsed laser are made on a shot-by-shot basis to determine its line shape, weighted mean frequency, and integrated out-of-band energy, *i.e.*, the spectral purity. A set of three instruments has been developed for measuring these quantities for the pulsed laser on a shot-by-shot basis. These are:

1. a 0.5 m grating spectrometer with a diode array readout for measuring the frequency to within 0.25 cm^{-1},
2. a high resolution wavemeter (0.0037 cm^{-1} resolution) which uses a Fizeau interferometer (5 cm plate separation and an 8 arc-sec wedge) to provide the line shape and relative frequency measurement to an accuracy better than 2.5×10^{-4} cm^{-1}, and
3. a multipass absorption cell (White Cell) filled with oxygen, or a long path atmospheric absorption measurement utilizing a target board placed at about 850 m from the laser.

These instruments were developed and modified considerably during the course of the evolution of the P-T lidar program to provide accurate spectroscopic measurements of the laser output and constitute a unique capability. In the first two sections of this chapter, we describe in detail the Fizeau wavemeter and the techniques used to reliably measure the frequency of multimode pulsed lasers when speckles or other spatial nonuniformities are present in the input to the wavemeter.

Measurements of the frequency of the etalon tuned alexandrite laser showed the presence of multiple longitudinal and transverse modes in its spectrum, and the laser frequency stability was not adequate in both the short- and long-term for DIAL temperature measurements. While the frequency jitter (*i.e.*, short-term frequency variation) was within tolerable limits for pressure measurements, the frequency drift (*i.e.*, the long-term variation) was unacceptably large. By measuring the temperature of various components in the laser, it was found that the frequency drift was primarily thermal in origin. Several modifications were made to the laser to improve the thermal stability of the laser, which in turn reduced the frequency drift to within acceptable limits for pressure measurements. Details of the measurements of laser frequency and the modifications made to the laser are presented in the third section of this chapter. Injection seeding with a frequency stabilized AlGaAs diode laser was utilized to achieve frequency stable operation of the on-line alexandrite laser. The fourth section presents the details of the spectral measurements of the injection seeded laser. The spectral purity of the injection seeded standing wave laser was found to be much lower than that required for temperature measurements. An injection seeded traveling wave ring laser that was developed

separately for providing a higher spectral purity was tested. In the last section of this chapter, we present the measurements of the spectra, frequency and spectral purity of the injection seeded ring laser.

HIGH RESOLUTION WAVEMETER

A novel laser wavemeter (Cotnoir, 1984) has been applied to the measurement of both the mean wavelength and the spectral profile of a line-narrowed alexandrite laser operating at PRF's in excess of 10 Hz. Wavemeters must be used as laser monitors in differential absorption lidar (DIAL) measurements of atmospheric pressure (Chapter 1), temperature (Chapter 2), and constituents (Browell, *et al.*, 1979, 1981) when there is a strict requirement for good spectral registry between absorption lines (*e.g.*, H_2O, O_2, and SO_2) and the output of a pulsed laser.

The effects of a finite laser linewidth and of deviations from the absorption line center on lidar measurements have been analyzed in Chapters 1 and 2 and by Megie (1980). In general, unless the emitted energy is contained within a few tenths of the absorbing linewidth, corrections to effective absorption will be required. In this case, it is necessary to know the exact wavelength of the laser emission and its spectral shape. For pressure and temperature profiling using the *A* band of O_2, these properties must be known with a frequency resolution in the range 0.001 cm^{-1} to 0.003 cm^{-1}, depending upon the circumstances of the measurement.

The shot-by-shot lineshape of the line-narrowed alexandrite laser is not well represented by a simple mode such as a Gaussian. Schwemmer, *et al.* (1987) have made observations of an alexandrite laser output that has three cavity modes asymmetrically spaced 0.011 cm^{-1} and 0.015 cm^{-1} from the central mode. The relative intensity of these modes also varies markedly from shot to shot. Our simulations indicate, however, that because each of these modes is spectrally narrow, the output of the laser can be approximated by a "stick model" consisting of the frequency of, and the integrated energy in, each active mode. In this case, each mode frequency must be known to 0.0005 cm^{-1} and the mode energies to a few percent. Chapter 13 includes a detailed error analysis of the laser line shape effects.

We have developed, in collaboration with the University of Maryland, an instrument to measure, in real time, the wavelength and lineshape of an alexandrite laser. Since it is intended for use in airborne experiments, it is compact and rugged (Figure 7-1). It fits into a standard EIA equipment rack, taking up only seven slots (22.5 cm). Optical input is via a fiber optic cable (50 μm core, graded index). Data and control pass to and from a main computer through a double width CAMAC (IEEE-583) module and up to 15 m of 52-conductor cable. In addition, reconstructed digitized data are made available on the front panel to drive an X-Y display or an oscilloscope. Figure 7-2 shows a photograph of the instrument with the cover removed.

The optical elements of the instrument (Figure 7-3) consist of a two-beam Fizeau wedge (Morris, *et al.*, 1984) (length 1 mm, wedge 3 arc-min, reflectivity 0.04) followed by a multiple-beam high resolution wedge interferometer (length 50 mm, wedge 8 arc-sec, reflectivity 0.92). The collimated beam from the off-axis parabola passes first through the two-beam wedge and then the multibeam wedge. The fringe pattern from each wedge is detected by a Reticon photodiode array having 1024 elements on 25 μm centers. If the two-beam wedge were replaced by a partial reflector and the multibeam wedge removed, the optical signal recorded by each photodiode array would be the same. Consequently, the speckle information from photodiode array 1 can be used to correct for the speckle on array 2. With the wedges in place, the speckle signal on array 1 is 100% modulated by a fringe pattern of frequency about 3 mm^{-1}. The speckle signal is seen to have a spatial frequency between 0.04 mm^{-1} to 0.4 mm^{-1}. Since the peaks of these fringes occur at a frequency more than twice that of the speckle signal, the latter can be reconstructed from these fringe data.

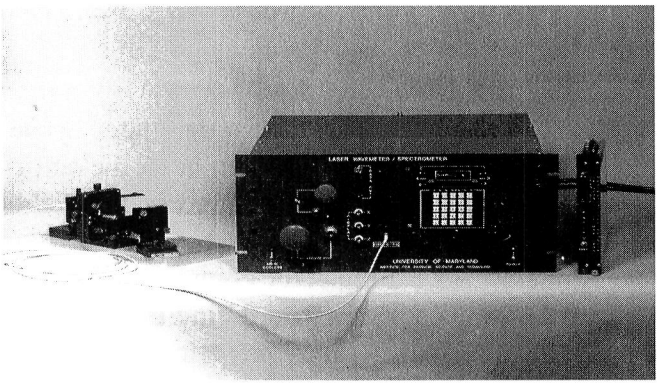

Figure 7-1. Photograph of the wavemeter in a standard EIA equipment rack. The keypad for controlling the operation of the wavemeter, the optical input and vacuum connections can be seen on the front panel.

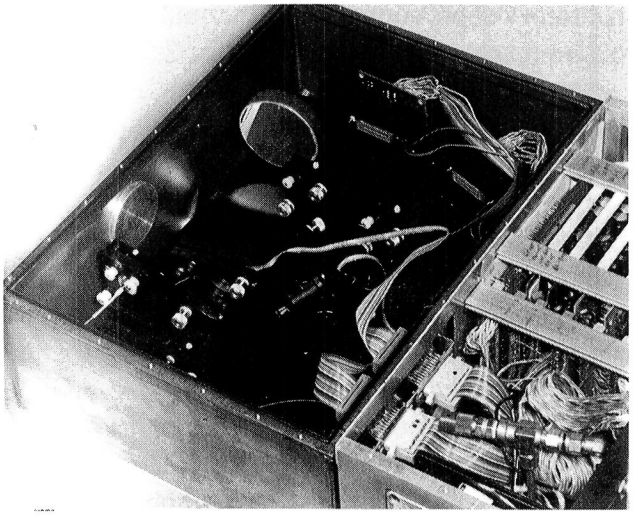

Figure 7-2. Photograph of the interior of the wavemeter showing the collimating optics, the two etalons, and the photodiode arrays.

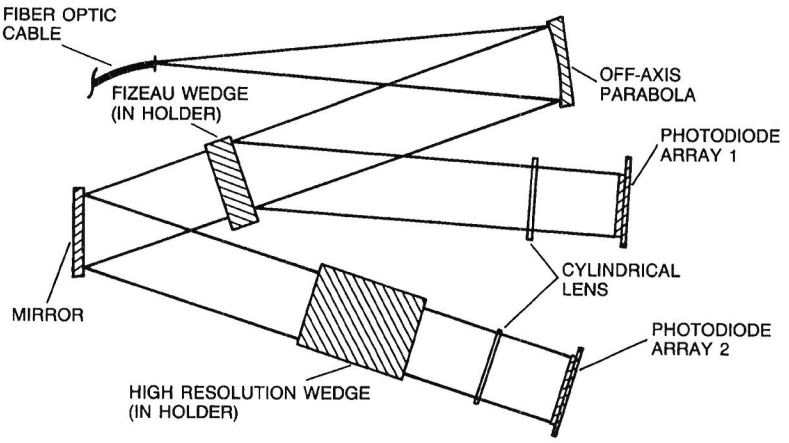

Figure 7-3. A schematic diagram of the optical layout of the wavemeter.

The centroid of the wavelength of the laser output is computed from the two-beam wedge fringe pattern using a modification of Snyder's algorithm (Snyder, 1980). We have found it necessary to have an *a priori* knowledge of the laser frequency to about 2 cm^{-1} to determine the order of interference in the wedge. We can then compute the centroid frequency to about 0.005 cm^{-1}.

The multibeam wedge has a free spectral range of 0.1 cm^{-1} and an optical resolution of 0.0037 cm^{1}. It modulates the transmitted beam with a signal corresponding to the lineshape (and wavelength) of the laser. The laser line shape is observed directly on photodiode array 2. In order to properly interpret the results, it is necessary to correct the observed line shape for the 8% modulation remaining from the first (two-beam) wedge and for the laser speckle. The absolute frequency of the laser can be measured to the accuracy of the calibration source, about 0.001 cm^{-1}. The wedge angle of this interferometer is chosen such that each photodiode corresponds to a spectral increment of 0.00025 cm^{-1}. The stability of the wedge under ordinary

laboratory conditions (*i.e.*, no thermal controls) is 1 part in 10^6 over a period of 130 minutes. This corresponds to a temperature variation of about 2 K.

The advantage in using a two-beam wedge in combination with the multibeam one is that the plates of the former are uncoated and thus free of the reflection phase shift dispersion observed in multilayer dielectric coatings (Baumeister and Jenkins, 1957). This dispersion, unless corrected, can cause large errors in the measurement made with the multibeam wedge. This is especially apparent if the dispersion is expressed as a change in the effective length of the interferometer. In our instrument, for example, the computed length of the wedge is 5.002 ±0.005 cm at 13160 cm^{-1} and 5.0047 ±0.0001 cm at 13125 cm^{-1}. Using the centroid wavelength measured by the two-beam (dispersionless) wedge, the effective length of the multibeam wedge can be obtained from a calibration table and the necessary correction made. However, due to the multi-spatial mode output of the alexandrite lasers, the absolute wavelength measurement of the two-beam wedge often had errors of one or more free spectral ranges. Consequently, this wedge was removed from the wavemeter and a grating spectrograph was used to detemine the absolute wavelength.

LASER WAVELENGTH MEASUREMENT IN PRESENCE OF SPECKLE

If the light input to the wavemeter contains speckle, the fringe pattern produced by the Fizeau wedge is modulated by the speckle field. Thus, the line shape and wavelength obtained from the fringe patterns will be erroneous. We present the results of an investigation of measuring the frequency of a multi-mode continuous He-Ne laser and also of a pulsed alexandrite laser with a Fizeau wavemeter when speckle is present.

Figure 7-4 shows the schematic layout of the wavemeter utilized for our experiments. The high resolution multibeam Fizeau etalon used in the wavemeter has a wedge angle of 8 arc-sec and coated plates (92% reflectivity) spaced by 5 cm. The output fringe pattern from the Fizeau etalon falls on a 25 mm wide 1024 element silicon photodiode array. During normal operation, the output of the alexandrite laser contains mainly three longitudinal modes and several transverse modes (Schwemmer, *et al.*, 1987). In view of the multilongitudinal and transverse mode nature of the laser output, it is necessary for any measurement of its frequency to ensure that the laser light input into the wavemeter contains all the component modes in their original proportions. Because the beam propagation characteristics of each mode are different, the input optics have to accommodate the full range of beam divergences present.

Laser light is input through a 50 μm core graded-index optical fiber and is collimated by an off-axis parabolic mirror before being incident on the Fizeau etalon. This multimode optical fiber acts both as a 50 μm pinhole and as a mode scrambler for the laser spatial modes so that the light incident on the Fizeau etalon contains all the spatial modes of the laser. However, the use of the optical fiber introduces speckle in the output from the fiber. Speckle elements of varying sizes ranging from 2.5 to 10 mm are present in the collimated beam, with the result that the intensity of light incident on the 25 mm aperture of the Fizeau etalon is highly nonuniform. Also the intensity distribution of the speckle field is quite random because the number, size and the intensity of speckle elements all change for every position of the optical fiber cable. Figure 7-5 shows photographs of the light intensity distributions incident on the etalon for three arbitrary positions of the optical fiber. Figures 7-6a and 7-6b show the effect of the speckles on the spectrum produced by the Fizeau etalon. From these figures it is easy to see that any attempt to obtain either the centroid frequency or the relative energy of the laser modes would be grossly inaccurate. There are other approaches to spatially mix the laser modes, such as an integrating sphere or a diffuser. However, even in these situations, speckle is generated.

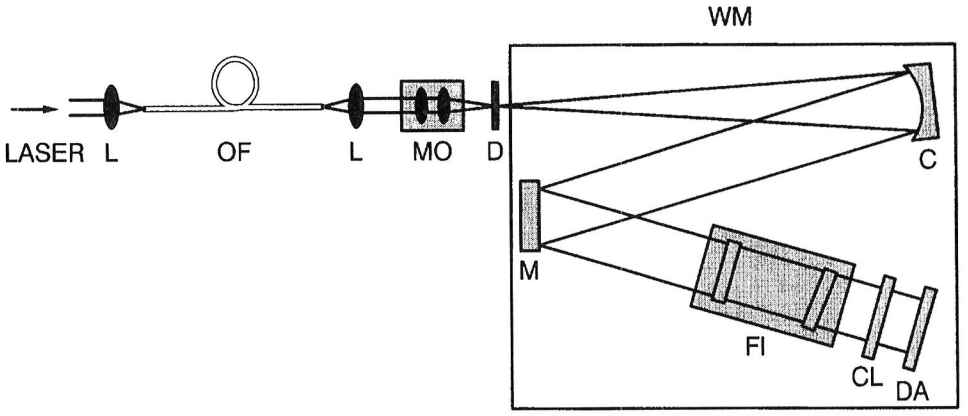

Figure 7-4. Schematic of the experimental setup. The laser beam is coupled using a lens (L) into a multimode optical fiber (OF). A microscope objective (MO) focuses the beam onto a pinhole. Subsequently a thin diffuser (D) was attached to the pinhole to reduce the effect of speckle. Within the wavemeter (WM), an off-axis parabolic mirror (C) collimates the beam which is reflected by a mirror (M) and is incident on the Fizeau etalon (FI). The output of the etalon is focused on a photodiode array (DA) with a cylindrical lens (CL).

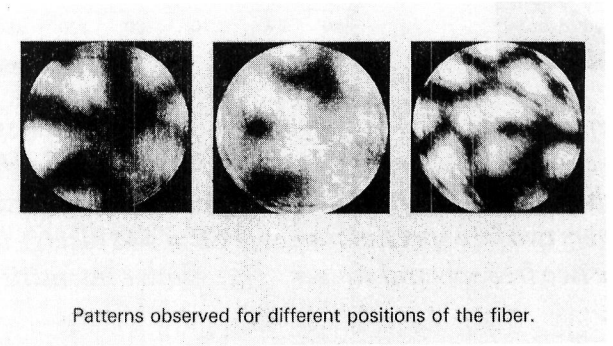

Patterns observed for different positions of the fiber.

Figure 7-5. Photographs of the light intensity distribution resulting after a He-Ne laser beam is propagated through the multimode optical fiber. Photographs of the collimated beam were taken at the input to the Fizeau etalon (FI) using the setup shown in Figure 7-4. The pictures show speckle sizes and distributions resulting from three slightly different positions of the optical fiber.

It may be noted that the size of the speckle in the collimated beam from the optical fiber is on the order of the same size as the spatial extent of the fringe pattern in a free spectral range (~10 mm) for our Fizeau etalon. Our approach to make the laser spectral measurement less sensitive to the spatial position of individual speckle elements consists of a method for reducing the speckle size and increasing their number. We have found that a thin diffuser is well suited to accomplish this. Conventional diffusers, such as ground glass and diffuse opal plastic screens, are fairly thick and can be considered as a random three dimensional array of apertures or scatterers. Light scattered by a thick diffuser is spread over a large angle which makes it difficult

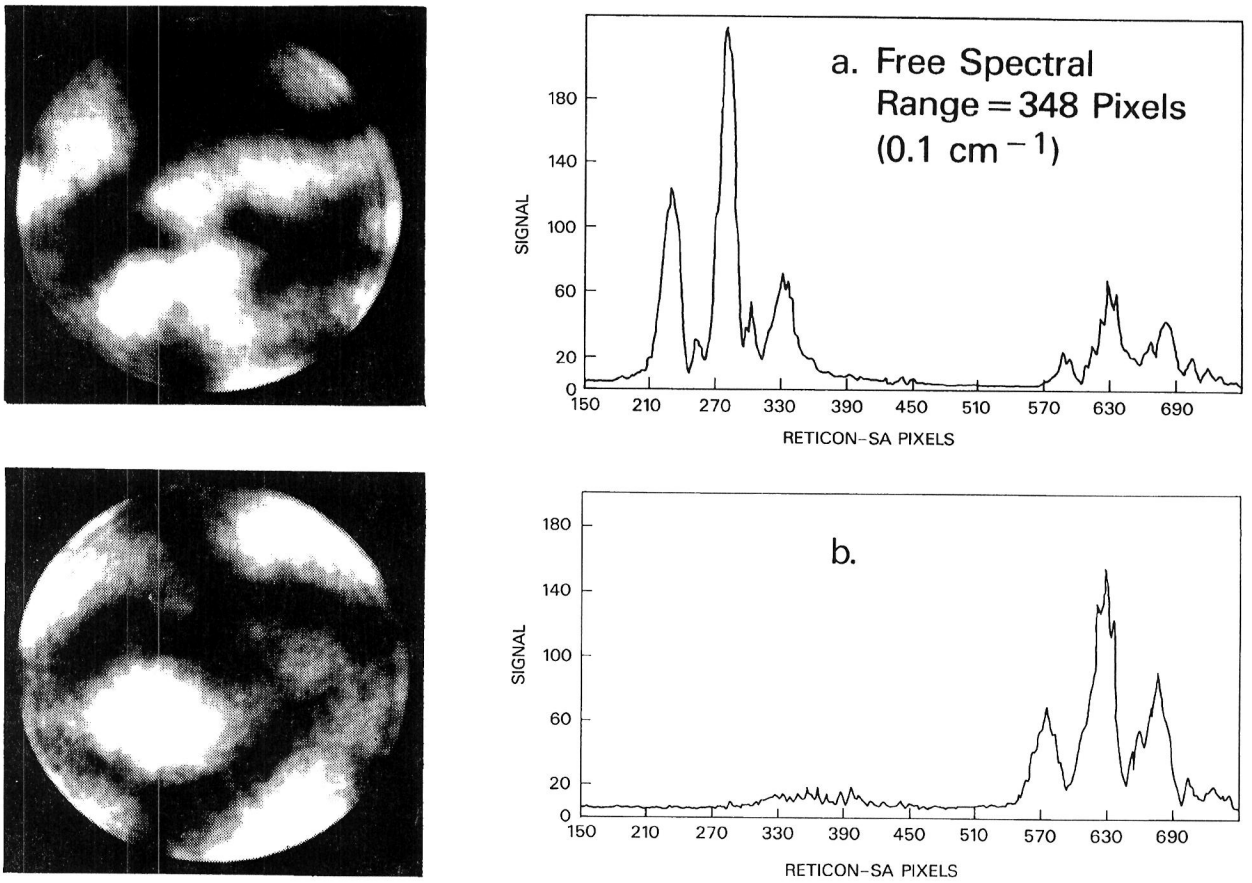

Figure 7-6. The consequences of the speckle from the optical fiber on the spectrum are demonstrated in the figure. The Fizeau etalon spectrum of a three longitudinal mode He-Ne laser measured with the photodiode array is shown on the right and corresponds to the intensity distributions shown on the left. The spectrum covers two free spectral ranges (FSR = 348 pixels), and we see vast differences between the spectra in the two free spectral ranges. The relative intensities of the three longitudinal modes are also different.

to collect and collimate the scattered light. On the other hand, a thin diffuser such as a roughened mylar film consists essentially of a two dimensional array of scatterers. A large fraction of the light scattered by a thin diffuser is confined to a smaller forward angle, in comparison to the thick diffuser. Hence, it can be collected easily and results in an increased throughput.

In our experiments, the light from the optical fiber is collected by a fast lens and taken to a spatial filter consisting of a 10x microscope objective and a large (50 μm) pinhole, and collimated by an off-axis parabolic mirror, as shown in Figure 7-4. The thin diffuser, which is a 60 μm thick roughened opal mylar film, is placed next to the pinhole. By slightly varying the position of the diffuser near the focus of the microscope objective, the size of the speckle in the collimated beam can be varied from about 25 mm to as small as 0.25 mm. Figure 7-7 shows the speckle patterns produced by the thin diffuser. The thin diffuser can be considered as consisting of an array of apertures or scatterers of 3 to 4 μm size. The smallest size of speckle used was about 0.25 mm. This limit was set by the greatest displacement of the diffuser from the focus that was still able to produce a well collimated beam for the Fizeau etalon. Further displacement of the diffuser tended to degrade the quality of the fringes produced by the Fizeau etalon, because of the reduction in the finesse (~35). For this condition, the beam spot size at the diffuser is fairly large (>100 μm), and a pulse

energy of about 1 μJ is required for the spectrum to be detected with an acceptable *S/N* ratio at the diode array detector, which corresponds to an energy density of the beam spot of 0.01 J/cm^2.

Reducing the size of the speckle caused orders of magnitude improvement in the variance of the spectra, but significant variance in the centroid frequency computed from the spectra is still present. The variance introduced by the speckle was further reduced by integrating the light from the etalon in the vertical direction along the length of the fringes. Although a cylindrical lens can be used to accomplish this, there is considerable room for error because the size of the detector (25 μm high by 25 μm wide) calls for very accurate positioning of the lens and detector array, and also for an aberration-free lens. An array with elements that are 2.5 mm high is more convenient to use.

For the pulsed laser experiments presented here, the Fizeau wavemeter spectra were detected by the diode array. The output of the array was digitized and sent to the pressure-temperature lidar data system where it was acquired on a shot by shot basis and stored along with other data from the lasers. The details of the pressure-temperature lidar data system have been given previously. Spectra from the CW He-Ne laser were also acquired in a similar manner, except that the light falling on the detector array was integrated for a short duration (100 to 200 ms). The centroid frequency of every shot, its variance, as well as the relative intensities of the different fringes (corresponding to the different modes) present in any free spectral range and their variance were computed. After a preliminary series of experiments with a three mode He-Ne laser, the pulsed high resolution alexandrite laser was used for the rest of the experiments.

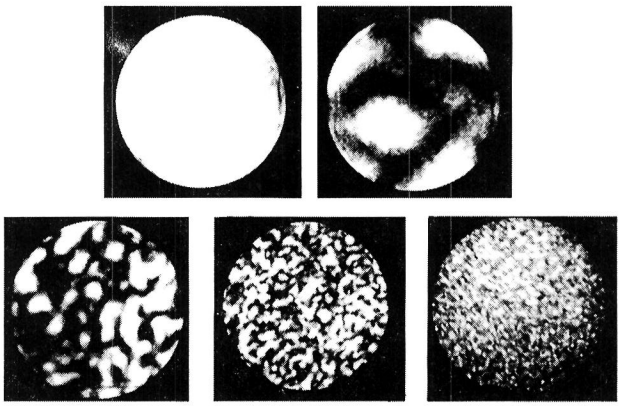

Figure 7-7. A thin diffuser (roughened mylar plastic film) attached to the pinhole D (see Figure 7-4) is used to modify the speckle size. Photographs of the collimated beam show successively smaller speckles. Picture at top left shows a single speckle element that is obtained when the diffuser is placed at the focus of the microscope objective. As the diffuser is moved away, successively smaller speckles are obtained.

Figures 7-8a and 7-8b show two He-Ne laser spectra taken with the thin diffuser and the large array detector. It is seen that in Figure 7-8a the speckle size is larger than that in Figure 7-8b. It was found that the variance in the centroid frequency, which was of the order of the spacing between the laser modes without the thin diffuser, reduced to less than 10% of the spacing when the thin diffuser and vertical integration were utilized. With the speckle size reduced to 0.25 mm (see Figure 7-9), the variance in spectra was found to be about 7%. Because the speckle patterns change randomly with any displacement of the diffuser, further improvement is achieved by averaging the signal over a number of measurements where the diffuser was moved in its own plane between two measurements. Figure 7-9 shows the spectrum of the same laser as in Figures 7-8a and 7-8b, but here the speckle size is 0.25 mm and 20 spectra are averaged. The variance in spectra was found to be about 3%. Variance in relative mode energies, which were as high as 100% with the optical fiber alone, were reduced to below 20% with the thin diffuser and vertical integration. Averaging improved this number further to less than 12%.

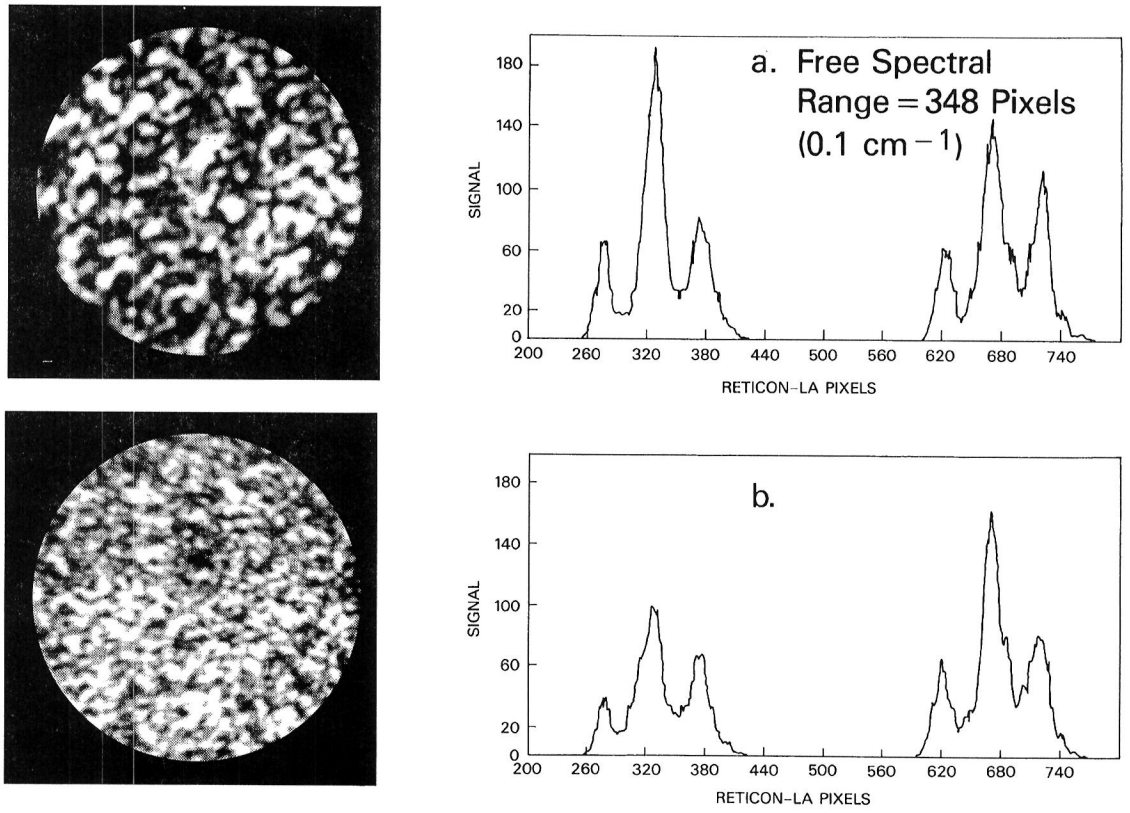

Figure 7-8. Effect of reducing the size of speckle elements is seen in the two spectra of the three mode He-Ne laser. As in Figure 7-6, the intensity distribution of light incident on the Fizeau etalon is shown on the left, and the resulting spectrum on the right. Here the speckle size is much smaller than that in Figure 7-6, and the fringes are integrated in the vertical direction by using a 2.5 mm high photodiode array. In Figure 7-8 the speckle size is smaller and the spectrum has much less variance.

An infrared sensitive film was used to photograph the pulsed alexandrite laser intensity distribution in the collimated beam incident on the Fizeau etalon. Figure 7-10 shows one such photograph where the speckle reduction technique has been incorporated. Figure 7-11 shows a photograph of the fringes formed by the Fizeau etalon, from a single alexandrite laser pulse, while Figure 7-12 is a typical spectrum of the injection seeded pulsed alexandrite laser taken with the Fizeau etalon after incorporating the speckle size reduction.

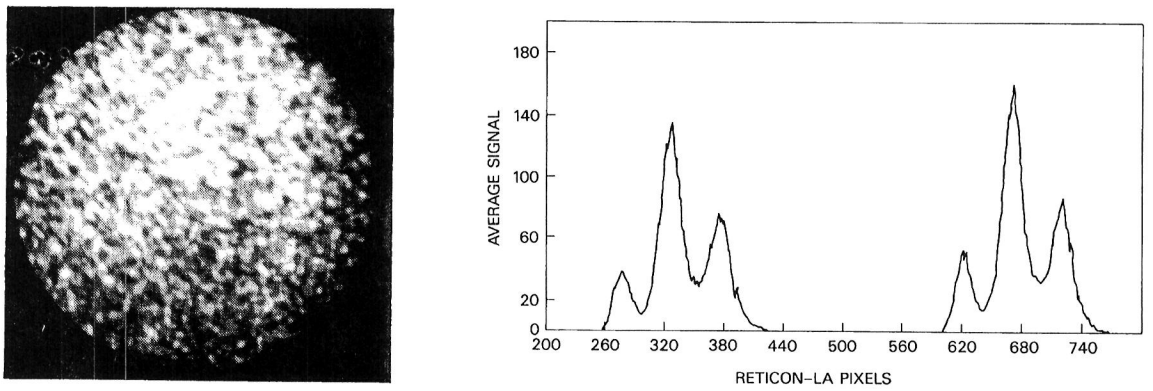

Figure 7-9. Speckle pattern and the spectrum of a He-Ne laser for the smallest speckle size. The average of 30 spectra is shown on the right.

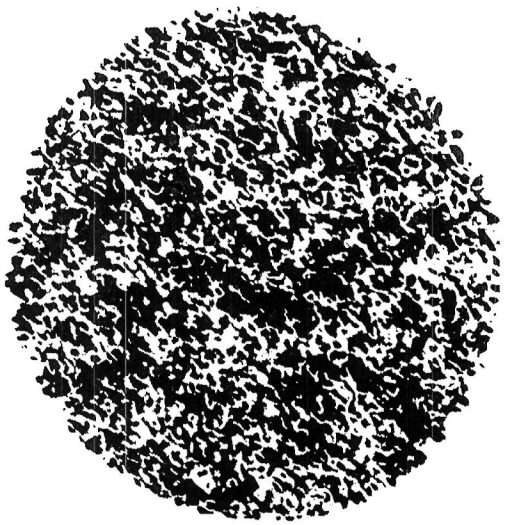

Figure 7-10. Photograph of the collimated beam from a Q-switched alexandrite laser. The photograph was made on an infrared film and is of a single shot of the laser after it was passed through the thin diffuser and collimator.

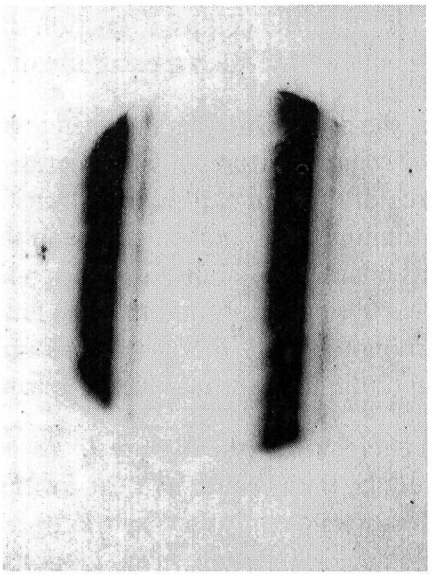

Figure 7-11. Photograph of the Fizeau fringes from the spectrum of an alexandrite laser.

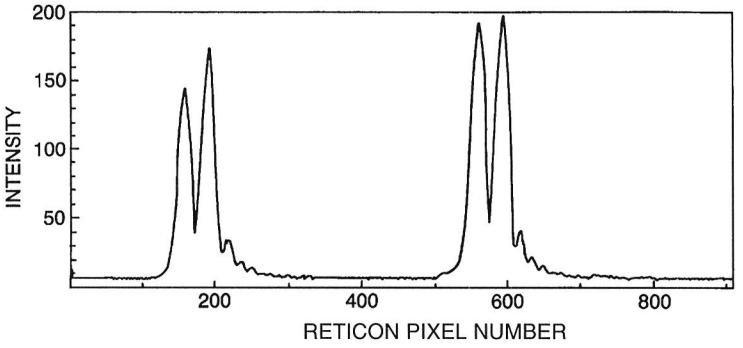

Figure 7-12. Single-shot spectrum of an injection seeded alexandrite laser as measured by the photodiode array.

ETALON-NARROWED ALEXANDRITE LASER FREQUENCY STABILITY

A series of measurements of the on-line alexandrite laser frequency was performed using the wavemeter, after mixing the spatial modes of the laser with a diffuser. Speckle produced by the mixing causes serious problems in obtaining the spectra. The effect of speckle on the wavemeter spectra was reduced by incorporating the techniques described above. Figure 7-13 shows a time series of the location of the centroid of the laser output spectrum measured by the wavemeter. The centroid position is calculated as a pixel location. This location is converted into a relative frequency by noting that each free spectral range of the Fizeau etalon (0.1 cm^{-1}) is spanned by 401 pixels, which means each pixel corresponds to about 0.000249 cm^{-1}. An examination of the figure shows the presence of both short and long term variations of frequency. The short-term instability was found to be a shot to shot frequency jitter, with a standard deviation of 0.004 cm^{-1}, in addition to a slower variation that is due to a drift. A long-term measurement of the laser frequency was performed by using a long path absorption cell containing oxygen. The laser frequency was tuned to the edge of an oxygen line where the absorption changes steeply with small changes in frequency. By monitoring the transmission of the cell as a function of time, the change in laser frequency is determined. Figure 7-14 shows the result of one such measurement, and it shows clearly a monotonic drift in laser wavelength.

To examine the possibility that this drift is of a thermal origin, the temperature of each of the optical elements of the laser was monitored using thermocouples and a data logger. Figure 7-15 shows the measured temperatures of the thin etalon, the birefringent tuner, the output coupler mirror and a copper block placed inside the tuning optics enclosure. Each time the flashlamps were turned on or off the temperature of the components changed by about 2 K. Such large changes in temperature result in major changes in the output wavelength. It was also found that the temperature of the tuning elements housed in the optical enclosure tended to monotonically increase by as much as 1 to 2 K/hr during continuous operation of the laser that contributed to the long term frequency drift.

The optics enclosure of the high resolution alexandrite laser is of invar construction and is insulated on the inside to reduce the transfer of heat from the laser pump chamber. Electric heaters are placed inside the optics enclosure and controlled by a temperature regulator to maintain a constant elevated temperature in the optics enclosure. Since our investigations showed that the temperature regulation was not adequate, the thermal behavior of the enclosure was analyzed in detail and modified.

Several modifications were made to improve the thermal stability of the optics enclosure. The thermal mass of the enclosure was increased significantly by the addition of copper blocks. This increase in thermal mass serves to reduce the temperature excursions. Thermal insulation for the optics box was improved, and the convection of hot air from the heated pump chamber was prevented. Cooling jackets were attached to the pump chamber housing to reduce heat transfer to the optics enclosure. A more effective temperature regulator was used to control the heaters embedded in the walls of the optics enclosure, and the temperature set point was increased to maintain adequate control.

A continuous dry nitrogen purge of the laser head is required to displace the oxygen from the optical path in the laser, which would otherwise suppress lasing at the center of the oxygen absorption lines. The purge gas was preheated to the temperature of the optical enclosure before being admitted into the enclosure. The preheated gas flow is directed across the optical elements and exits from the optics enclosure to the pump chamber and the rest of the laser head. Significant temperature gradients can exist between the etalons and the enclosure, since the optical mounts and the etalons have a high thermal resistance. The purge gas flow reduces these gradients and also effectively limits the convective flow of gases from the pump chamber into

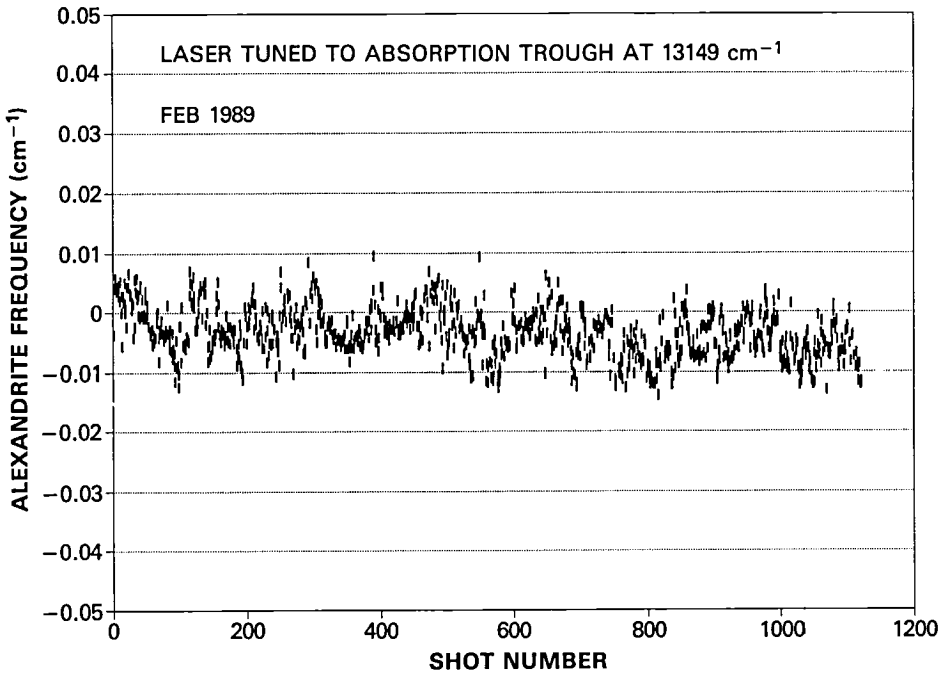

Figure 7-13. Short-term frequency stability of the etalon line-narrowed alexandrite laser. This figure shows the location of the centroid as a relative frequency on the photodiode array that is used to detect the fringes produced by the Fizeau etalon. The horizontal axis spans 2 min. The standard deviation of frequency is 0.004 cm^{-1}.

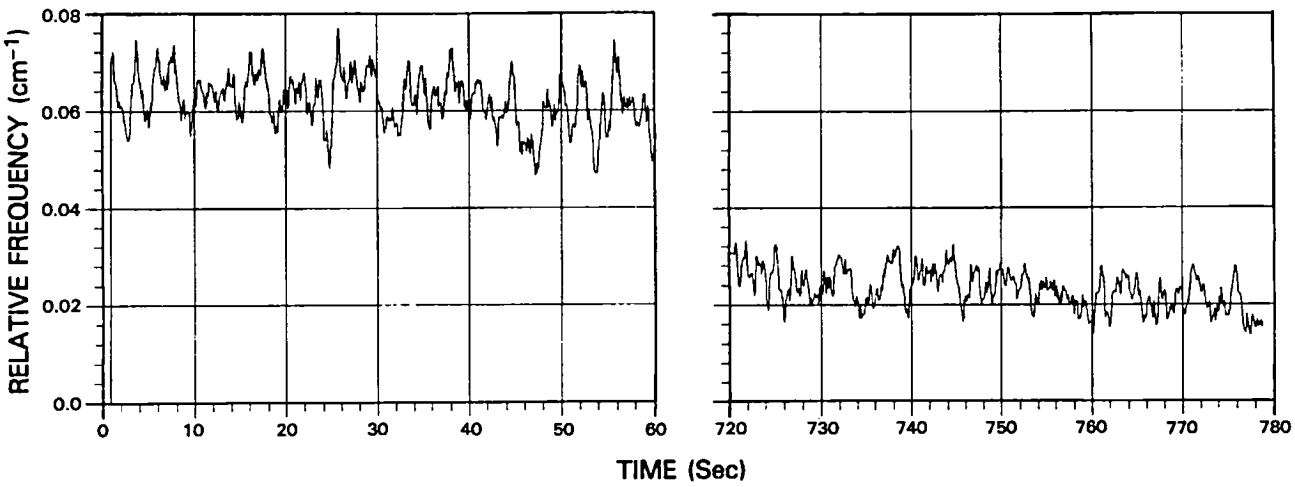

Figure 7-14. Long-term frequency stability of the etalon line-narrowed alexandrite laser, showing the monotonic drift of the measured frequency. This drift was caused by the temperature change of the laser tuning optical components. The transmittance of the laser through a multipass gas cell while tuned to the edge of an absorption line was used to determine the frequency stability.

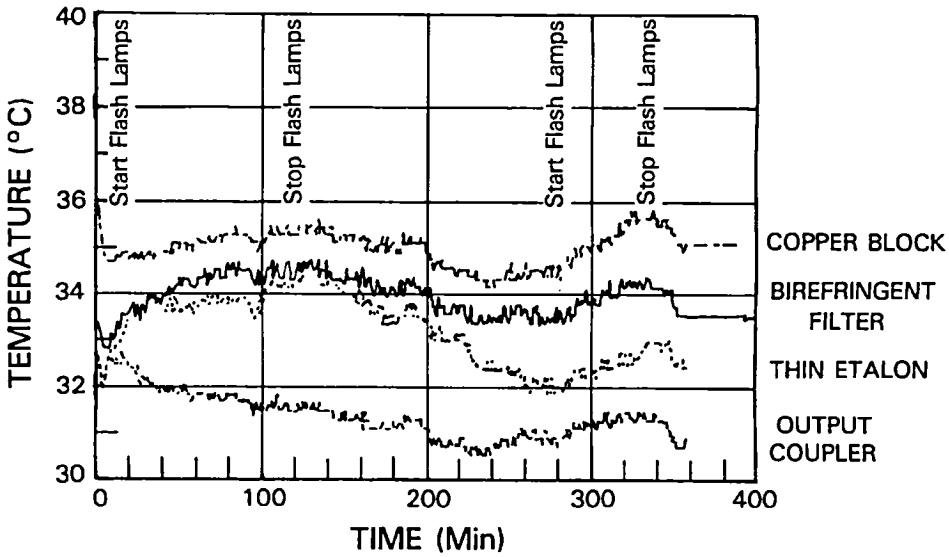

Figure 7-15. Temperature of the laser frequency tuning optical components: the thin etalon and the birefringent filter, and a copper block placed inside the tuning optics enclosure, measured before any modifications were made. The large temperature fluctuations observed show poor thermal stability and inadequate temperature control. The transients indicated on the figure are: turning on the flashlamps after 10 min and 280 min, and turning off the flashlamps after 120 min and 340 min.

the enclosure which can cause significant perturbations. A photograph of the laser head is shown in Figure 7-16, and shows the modifications that were incorporated into the laser.

The pressure-temperature lidar was placed on board the NASA Electra aircraft and several aircraft flights were carried out during May-June 1989, for measurements of the atmospheric pressure field with the lidar looking down from the aircraft. Only the birefringent filter and the thin etalon were used for the pressure measurements, yielding a frequency bandwidth of 0.08 cm^{-1}. With the above modifications, the passive frequency stability of the laser was found to be adequate for the pressure measurements. Figure 7-17 shows the measured temperature of frequency tuning components during one aircraft flight. For these flights the etalon temperature was maintained constant to within ±0.1 K over the entire flight (~2 hr), which translates to a frequency stability of $\pm 5 \times 10^{-4}$ cm^{-1}.

Any further improvements in the long-term frequency stability require an active stabilization technique. The wavemeter can be used to measure the laser frequency and also serve as a feedback element to correct for laser frequency changes. The layout of this scheme is given in Figure 7-18. An error signal is generated by comparing the laser frequency with a stable reference frequency. The error signal is applied to the high resolution piezoelectric etalon to change the etalon spacing by an appropriate amount. The sequence of operations of the feedback system is as follows: the lidar system computer initializes the wavemeter and triggers the laser, the fringe data from the wavemeter are acquired, and the centroid frequency of the laser is computed. An error signal is generated by referencing the centroid frequency to that of a stable source, such as a stabilized He-Ne laser, and averaging over a number of shots. A correction voltage corresponding to the error is applied to the piezoelectric etalon. The crucial components required for this scheme, such as a technique for measuring the laser frequency in the presence of speckle (described above), an optimal algorithm

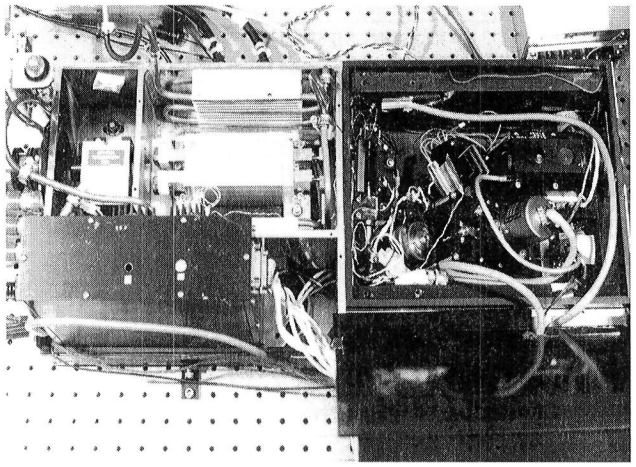

Figure 7-16. The photograph shows the Alex II laser head with its three main enclosures. The enclosure on the left contains the Q-switch, and the pump chamber is in the middle. Water jackets were added to reduce heat flow to the optical enclosure on the right. The thin etalon, the birefringent filter (BRF), and the PZT etalon are in this enclosure. Copper blocks are attached to the walls to increase the thermal mass. The temperature controller utilizes the sensor attached to the BRF. Ten thermocouples monitor the temperature of the components.

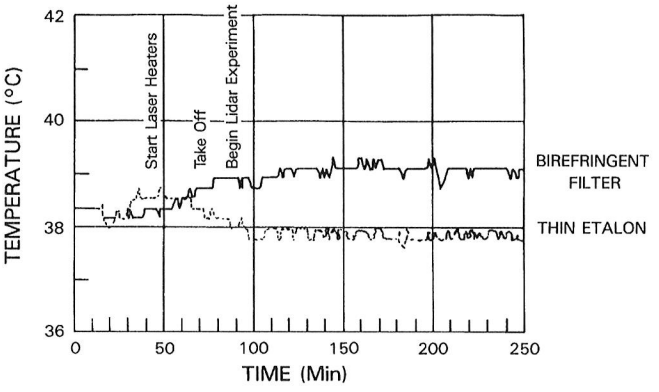

Figure 7-17. Temperature of the thin etalon and the birefringent filter, measured during the aircraft flight experiment of the pressure-temperature lidar on June 11, 1989. The thermal stability has been improved by making modifications to the laser. It may be noted that the flashlamps were turned on at the 50 min mark, and the temperatures have stabilized at the 100 min mark.

for determining the centroid of the laser frequency in real time, and the necessary hardware for converting the error signal to a voltage, have all been developed.

Figure 7-19 shows the flow diagram of the algorithm developed for determining the centroid frequency from the spectrum measured by the Fizeau wavemeter. The component modules were all optimized to rapidly process the digitized output, and determine the following:

1. the baseline, which includes any stray light and broad band laser emission,
2. any pixels that show signal saturation,
3. the location of peaks and subsequent grouping into their respective orders (free spectral ranges): note that there are fringes corresponding to two or three different orders,
4. the group of fringes belonging to the same order and in the center of the aperture and not truncated, and
5. the centroid of the fringe group.

The algorithm has been tested with both CW and pulsed laser spectra and has determined the correct centroid frequency under almost all possible observable conditions. When the full routine is implemented on a 33 MHz 80386 processor IBM PC, the cycle time was under 35 ms, which is adequate for real time operation at 10 Hz.

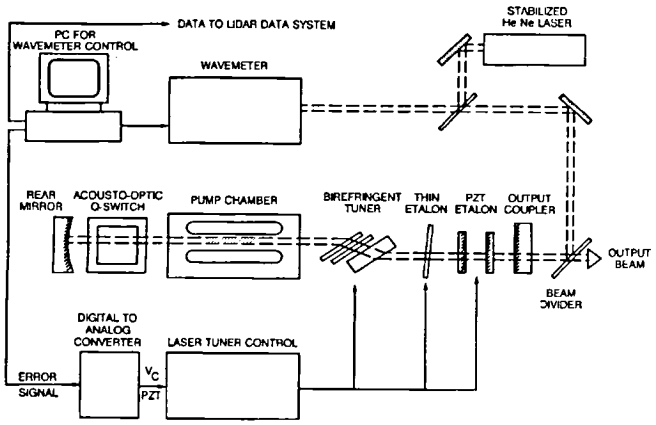

Figure 7-18. Schematic layout of the high resolution etalon-narrowed alexandrite laser incorporating the wavemeter for frequency stabilization. The digitized signal from the photodiode array in the wavemeter is acquired by the PC. An error signal generated by comparing the computed centroid frequency with that of the reference (He-Ne laser) is applied to the PZT etalon.

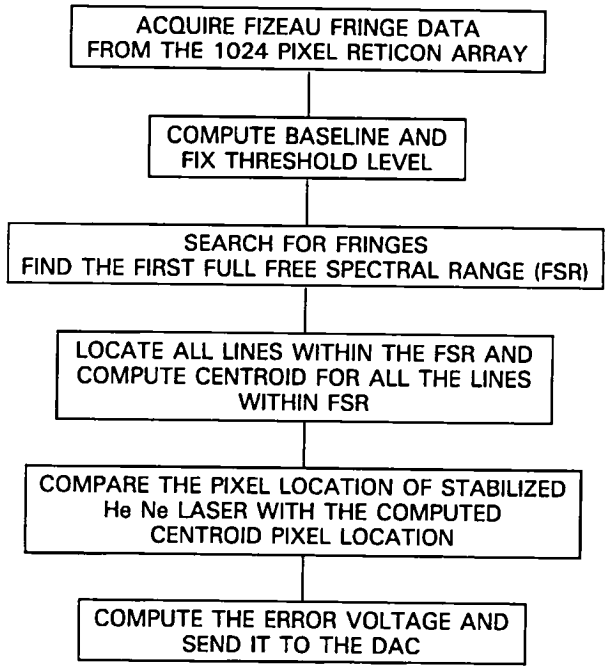

Figure 7-19. Flow diagram of the algorithm implemented for real time computation of the centroid frequency of the 10 Hz high resolution alexandrite laser. The last two modules are used to determine the feedback error signal to stabilize the frequency of the etalon-narrowed alexandrite laser.

INJECTION SEEDED ALEXANDRITE LASER FREQUENCY STABILITY

In this section, we present the results of measurements of the frequency stability and the spectrum of the injection seeded alexandrite laser.

In the preceding section frequency measurements of the etalon-narrowed laser with the Fizeau wavemeter show that its frequency stability is marginal for temperature measurements. We achieved an RMS frequency jitter of ± 0.004 cm^{-1}, but we require a maximum variation of ± 0.005 cm^{-1} for low altitude airborne or ground-based lidars, and ± 0.0005 cm^{-1} for high altitude airborne or spaceborne lidars. In light of this observation, injection seeding as an alternate approach to frequency tuning, controlling the linewidth, and stabilizing the frequency was implemented on the high resolution alexandrite laser.

The high resolution spectra of both the diode and the alexandrite laser were obtained with the wavemeter. As mentioned previously the optical resolution of the wavemeter is 0.0033 cm^{-1} (100 MHz), the detector element spacing is 2.5×10^{-4} cm^{-1}, and the wavemeter has a drift of <0.004 cm^{-1}/hr. Figure 7-20 shows a single shot injection seeded alexandrite laser spectrum taken by the wavemeter. Typically the spectral bandwidth of the laser diode is about 0.0073 cm^{-1} (220 MHz), and since the longitudinal modes of the on-line alexandrite laser are spaced at about 0.007 cm^{-1}, its output contains two modes on the average. Figures 7-21 and 7-22 show the variation of the centroid frequency with time. On examining Figure 7-21, it is seen that when the diode laser is stabilized, the alexandrite laser frequency is held constant to within ± 0.002 cm^{-1} of the line center, an improvement by a factor of two over the etalon-narrowed laser frequency jitter (Figure 7-13). The long term

drift matches that of the diode seed laser, which is about 100 times better (Figure 7-20) than the passively stabilized cavity (Figure 7-14).

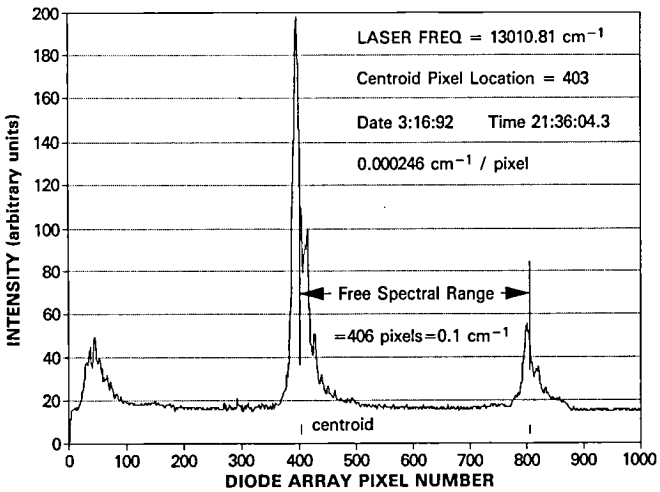

Figure 7-20. Fizeau wavemeter spectrum of injection seeded alexandrite laser.

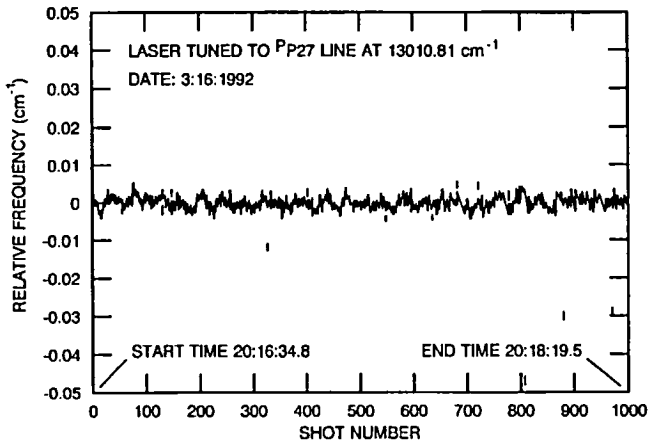

Figure 7-21. A time series of the centroid frequency of the injection seeded alexandrite laser. The injection seed diode laser is feedback stabilized by a photoacoustic absorption cell containing oxygen. Laser pulse repetition rate is 10 Hz.

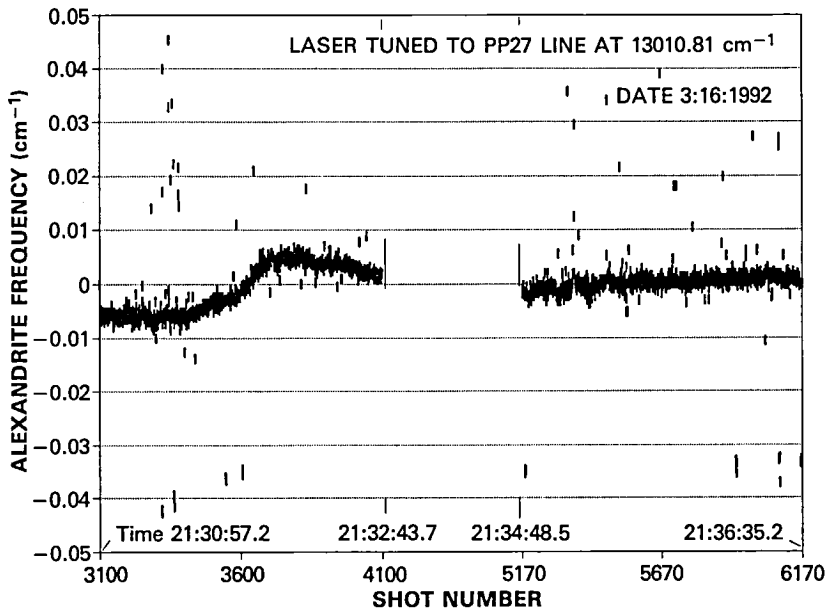

Figure 7-22. Same as in Figure 7-21, except that the injection seed diode laser is not feedback stabilized. Data was not recorded for the 2 min gap in the center.

On the other hand, when the diode laser is not feedback stabilized, frequency variations of ± 0.005 cm^{-1} are seen over periods of the order of a few minutes. These variations correspond to the accuracy and stability of the diode laser current supply (0.01 mA) and temperature control (0.1 K). It is also observed that there are a few isolated shots whose frequency is grossly different. These shots correspond to situations where the seed laser has either suffered a mode hop or the seeding is ineffective. During an extended experiment, the wavemeter is used to analyze the spectrum of every shot, and this provides an effective means for detecting shots which are improperly or imperfectly seeded.

The spectral purity of the injection seeded laser has been investigated. An examination of the spectrum of the 30 mW seed laser revealed the presence of weak lines on either side of the principal central mode, at a mode spacing of about 2.88 cm^{-1}. The power in the two modes adjacent to the principal mode was about 0.3% at a diode drive current of 130 mA. The side modes can also seed the laser, since they are within a half-width of the band pass of the birefringent filter tuner, and the output corresponding to the side modes constitutes a spectrally impure output. The spacing between longitudinal modes is about 5 cm^{-1} for the 3 mW diodes, and, as can be expected, the tendency for seeding on the side modes of the diode is reduced considerably with the 3 mW diodes. As mentioned earlier however, the power available with a 3 mW diode is barely adequate for seeding. Therefore, an external etalon is needed to suppress the intensity of the 30 mW diode laser side modes to below 0.05% before it is used to seed the alexandrite laser.

SPECTRAL PURITY

Spectral impurity is a major source of experimental error in DIAL measurements (Cahen and Megie, 1981; Ehret, *et al.*, 1993; Ismail and Browell, 1989; Theopold and Bosenberg, 1993). By injection seeding a standing wave alexandrite laser with a stabilized diode laser, the required frequency stability and spectral bandwidth were achieved. However, a significant amount of out-of-band radiation was present, giving a spectral purity of $\leq$94%. To improve the spectral purity, a traveling-wave, three-mirror ring alexandrite laser was integrated into the Pressure-Temperature lidar to replace the standing wave on-line laser. The seed laser and optics were modified to eliminate some sources of spectral impurity. A significant improvement in the spectral purity resulted from these changes. In this section, we present some measurements of the spectral purity of the injection seeded alexandrite ring laser.

A spectral purity relevant to DIAL measurements is defined as the ratio of the laser energy contained within a narrow bandwidth (of the order of a few linewidths of the absorption line) to the total output energy. Hence, a long path cell filled with oxygen (absorption linewidth $\approx$ 0.1 cm^{-1} at 1 atm pressure) will act as a narrow band notch filter centered on the absorption line. The extent of spectral impurity in the laser output is determined by a measurement of the transmittance of the laser beam through the cell. By choosing a strong absorption line with an absorption coefficient and a long path length such that the transmittance at line center is approximately zero, the residual transmittance is then the amount of spectral impurity. A multipass White cell containing an atmosphere of pure oxygen with a total path length of about 60 m was used. As a check and to fully saturate the absorption at the line center, the laser beam was also directed along a horizontal atmospheric path at a retro-reflecting target board placed 850 m away. The $^{P}P11$ line at 764.07 nm, with a line strength of 7.6 cm^{-1}/molecule/cm^2, was chosen. All transmittance measurements were normalized for the laser energy (or power for the CW laser) and also for the transmission through the same path at a nearby non-absorbing (off-line) wavelength.

Spectral impurity in an injection seeded laser can arise from spatial hole burning in a standing wave resonator cavity, an imperfect match between the transverse modes of the seed and slave lasers, impurities in the seed laser, or the seed laser frequency not being resonant with the slave laser longitudinal modes. By using a traveling wave ring laser, the spatial hole burning normally encountered in a standing wave resonator is avoided. The tendency of the ring laser to oscillate in both directions is suppressed by the injected seed laser beam that ideally forces the oscillations along the direction of the seed beam. When the transverse modes of the two lasers are not matched, the slave laser is free to oscillate in the unseeded modes over the entire spectral bandwidth of the laser in both directions, giving rise to spectral impurities. A good mode match is obtained when both the seed and slave lasers are operating in the TEM_{00} mode.

A stable single longitudinal mode (SLM) diode laser is used to injection seed the alexandrite laser. It is evident that any spectral impurities present in the seed laser would give rise to spectral impurities in the slave laser output as well. Commercial SLM AlGaAs diode lasers with 3 mW and 30 mW output were found to contain several weaker lines (from different longitudinal modes of the cavity) which contribute a significant fraction to the output ($\approx$ 2 to 3%). Broadband radiation of the order of 1% over the entire bandwidth of the laser diodes is also present. External cavity diode lasers which are expected to have high spectral purity were not available for this study. In order to achieve a high spectral purity in the seed laser, we also used a 100 mW index guided single mode AlGaAs laser, with a wavelength of 776 nm at 25°C, in a specially designed vacuum enclosure with multistage thermoelectric coolers.

The wavelength of the diode laser is coarsely tuned to the middle of the *P* branch of the oxygen *A* band by cooling the diode to between -25 and -35°C and then tuning precisely by a combination of temperature and current control. In the experiments reported here, the diode laser wavelength was passively maintained constant by using an ultrastable current source and a temperature controller. Its output contained many weaker lines spaced at 1.5 cm^{-1} whose combined output power was about 5% of the total. The spectral impurity of the diode laser was determined by tuning it to the $^{P}P11$ line and measuring its transmittance through the White cell. Three solid etalons of lengths 0.1 mm (90% *R*), 1 mm (75% *R*), and 2 mm (75% *R*) were used to filter out the side bands. The spectral impurity was reduced to about 0.35% after filtering with the three etalons.

Figure 7-23 shows the schematic of the alexandrite ring laser together with the optical train used for injection seeding, and the diagnostics used in our experiments. A TEM_{00} transverse mode distribution across the seed beam is obtained by utilizing a collimating lens CL_1, an anamorphic prism pair APP, a spatial filter SF containing a 10x microscope objective lens with a 16 μm pinhole, and a second collimating lens CL_2. Optical feedback from the slave laser is prevented from reaching the seed laser by three optical isolators OI (each consisting of a Faraday rotator and two polarizers), providing more than -90 db isolation. Two intracavity sapphire apertures (with diameters of 2.5 mm and 4 mm) were placed on either side of the pump chamber to force the laser to operate in the lowest order transverse modes.

The laser output spectra were analyzed with a spectrometer having 0.25 cm^{-1} resolution and the wavemeter. The effect of various operating parameters on the spectral purity of the injection seeded alexandrite laser was investigated. The parameters that were varied included: spectral filtering of the diode beam to remove the side bands, broadening the linewidth of the diode laser, and changing the divergence of the seed laser beam.

Continuous dry nitrogen gas purging was used to remove the atmospheric oxygen present in the laser cavity, in order for the low-gain alexandrite laser to operate on an oxygen line. The spectrum of the unseeded Q-switched alexandrite laser output shows a sharp dip at all oxygen lines, which disappears after 30 to 40 minutes of purge. Absorption by oxygen lowers the laser gain at the line center, causing the laser to oscillate

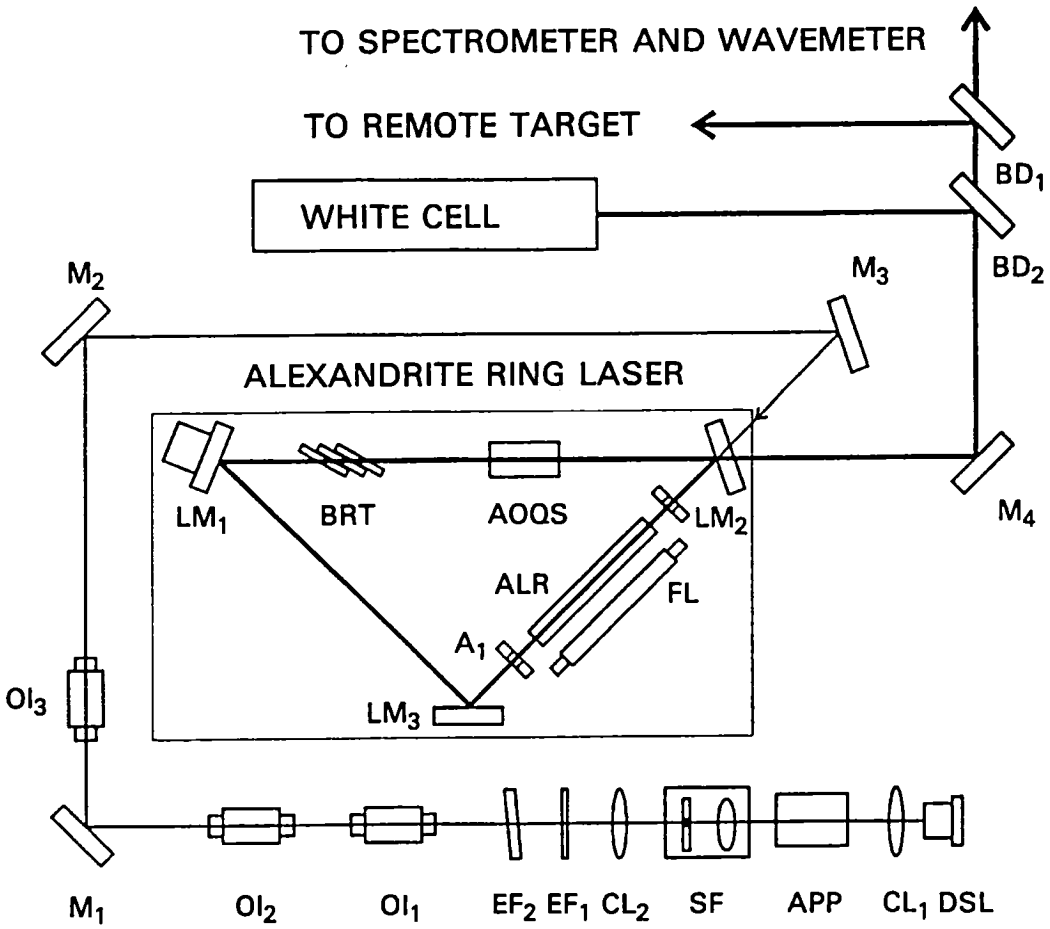

Figure 7-23. Schematic of the injection seeded ring laser. A_1, A_2: Apertures; ALR: Alexandrite Laser Rod; AOQS: Acousto-optic Q-Switch; APP: Anamorphic Prism Pair; BD_1, BD_2: Beam Dividers; BRT: Birefringent Tuner; CL_1, CL_2: Collimating Lenses; DSL: Diode Seed Laser; EF_1, EF_2: Etalon Filters; FL: Flashlamp; LM_1 - LM_3: Ring Laser Mirrors; M_1 - M_4: Mirrors; OI_1 - OI_3: Optical Isolators; SF: Spatial Filter.

all over the bandwidth of the BRT, severely reducing the spectral purity. It may be noted that it is not possible to totally eliminate all the oxygen in the laser cavity, but only to reduce it to a low level.

The spectrum of the injection seeded laser contains a number of lines corresponding to the side bands of the diode. When etalons were used to filter the diode beam, all other side bands were filtered out except for one or two weak side bands that appear on some of the shots. The best spectral purity measured was about 96.3% using the White cell, at the center of the $^{P}P11$ line. The intrinsic linewidth of the 100 mW diode laser is only 15 MHz and is comparable to the linewidth of the slave laser. Without an active cavity length control, the seed laser wavelength is resonant with the slave laser for only some of the shots. For the rest of the shots, a small fraction of the total seed power in the cavity is utilized by the slave laser modes which are spaced by 200 MHz. To increase the useful seed power, the diode linewidth was broadened by the addition of white noise to the diode laser power supply. The experiment was limited in scope because of the 2 MHz bandwidth of the diode laser power supply. Even with these limitations, the spectral purity improved to 97.5%.

In the final set of measurements, the frequency of the seed laser was scanned in steps across the oxygen line at 764.07 nm. The off-line wavelength was set at 764.3 nm. For this set, no diode laser line broadening was utilized, and the spectral filtering of the diode beam was optimized at a slightly different wavelength. Data was collected simultaneously from the target board as well as from the White cell. Figure 7-24 shows the residual spectral impurity as the seed laser is scanned across the $^{P}P11$ line. The mean spectral impurity measured at the line center was 1.9% using the target board data and 4.5% using the White cell data. When shots that had high values of transmittance (4 standard deviations away from the mean) were filtered out, the mean spectral purity was 98.6% for the target board and 95.8% for the White cell at the line center. By incorporating active cavity length control and a feedback system to keep the slave laser in resonance with the seed laser frequency, further improvements in spectral purity are expected.

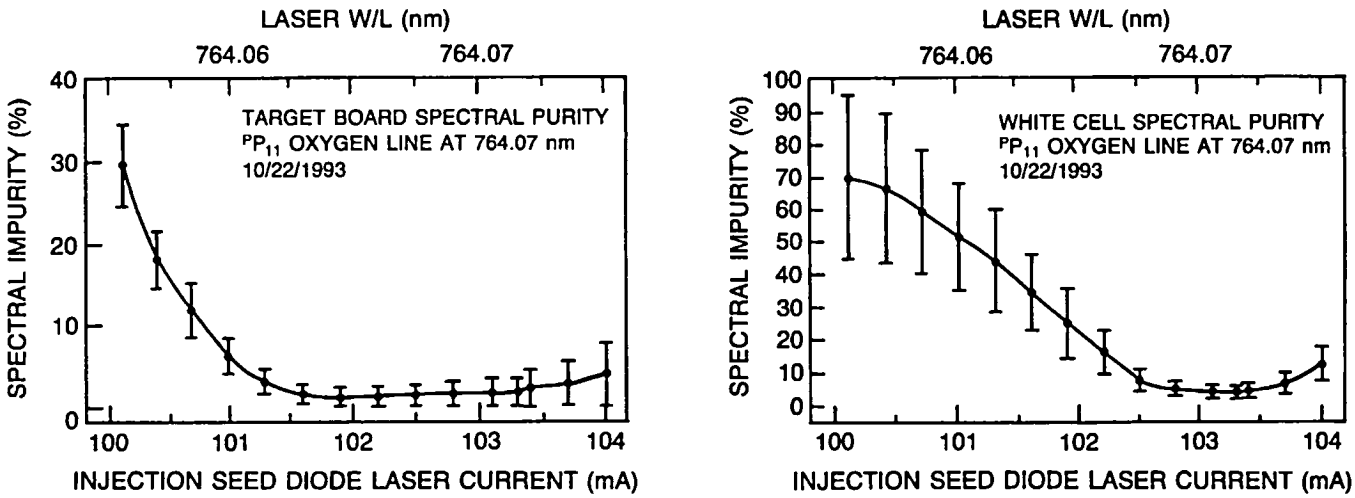

Figure 7-24. Mean spectral impurity of injection seeded alexandrite ring laser measured using the target board (left) and the White cell. Each point is the average of 1000 shots.

CHAPTER 8 RAMAN SCATTERING RECEIVER CHANNEL

INTRODUCTION

Since different scattering processes (*viz.*, Rayleigh, Mie, and Raman) affect the absorption of the on-line laser on the return path through the atmosphere, in order to calculate the absorption, we need to find the backscatter ratio to determine the fraction of the return signal due to molecular (Rayleigh) and aerosol (Mie) scattering. The backscatter ratio is defined as one plus the ratio between the Mie and Rayleigh backscatter coefficients. However, without having an independent means of determining either the aerosol or molecular backscatter coefficient, we cannot determine the fraction of the return signal that is due to each component. By placing a Raman channel in our data system, we will have a direct means of determining the molecular component of the backscatter ratio nearly independent of the aerosol component.

BACKGROUND

When a pulse of monochromatic light passes through the atmosphere a portion of the light is absorbed, a portion is transmitted, and the rest is scattered in all directions. The light that is scattered back in the direction of the transmitting source is called backscatter. The major scattering phenomena that occur in the atmosphere in order of relative backscatter strength at 770 nm are: Mie, Rayleigh, Brillouin, and Raman (Figure 8-1). These are divided into two basic types: elastic and inelastic scattering. Elastic scattering occurs when the energy of the photon is unchanged during the scattering process, while inelastic scattering occurs when the energy of the photon changes during the scattering process.

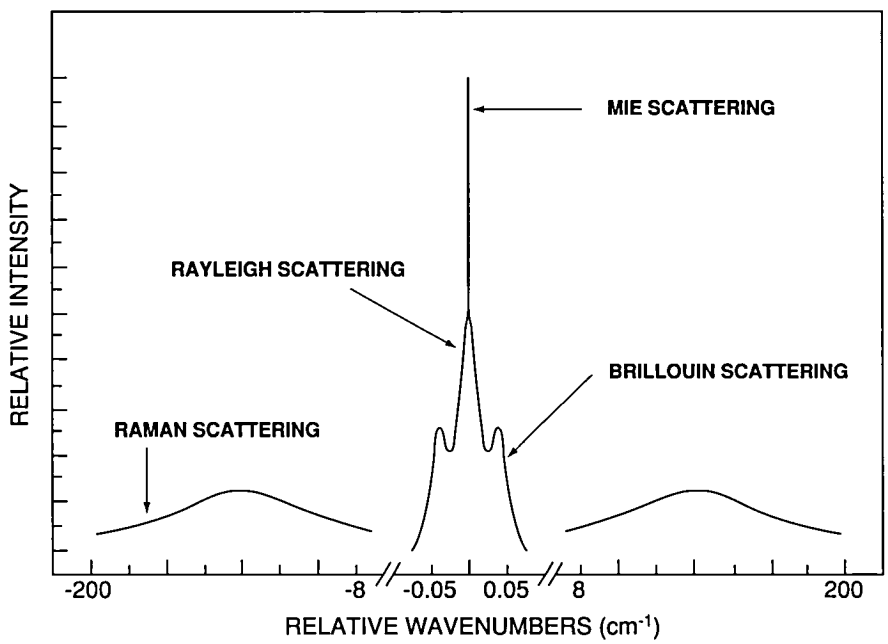

Figure 8-1. Types of atmospheric scattering phenomena showing their relative intensity and displacement from the laser line.

Mie scattering is the strongest form of elastic scattering of light by atmospheric particles. The size of these particles is on the order of or larger than the wavelength of the laser light, and include dust and aerosol particles. Rayleigh scattering is the second strongest type of elastic scattering phenomena and involves molecules in the atmosphere. The Rayleigh backscatter line shape is broadened due to a Doppler shift caused by the random thermal motion of these scattering molecules, and is called Doppler broadening. Brillouin scattering is scattering from sound waves generated by natural thermal fluctuations. These waves also impart a Doppler shift on the photons they scatter. The weakest type of scattering is Raman, an inelastic scattering process by atmospheric molecules. The photon frequency is shifted due to an interaction between the photon and the internal states of the molecule, in this case oxygen and nitrogen. The portion of energy that is backscattered from all scattering processes is collected by a telescope on the lidar receiver platform and focused on a detector. The detector converts the energy to an electrical signal, which is then digitized and stored by a data system for later analysis.

To obtain the absorption by the DIAL technique there are some basic assumptions. The optical properties of the atmosphere are considered equal for both laser frequencies, except for the resonant absorption by oxygen. Second, the two laser beams illuminate the same scattering volume almost simultaneously, whereby the atmosphere is considered frozen. Third, no absorption of another gas occurs within the two laser frequency interval. Fourth, but only for the most simplistic view, the laser spectral line shape is considered unaltered as the laser propagates through the atmosphere.

As Figure 8-2 illustrates, on the outgoing path through the atmosphere the initial spectral line shape of the on-line laser, before any scattering occurs, is much narrower than the spectrally broader oxygen absorption line. In the case of Mie scattering, the absorption on the return path is essentially the same as that on the outgoing path since the signal is elastically scattered with little change in the shape of the incident spectrum. However, for Rayleigh scattering, the signal is broadened in the scattering process due to the Doppler effect since the molecules are in motion having an ensemble of velocity components along the line of sight of the laser beam. The backscattered radiation is now absorbed less on the return path through the atmosphere. This introduces a major source of error in the data analysis if not treated properly. To correct for this error, the differential absorption is calculated using the backscatter ratio after determining the fraction of the return signal due to Mie and Rayleigh scattering. The fraction of the return signal that is due to each component cannot be determined directly without having an independent means of determining one of them.

The backscatter ratio is currently inferred indirectly by using the off-line return signal and the density profile calculated from radiosonde measurements of temperature versus pressure-altitude. The Rayleigh scattering at a given range is directly proportional to the density at that range. As an example, Figure 8-3 shows the off-line return signal versus altitude with a Rayleigh only profile superimposed on it. The off-line return signal is a combination of both Rayleigh and Mie backscatter. At an altitude of 10 km, just under the tropopause, there is a dip in the return signal. This is the spot where the atmosphere is assumed to be free from aerosols; hence, the signal there should only be due to Rayleigh scattering. The Rayleigh profile is fitted to intersect the off-line return signal at this point by adjusting a proportionality constant of the density profile. To get the backscatter ratio we divide the off-line return signal by the atmospheric Rayleigh profile. This ratio is used to determine the spectral shape of the on-line return signal affected by Doppler broadening so that appropriate corrections can be made to the data. The density profile currently used is derived from radiosonde data taken at Washington Dulles Airport. There are several problems using this scheme: 1) one point is used to fit the radiosonde and off-line return signal data, 2) this technique is not applicable for test measurements in the field, especially over the ocean and land masses where radiosonde measurements are scarce, 3) Dulles Airport is approximately 54 km from Goddard, and the density profile at Dulles and Goddard may not be the same,

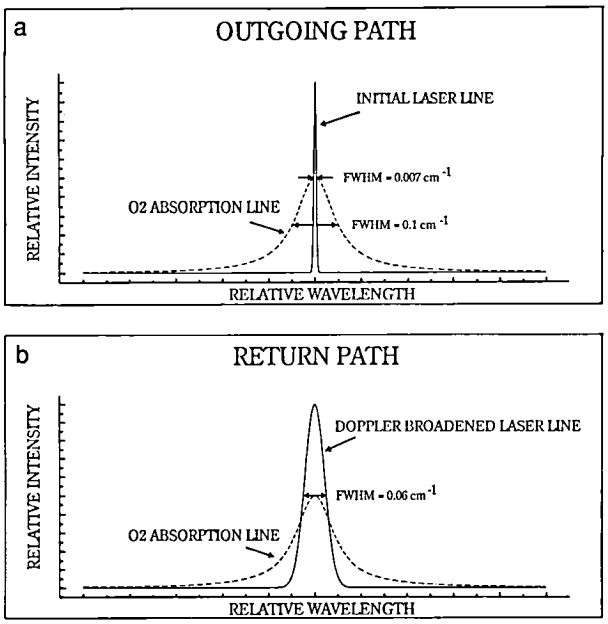

Figure 8-2. a) The line shape of the laser on the outgoing path through the atmosphere before any scattering occurs with respect to the oxygen absorption line. b) The Doppler broadened line shape of the laser on the return path through the atmosphere after scattering with atmospheric molecules has occurred.

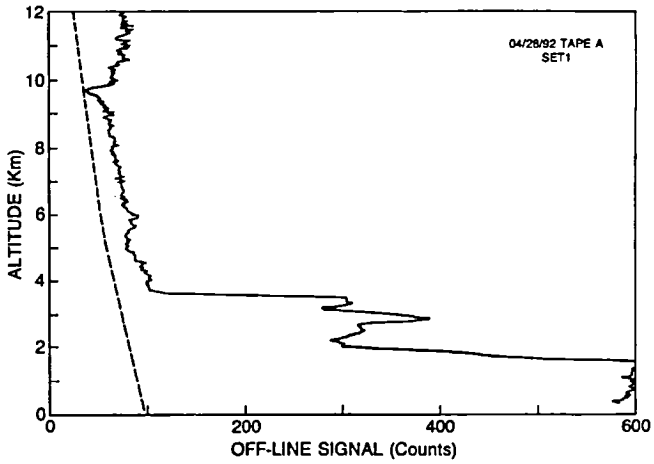

Figure 8-3. The range corrected off-line return signal (solid line) versus altitude, along with a Rayleigh profile (dashed line), calculated from radiosonde data.

and 4) since radiosondes are only taken twice a day, we have to use radiosonde data which are taken closest to the time of the measurements. By placing a Raman channel in our data system, we will be able to get a direct measurement of the density profile along the line-of-sight of our laser beam and at the same time we make our measurements.

RAMAN SCATTERING

Raman scattering refers to the inelastic scattering of photons by a medium, in this case a gaseous medium. This process involves an exchange of a significant amount of energy between the scattered photon and the internal states of the scattering molecule. These states include the rotational, vibrational, and electronic modes of the molecule. The Raman scattering process can be thought of classically as a two-photon process whereby the incident photon is absorbed by a molecule causing the molecule to enter a virtual state. The molecule returns to a stable quantum state after emitting a photon of lesser or greater energy depending on whether the final quantum state of the molecule is higher or lower than the initial state.

Figure 8-4 illustrates a typical energy level diagram for a linear diatomic molecule such as oxygen or nitrogen. Included are three vibrational energy levels, $V = 0$, $V = 1$, and $V = 2$. Within each vibrational mode there are numerous rotational energy levels; however, only four are shown. The electronic modes are not shown because they are very far apart. For any molecular species, the structure of the Raman spectrum is unique and is determined from the quantum mechanical selection rules for that species. According to the selection rules

for linear diatomic molecules, the allowed change in the rotational quantum number J is 0, ±2 while the allowed change in the vibrational quantum number V is 0, ±1 (Hertzberg, 1950).

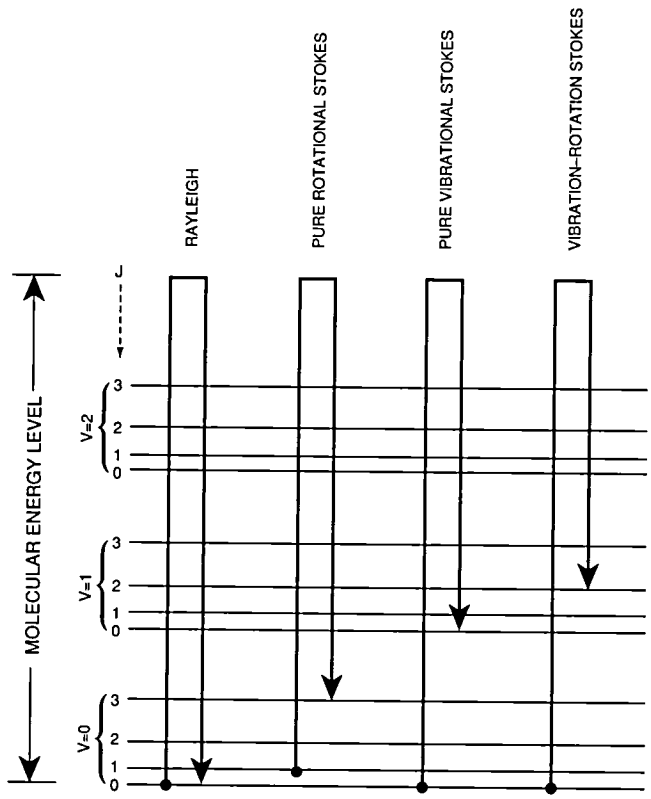

Figure 8-4. Molecular transitions of a typical O_2 or N_2 molecule contributing to Raman and Rayleigh scattering.

Raman Transitions

As an example, for Rayleigh scattering the molecule starts out in the $V = 0$, $J = 0$ quantum state, absorbs a photon, then returns to the initial state. Since the molecule did not change energy levels, a photon is emitted with the same energy and frequency as the initial photon, if the Doppler effect is not considered. The Raman scattering process is similar, except the molecule will change to a different energy level. To illustrate a rotational mode transition, consider a molecule initially in the $V = 0$, $J = 1$ level when it absorbs a photon causing the molecule to go to the $V = 0$, $J = 3$ energy level. Since the molecule used some of the photon's energy to get to the higher rotational energy level, the molecule will emit a new photon with a lower energy and frequency, thus making the photon appear on the "red" side of the spectrum, called a Stokes shift. The same explanation holds for an anti-Stokes shift, except that when the molecule interacts with a photon it goes to a lower energy level emitting a photon with a higher energy and frequency causing the photon to appear on the "blue" side of the spectrum.

The same consideration is true for the vibrational transition as for the rotational one. For a pure vibrational transition, assume the molecule is initially in the $V = 0, J = 0$ level when it interacts with a photon causing the molecule to go to the $V = 1, J = 0$ level. Since the molecule absorbed more of the photon's energy to get to the higher vibrational energy level, the molecule will emit a new photon with lower energy and frequency than the pure rotational case, making the photon appear further on the Stokes side of the spectrum. This pure vibrational transition is known as the Q-branch. The opposite is true for the anti-Stokes side of the spectrum where the molecule changes to a lower vibrational energy level.

The vibration-rotation transition is a combination of both transitions in that the molecule not only goes up or down one vibrational energy level, but also goes up or down two rotational energy levels. The emitted photon's frequency will be displaced relative to the pure vibrational transition Q-branch. The transitions for which $\Delta J = 2$ make up the O-branch while those with $\Delta J = -2$ are the S-branch.

Figure 8-5 illustrates the vibrational and rotational transitions of the Raman spectrum of the oxygen and nitrogen molecules. To show the Raman spectrum clearly, the Rayleigh, Mie, and Brillouin spectrum are not apparent since they occur within 0.2 cm^{-1} of the laser line frequency. Since the energy levels for the pure rotational quantum states are relatively close together, the associated frequency shift of the significant rotational Raman lines are close to the laser line (<250 cm^{-1} or ≤10 nm at 760 nm). The oxygen and nitrogen Raman spectrum are intermixed in this area. However, the energy levels for the vibrational quantum states of N_2 and O_2 are further apart causing the associated frequency shift of the vibrational Raman lines to be further from the laser line. For oxygen, the vibrational Raman shift from the laser line is 1556 cm^{-1} (or 105 nm), while for nitrogen the vibrational Raman shift is 2330 cm^{-1} (or 170 nm). The total integrated intensity of the Stokes transitions is higher than the integrated anti-Stokes intensity by ~10. Also, the total integrated intensity of the pure rotational Raman lines is larger than the total integrated vibrational intensity by ~100.

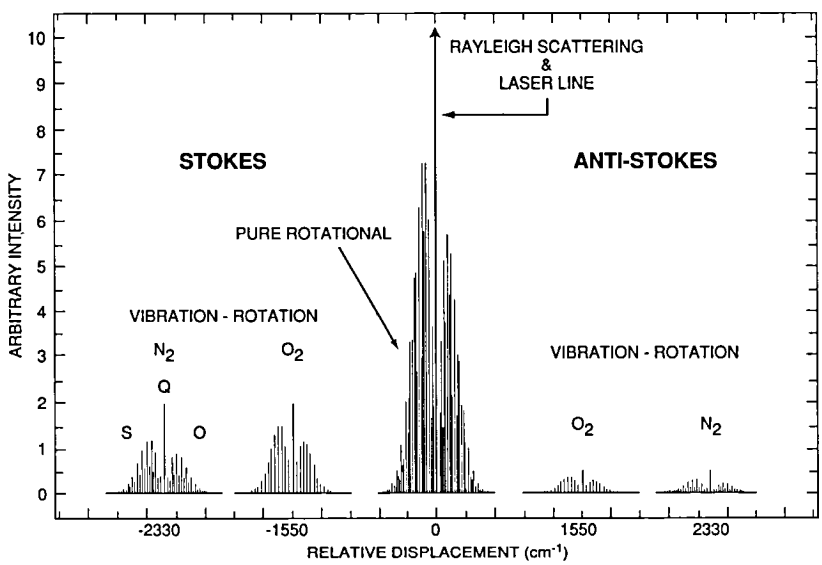

Figure 8-5. Raman backscatter spectrum of O_2 and N_2 showing the three forms of molecular transitions (rotation, vibration, and rotation-vibration) with their relative displacement and intensity with respect to each other.

Raman Intensity

The radiant intensity of a particular rotational Raman line (for unit molecular number density) is given by (Lapp, *et al.*, 1973),

$$S_J = \sigma_J \times F_J, \tag{8-1}$$

where F_J is the fraction of molecules in the rotational state J called the rotational population distribution function, and σ_J is the differential rotational Raman scattering cross section for state J. The fraction of molecules F_J in rotational state J is given by

$$F_J = g_I \frac{(2J+1)}{Q_{rot}} \exp\left\{-\frac{hcB_o J(J+1)}{kT}\right\}, \tag{8-2}$$

where g_I is the nuclear spin weighting factor, J is the quantum number for total angular momentum, h is Planck's constant, c is the speed of light, k is Boltzmann's constant, T is the temperature, B_o is the rotational constant for the lowest vibrational energy level ($V = 0$) and Q_{rot} is the rotational partition function.

The nuclear spin weighting factor g_I is dependent on the nuclear spin I of the molecule, and is equal to $(2I + 1)(I + 1)$ for symmetric molecular levels (even N_2 and odd O_2 J lines), and $(2I + 1)I$ for antisymmetric molecular levels (even O_2 and odd N_2 J lines). Since nitrogen has a nuclear spin of one, the rotational lines with even J values will be twice as strong as the lines with odd J values. Oxygen has a nuclear spin of zero; therefore, the rotational lines with even J values do not exist. The rotational partition function Q_{rot} for the ground states of homonuclear molecules is given by the approximate relation (Lapp, *et al.*, 1973):

$$Q_{rot} = (2I+1)^2 \frac{kT}{2hcB_o}. \tag{8-3}$$

The differential rotational Raman scattering cross section σ_J is expressed in terms of the Placzek-Teller coefficients in their simplified form,

$$\sigma_J = C[\omega_o - \omega(J)]^4 b_{J\to J'}, \tag{8-4}$$

where C is a constant for either nitrogen or oxygen and is normally experimentally determined, $[\omega_o - \omega(J)]$ is the Raman shift, and $b_{J\to J'}$ is the rotational line strength for the transition $J\to J'$ and is given by a specialization of the Placzek-Teller coefficients. For nitrogen, these coefficients are

$$b_{J\to J+2} = \frac{3}{2}\frac{(J+1)(J+2)}{(2J+1)(2J+3)}, \tag{8-5}$$

for the Stokes lines, and

$$b_{J\to J-2} = \frac{3}{2}\frac{J(J-1)}{(2J+1)(2J-1)}, \tag{8-6}$$

for the anti-Stokes lines.

Oxygen has a triplet ground state, making the theory for predicting the Raman spectrum more complex. Because of the triplet ground state, the interaction between the electronic spin and the nuclear rotation has to be taken into account. When this is done, quantum theory predicts that oxygen also has allowed rotational quantum numbers $\Delta J = \pm 1$ which produce spin-satellites in the Raman spectrum that are displaced about 2 cm^{-1} on each side of each rotational line and have low intensity. The intensity of these spin-satellites decreases very rapidly with increasing rotational quantum number. However, the total intensity calculated for each value of the nuclear angular momentum quantum number (N) for oxygen (using a specialized theory for the triplet ground state) is the same as the total intensity predicted by an equivalent singlet diatomic theory (as with nitrogen, which is much easier to use). Therefore, it is appropriate to use the same theory for both nitrogen and oxygen, utilizing the allowed rotational quantum numbers $\Delta J = 0, \pm 2$.

By combining Eqs. (8-1) through (8-6), the intensity for each rotational Raman line takes the form,

$$S_{J_S} = K_o \frac{(J+1)(J+2)}{(2J+3)} \frac{g_I[\omega_o - \omega(J)]^4}{(2I+1)^2 T} \exp\left\{-\frac{hcB_o J(J+1)}{kT}\right\} \tag{8-7}$$

for the Stokes rotational Raman lines, and

$$S_{J_A} = K_o \frac{J(J-1)}{(2J-1)} \frac{g_I[\omega_o + \omega(J)]^4}{(2I+1)^2 T} \exp\left\{-\frac{hcB_o J(J+1)}{kT}\right\} \tag{8-8}$$

for the anti-Stokes rotational Raman lines, where

$$K_o = C\left(\frac{3hcB_o}{k}\right).$$

The line shape of each Raman line is characterized by a Voigt function to account for the effects of both Doppler and pressure broadening (Burlbaw and Armstrong, 1983).

DETECTION OF RAMAN SIGNAL

For a Raman channel to be beneficial, the measurement must be temperature insensitive so the Rayleigh profile doesn't fluctuate with temperature and must also have adequate rejection of the Rayleigh line from the Raman spectrum. There are several possibilities for detecting the Raman signal, such as: 1) pure rotational (Stokes and/or anti-Stokes), 2) vibration-rotation for oxygen (Stokes or anti-Stokes), or 3) vibration-rotation for nitrogen (Stokes or anti-Stokes). Numerous experiments have been performed utilizing each Raman band for different applications. One such study involves using the Raman vibration-rotation band to measure the density concentration of various molecules in combustion systems (Lapp and Penney, 1974), while others utilize the Raman rotational band for the study of atmospheric density (Lapp, *et al.*, 1973) and temperature (Arshinov, *et al.*, 1983; Chanin, *et al.*, 1992; Vaughan, *et al.*, 1993).

The advantages of using the pure rotational Raman band are that the spectrum has a higher backscatter cross section and the photomultiplier tube (PMT) detectors have a higher quantum efficiency at the wavelength being used. The major disadvantage of using the pure rotational Raman is that it begins close (~12 cm^{-1}) to the Rayleigh line, requiring careful filtering and design. Conversely, the advantage of using the

vibration-rotation Raman band, either Stokes or anti-Stokes, is that the Raman spectrum is relatively far from the Rayleigh line, allowing for simpler filtering and a less stringent design.

Table 8-1 shows the relative detection strengths of each Raman band. To make the comparison more apparent, each Raman band cross section is referenced to the Rayleigh cross section, with the Rayleigh cross section normalized to 1000.

Since the detected signal is determined mainly by backscatter cross section, detector quantum efficiency, and atmospheric number density, the product of these three quantities will give the relative signal strength of each Raman band. The relative signal strength of the pure rotation Raman band is higher than any other Raman band by a factor of ~250. Thus, the rotation Raman band is a good choice for measuring the density profile even though the separation of the Rayleigh and Raman signal is more difficult.

Table 8-1. Relative signal strength of pure rotational Raman and vibration-rotation Raman transition bands relative to the Rayleigh signal strength. Cross sections are scaled to 770 nm from 337.1 nm as given by Measures (1984) using ω^4 dependence.

	Rayleigh	Pure Rotation	Vibration-Rotation			
			Stokes		Anti-Stokes	
	$(O_2 + N_2)$		O_2	N_2	O_2	N_2
Wavelength (nm)	770	760-780	875	940	665	600
True cross section	1.4×10^{-28}	4.8×10^{-30}	1.7×10^{-31}	1.3×10^{-31}	1.7×10^{-32}	1.3×10^{-32}
Relative cross section	1000	34	1.2	0.93	0.12	0.093
Quantum efficiency (%)	10.0	10.0	3.5	0.1	12.0	15.0
Number density	1	1	0.2	0.8	0.2	0.8
Relative signal	100	3.4	8.4×10^{-3}	7.4×10^{-4}	2.9×10^{-3}	1.1×10^{-2}

Rayleigh Line Rejection

It was necessary to determine the best method for separating the Rayleigh line from the Raman signal so that as much of the Raman signal as possible could still be detected. Many experiments have been performed using different techniques for rejecting the Rayleigh line from the pure rotational Raman spectrum. Since the rotational Raman intensity is weaker than the Mie intensity by two or more orders of magnitude, the device chosen must suppress the Rayleigh and Mie contribution by a factor of at least 10^6 in the Raman channel to keep errors in the Mie signal from contaminating the density measurement below 0.1%. Some techniques and devices used to isolate the rotational Raman spectrum while rejecting the Rayleigh and Mie components are interference filters (Chanin, *et al.*, 1992; Vaughan, *et al.*, 1993), monochrometers (Arshinov, *et al.*, 1983), holographic notch filters (Carrabba, *et al.*, 1990; Yang, *et al.*, 1991), and Fabry-Perot interferometers (King, 1976; Burlbaw and Armstrong, 1983).

Most research involving rotational Raman is based on observing only a small region of the Raman spectrum where the temperature sensitivity is utilized. However, in order to use the rotational Raman spectrum for density measurements, the detected spectrum needs to be temperature insensitive. Even though the peak intensity of the rotational Raman spectrum shifts in response to temperature changes, as shown in Figure 8-6, the temperature sensitivity can be reduced substantially by detecting the entire rotational Raman spectrum, or a significant portion of it. Our analysis showed that in order to achieve a temperature insensitive Raman return signal, an 80 cm^{-1} bandwidth filter centered 80 cm^{-1} from the laser line is needed on either the Stokes or anti-Stokes side of the rotational Raman spectrum, if the entire rotational Raman spectrum could not be detected.

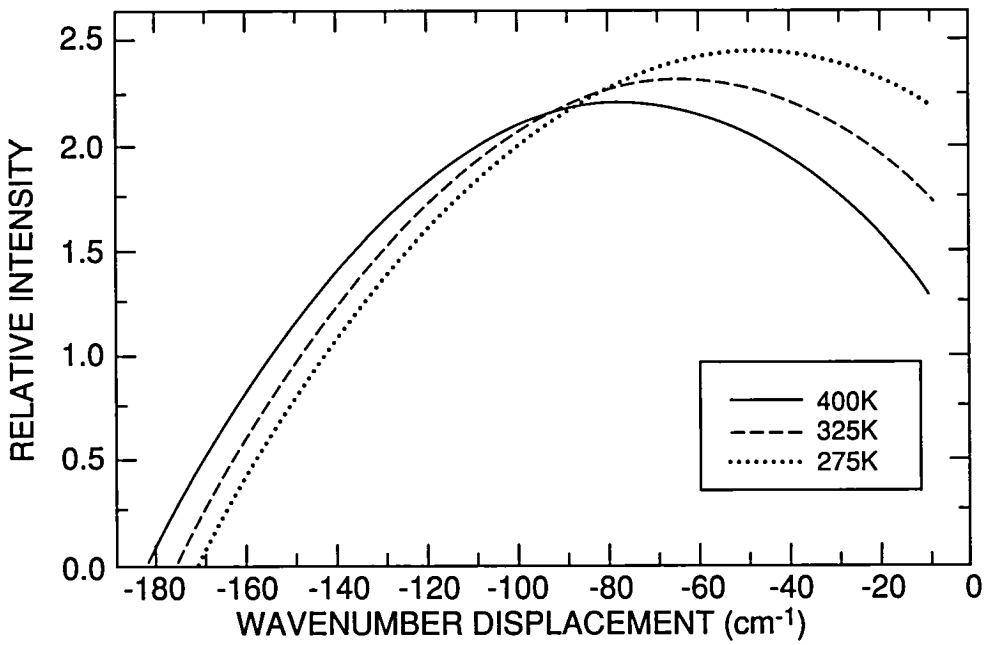

Figure 8-6. Envelope of the Stokes Raman spectrum showing the shift in the peak intensity of the spectrum towards the laser line as the temperature decreases from 400 K to 275 K.

Instruments

Several techniques were explored to determine if the required temperature insensitivity and Rayleigh line rejection could be obtained. Interference filters do not simultaneously provide a steep enough spectral slope (≥3 optical densities in 12 cm^{-1}) and the large bandwidth required to achieve the temperature insensitivity needed for detecting the Raman signal. Monochromators do provide adequate separation between the Rayleigh line and the Raman spectrum; however, in order to achieve the required rejection of the Rayleigh line, a double-grating monochromator is needed. The problem with using a two-stage monochromator, as shown in Figure 8-7, is that the dispersed Raman output of the first stage is spread out too far to be useful as input to the second stage. This approach is not well suited to detect a large portion of the Raman spectrum without considerable modification to the monochromators and use of a complex optical setup.

Holographic filters, while similar in function to gratings but used like interference filters, have a much narrower spectral bandwidth and a steeper spectral edge. They are used extensively in the field of Raman spectra. Raman spectra have been observed to within <200 cm^{-1} using a holographic Bragg diffraction filter (Carrabba, *et al.*, 1990). Recent developments in holography have enabled researchers to acquire Raman spectra as

close as 72 cm^{-1} using holographic notch filters (HNF) (Yang, *et al.*, 1991). The HNF is a simple device (Owen, 1992)[5] that can be used to separate the Rayleigh and Raman spectra and also act as a dichroic beamsplitter, so both signals can be detected simultaneously, as shown in Figure 8-8. By illuminating a HNF with a collimated beam from the telescope, the Rayleigh component (the part that is notched out) will be diffracted at an acute angle, while the Raman component (the part that is not notched out) is transmitted through the HNF with no separation or divergence in the Raman spectrum. Each HNF can provide up to 3 O.D. rejection of the Rayleigh line with an average transmission of approximately 40% of the Raman spectrum. However, even with the advances in holographic filter technology, the HNF transmission function is not sufficiently spectrally narrow to acquire both the Raman Stokes and anti-Stokes spectra and does not provide a steep enough spectral edge, as shown in Figure 8-9. This results in a change in the detected intensity as a function of temperature as well as density, causing a substantial error in the density profile. Therefore, the HNF will not satisfy the temperature insensitivity requirement of the detection system.

The device that meets all detection system requirements and allows for the measurement of the Rayleigh and the entire pure rotational Raman spectra of oxygen and nitrogen while simultaneously providing adequate Rayleigh line rejection from the detected Raman signal is the Fabry-Perot interferometer (FPI). Most applications using FPI's involve using this device in transmission. There has also been research involving FPI's used to measure a spectral feature of the rotational Raman spectrum by aligning the free spectral range of the FPI to match the periodic frequency separation of the Raman lines of the nitrogen molecule (Burlbaw and Armstrong, 1983). FPI's have also been used as a rejection filter to eliminate the unwanted Rayleigh or Raman spectra (King, 1976). For this application, we must measure both the Rayleigh and Raman signals simultaneously while having as little cross-talk between the Rayleigh and Raman channels as possible. By taking advantage of the periodic structure of the rotational Raman spectrum and the regular transmission

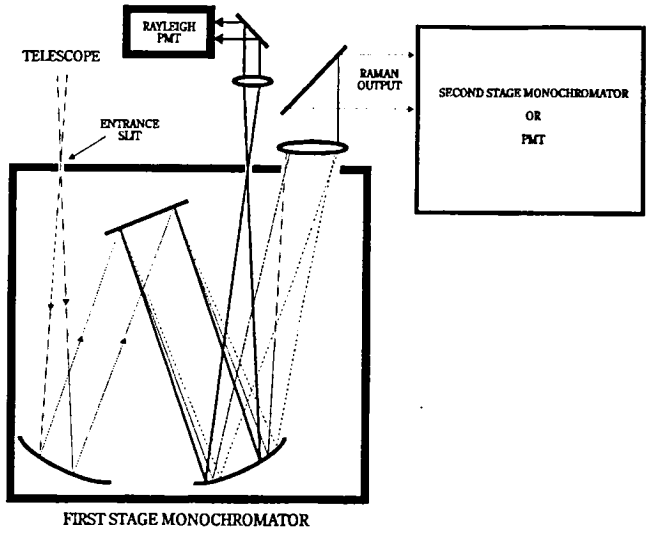

Figure 8-7. Rotational Raman and Rayleigh backscatter separation and detection using a two stage monochrometer.

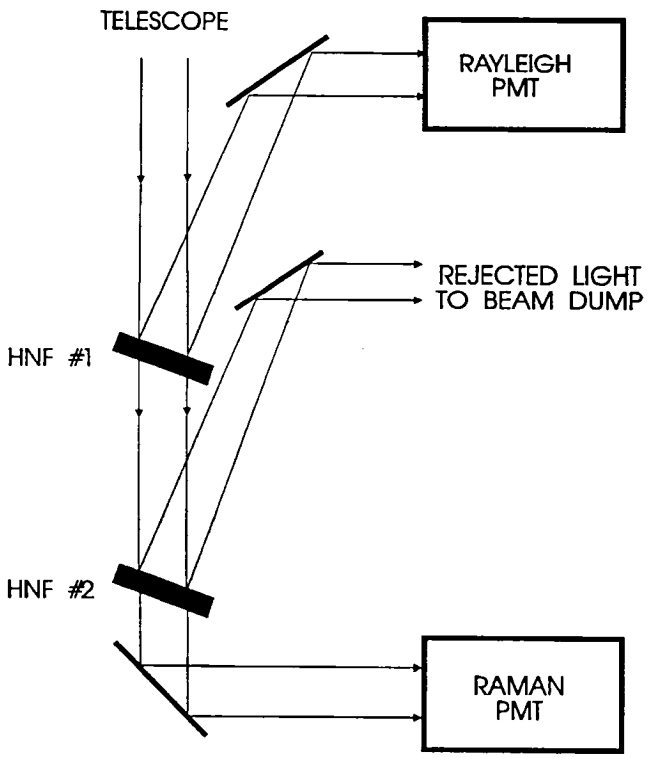

Figure 8-8. Rotational Raman and Rayleigh backscatter separation and detection using two holographic notch filters.

[5] Preprint of "Holographic Optical Components for Laser Spectroscopy Applications" from Holographics International.

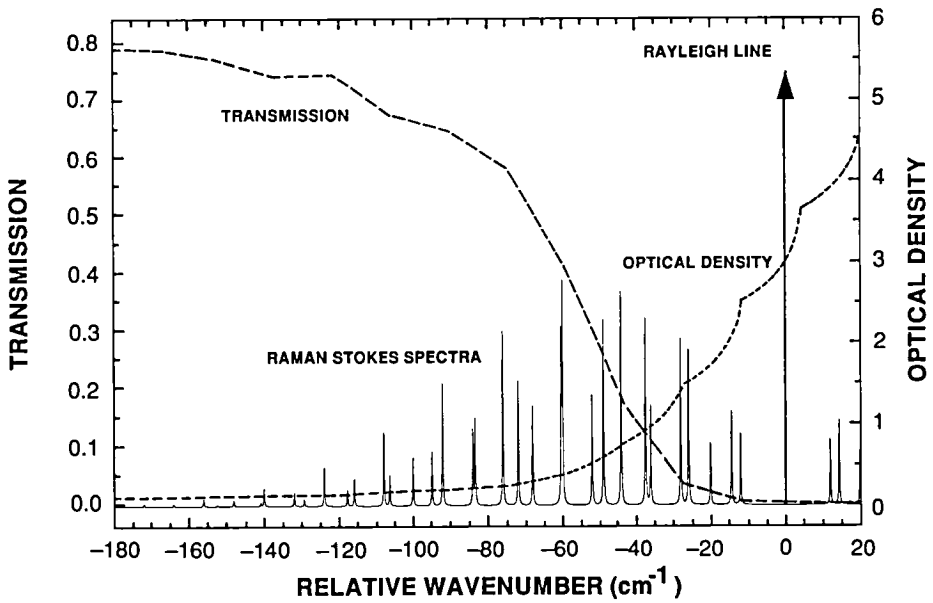

Figure 8-9. Stokes rotational Raman and Rayleigh intensity profile superimposed with a HNF transmission and optical density function. The HNF is positioned to ensure 3 optical densities of isolation between the Raman and Rayleigh spectra using a single HNF.

intervals of the FPI, it is possible to design an FPI that will not only transmit the Rayleigh and Mie spectrum but also reflect the rotational Raman spectrum.

Theoretical Considerations

The FPI consists of two partially transmitting flat mirrors placed parallel to each other constituting an optical cavity. The shape of the FPI transmission function can be expressed in terms of the Airy function (Vaughan, 1989) as

$$A(\varphi)=\left[1+\frac{4R}{(1-R)^2}\sin^2\left(\frac{\varphi}{2}\right)\right]^{-1}, \tag{8-9}$$

where R is the reflectivity of the etalon substrate and coating, and $\varphi = 2\pi\omega\eta d\cos\theta$, where ω is the frequency, η is the refractive index of the medium between the plates, d is the plate separation, and θ is the angle between the input beam and the surface normal of the FPI. A fixed spaced FPI is called a Fabry-Perot etalon. Since the rotational Raman spectrum has "gaps" ~6 cm^{-1} wide every 40 cm^{-1}, the transmission peaks of the etalon, called the free spectral range (FSR), can be designed such that they occur within these gaps as shown in Figure 8-10. The etalon transmission peaks are also shown in Figure 8-11 with an expanded view of the rotational Raman Stokes spectrum of air. The transmission function of an air gap etalon can be obtained in terms of the Airy function as

$$I_t=\left[1-\frac{A_S}{(1-R)}\right]^2 A(\varphi), \tag{8-10}$$

where A_s is the absorption and scattering loss of the etalon substrate and coating.

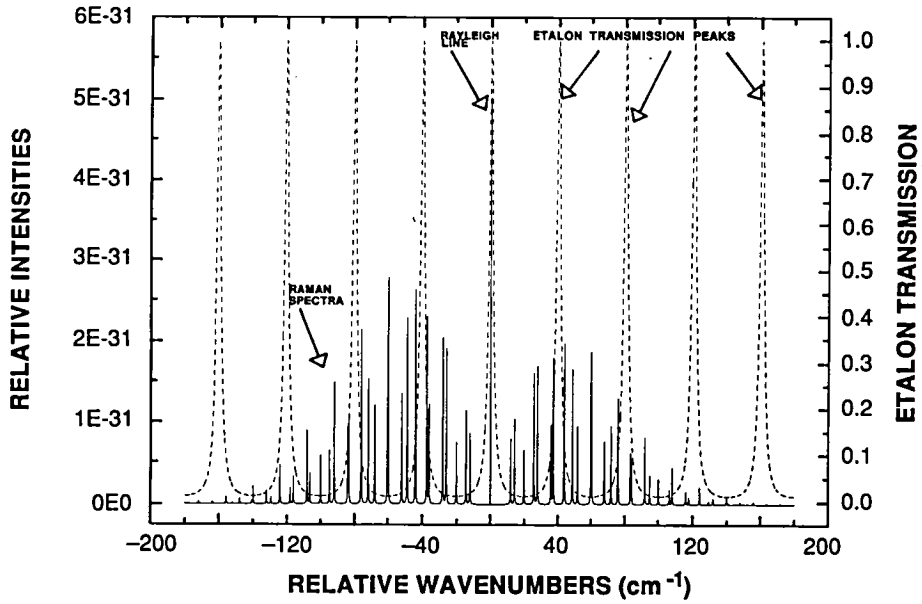

Figure 8-10. Rotational Raman and Rayleigh intensity profile superimposed with an etalon transmission function. The etalon, with a reflectivity of 80% and a FSR of 40 cm^{-1}, is positioned to ensure the transmission of the Rayleigh line, and the subsequent transmission peaks occur within the 6 cm^{-1} gaps in the Raman spectrum.

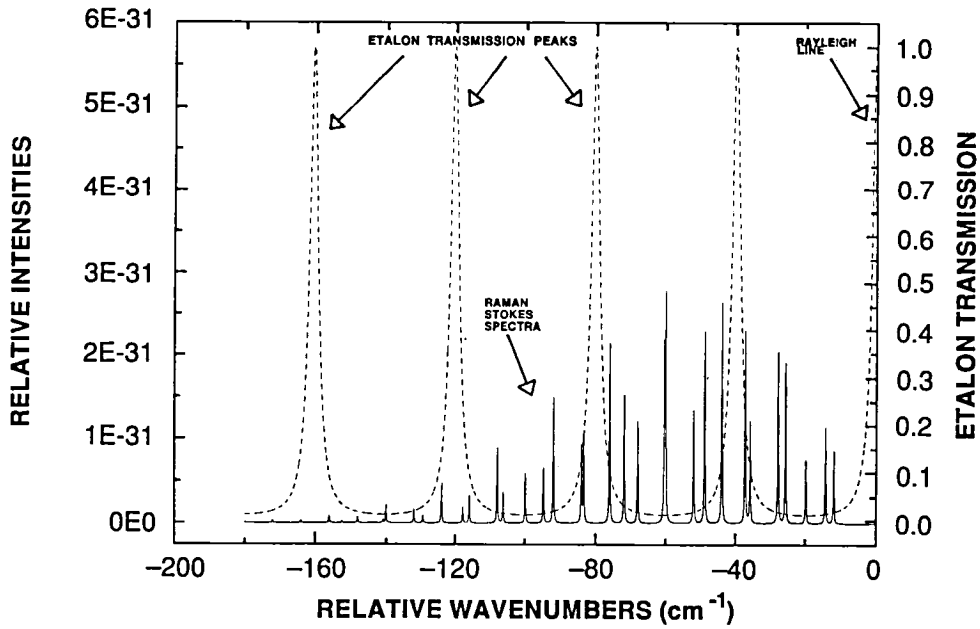

Figure 8-11. An expanded view of the rotational Raman and Rayleigh intensity profile superimposed with an etalon transmission function.

Since most transmission applications of etalons are for spectral line shape and frequency determination, many researchers disregard the absorption and scattering loss term in the reflected component assuming the reflected component is just the complement of the transmitted component. By using the reflected component of the etalon to measure the Raman spectrum, it is necessary to take the absorption and scattering loss term into account, because the reflected Rayleigh signal can contaminate the Raman signal substantially, causing large errors. The reflected component of an air gap etalon can also be written in terms of the Airy function (Vaughan, 1989) as

$$I_r = (1 - A_S)\left[1 - A(\varphi) + \frac{A_S^2 R}{(1 - A_S)(1 - R)^2} A(\varphi)\right]. \tag{8-11}$$

The effects of the absorption and scattering loss on the etalon transmission and reflection can be seen in Figure 8-12. With the advancement in coating technology, it is now possible to achieve an absorption and scattering loss of < 0.005% using a coating technique called ion sputtering, instead of the standard evaporated beam coating technique. As the absorption and scattering loss decreases from 0.2% to 0.005%, the reflected component of the Rayleigh signal also decreases. The decrease in the reflected Rayleigh component is critical in order to use the etalon in reflection for measuring the Raman signal, since the Rayleigh signal is initially two orders of magnitude larger than the Raman signal.

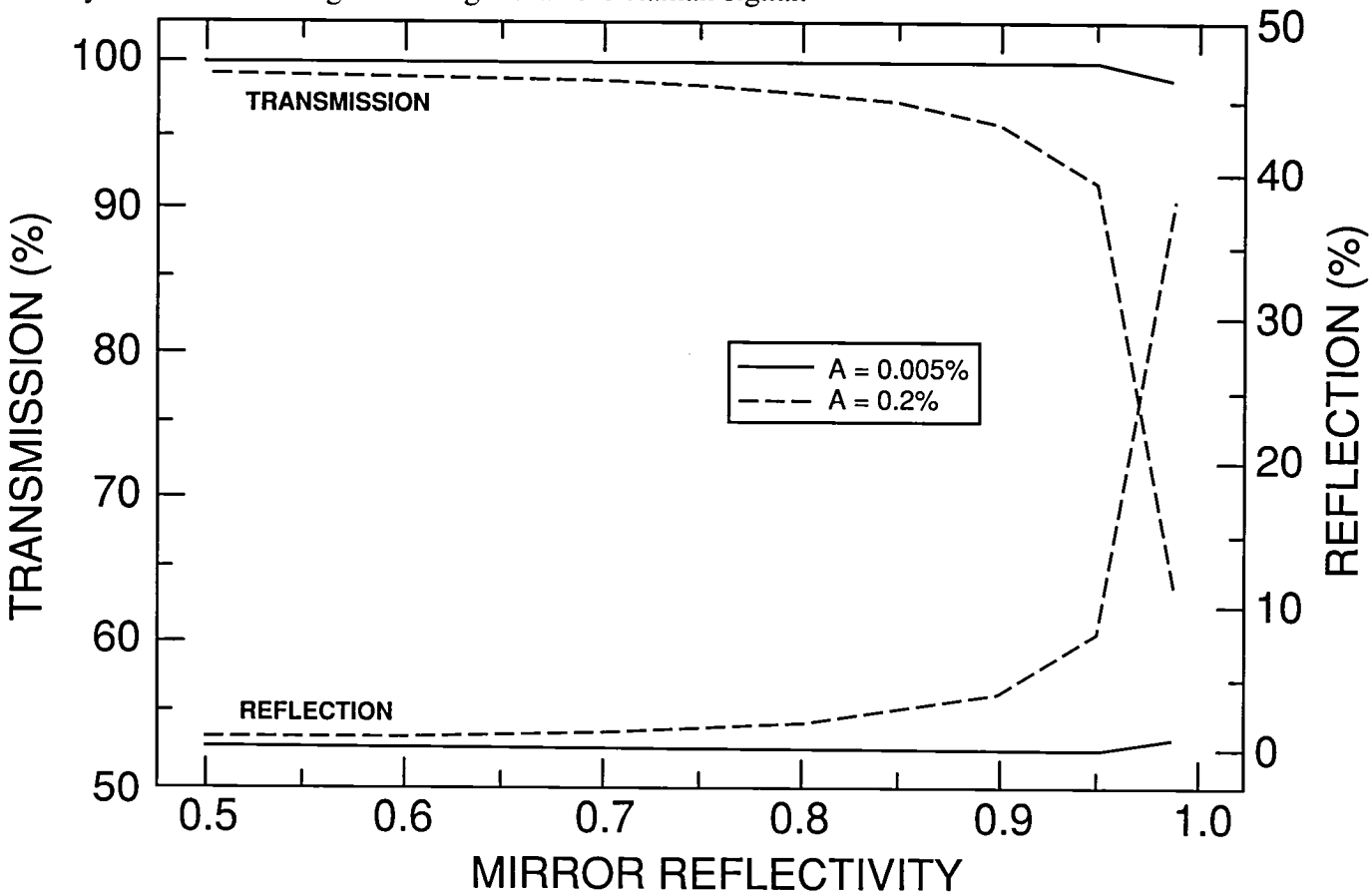

Figure 8-12. Etalon transmission and reflection of the Rayleigh line for two different absorption and scattering coefficients as a function of etalon reflectivity.

The transmission of the FPI as given in Eq. (8-9) considered only the reflectivity of the plates. The overall finesse of the FPI is affected also by other considerations, such as the flatness of the plates, the defect in the plates, and the size of the pinhole. Each of these could be considered as contributing its own finesse to the total instrument finesse. The finesse of a Fabry-Perot etalon is the key measure for the interferometer to resolve closely spaced lines. Assuming that the total instrument finesse F_o is related to the sum of the inverses of the squares of these finesses (Brulbaw and Armstrong, 1983) as

$$\frac{1}{F_o^2} = \frac{1}{F_r^2} + \frac{1}{F_f^2} + \frac{1}{F_p^2} + \frac{1}{F_d^2} \tag{8-12}$$

where F_r is the reflectivity finesse, F_f is the flatness finesse, F_p is the pinhole finesse, and F_d is the defect finesse, the Airy function is now modified to

$$A(\varphi) = \left[1 + \left(\frac{2F_o}{\pi}\right)^2 \sin^2\left(\frac{\varphi}{2}\right)\right]^{-1}. \tag{8-13}$$

According to Eq. (8-13), the different finesses are included in the Airy function through F_o, thus allowing the etalon to be characterized by an effective reflectivity.

Experiment

An experiment was performed to determine if the assumption of Eq. (8-12) and the relation in Eq. (8-13) are a good representation of the finesse. The transmitted intensity of a laser diode was measured through a solid etalon of known mirror reflectivity and thickness, and then the pinhole size was changed from 50 μm to 25 μm in order to change the instrument finesse, as shown in Figure 8-13. By tuning a 100 mW laser diode through an etalon fringe, using current to tune the laser diode, the line shape and peak transmission of the etalon can be determined for a given set of conditions. An anamorphic prism is used to collimate the laser diode beam because each axis of the laser diode diverges at a different rate. Detector #1 is used to normalize the transmission because the laser diode output energy increases as its current increases. The photo-acoustic cell is used as a reference to calibrate the diode current tuning rates using two known oxygen absorption line frequencies within the scanning range of the laser diode. A chopper is used to modulate the beam for phase sensitive detection by the lock-in amplifier. The lock-in amplifiers are used to filter out noise and integrate the small signal from the detectors and convert it to a DC voltage. The oscilloscope and computer are used to average the signal and perform statistics on the data.

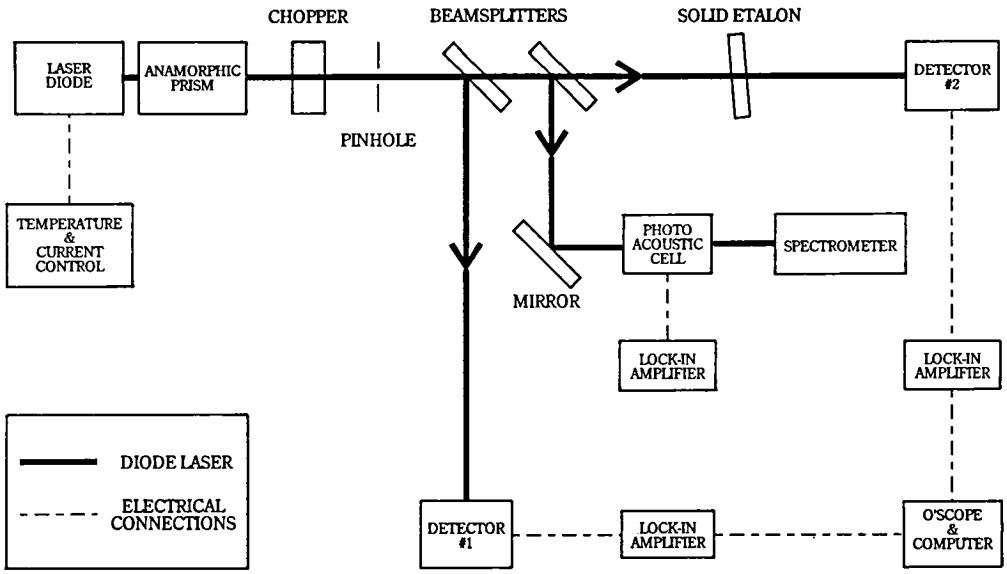

Figure 8-13. Block diagram of the experimental setup to determine if the transmission function of an etalon can be characterized by an effective reflectivity when the instrument finesse changes.

Results

Figure 8-14 shows the experimental and theoretical transmission functions of a solid etalon using a laser diode as the beam source. The modified Airy function from Eq. (8-13) was used to fit the experimental transmission function in an attempt to characterize the line shape by using an effective reflectivity. The Airy function maximum was normalized to the peak experimental relative intensity. The basic shape of the etalon transmission can be partially characterized by the modified Airy function. The line shape at the top portion of the etalon transmission function agrees with the shape of the Airy function but quickly diverges at the half maximum point. The "bump" in the etalon transmission corresponds to a longitudinal mode of the laser diode; these modes are spaced approximately 10^{-4} μm apart. These side bands make up a few percent of the total intensity of the laser diode output. An effective reflectivity and bandwidth for this experimental setup can be obtained to a reasonable approximation by curve fitting an Airy function to the data obtained from this experiment. The average effective reflectivity obtained from several measurements is equal to 79.5%; however, according to the instrument finesse [$F_o = 22$ with an error of ±15% from Eq. (8-12)], the effective reflectivity should have been 86.8% with a variance of ±2.5%. This experiment was performed several times, but the effective reflectivity obtained by curve fitting the data was different each measurement. The effective reflectivity was inconsistent between measurements taken on the same day, with no disturbances. A typical spread between measured effective reflectivities was 3%, while the expected spread should have been <1%. Since the experiment was not repeatable for a given set of conditions, no data was taken for the 25 μm pinhole.

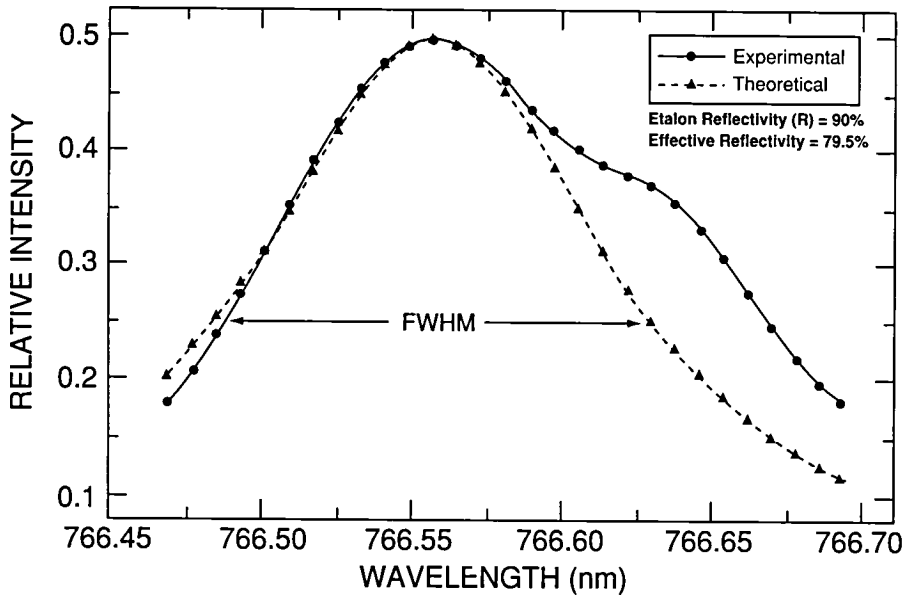

Figure 8-14. Experimental transmission function of a solid etalon using a laser diode as the beam source and characterized by a theoretical transmission function, based on the Airy function with an effective reflectivity of 79.5%.

Analysis

Even with the variation in the experimental effective reflectivities, the discrepancy between the experimental and theoretical effective reflectivities shows that the shape of the transmission function of an etalon may not be simply characterized by an effective reflectivity in the modified Airy function. The true shape of the instrument transmission function is a convolution between the reflectivity, flatness, pinhole, and defect finesses and must also be convolved with the source function to get the transmitted intensity profile. The line shape of the reflectivity finesse (Airy function) is Lorentzian, while the line shape of the flatness and defect finesse are Gaussian, assuming the coatings are uniform and the defects are randomly distributed over the entire substrate. The line shape of the pinhole finesse is a "top hat", assuming the pinhole is positioned on axis at the center of the fringe pattern in the focal plane and is uniformly illuminated. A good treatment of convolving different line shapes has been described by Vaughan (1989). It is clear that the resultant intensity profile, which is the convolution of a Lorentzian, three Gaussian, and a " top-hat" profile, cannot simply be characterized by a single Lorentzian profile, as Eq. (8-13) indicates. Therefore, the assumption that all of the instrument finesses add like Gaussians [Eq. (8-12)] is not an accurate representation of the true instrument finesse.

Any errors in this experiment can be attributed to the equipment used, the optical alignment, and the calculation of the instrument finesse. The laser diode, for example, is not a well collimated device. By changing the laser diode wavelength (by current or temperature), the output power, spectral bandwidth, side band intensity, and beam divergence also change. The change in output power can be normalized as was done in this experiment. However, the change in the spectral bandwidth, side band intensity, and beam divergence can cause abnormalities in the detected beam shape. The laser diode beam along the x and y axes diverge at different rates and are not coplanar, causing astigmatism in the beam. To correct for the different divergence rates, an anamorphic prism had to be used to collimate the beam. However, the available anamorphic prisms

did not match exactly the divergence ratio of the laser diode. The optical alignment of the system, especially the pinhole, could be improved. Given more time, the necessary optical alignment may have been achieved.

DESIGN CONSIDERATIONS

The design of the etalon is based on considerations set forth by the rotational Raman spectrum. Since the Raman signal is relatively weak in comparison to the Rayleigh and Mie signal, in order to use the etalon in reflection, the absorption and scattering loss of the coating must be very low, requiring the use of ion sputtering as the coating process (at this time). This process involves raising and lowering the temperature of the substrate which causes stress on the substrate. This forces the use of an air gap etalon, which can have thicker substrates, instead of a solid etalon, because the stress involved by ion sputtering may deform a thin solid etalon, rendering it useless. The substrates are made of fused silica and must be separated by 0.0125 cm in order for the FSR of the etalon to equal 40 cm^{-1}. The plate separation can be accomplished by optically contacting three Zerodur spacers spaced 120° apart to the inner surface of the substrates. Zerodur is used as the spacing material due to its low thermal expansion coefficient. A single etalon, even with the great advances in coating technology, cannot provide adequate rejection of the Rayleigh line, thus requiring the need for two etalons. However, instead of the complications of two etalons, it is easier to pass the beam through a single etalon twice, hence double passing the etalon, as shown in Figure 8-15.

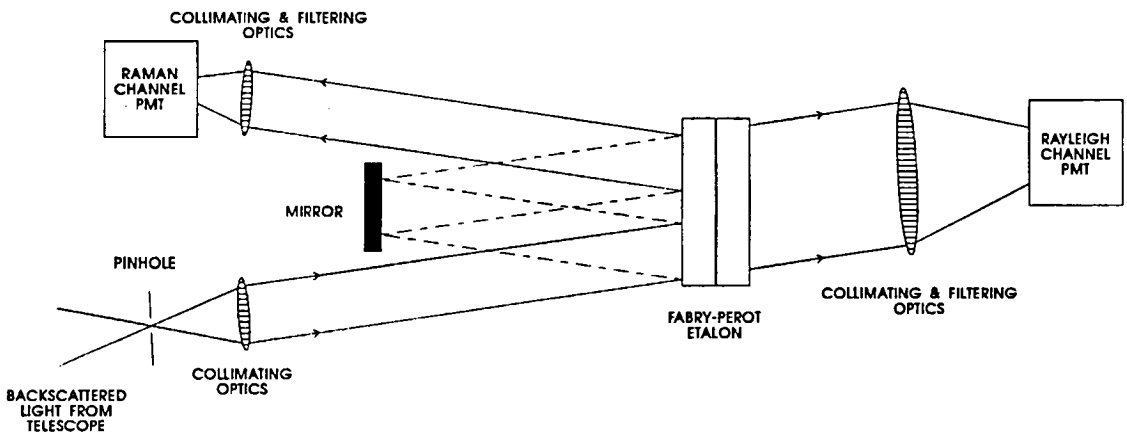

Figure 8-15. Raman and Rayleigh receiver channel based on double passing the return signal through an air-gapped Fabry-Perot etalon.

Figure 8-16 shows the percentage of the reflected Raman and Rayleigh signals as a function of the etalon reflectivity, after double passing the etalon. Included in this figure is the reflected Rayleigh to Raman signal ratio. In order for the reflected Rayleigh signal to be <0.01% of the reflected Raman signal, the etalon reflectivity should be ~80% or less.

Referring to Table 8-2, using a double pass etalon with an effective reflectivity of 80% and a FSR of 40 cm^{-1}, it is possible to reflect over 88% of the total rotational Raman signal while only reflecting ~4 x 10^{-5} percent of the Rayleigh and Mie signal. The transmitted component of the Rayleigh and Mie signal can be as high as 99%. The signals reflected by double passing this etalon will achieve the desired Rayleigh to Raman signal ratio of 0.01% within an atmospheric temperature range of 200 to 300°C.

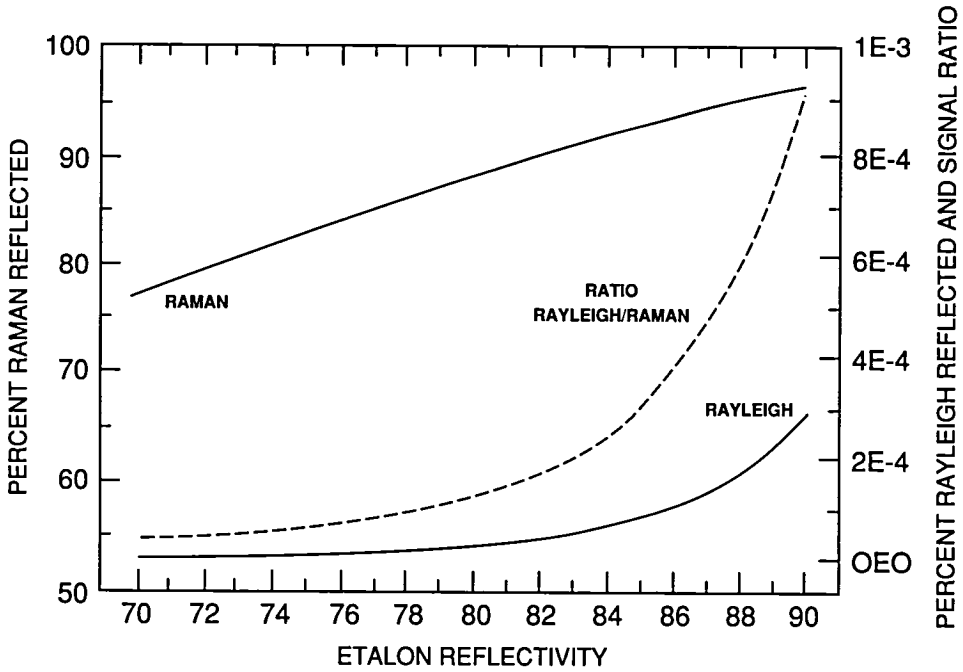

Figure 8-16. Reflected Raman and Rayleigh plus Mie intensity as a percentage of total intensity collected by the telescope. The dashed line is the ratio of the reflected Rayleigh plus Mie intensity to that of the Raman intensity; a ratio of 10^{-4} is desired (read on the right axis).

Table 8-2. Relative signal strengths of rotational Raman and Rayleigh and Mie spectra.

	Relative Intensity at 200 K		Relative Intensity at 300 K	
	Raman	Rayleigh and Mie	Raman	Rayleigh and Mie
Total	3.4437×10^{-30}	1.0613×10^{-27}	3.4331×10^{-30}	1.0613×10^{-27}
Reflected	3.0405×10^{-30}	3.9805×10^{-34}	3.0275×10^{-30}	5.1933×10^{-34}

CONCLUSION

The use of an external cavity diode as the tunable laser source would be a major improvement to the experiment, because it can be tuned over a range of wavelengths while maintaining a constant output power. It would also substantially improve the collimation of the laser diode beam, possibly eliminating the need for an anamorphic prism. By using an external cavity diode and carefully aligning the optical components, the effects of beam steering can also be reduced considerably. Better optical alignment of each component, especially the pinhole, would improve the experimental results substantially.

With the ion sputtering advancement in coating technology, the use of an air gap etalon to simultaneously separate the rotational Raman spectrum of oxygen and nitrogen from that of the Rayleigh and Mie spectra can provide adequate signal strength for the detection of both signals, and, most importantly, provide adequate Rayleigh line rejection. The etalon can be fabricated in just a few months and can be quickly implemented

into the existing lidar system with minor modifications to the optical layout. The technique described herein to directly measure the density using the rotational Raman spectrum will provide the information necessary to improve the data analysis for the remote measurement of the atmospheric temperature profile. The ability to measure the Rayleigh profile would also be very beneficial to other lidar remote sensing projects.

CHAPTER 9 CW LASER MEASUREMENTS

INTRODUCTION

Early in this program, a horizontal path CW laser and hard target were employed in a proof-of-concept experiment of the temperature technique (Chapter 2), because pulsed tunable lasers of sufficiently narrow bandwidth were unavailable. The integrated absorption of the CW laser beam was therefore obtained over a two-way horizontal path. Because the CW laser linewidth was ~10 MHz, it can be considered monochromatic compared to the absorption linewidth. Use of a hard fixed target insures the return light will also remain monochromatic. This allows us to make the simplifying assumption of monochromicity in the following analysis.

THEORY

Following the discussion in Chapter 2 up to Eq. (2-9), the Voigt lineshape function at line center can be written as (Penner, 1959)

$$f(0) = f' \exp a^2 \left[\frac{2}{\sqrt{\pi}} \int_a^\infty \exp(-y^2) dy \right] = f' \exp a^2 (1 - \operatorname{erf} a), \tag{9-1}$$

where erf represents the error function. The value and range of a depend upon the molecular species being analyzed. For oxygen,

$$a = 2.14 \times 10^5 \frac{b_c^0}{\nu_0} \frac{P}{T}. \tag{9-2}$$

Using values from Burch and Gryvnak (1969) for the temperature sensitive high J quantum number lines in the P branch of the oxygen A band, a is <3.0 at the Earth's surface and decreases with altitude. The range of a allows an accurate analytical approximation to Eq. (9-1) to be developed using tables for the error function (NBS-AM, 1954):

$$f(0) = \frac{1}{3b_c} \left[1 - \frac{\exp(1)}{10a} \right]. \tag{9-3}$$

This expression for the line shape function at line center is accurate to better than 0.1% within a couple of kilometers of the Earth's surface (a >1.7). Accuracy is better than 0.7% within the remainder of the troposphere (a > 0.75). Figure 9-1 shows the percent deviation of Eq. (9-3) from an exact calculation of the Voigt integral at line center. This expression was developed to show clearly the effects of pressure and temperature at line center.

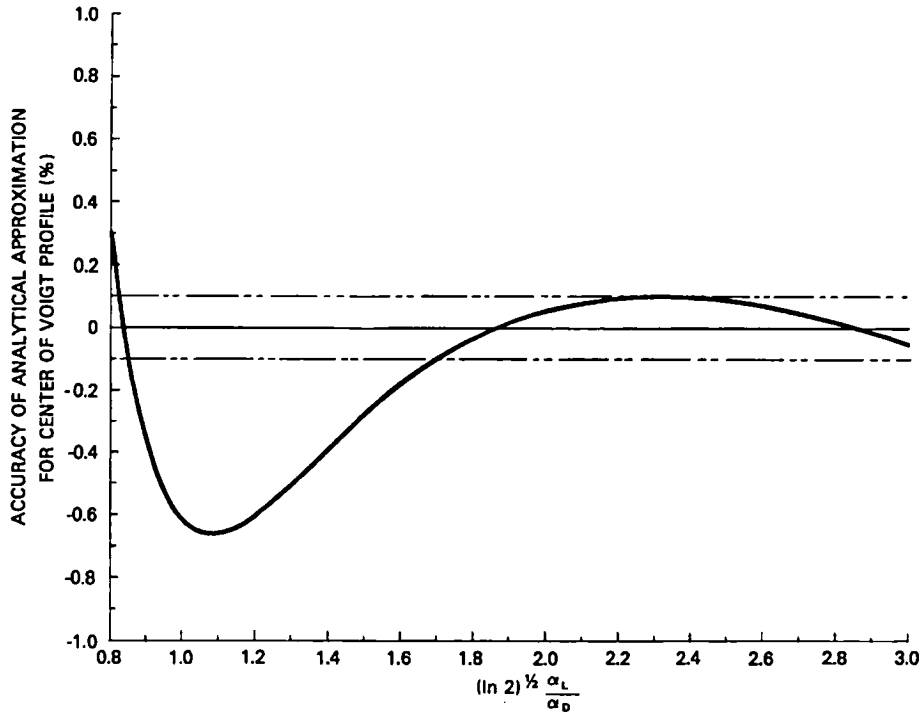

Figure 9-1. Percent difference in the fit of Eq. (9-3) to the Voigt line shape function at line center.

Using Eq. (2-9) and the above relations, it can be shown that, at line center, the resonant absorption is

$$K_0 = A_0 T^{-3/2}(1-q^*)\exp\left\{-\frac{1.439E''}{T}\right\}\left[1-\frac{\exp(1)}{10a}\right], \tag{9-4}$$

where

$$A_0 = \frac{qn_0}{3}T_0^{3/2}\frac{S(T_0)}{b_c^0}\exp\left\{\frac{1.439E''}{T_0}\right\}. \tag{9-5}$$

The percent change of the absorption coefficient with percent change in temperature can be found by differentiating Eq. (9-4) and dropping the weak pressure dependent terms:

$$\frac{dK_0}{K_0} \cong \left(\frac{1.44E'}{T}-\frac{3}{2}\right)\frac{dT}{T} = g\frac{dT}{T}. \tag{9-6}$$

Likewise, the sensitivity of the temperature determination to measurement errors in the constant term A_0 can be found:

$$\frac{dT}{T} \cong -\frac{1}{g}\frac{dA_0}{A_0}. \tag{9-7}$$

Similarly, variations in the other multiplicative factors in Eq. (9-4), *i.e.*, $(1 - q^*)$ and the line shape factor $(1 - e/10a)$, affect temperature through the same mathematical form as A_0 in Eq. (9-7).

As expected, Eqs. (9-6) and (9-7) show that the temperature sensitivity of a laser measurement will increase as higher energy lines are used, while there is a corresponding desensitization to both random and systematic errors. A tradeoff is made, however, since there is a loss in total absorption due to decreasing line strength at higher energy levels.

EXPERIMENT

The experimental layout is shown in Figure 9-2. The target used is a 1 m^2 of 3M2870 silver encapsulated lens sheeting located 1 km from an observatory housing the laser and a 0.75 m Cassegrainian telescope receiver. The target gives retroreflective returns of <20 mrad divergence. The path of the laser beams passes over a valley at a height of 10 to 20 m. Temperature monitoring for ground truth was conducted near the observatory (Figure 9-3).

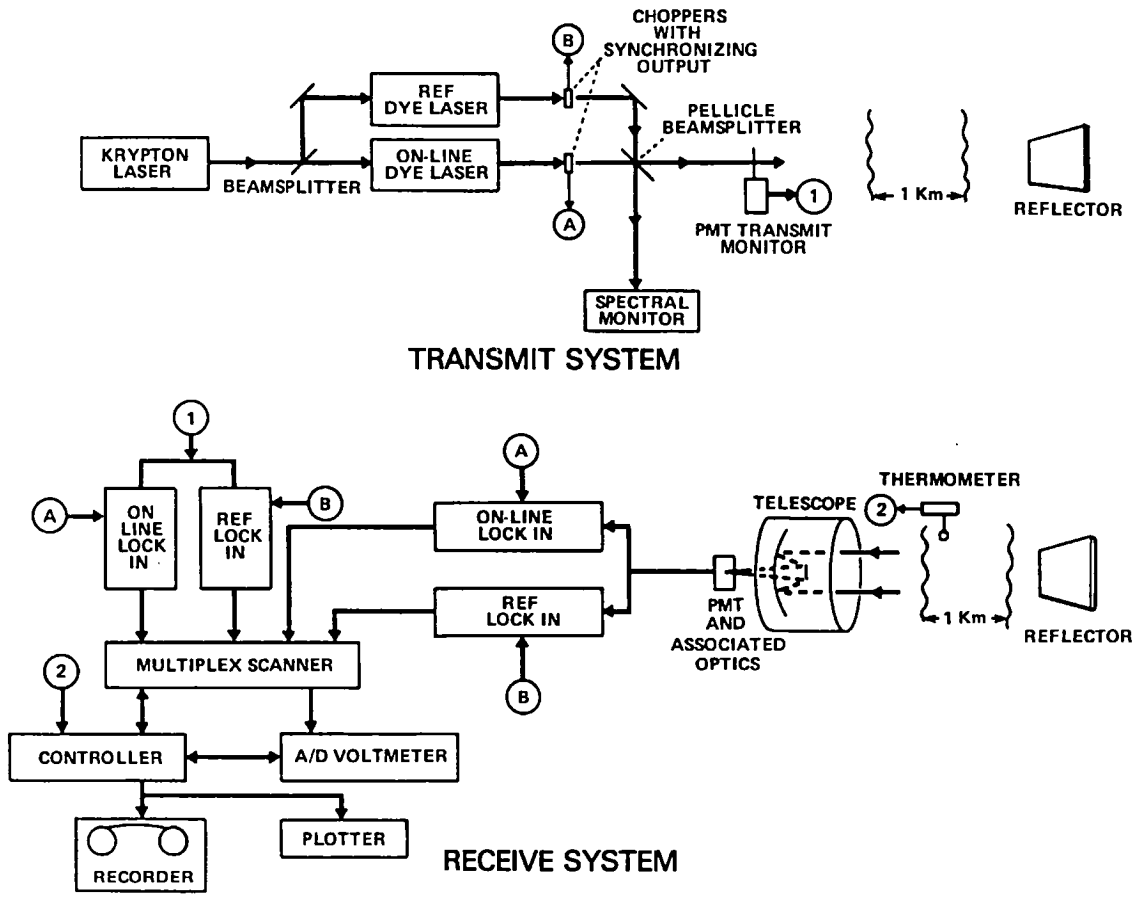

Figure 9-2. Configuration of the fixed target experiment.

Figure 9-3. Photograph of the CW laser remote sensing observatory at the Goddard Optical Research Facility.

A Spectra-Physics krypton laser developing 4 to 6 W of CW power drives both a Coherent model 599 high resolution tunable dye laser ($\Delta\nu<10^{-3}$ cm^{-1}) used for the line center measurement and a Coherent model 595 medium resolution ($\Delta\nu<0.1$ cm^{-1}) tunable dye laser used for the reference. The reference frequency was located within 1.0 cm^{-1} of line center. Both dye lasers used oxazine in ethylene glycol as the lasing medium. The krypton beam is divided with ~60% going to the high resolution laser and 40% to the reference laser for simultaneous transmission. On-line output of the high resolution laser is ~50 mW.

Each dye laser output is mechanically chopped at a different frequency to provide for synchronous lock-in amplifier detection so that simultaneous measurements can be made using only one photomultiplier tube (PMT) to monitor the outgoing signals, and one PMT for the return signals. Background is reduced by a 10 nm spectral bandpass filter on the receiving PMT. Overlapping, collinear transmission of the two laser beams is achieved using a pellicle beam splitter. About 92% of the reference laser power is lost with this method, but this merely serves to better equalize the two signals since the low resolution laser is about ten times more efficient than the high resolution unit, and its transmitted signal is not reduced by absorption. A field lens is used to image the telescope objective onto the PMT for uniform illumination despite the effects of atmospheric scintillations.

Line selection is accomplished with an oxygen-filled White cell, while line center is found by determining the signal minimum after sending the beam through the atmosphere and tuning the laser through the resonant line. Frequency stability is monitored using a 0.25 cm^{-1} free spectral range interferometer with a finesse of ~200. The reference laser frequency is monitored using a spectrometer capable of 1.5 cm^{-1} resolution. Centering of the laser frequency was accomplished and maintained to better than 2 x 10^{-3} cm^{-1}. Both lasers are collimated to produce a 0.3 m spot size at the target board which can then be monitored visually using a low pass spectral filter on a closed-circuit television system. Calibration of the system is accomplished by tuning the high resolution laser to the reference laser frequency and measuring the transmission and signal returns. This measurement is then used to normalize subsequent data runs.

A total of four lock-in amplifiers set for 3 sec filtering are used: two to monitor transmission and two for reception. The ratio of signals from these units can be used to determine K_ν, which is considered to be constant along the path with a range of R = 1061 m. Run times of <1 min could be used. Data was collected on eight different days within a period of a month.

RESULTS

For the given experimental arrangement, the 13010.81 cm^{-1} (768.38 nm) oxygen line ($J = 27$) was chosen as offering optimum temperature sensitivity and absorption. Figure 9-4 is a plot of the absorption coefficient measured over the 2 km path with respect to the thermometer measured temperature. The relative humidity and barometric pressure were recorded and used to correct the measured absorption coefficients to values for dry air at standard pressure. The humidity corrections were <0.8%, averaging 0.4%. Overall barometric variations were <1% which resulted in corrections of <0.15%. Given the ground state energy for this line of $E'' = 1084\ cm^{-1}$, from Eq. (9-6) it is found that $g \cong 4$, resulting in a significant desensitization to these error sources in temperature determination. A value of A_0 was calculated from Eq. (9-4) for each measured absorption coefficient using a value of 0.045 cm^{-1} at standard temperature and pressure for the collision broadened line halfwidth extrapolated from Burch and Gryvnak (1969). The average value and standard deviation of $A_0 = 1100 \pm 25\ K^{3/2} m^{-1}$ was determined and used in deriving the fitted curve shown in Figure 9-4. It may be noted that the calibration procedure used to determine the scaling constant A_0 normalizes the effects of errors in the molecular line strength and width to first order. By using the value of line strength from Burch and Gryvnak (1969) adjusted to standard temperature, $S(T_0) = 1.52 \times 10^{-29}$ $molec^{-1}\ m^2\ cm^{-1}$, and line width as determined above, the value of A_0 calculated from Eq. (9-5) is ~30% less than our experimentally determined value. This discrepancy could arise because this is a weak line whose parameters are difficult to measure by conventional techniques.

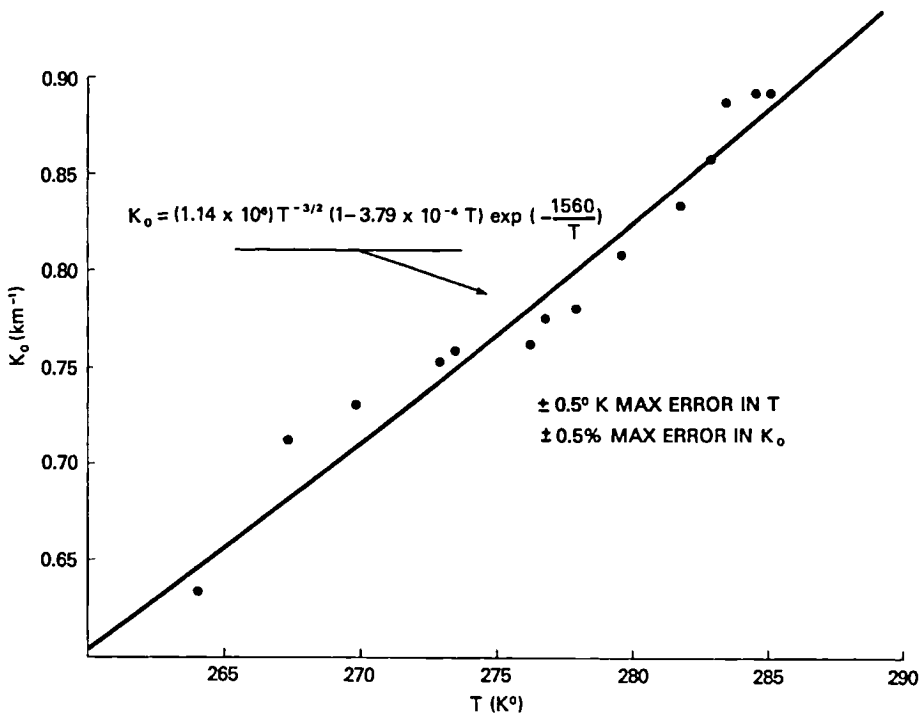

Figure 9-4. Measured absorption coefficient as a function of thermometer measured temperature. The solid curve is a fit with Eq. (9-4).

Given the absorption coefficient, the natural logarithm of Eq. (9-4) can be rearranged to solve iteratively for temperature:

$$T_{n+1} = \frac{1.44E''}{\ell n\left[A_0(1-q^*)T_0^{-3/2}\left(1-\frac{e}{10a}\right)K_0\right]}. \tag{9-8}$$

This equation converges rapidly. The initial seed temperature is not critical. Figure 9-5 is a scatter plot of the experimentally determined temperature along the path with respect to the thermometer measured temperature. The average noise in each laser transmission measurement was 0.5%, which, with a similar noise in the calibration measurement used for normalization, corresponds to a random error of 0.3 K in the temperature measurement. This follows since an error in the absorption coefficient is related to an error in transmission by a factor of the inverse optical depth, *i.e.*, the absorption coefficient times the total path. The corresponding temperature error then follows from Eq. (9-6). The thermometer temperature could be read to 1 K. The standard deviation of the scatter plot is 1.5 K.

A significant portion of the difference between the laser and thermometer measured temperature arises from the integrated path nature of the laser measurement, as opposed to the single point thermometer measurement. It is felt, therefore, that the laser measured temperature properly represents the mean temperature of the total path to an accuracy of 0.6 K, which is the combined random noise in both the calibration and actual measurement.

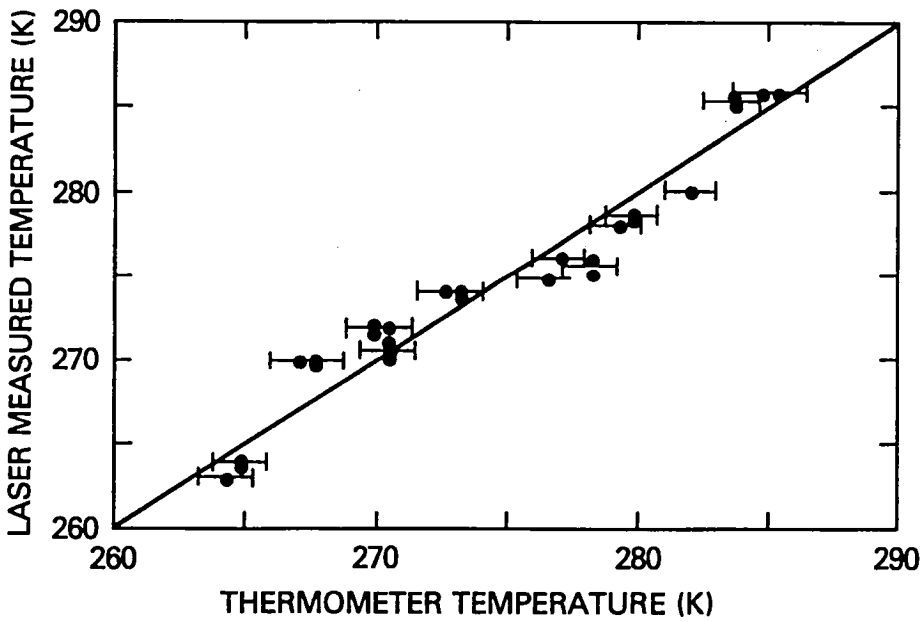

Figure 9-5. Scatter plot of the laser measured temperature with respect to the single point thermometer temperature.

CHAPTER 10 AIRBORNE AND GROUND-BASED PRESSURE PROFILE MEASUREMENTS

This chapter describes the first high accuracy remote measurements of the atmospheric pressure profile. The first ground-based measurements were made after integrating one alexandrite laser functioning as the on-line laser, with a ruby pumped dye laser as the off-line laser. The aircraft and later ground-based measurements were made using the dual alexandrite system.

For the aircraft measurements, the on-line laser was spectrally narrowed using only the thin etalon and birefringent tuner and had a linewidth of 0.08 cm^{-1}. For the ground-based measurements, all three tuning elements were utilized, giving a linewidth of 0.015 cm^{-1}.

The transmission, due to the integrated path absorption by oxygen, is determined from the ratio of the normalized signal returns at the trough and reference frequencies, as given by Eq. (1-2). Three different methods of averaging are used in processing the data:

1. Calculate the transmission from each shot and then average the transmission over multiple shots.
2. Calculate the optical depth, which is the logarithm of the transmission, from each shot and then average the optical depth over multiple shots.
3. Average each signal over multiple shots and then calculate the transmission.

For high signal-to-noise measurements such as we typically found in our aircraft measurements, the three methods produce essentially identical results. However, in the case of low signal-to-noise, disparate results are obtained. This occurs since high noise will periodically produce very small signals, and division by near zero signals in methods (1) and (2) gives disproportionately large values for the average transmission. For the case of low signal-to-noise, method (3) gives good results. We note that method (3) weights the transmission toward those shots with large signal values associated with high aerosol backscatter. Figure 10-1 is an example of the atmospheric return signals for a 100-shot average at the on- and off-line frequencies for the aircraft measurements which we will discuss shortly. The photomultiplier output was filtered with a 2 MHz bandwidth low pass filter. We note that the signal-to-noise for a single shot varies from 10/1 to 20/1, and for a 100-shot average varies from 100/1 to 200/1. For these data, the aircraft altitude was 2790 m, and the photomultiplier detector was gated on at an altitude of ~2200 m to block the effects of intense near-field scattering. As shown, the signals at both the on- and off-line frequencies are saturated above 1800 m. Figure 10-2 is an example of the atmospheric transmission due to resonant absorption by oxygen, as calculated from method (3) for a 100-shot average.

To accurately obtain the transmission, we subtract any bias from the return signals. This is particularly important for low signal levels. We take data at a 5 MHz sampling rate for a period of 100 μsec. For the downward-viewing aircraft data, the round-trip signal return is completed in <20 μsec for an altitude of 2790 m. We have observed a small signal induced bias on the PMT output associated with large signals backscattered from the Earth's surface. This bias gradually decays to zero over a period of tens of microseconds. The zero level is found from separately averaging the data in the on- and off-line signals for each shot for the 95 to 100 μsec time period. In this time period, the signals have decayed to a fairly constant level for both the aircraft and ground-based data.

These data were taken before the addition of a rephaseable time base to clock the digitizers; therefore, jitter in the digitizer time base caused errors in the altitude registration between the on- and off-line signals of up to 0.4 elements (12 m). This caused significant errors in the determination of the transmission and in the

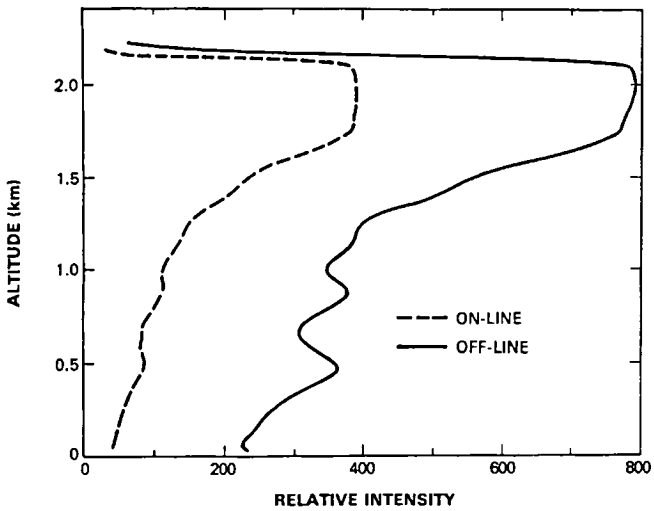

Figure 10-1. Relative intensity of the atmospheric backscattered lidar signals from the on- and off-line lasers for aircraft measurements at 2790 m altitude. The photomultiplier detector is gated on at 2200 m altitude. Results are for a 100-shot average (2 km horizontal resolution) and a 30 m vertical resolution.

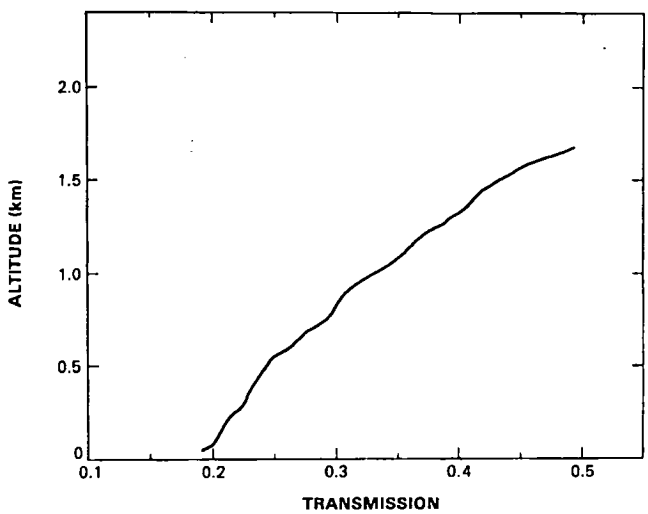

Figure 10-2. Transmission due to atmospheric oxygen absorption for the 100-shot average aircraft measurements of Figure 10-1.

atmospheric pressure profile. It was particularly evident in the presence of strong aerosol layers. To correct for this effect, we introduced sub-element time shifts of 3 to 12 m by interpolating the signal data. The shift is found by minimizing the variance in the transmission due to aerosol layers.

A modified version of Eq. (1-9) including only first order terms is used to find the pressure profile. That is,

$$\left| \int_{z_1}^{z} K(\nu) dz \right| = C \left| p^2 - p_1^2 \right|. \tag{10-1}$$

We note that for the range of altitudes used for our measurements, the errors due to higher order terms are <0.02%. To account for unknowns, such as uncertainties in the oxygen line parameters which are implicitly contained in Eq. (10-1), the pressure data from a radiosonde and measured values of the integrated absorption coefficient are used to find the value for C. Given this calibration constant, the pressure profile $p(z)$ is then found from Eq. (10-1).

Airborne measurements of the atmospheric pressure profile were made at 10 p.m. on 20 November 1985 using the Goddard lidar facility on the Wallops Lockheed Electra aircraft. Data were taken along the flight line extending from Sea Isle, DE (39°05′N/74°45′W) to Point Lynus (38°01′N/72°39′W), ~220 km off the coast of Delaware. Figure 10-3 shows data taken 115 km from Sea Isle, DE for an aircraft altitude of 2790 m. The lidar system was set up to measure pressure with the on-line laser tuned to the absorption trough at 13147.3 cm^{-1} and with the reference laser tuned to a nonabsorbing frequency near 13170.0 cm^{-1}. The lidar signal returns were sampled with a 200 nsec range gate (30 m vertical sampling) and averaged over 100 shots. The figure shows a comparison of the lidar measured pressure profile to radiosonde data taken 2 hours earlier at Wallops Island, VA (37°51′N/75°28′W). The average deviation of the lidar pressure profile data from the radiosonde data is ~1.7 mbar. We note that the noise level of the raw lidar data was close to the theoretical limit for the instrumental configuration. Figure 10-4 shows the two-dimensional structure of the

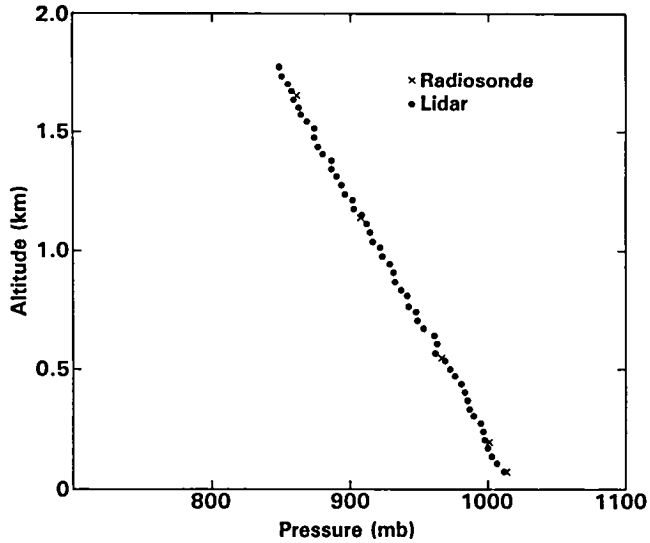

Figure 10-3. Lidar pressure profile measured along the flight track 115 km from Sea Isle, DE at an aircraft altitude of 2790 m for a 100-shot average (2 km horizontal resolution) and a 30 m vertical resolution for the data of Figures 10-1 and 10-2. Also shown are the results of radiosonde measurements at Wallops Island, VA (37°51'N/75°28'W).

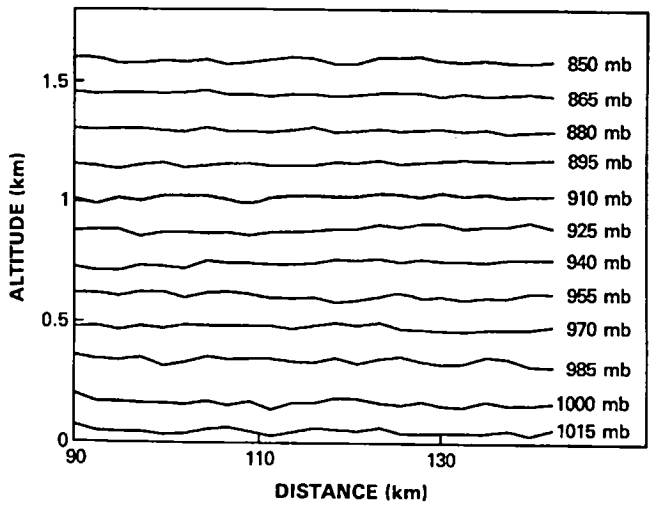

Figure 10-4. Altitude of constant pressure levels for selected pressures at intervals of 15 mbar measured by the lidar along the flight track every 2 km for various distances from Sea Isle, DE.

pressure field measured along the flight track. The figure was constructed from 23 independent pressure profiles obtained once every 2.25 km, with linear interpolation between points, for various distances from Sea Isle, DE. The data are displayed as the altitude of constant pressure levels for selected pressures shown every 15 mbar. These data were calculated from the measurements of pressure versus altitude (at 30 m intervals) by interpolating for the altitudes of constant pressure levels. The slopes of the 850 and 1000 mbar levels agree with the analysis of the National Weather Service for 6 p.m. on 20 November 1985 to within 0.15 m/km. The agreement of both the means and slopes of the pressure profile data gives a high confidence level in the instrumental performance, reliability, and the capability to collect meteorologically meaningful data.

Ground-based measurements were made from the Goddard Space Flight Center in Greenbelt, MD (39.00°N/76.85°W) using a dye laser and one alexandrite laser in March 1983 (Schwemmer, *et al.*, 1984). Measurements using two alexandrite lasers were made in October 1985. Figure 10-5 shows the pressure profile measured by the lidar on 17 October1985 using the trough at 13150.9cm^{-1}. The return signals were sampled at 200 nsec intervals and averaged over 100 shots to reduce the effects of random noise. The detector bandwidth corresponds to 37.5 m vertical resolution and a 20 sec integration time. A 10 nm bandpass optical filter was used in the receiver to reject background radiation. Radiosonde pressure data taken at Washington Dulles Airport (38.98°N/77.46°W) 5 hours after the lidar data are shown for comparison. The standard deviation of the lidar pressure data from the radiosonde data is 2.0 mbar.

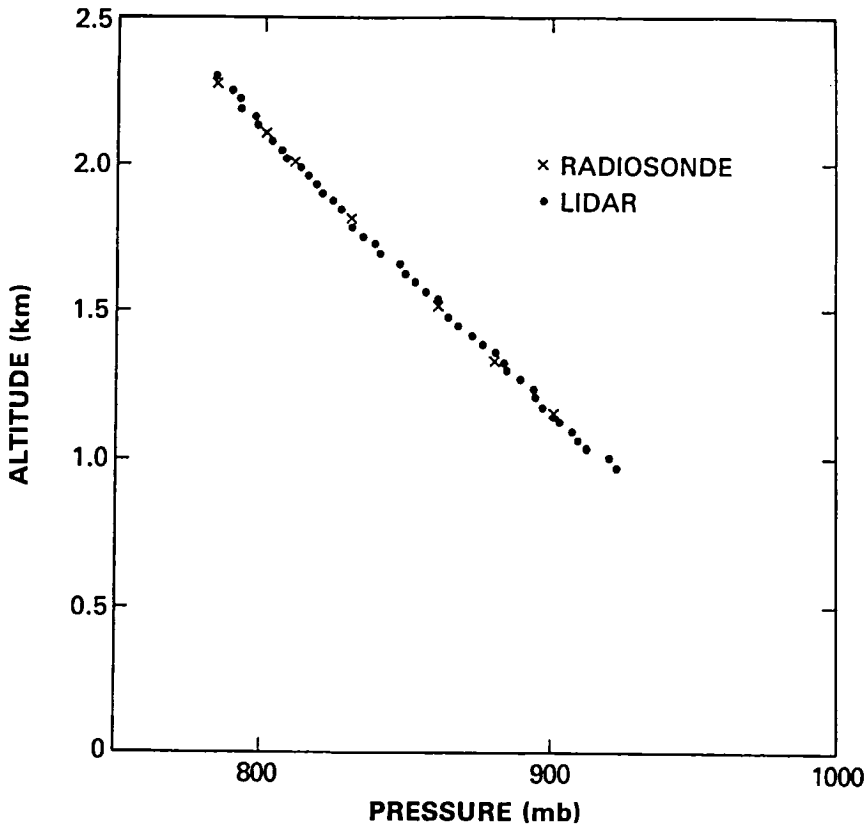

Figure 10-5. Lidar pressure profile measured at Goddard Space Flight Center, Greenbelt, MD (39°00′N/76°51′W) with an upward viewing lidar for a 100-shot average and a 30 m vertical resolution. Also shown are radiosonde measurements at Dulles Airport (38°59′N/77°28′W).

CHAPTER 11 MESOSCALE GRAVITY WAVE OBSERVATIONS

INTRODUCTION

Gravity or buoyancy waves have long been recognized as an interesting and ubiquitous atmospheric phenomenon. Gravity waves influence cloud formation, trigger and organize convective cells and precipitation, produce and interact with turbulence, and transport momentum and energy both horizontally and vertically (Einaudi, *et al.*, 1978, 1979) . Recognition of the importance of mesoscale and microscale atmospheric processes and their potential impact on the larger scale has increased attention on gravity waves over the last two decades.

The observational study of gravity waves, however, has been mostly limited to analysis of surface microbarograph observations (*e.g.*, Keliher, 1975; Einaudi, *et al.*, 1989) or other ancillary information such as surface wind and precipitation records and patterns in radar-observed precipitation and satellite-observed cloud fields (*e.g.*, Erickson and Whitney, 1973; Stobie, *et al.*, 1983; Pecnick and Young, 1984; Bosart and Seimon, 1988). Clark, *et al.* (1981) and Smith (1988c) have also incorporated *in situ* measurements from a light aircraft into their analysis of undular bores. Until recently, acoustic sounding (sodar) has provided the only means of remotely probing the internal structure of these waves (*e.g.*, Brown and Hall, 1978; Cheung and Little, 1990). As a result, the extensive body of theory addressing the internal structure, generating mechanisms, and propagation of mesoscale atmospheric waves (*e.g.*, Gossard and Hooke, 1975; Lindzen and Tung, 1976; Lalas and Einaudi, 1976; Maxworthy, 1980; Rosenthal and Lindzen, 1983; Chimonas and Grant, 1984; Canavero, *et al.*, 1990) has primarily relied on matching boundary conditions at the surface for quantitative confirmation. Laboratory studies utilizing liquids, such as Thorpe (1978) and Rottman and Simpson (1989), have provided a useful alternative means of investigating the structure of buoyancy waves and density currents.

Significant progress has recently been made in developing active remote sensing systems capable of probing the internal structure of mesoscale waves at high temporal or spatial resolution, or both. Very high frequency (VHF) Doppler wind profilers (Lu, *et al.*, 1984; Ramamurthy, *et al.*, 1990), Doppler radar (Doviak and Ge, 1984; Fulton, *et al.*, 1990), and Doppler CO_2 infrared lidar (Post, and Neff, 1986) have been used to resolve mesoscale flows. Raman lidar (Melfi, *et al.*, 1989; Koch, *et al.*, 1991) and differential absorption lidar (Browell, *et al.*, 1991) have provided unprecedented descriptions of moisture fields at high resolution. Utilization of these capabilities for studies of mesoscale tropospheric phenomena is just beginning. The early results, however, are exciting. For example, Ramamurthy, *et al.* (1990) and Malhotra, *et al.* (1991) provided an unprecedented analysis of height-dependent wind structure and vertical displacements derived from wind profiler observations of large mesoscale solitary wave events that triggered strong wind gusts and dramatically influenced precipitation. Doviak, *et al.* (1991) made use of Doppler radar observations of a thunderstorm-generated solitary wave for a critical comparison with the weakly nonlinear theory of wave propagation, while Koch, *et al.* (1991) utilized Raman lidar observations to derive a detailed characterization of an intense atmospheric undular bore.

This chapter includes further analysis of the high resolution pressure profiles obtained using our airborne DIAL system introduced in the preceding chapter. The data were obtained during a test flight of the system in 1985. Technical difficulties and inclement weather limited the amount of data that were obtained. Nonetheless, analysis has revealed the presence of a strong wave feature in the pressure field that we interpret as an intense mesoscale gravity wave. Our purpose here is to illustrate the potential of DIAL pressure measurements for characterizing the spatial and temporal structure of mesoscale waves using data from this serendipitous encounter.

The DIAL observations of mesoscale gravity waves are described in the following section. Other evidence for gravity wave activity is then given. The synoptic setting and meteorological conditions are presented and discussed in the final sections of this chapter.

DIAL PRESSURE PROFILE OBSERVATIONS

Airborne measurements of atmospheric pressure profiles were made at 0300 UTC 21 November 1985 (10 p.m. local standard time) over a 52 km segment of a flight line extending from Point Lynus (38°01'N/72°39 'W) to Sea Isle, NJ (39°05 'N/74°45 'W) from an altitude of 2790 m. The aircraft heading was about 305° (toward the northwest). The terminus of the data leg was located ~100 km southeast of Atlantic City, NJ and 170 km northeast of Wallops Island, VA (Figure 11-1).

The average pressure profile derived for the entire data leg (2300 lidar shots over about 8 min) is shown in Figure 11-2 along with the 0000 UTC rawinsonde soundings from Atlantic City (ACY) and Wallops Island (WAL) on 21 November. The DIAL pressure measurements were sampled at vertical resolution of 30 m with some overlap, since the receiver bandwidth corresponds to a 37.5 m vertical resolution. The measurements extend from an altitude of 60 m to 1.59 km. The pressures observed at WAL are systematically greater than those observed at ACY. Similarly, the DIAL measurements are greater than those at WAL by a comparable amount, except at the lowest and highest levels where low signal and receiver saturation, respectively, may become significant factors. These differences are consistent with the synoptic situation (Figure 11-1), where the analyzed surface pressure gradient points toward the southeast, as also found on the 850 mb analysis at 0000 UTC. Supplemental radiosonde ascents made at 0100 and 0230 UTC from Wallops Island are nearly indistinguishable from the 0000 UTC sounding there in terms of the pressure profile.

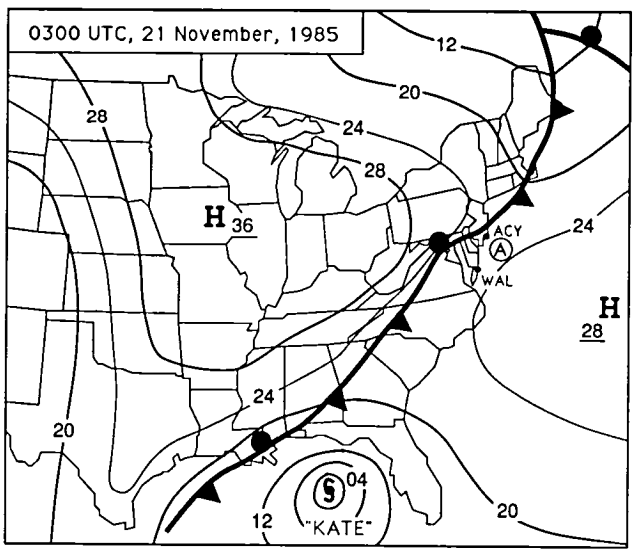

Figure 11-1. Surface analysis for 0300 UTC 21 November 1985. Location of National Weather Service rawinsonde stations at Atlantic City (ACY) and Wallops Island (WAL) and experiment location (A) are noted.

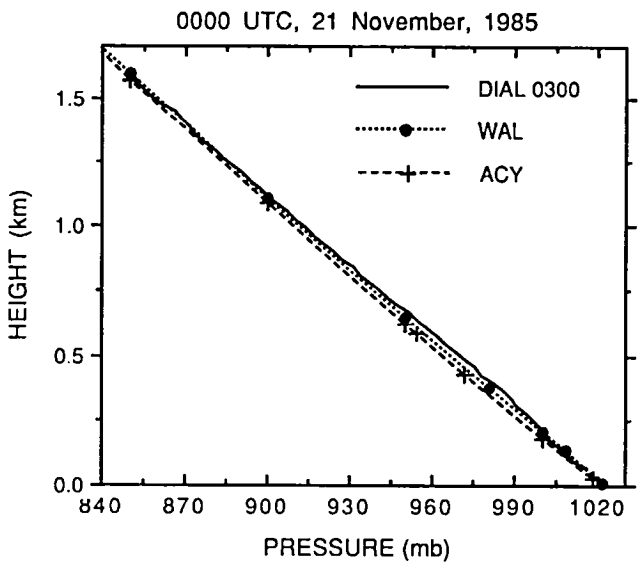

Figure 11-2. Pressure profile observed by the airborne DIAL system averaged over a 52 km flight line at 0300 UTC and rawinsonde observed pressure profiles at 0000 UTC 21 November 1985 from nearby locations.

The data record was divided into segments of 100 lidar shots, and a pressure profile was derived for each of the 23 independent segments, allowing analysis of the two-dimensional structure of the pressure field at a horizontal resolution of 2.26 km. Deviations of the observed pressures from the data leg average pressure profile are shown in Figure 11-3. Negative deviations are shaded dark (low pressure), and positive deviations are light (high pressure). The left side corresponds to the end of the data leg and is closest to the coast. The pattern of pressure perturbations exhibits a noisy appearance with a root-mean-square (rms) magnitude of 1.6 mb. This is less than 0.2% of the retrieved pressures, and is very close to the expected accuracy. The largest deviations are +5.7 and -6.0 mb with 65% of the values within ±1.5 mb and 88% within ±2.5 mb. The frequency distribution is approximately Gaussian.

A large scale pattern is evident in the pressure deviation field. This is clearly seen in Figure 11-4, where a 3-point running mean filter has been applied in the vertical (six passes) and horizontal (two passes) directions. The result is a 13-point scheme in the vertical with a half-power response bandwidth of 150 m or 5 data points and a 5-point triangular weighting scheme (0-1-2-3-2-1-0) in the horizontal with a half-power response bandwidth of 6.78 km or 3 points. Application of this high frequency filter has reduced the maximum perturbations to +1.7 and -2.2 mb. A distinct wavelike pattern is seen, particularly between the 0.7 and 1.2 km levels where high pressure is found toward the coast (left) and low pressure farther offshore. The maximum peak-to-peak horizontal pressure difference is about 3.5 mb and occurs at a height of 0.78 km. The centers are separated by about 30 km, corresponding to a horizontal wavelength of 60 km. Below, the pattern is reversed. This is illustrated in Figure 11-5, where the differences between the horizontal average of the pressure profiles over the leftmost (toward the coast) and rightmost 20 km of the data leg are shown. A phase reversal occurs at a height of about 0.6 km, and a vertical wavelength of about 1 km is found.

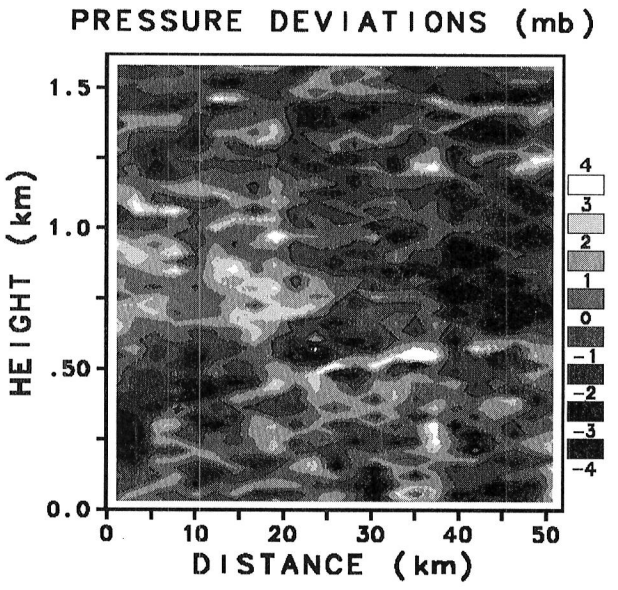

Figure 11-3. Height-dependent deviation of remotely sensed (DIAL) pressure from horizontal average along a 52-km flight line. Dark shading indicates regions of negative (low) pressure deviations, while light shading indicates positive (high) pressure perturbations. Contours at 1 mb intervals.

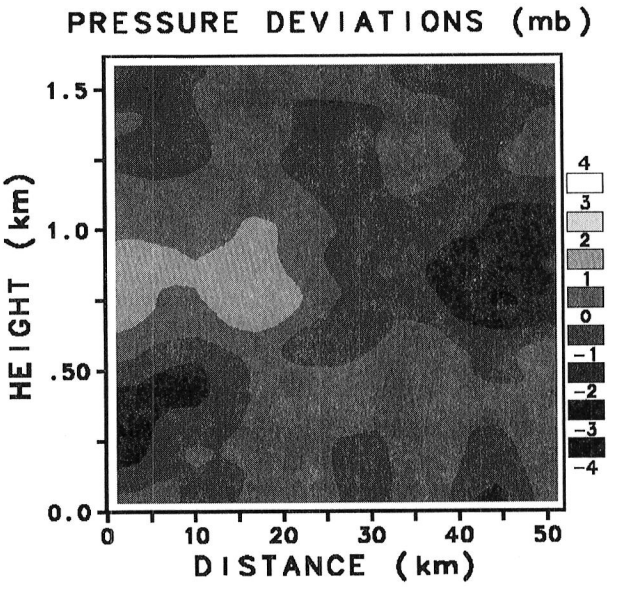

Figure 11-4. Same as Figure 11-3 except for application of a spatial filter.

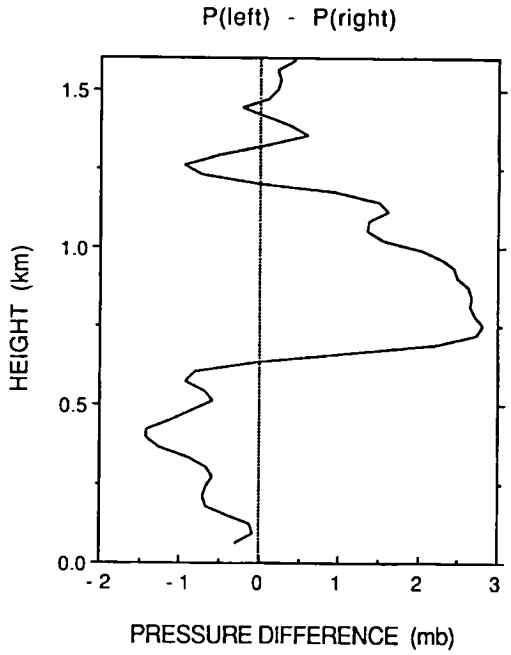

Figure 11-5. Difference between the remotely sensed pressure profile horizontally averaged over the last (left) and first (right) 20 km of a 52 km flight line (see Figure 11-3).

Near the surface and above the 1.2 km level, the larger scale feature is not evident. This is further illustrated in Figure 11-6, where the horizontal distribution of the pressure deviation along the flight track is shown for four layers. The deviations have been vertically averaged over layers that are 270 m thick (9 data points). The 60 km wavelength structure is evident in the layers from 0.36 to 0.5 km and from 0.78 to 1.02 km (layer average pressures of 972 and 918 mb, respectively), as is the previously noted phase reversal. Nearly four complete shorter wavelength cycles are found in the layers from 0.06 to 0.3 km and from 1.14 to 1.38 km (1003 and 878 mb, respectively) corresponding to a horizontal wavelength of about 15 km. Some of these features exhibit good coherence in the vertical, *e.g.*, the peak near 37 km from the data leg terminus.

Our interpretation of these observations is that the 60 km feature is a strong mesoscale gravity wave. Further evidence for this interpretation is given in the following section. The smaller scale 15 km features seen in Figure 11-6 (and in Figure 11-4), which are particularly evident at the upper (Figure 11-6a) and lower levels (Figure 11-6d), may also correspond to gravity waves. Before proceeding, we offer the following discussion of potential error sources affecting the measurements.

The instrument configuration, data system, and data processing procedures for this experiment are estimated to yield random errors of about ±1.5 mb (rms), as detailed in Korb, *et al.* (1989) and the references provided therein. This is very close to the observed variance, and led us to conclude that the measurements were accurate to this level. The appearance of the 60 km feature, however, has caused us to re-examine this issue in order to ascertain if such a pattern might result from instrumental or sampling characteristics, rather than actual structure in the atmospheric pressure field. Candidate error sources are required to have a significant nonrandom component over hundreds of successive lidar shots.

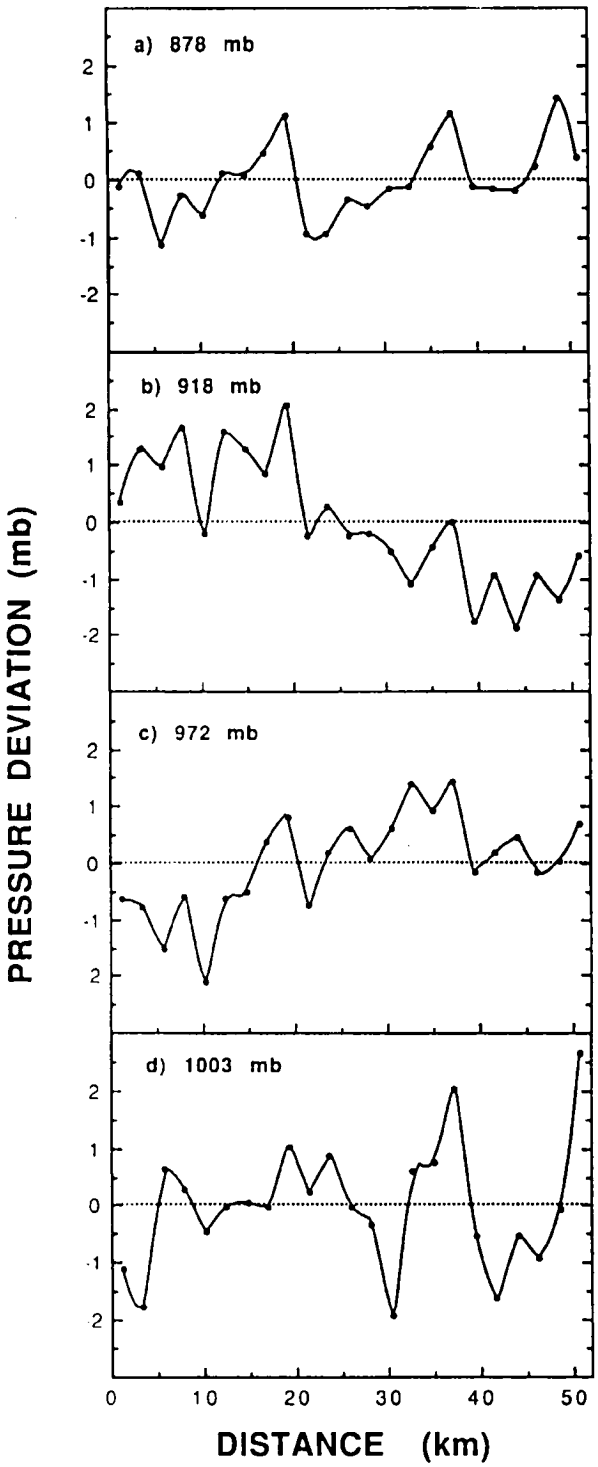

Figure 11-6. Deviation of remotely sensed pressure from the horizontal average along a 52 km flight line at heights of (a) 1.26 km, (b) 0.9 km, (c) 0.43 km, and (d) 0.18 km. Deviations have been averaged over 270 m deep layers (nine data points) centered on these heights. Corresponding layer mean pressures are 878, 918, 972, and 1003 mb, respectively.

Spectral jitter (shot-to-shot) is one source of random error and was included in the estimate of system noise given by Korb, *et al.* (1989). Although minimized in the absorption trough method used here, a shift in lidar spectral frequency affects the entire profile of returns from an individual shot. Thus, significant drift in spectral frequency would produce a horizontal trend in the derived profiles at all levels. The observed phase reversal in the 60 km wave feature (Figure 11-5) is not consistent with this characteristic.

The determination of the location of the sea surface in the lidar return is another source of error, since the altitude assignment proceeds upward from the surface. The ability to make this determination is limited by the speed and accuracy of the interval timing mechanism used for sampling the detector. As in the case of spectral jitter, an error in locating the surface biases the entire profile. For the system used here, the surface location for an individual shot is accurate to better than ±10 m (±1 mb) and much better than this for the 100-shot averages used in deriving the individual pressure profiles.

Thus, neither of these potential error sources appears capable of generating the observed response in terms of the observed phase reversal of the 60 km wave feature. Fluctuations in transmitted laser power were monitored and taken into account in this method. Other possible sources of error, such as jitter in the timing circuit, are not likely to produce nonrandom behavior at the required scales. Variations in aircraft attitude or altitude along "level" flight lines yield errors of <0.1 mb in magnitude. We conclude that the larger scale wave feature is not a result of instrument error.

OTHER EVIDENCE FOR MESOSCALE WAVES

Satellite imagery

Independent evidence for the possible existence of mesoscale gravity wave activity within the experiment area comes from GOES (Geostationary Operational Environmental Satellite) infrared imagery. Distinct cloud bands resembling a wave train are found in the cirrus outflow emanating from Hurricane Kate (Figure 11-7). This "wave train" extended from Alabama into Virginia and the Delmarva region and was continuously observed over many hours. The wavelets were oriented transverse to the upper level flow with a wavelength of 25 to 30 km. The banded structure was most apparent in the optically thinner portions of the cirrus shield. As cloud optical thickness increased with time, the transverse cirrus cloud bands became more difficult to discern as the contrast within the scene decreased. The width of the wave-containing channel expanded near the coast, where there is indication of increased separation of the cloud bands. The cirrus cloud bands were barely discernible in the visible satellite imagery from 20 November, but were more evident in the early morning imagery on 21 November. Lower level transverse cloud bands (~10 km separation) were also found in visible imagery over the Appalachian Mountains in West Virginia.

Assuming that the observed pressure wave (Figure 11-4) was oriented with the transverse cirrus cloud bands and adjusting the observed wavelength (~60 km) along the flight track for aircraft heading, a wave-normal wavelength of ~40 km is obtained. This is larger than, but not too different from, the observed wavelength of the cirrus cloud bands, especially considering the uncertainty in estimating the wavelength from a sample comparable to a single wave cycle. Similarly, the shorter wavelength (~15 km) seen in the DIAL observations translates into a wavelength of ~10 km normal to the observed cloud bands.

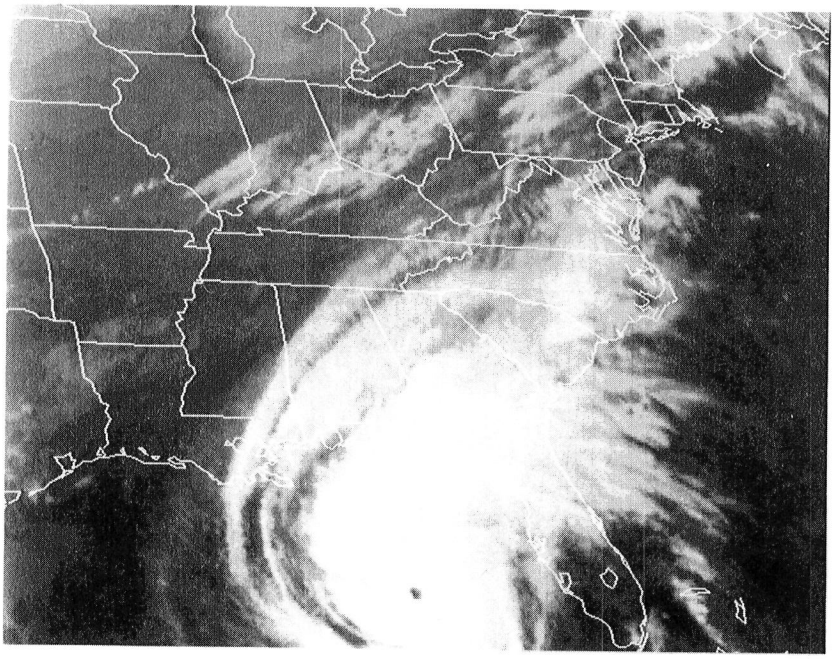

Figure 11-7. GOES infrared imagery from 2200 UTC 20 November 1985. Transverse cirrus cloud bands are most clearly seen in Virginia.

Aerosol structure

The strength of the returned signal for the reference lidar channel is determined by the intensity of radiation backscattered by aerosols. A height versus location display of range-normalized return intensity for the reference lidar channel is shown in Figure 11-8. Regions of comparable return intensity may be interpreted as regions of comparable aerosol concentration. Normalization to constant surface height has not been performed for this image, as evidenced by the small variations in the location of the surface return seen at the bottom. The high frequency vertical striping (offset) seen here is primarily a result of fluctuations in transmitted laser power. Recall that the pressure profiles are derived using the measured transmittance, where this effect is eliminated.

A wave structure with a trough-to-ridge separation of ~20 to 25 km, that is, a wavelength of 40 to 50 km, is very evident around the 1.7 km level. This feature is smaller than that estimated from the DIAL pressure data and is much closer to that seen in the satellite imagery (~40 to 45 km wavelength along the flight track). The variation in the height of this feature corresponds to a wave amplitude of ~250 m. Subtle features near this level may indicate an even larger wave amplitude (~500 m). The appearance of this image bears a striking resemblance to a laboratory experiment on the breaking of finite amplitude internal gravity waves in a shear flow reported by Thorpe (1978). This phenomenon is distinct from the familiar Kelvin-Helmholtz instability, as discussed in Thorpe (1979).

The wave pattern is less evident at lower altitudes in this display, but is more apparent in other image enhancements. Nonetheless, it can be seen here that a feature near the 0.4 km level shows depressed elevation toward the coast (left), while the opposite is found near the 0.8 km level. This is consistent with the phase reversal found at the 0.6 km level for the larger scale wave feature in the pressure perturbation field

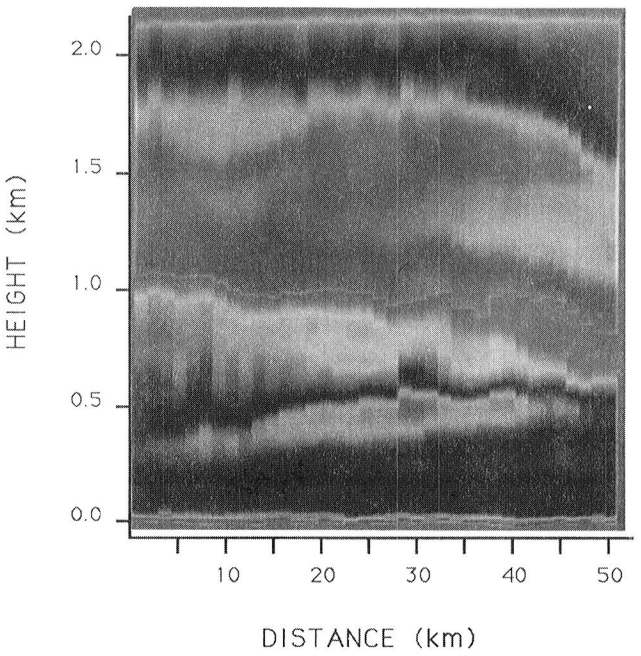

Figure 11-8. Image display of range-normalized return from the reference frequency lidar primarily depicting strength of aerosol backscatter.

(Figure 11-5) . Elevated heights are associated with regions of high pressure and depressed heights with regions of low pressure (Figure 11-4).

Barograph observations

National Weather Service (NWS) barograph data were examined for all stations in New Jersey, Maryland, Delaware, and Virginia. Only 4-day strip chart data were available. We were unable to obtain any special microbarograph observations or 24-hr charts. A wavelike feature was found in the trace from Atlantic City just prior to the time the DIAL observations were obtained (Figure 11-9). The initial sharp pressure rise (left) may be associated with a restart of the recorder at about 0100 UTC. The amplitude of the wave feature (~0.2 mb) is much less than that observed with the DIAL system (~3.5 mb). This might be partly attributed to the damped response of the NWS sensor. Alternatively, strong amplification may have occurred as the wave moved offshore, where a very stable marine boundary layer was present.

Pressure traces from other coastal stations in the Delmarva region also showed disturbances at about this time. The quality of the data records, however, as well as differences between stations, makes any analysis highly uncertain. Stations to the north did not show comparable features. This may indicate that mesoscale wave activity was confined to a fairly narrow channel, which is consistent with the observed cirrus cloud band patterns.

Taken together with the DIAL-observed wavelength, the observed duration of the wave at ACY indicates a wave propagation speed of ~20 m/sec. Three larger amplitude (~0.4 mb), but comparable duration, wave features were detected between 2330 and 0130 UTC at the Baltimore-Washington International Airport (BWI). The line from BWI to ACY roughly parallels the direction normal to the observed cirrus band features (Figure 11-7). If waves are assumed to have propagated from BWI to ACY, then the speed of propagation was between 15 and 30 m/sec, which is within the range of reported horizontal phase speeds for waves of this scale (~10 to 40 m/sec) .

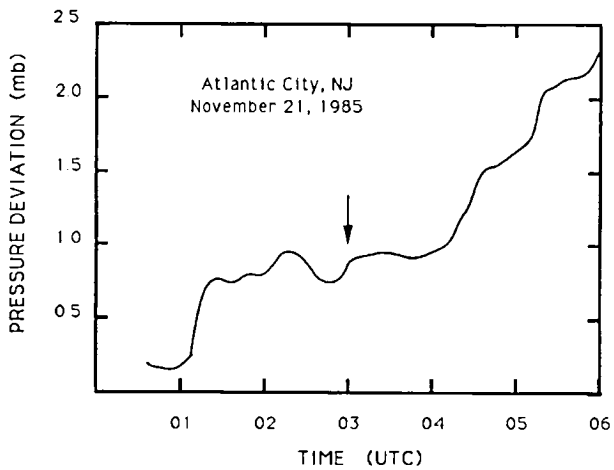

Figure 11-9. Barogram trace (relative scale) from National Weather Service station at Atlantic City (ACY) for 21 November 1985. Arrow indicates approximate time of offshore DIAL pressure-profile measurements. The initial sharp pressure rise (left) may be associated with a restart of the recorder at about 0100 UTC.

Synoptic setting

The synoptic situation in which the DIAL pressure profile observations were made was similar in some respects to the synoptic setting described by Uccellini and Koch (1987) as common to observed mesoscale wave disturbances with wavelengths from 50 to 500 km, surface pressure perturbation magnitudes from 0.2 to 7.0 mb, and propagation speeds of 10 to 40 m/sec. A strong jet streak propagating toward an upper tropospheric ridge axis existed to the northwest of the experiment area, as shown in Figure 11-10. Wind speeds >65 m/sec were observed from northern Illinois to western New York at the 250 mb level. Although winds at WAL and ACY were only ~35 m/sec at 260° at this level (~10.8 km), winds >50 m/sec were observed at higher levels, as shown in Figure 11-11. The inflection axis between the 250 mb trough and ridge axes occurred over northern Maine in the exit region of the jet streak, and trailed southward along the coast into western Virginia, where a transition to a diffluent pattern in the geopotential height field was analyzed (Figure 11-10) . The anticyclonic curvature of the flow associated with the cirrus wavelets (Figure 11-7) indicates that the inflection axis extended westward from Virginia and bounded the wave channel on the north and west. Strong vertical wind shear was observed in this region of anticyclonic horizontal wind shear.

In contrast, the situations described by Uccellini and Koch (1987) were generally located closer to the jetstream axis (see their Figure 11-1) in the exit region downwind of the inflection axis. The presence of Hurricane Kate clearly differentiates the present case. Gravity wave activity, as evidenced by transverse banded structure in the outflow cirrus shield, is not uncommon in tropical cyclones.

Uccellini and Koch (1987) also note that conditions necessary to form a wave duct were present in many of the cases they considered. A duct is formed when a stable layer lies beneath a less stable layer capable of reflecting vertically propagating waves (Lindzen and Tung, 1976). A critical layer aloft and a statically stable lower troposphere below an elevated frontal surface were usually identified. In most cases, warm air

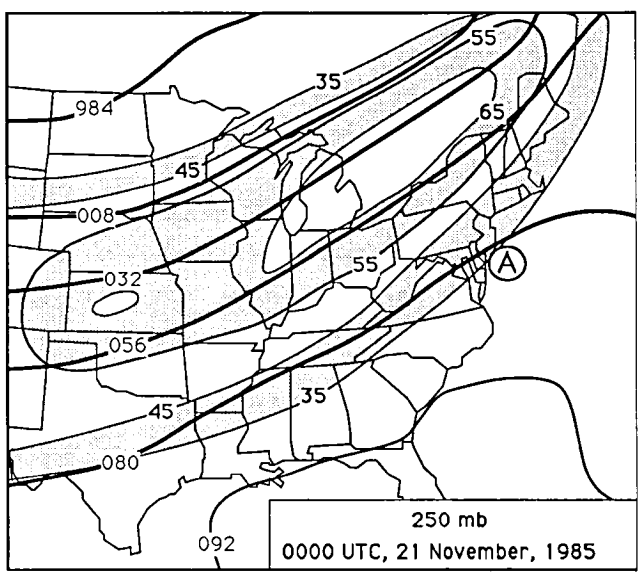

Figure 11-10. Analysis of geopotential height (dam, heavy lines) and wind speed (m/sec, thin lines and shading) on the 250 mb pressure surface at 0000 UTC 21 November 1985.

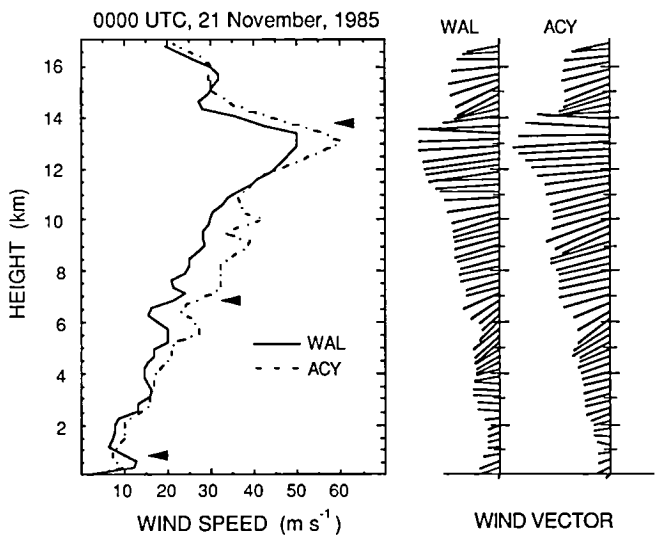

Figure 11-11. Rawinsonde-observed wind profiles from Atlantic City (ACY) and Wallops Island (WAL) at 0000 UTC 21 November 1985. Pointers indicate location of low Richardson number shear layers.

overrunning was observed in association with a surface warm front located to the southeast. In the present case, a surface cold front (Figure 11-1) was located to the southeast of the region where the mesoscale cirrus cloud bands were observed (Figure 11-7). The estimated wave propagation speed and observed winds (Figure 11-11) indicate that a critical level was present.

LOCAL SOUNDINGS

Upper troposphere

Temperature soundings from WAL and ACY at 0000 UTC are shown in Figure 11-12. Both soundings exhibit a high and cold tropopause (-67°C at 13.6 km and 160 mb at WAL). The upper troposphere was statically stable above 10.4 km at WAL and above 11.2 km at ACY, as evidenced by the slope of the corresponding potential-temperature profiles (Figure 11-12) . Vertical wind shear was fairly strong here, with magnitudes from 12 to 17 m/sec-km at ACY and from 7 to 12 m/sec-km at WAL (Figure 11-11). Richardson number R_i was >1.0 within this stable region, except for a relatively shallow (0.4 km) subtropopause layer above the level of maximum winds where values of 0.6 were found in both soundings. Although $R_i \leq 0.25$ is required for shear-generated waves, rawinsonde-observed $R_i \sim 0.5$ has frequently been associated with gravity-wave generation attributed to jet stream shear (Keliher, 1975; Gedzelman and Rilling, 1978; Gedzelman, 1983). Computations of vector wind shear and R_i reported here utilize the standard NWS rawinsonde product, where wind observations are interpolated to levels of thermodynamic observations with some smoothing. The "raw" 1 min wind observations shown in Figure 11-11 indicate somewhat larger shears.

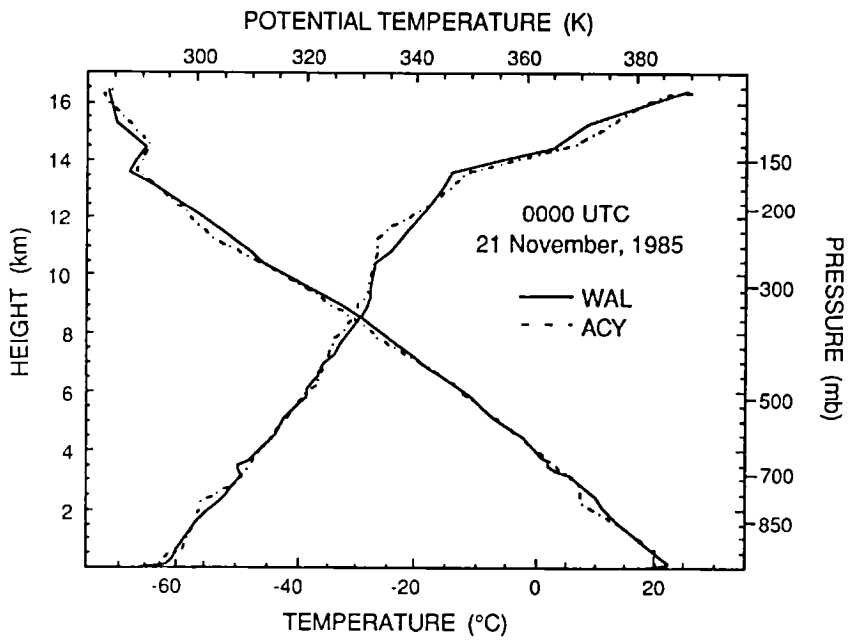

Figure 11-12. Rawinsonde-observed temperature and corresponding potential-temperature profiles from Atlantic City (ACY) and Wallops Island (WAL) at 0000 UTC 21 November 1985.

Conditionally unstable (or nearly so) conditions existed immediately below the upper tropospheric stable region in the layer from 9.0 to 10.4 km at WAL and from 8.9 to 11.2 km at ACY. Lapse rates were very near the appropriate ice pseudo-adiabatic lapse rate (G = 8.9 to 9.6°C/km versus G_i = 9 to 9.4°C/km). Saturation with respect to ice was observed 0.5 km above the base of this layer at ACY (humidity data ends at -38.5°C), with very dry conditions below (Figure 11-13). Relative humidity with respect to ice was less at WAL (78% at 9.3 km), but increased with height. Wind speeds at WAL were fairly constant through the conditionally unstable layer (Figure 11-11). Overall, ACY had low shear, but wind maxima were observed at the base and middle of the layer. As a result, values of R_i ranged from 1.3 to 7.1 at WAL with values from 0.7 to 2.0 at ACY.

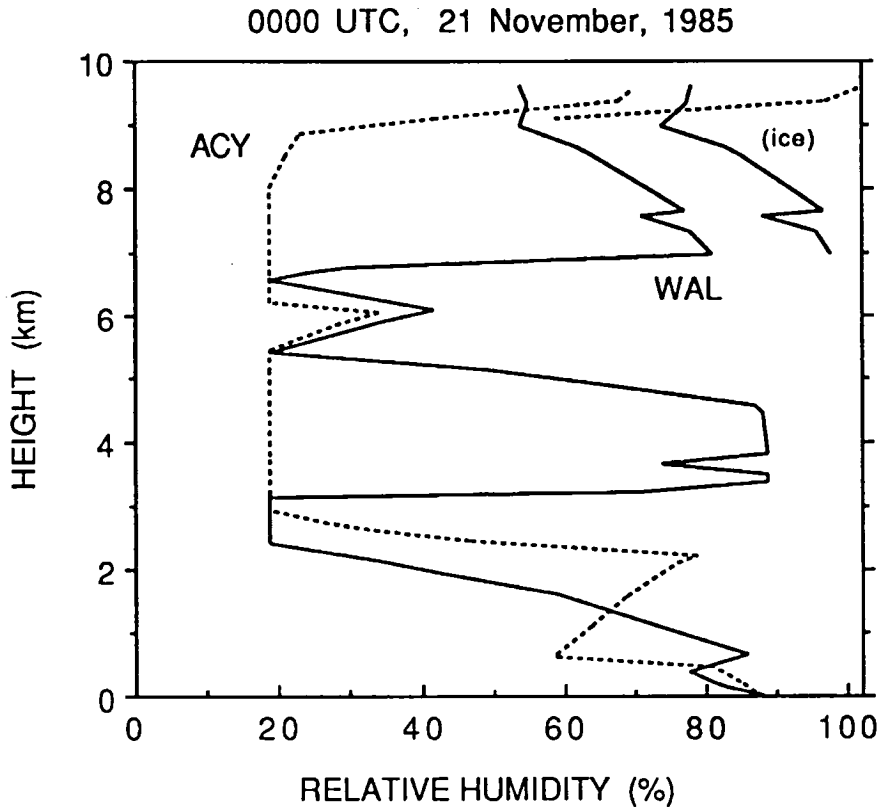

Figure 11-13. Rawinsonde-observed relative humidity profiles from Atlantic City (ACY) and Wallops Island (WAL) at 0000 UTC 21 November 1985. Corresponding profiles of relative humidity with respect to ice are also shown at upper levels.

Satellite observations indicate that the cirrus wave train was located in the upper tropospheric stable layer. Minimum equivalent blackbody temperatures approached -60°C in the southern portion of the wave channel, where the cirrus clouds were denser. Values from -30° to -50°C were observed over Virginia and the Delmarva area, where optical thickness was apparently less. Available moisture observations indicate that cloud base occurred in the underlying conditionally unstable (near ice neutral) layer. Thus, convective cirrus generation may have been occurring or developing near cloud base. This case is similar to the subtropical jet stream case reported by Sassen *et al.* (1989), where mesoscale organization (~100 km wavelength) was found in lidar and radar observations of a deep (6 km) extended cirrus system formed in a stable upper troposphere to the south of the jet axis. Cirrus generation was attributed to a relatively shallow subtropopause generating

layer and a convective layer near cloud base. Starr and Wylie (1990) have interpreted the occurrence of conditionally unstable conditions found near the base of extended jet stream cirrus systems as arising from the accumulated effects of evaporation of precipitating ice crystals. Differential temperature advection was also cited as a contributing factor. Although Sassen, *et al.* (1989) did not speculate on the origin of the mesoscale structure (~20 to 100 km) that is commonly observed in extended jet stream cirrus systems (Sassen, 1990, personal communication), Stevens, *et al.* (1989) suggested that asymmetric inertial instability associated with anticyclonic shear to the south of the subtropical jet core may have caused wave structure, comparable to that seen in the present case, in the case they examined.

Middle troposphere

Overall, a fairly stable thermal stratification was observed through the middle troposphere where $G = 6.8°C/km$ from 2.9 to 8.8 km at ACY and 6.5°C/km at WAL. The ACY sounding was very dry in this region, while the WAL sounding showed moist layers extending from 3.2 to 4.4 km and above 7.0 km (Figure 11-13). The shallow superadiabatic layer followed by a shallow isothermal layer associated with the lower moist layer at WAL (Figures 11-12 and 11-13) may indicate the presence of a thin cloud layer at 3.4 km. The observed temperature structure may be attributed to wetting-induced errors, although this cannot be confirmed. Similar, but much less pronounced, structure is found around the 6.1 and 7.6 km levels, where peaks in the humidity profile are also found.

The wind profiles exhibit significant fine structure in this region with good similarity between the WAL and ACY soundings. In particular, relatively strong shear was found in a layer from 6.5 to 7.5 km (Figure 11-11). Magnitudes exceeded 19 m/sec-km at WAL and 12 m/sec-km at ACY. As a result, R_i was <0.25 in the 6.5 to 7.0 km layer at WAL, while a value of 0.4 was observed in the 6.6 to 7.5 km layer at ACY, where the vertical resolution was less. Thus, vertical wind shear as a wave generating mechanism is strongly indicated in this dry layer that abuts the base of a moist layer in the WAL sounding.

Lower troposphere

The 0000 UTC Wallops Island sounding shows a strong, but shallow (120 m), surface inversion layer (Figure 11-14); otherwise, the lower tropospheric thermal stratification was fairly uniform and statically stable ($r = 5$ to 6.5°C/km) with no distinct boundary layer evident. Surface temperature was approximately equal to that of the adjacent waters, and winds were southerly (on-shore component) at this coastal location. Above the moist maritime surface layer, winds shifted to the west-southwest and increased abruptly, suggesting a low level jet at the level where a relative minimum in the humidity profile occurred (Figure 11-11). As a result of the strong wind shear, R_i values of ~0.1 were found in the layer from 130 to 370 m, giving a strong indication of the possibility of shear-generated waves; otherwise, lower tropospheric values of R_i ranged from ~1 just above the level of maximum winds to larger values.

A similar, but weaker, low level jet structure was detected in the Atlantic City sounding (Figure 11-11) with a corresponding minimum in relative humidity (Figure 11-13) . A temperature inversion existed near the 0.5 km level defining the top of the boundary layer (Figure 11-14) . The boundary layer is quite stable, with a weak surface inversion reflecting the early effects of nocturnal radiative cooling. Boundary layer winds were from the southwest, yielding a continental influence at this station that is more inland (~30 km) than Wallops Island. A second maximum in relative humidity was found near the 2 km level, where the temperature lapse rate was conditionally unstable. Nearly isothermal conditions existed above this feature where extremely dry conditions were observed, as at WAL. Corresponding lower tropospheric values of R_i generally ranged upward from ~1. A value of 0.6 was, however, computed for the conditionally unstable layer near 2 km.

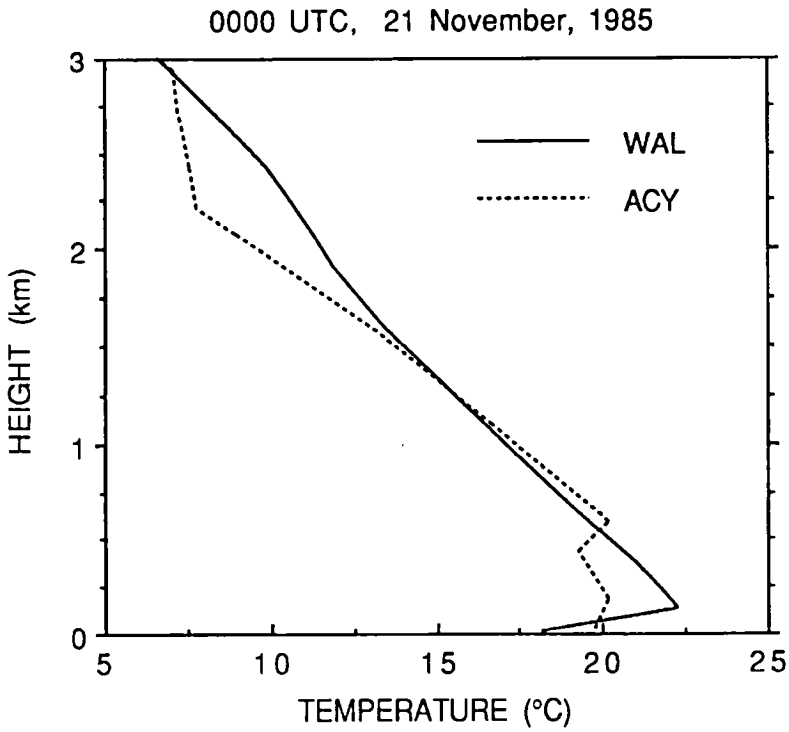

Figure 11-14. Rawinsonde-observed lower-tropospheric temperature profiles from Atlantic City (ACY) and Wallops Island (WAL) at 0000 UTC 21 November 1985.

DISCUSSION

Uccellini and Koch (1987) suggest that generation of mesoscale gravity waves through a geostrophic adjustment process at upper levels is a likely source mechanism in the cases they considered, which have some similarities to the present case. They also acknowledge that vertical wind shear may have been an important factor. No attempt has been made to quantify the possibility of geostrophic adjustment as a possible gravity wave generation mechanism in this case (*e.g.*, as in Koch and Dorian, 1988). Nevertheless, this seems to be a likely possibility, given the spatial extent of the upper tropospheric cirrus wave train and its location in an area where the upper level anticyclonic outflow from Hurricane Kate abutted the strong, cyclonic flow associated with the mid-latitude jet stream.

Three separate layers were identified where shearing instability was likely: a subtropopause layer above the jet maximum (R_i = 0.6), a mid-tropospheric shear layer (R_i ~ 0.25), and a lower tropospheric shear layer associated with a low level jet flow over a very stable marine surface layer (R_i = 0.1) . All three layers were statically stable and relatively shallow (400, 500, and 240 m, respectively). In general, the moisture and wind observations showed a consistent picture of laminated structure where distinct features in the wind profiles were associated with marked changes in the relative humidity profiles. Subsequent soundings at WAL (0100 and 0230 UTC) showed increased humidity in the previously detected moist layers (0000 UTC) that were still interleaved with very dry layers. Unfortunately, wind observations were not obtained for these latter soundings that were terminated near the 6.5 km level.

Given the spatial extent and wavelength of the upper tropospheric cirrus wave train, a duct would be required to sustain corresponding mesoscale gravity waves. We hypothesize that the four conditions required by the Lindzen and Tung ducting theory (Koch and Dorian, 1988) were satisfied in this case; that is, the duct must be statically stable, it must be capped by a highly reflecting layer (a conditionally unstable layer containing a critical level), it must not contain an energy absorbing layer (no internal critical levels where $R_i > 0.25$), and it must be thick enough to contain at least one-quarter of the vertical wavelength. The lower and middle troposphere were moderately stable in terms of thermal stratification ($G \sim 6.5°C/km$). A shallow, but quite stable, marine surface layer existed over the experiment area with a deeper stable boundary layer over the upwind land area. We are not able to document the existence of a critical level because of uncertainty regarding horizontal phase speed. A reasonable assumption of 30 m/sec, however, yields a critical level near the 9 km level at the base of an approximately 1.5 km deep conditionally unstable layer where ice saturation is indicated. An ice saturated layer with neutral thermal stratification with respect to ice saturated processes would serve as a highly reflecting layer for waves (despite $R_i > 1$ based on the lapse of dry potential temperature) and prevent the escape of wave energy from the duct.

Thus, it seems likely that mesoscale gravity waves of moderate amplitude (~0.2 mb) propagated into the region where a much stronger pressure wave (~3.5 mb) of comparable spatial scale (~40 km) was subsequently observed. We speculate that strong amplification of a mesoscale gravity wave occurred as it propagated out over the very stable marine boundary layer. Interaction of the larger scale wave with a low level shear layer ($R_i = 0.1$) may have resulted in generation of the smaller scale wave features (~10 km) that were also observed. The apparent vertical coherence and decreasing amplitude with height of these smaller scale, but still impressive, pressure waves indicate that they were evanescent (Figure 11-6). In contrast, the DIAL pressure observations of the larger wave might be interpreted in terms of a tilted, vertically propagating wave (Koch and Golus, 1988), as in Ramamurthy, *et al.* (1990), where the low pressure wave front slopes upward in the direction of propagation (lower left to upper right in Figures 11-3 and 11-4). Alternatively, the breaking of a finite amplitude internal gravity wave in a shear flow may have been observed, given the appearance of the aerosol image and its striking similarity to laboratory results reported by Thorpe (1978).

Finally, deep convection has often been cited as a potential source of mesoscale waves. Deep convection in advance of the approaching front (Figure 11-1) was observed in the present case. Moderate to heavy precipitation was reported in eastern Virginia and caused the termination of the flight (rain beginning on landing at Wallops Island, which was 170 km upwind of where the data were taken) . Although convective generation of mesoscale gravity waves is certainly a possibility, vertical wind shear or a geostrophic adjustment process seem to be more likely source mechanisms, given the persistence and extent of the cirrus wave train that by morning extended well into the Atlantic Ocean. This conclusion is consistent with findings of Uccellini and Koch (1987) and Koch, *et al.* (1988). A convective source or amplification mechanism, however, cannot be ruled out (Stobie, *et al.*, 1983; Einaudi, *et al.*, 1987). There is no evidence here to support a local thunderstorm density current source mechanism, such as a bore wave (Koch, *et al.*, 1991), given the available soundings and surface data.

SUMMARY AND CONCLUSIONS

Observations of the height-dependent pressure perturbation field associated with a strong mesoscale gravity wave have been reported. A wave amplitude of about 3.5 mb was measured with a corresponding observed vertical displacement amplitude of between 250 and 500 m within the lower troposphere. The wave-normal horizontal wavelength was estimated as ~40 km, though this assessment relies on adjustment of the observed wavelength (~60 km) to account for wave orientation. The latter was derived from satellite observations of

distinct wave structure in concurrent upper tropospheric cirrus cloud fields and rawinsonde-observed wind directions, since the pressure profile observations were obtained only along a single 52 km flight line.

Meteorological conditions were favorable for propagation of gravity waves. A wave duct ($N \sim 0.01$ sec^{-1}) extended from the surface to an altitude of 9 km and was capped by a 1.5 km deep, conditionally unstable ice saturated layer capable of acting as an efficient wave reflecting layer. Besides the patterns in the cirrus cloud field, gravity wave activity was indicated in the NWS barograph records at nearby upwind stations, albeit at a much smaller amplitude (~0.2 mb). Estimates of wave horizontal phase speed from the available observations are fairly uncertain (~15 to 30 m/sec), but indicate that a critical layer was located somewhere between a mid-tropospheric shear layer ($R_i \sim 0.25$ at 6.5 to 7.5 km) and the base of the overlying conditionally unstable layer at the 9 km level.

The synoptic setting was similar in many respects to that known to favor generation of mesoscale gravity waves. Following Uccellini and Koch (1987), wave generation through a geostrophic adjustment process associated with the transition from cyclonic to anticyclonic curvature in a region of appreciable vertical and horizontal (anticyclonic) shear within a strong jet stream seems a likely candidate in the present case. Shear instability, however, was found over three separate, statically stable but shallow (~500 m deep) shear layers located near the surface, within the duct and near the tropopause. An approaching frontal system and deep convective storms provide other potential gravity wave source mechanisms.

Our interpretation is that strong amplification, and possibly wave breaking occurred as a mesoscale gravity wave of moderate amplitude (~0.2 mb) propagated over a very stable marine boundary layer capped by a strong shear layer ($R_i \sim 0.1$). Wave structure in the aerosol field strongly resembled results of a laboratory experiment on the breaking of finite amplitude internal gravity waves in a shear flow, as reported by Thorpe (1978). Definition of smaller scale wave structure (10 km wave-normal wavelength) was less certain. We suggest that these were vertically coherent, evanescent gravity waves resulting from interaction between the larger scale wave and the lower tropospheric shear layer, where the amplitude of these features exceeded 3 mb.

Although the experiment was designed as a demonstration of concept and technological progress, the unique and serendipitous observation of a strong mesoscale gravity wave illustrates the potential of active remote sensing of the atmosphere using the DIAL technique. Such measurements provide a means to characterize the vertical structure of wave phenomena on the mesoscale, and therefore provide a means to confirm present theoretical predictions that have heretofore relied almost exclusively on surface observations. One can conceive of a future experiment in which active remote sensors are used to derive high resolution profiles of pressure, temperature, winds, and moisture, enabling a rather complete characterization of atmospheric structure. This would allow direct analysis of dynamical processes involved in the continual and mutual adjustment of the mass and momentum fields. Such a capability would likely have a major impact on our understanding of mesoscale processes in the atmosphere.

Moreover, the technique used here has the potential for making accurate, global pressure measurements from satellites. In conjunction with global wind observations from the Lidar Atmospheric Wind Sounder (LAWS) planned for the NASA Earth Observing System (Baker, 1991), such a system would enable analysis of the synoptic scale atmospheric mass and momentum fields without invoking geostrophic balance or comparable assumptions that are presently required.

Substantial improvements have been made to the experimental GSFC Airborne Pressure Lidar System since the 1985 test flight. These include direct monitoring of laser spectral frequency; improvements in laser spectral bandwidth, optical efficiency, and pulse repetition rate (horizontal resolution); and improvements in the data reduction algorithms. An independent altitude determination capability (separate analog detector) and meteorological sensors have also been added to the flight system. Test flights of the improved system were made in 1989. Multiple reverse heading and crossing flight lines were used to sample thunderstorm outflow and land-sea breeze phenomena. Excellent repeatability was found in sampling a pressure wave associated with the thunderstorm outflow.

CHAPTER 12 GROUND-BASED TEMPERATURE PROFILE MEASUREMENTS

DIAL atmospheric temperature profile measurements were made on 28 April 1992 using the frequency-stabilized diode laser injection-seeded alexandrite for the on-line laser. The injection-seeded laser was tuned to the $^{P}P27$ line of oxygen at 13010.81 cm^{-1} and the off-line laser set at a nonabsorbing frequency near 13008 cm^{-1}. The on-line laser energy was 12 mJ per pulse, and the off-line energy was set at 6 mJ. The lidar signal returns were measured with a 200 nsec range gate (30 m vertical sampling). The signals were averaged over 900 shots (90 sec). In order to analyze the data, the fraction of the signal scattered from aerosols and molecules is determined. The off-line signal is first range-squared corrected. We found a clean, nearly aerosol-free atmospheric return at 9.8 km altitude, just below the tropopause and used this region to determine the molecular backscatter at this altitude. The molecular return was then calculated as a function of altitude using the ratio of the atmospheric density at each altitude to that at 9.8 km. This could have been accomplished using a climatic estimate for the temperature profile and surface pressure from which the pressure profile and hence the density profile are determined. In our case, we used radiosonde data taken at the same time 54 km away. The backscatter ratio, one plus the ratio of the aerosol to molecular backscatter, was then determined, as shown in Figure 12-1, at vertical intervals of 30 m. The reference level near 9.8 km which corresponds to a minimum in the backscatter ratio is clearly evident.

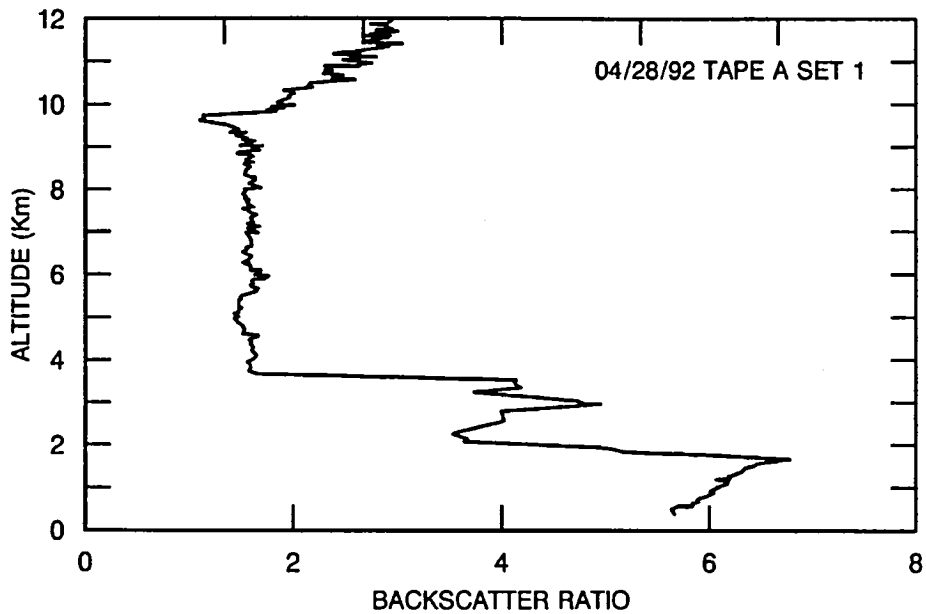

Figure 12-1. Backscatter ratio, the ratio of the sum of Mie and Rayleigh scattering to Rayleigh scattering, as calculated from the off-line signal.

The transmission due to the oxygen absorption is found as the ratio of the on-line to off-line signal. The differential absorption over various layers is calculated from the transmission for layer thicknesses of 300 m. The backscatter ratio is utilized, since different scattering processes affect the absorption on the return path from the atmosphere. The analysis also included a technique for correcting for laser spectral impurity, which was found to be 6%. For the outgoing path, the spectral width of the atmospheric absorption is much broader than the width of the spectrally narrow laser. In the case of aerosol scattering, the absorption on the return path is essentially the same as that on the outgoing path, since the signal is elastically scattered with no change in the shape of the incident spectrum. In the case of molecular (Rayleigh) scattering, the signal is

broadened in the scattering process due to the Doppler effect, since the molecules are moving with an ensemble of velocities along the line of sight of the laser beam. Thus, each spectral component of the incoming signal is scattered into a Gaussian spectrum with a width of $2b_d$, where b_d is the Doppler width. The resultant spectrum after scattering is the sum of these Gaussian spectra, with a width of $2b_d$ for each incoming spectral component. This spectrum is then only partially absorbed on the return path through the atmosphere, since it is spectrally broader than the absorption line. In addition, approximately 3% of the molecular scattered signal is Raman scattered. This signal is considered as being absorbed due to resonant absorption only along the outgoing laser path. The laser spectral impurity was treated as follows. The observed transmission is considered to have two components, one a narrowband spectrally pure component which is absorbed by the atmosphere, and a second spectrally impure component which is not absorbed. The laser spectral impurity is found by matching the observed to the calculated transmission at a relatively high altitude (6.5 km), where the transmission is small, known, and far above the temperature measurement region. As a result, the correction could be made in two iterations in a manner which is relatively independent of the temperature measurement. Non-homogeneous scattering had a significant effect on the measured temperatures, and corrections for this were made.

The differential absorption for each of the measured layers is calculated using the backscatter ratio to determine the fraction of the signal scattered by aerosol and molecular processes. The temperature profile is then calculated by finding the temperature for each layer such that the calculated differential absorption agrees with that which is measured. A single point calibration procedure using radiosonde data is used to calibrate the molecular absorption line parameters to the measured data.

The resulting temperature profile is shown in Figure 12-2 for a vertical resolution of 300 m (on 150 m spacing) and a 900 shot average. The radiosonde profile taken at Washington Dulles Airport, 54 km away, is also shown for comparison. The average deviation of the lidar and radiosonde data is 0.9 K. The inversion feature just below 2 km altitude matches the shear aerosol layer which is clearly shown in the backscatter ratio. Similar DIAL measurements have also been recently reported by Theopold and Bosenberg (1993) for a somewhat smaller altitude range.

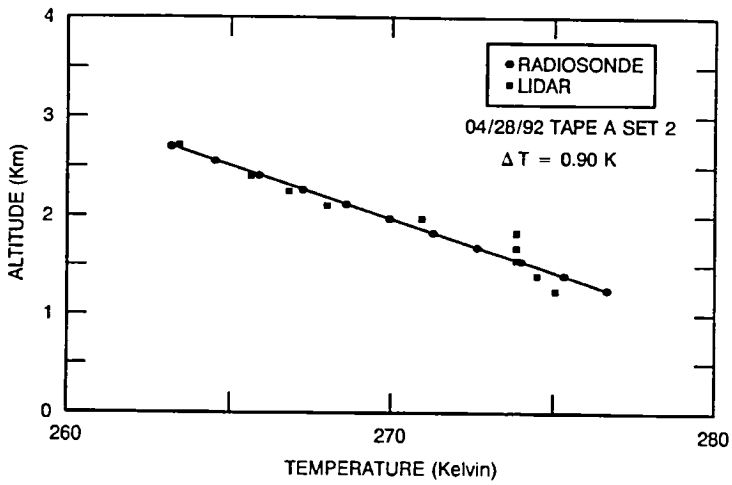

Figure 12-2. Lidar temperature profile measured at Goddard Space Flight Center with the upward-looking lidar, smoothed to a 300 m vertical resolution. Radiosonde measurements of temperature made at nearby Washington Dulles Airport are shown for comparison.

CHAPTER 13 ADVANCED ER-2 LIDAR FOR MESOSCALE METEOROLOGICAL STUDIES[6]

LASE

The development of lidar systems to monitor atmospheric parameters began in the early 1960's. Lidar was shown to be valuable in studying aerosol structures, both in the troposphere and stratosphere. In the early 1970's, considerable effort was expended on the development of systems to measure atmospheric constituents such as water vapor, ozone, carbon dioxide, and other minor species using differential absorption, Raman, and resonance fluorescence techniques. Somewhat later, research was conducted to apply lidar to the measurement of atmospheric state variables, including temperature, pressure, and winds, in addition to moisture. During the mid-1970's, ground-based lidars were converted for operation on aircraft. The ability to rapidly survey atmospheric variables over large areas from aircraft was demonstrated, and it proved valuable in studying mesoscale meteorological and air pollution problems.

Because of the potential of lidar, and its utility as a remote sensing tool from aircraft, NASA Headquarters formed a working group to assess the scientific return from a lidar on the Space Shuttle. The Shuttle Lidar Working Group began its deliberations in 1977. It was comprised of members from the academic and NASA communities, as well as from the international community. The group published a final report in 1979, which strongly endorsed the concept of a lidar on the Shuttle. It identified seven major scientific objectives which could be addressed by 26 different lidar experiments. However, NASA Headquarters decided that an intermediate step was necessary prior to flying a lidar system in space. That intermediate step was the development of a "hands off" automated lidar system for flight on a high altitude aircraft.

A program designated the Laser Atmospheric Sensing Experiment (LASE) was initiated to develop an advanced lidar system to be flown on the NASA ER-2 aircraft for the study of mesoscale meteorological processes. The program is designed so that the technology developed and demonstrated on board the ER-2 is to be directly applicable, wherever possible, to an eventual spaceborne system. LASE is managed by the NASA/Langley Research Center (LaRC). Overall development activity is envisioned to be a cooperative endeavor between NASA and Centre National d' Etudes Spatiales/Centre National de la Recherche Scientifique (CNES/CNRS) in France. The lidar system will be designed and constructed in a modular fashion so that various lasers, wavemeters, and detector packages can be accommodated. The system will be operated in several different configurations during the lifetime of the program. The development, testing, and application of each configuration will be a separate phase of the program. Phase I includes the design and development of the basic lidar system. LaRC is responsible for the construction of the system, with the NASA/Goddard Space Flight Center (GSFC) providing two tunable alexandrite lasers and CNES/CNRS participating in the scientific definition. The objective of the Phase I configuration is to measure moisture profiles from the ER-2 utilizing a differential absorption lidar (DIAL) measurement of water vapor lines near 720 nm. LaRC is responsible for the scientific direction of Phase I, with participation by GSFC and CNES/CNRS.

The scientific objectives of LASE Phase II are to participate in studies of mesoscale meteorological phenomena, such as stratospheric-tropospheric exchange, boundary layer growth, and storm development. Extratropical cyclogenesis is considered in detail because of its scientific importance. The discussion also provides an

[6]The material in this chapter originally appeared as a research and development proposal to modify and use the ER-2 Laser Atmospheric Sensing Experiment (LASE) lidar for a Phase II project in order to make differential absorption lidar (DIAL) temperature measurements. It was submitted to NASA Headquarters and the Centre National d' Etudes Spatiales (CNES) in France in June 1985, with an update submitted 13 months later. The LASE Phase I instrument was integrated into the NASA ER-2 aircraft for the first time in spring 1994. Although the LASE instrument has undergone design changes since the work was performed, descriptions of the LASE Phase I instrument herein are as written in 1985 in order to keep information in context.

estimate of the measurement resolution and accuracy needed to study mesoscale processes. Such studies are based on the measurement of temperature, pressure, and water vapor distributions in the lower atmosphere using the DIAL technique. The temperature and pressure measurements are a new capability which will be developed for the ER-2 aircraft under the Phase II program. They will be observed using absorption in the molecular oxygen *A* band near 760 nm. The water vapor measurement capability is being developed separately in the Phase I LASE program, using water vapor absorption lines near 720 nm. Since the Phase II lidar system will not measure all atmospheric state variables simultaneously, it will be necessary to fly the system with other advanced sounding instruments which operate in the infrared and microwave portions of the electromagnetic spectrum. The technical objectives of LASE Phase II are to develop a high resolution dual wavelength alexandrite laser, an associated wavelength control subsystem (wavemeter), and a spectrally narrowband receiver package, which will operate autonomously on the ER-2 aircraft to measure temperature and pressure, in addition to water vapor.

Analysis and simulations show that the temperature experiment can produce measurement accuracies better than 1 K for 0.5 km vertical resolution and 10 km spatial averaging over the altitude range 0 to 15 km. The pressure profile simulations show accuracies better than 0.3% for 0.25 km vertical resolution and 5 km spatial averaging for the altitude range from 0.5 to 11 km. For surface pressure, accuracies better than 0.2% (and precision better than 0.1%) will be obtained for 15 m vertical resolution and 1 km spatial averaging. Water vapor distribution can be measured in the lower and middle troposphere with an accuracy better than 5% for 0.25 km vertical resolution and 10 km spatial averaging. Cloud top heights are determined with 0.005 km accuracy, and aerosol distributions in the boundary layer are measured with 0.05 km vertical resolution for 0.5 km spatial averaging.

The philosophy regarding the Phase II lidar system is: (1) to utilize as much of the Phase I lidar system as possible to satisfy the Phase II science requirements, (2) to maintain the modular integrity of the LASE system, and (3) to stay within the weight, power, and other constraints of the aircraft. The Phase I transmitter will be improved to provide greater frequency stability (0.1 pm) and narrower bandwidth (0.3 pm). The laser tuning range for the temperature and pressure measurements is 760 to 770 nm, which corresponds to a high gain region of the alexandrite laser. This allows the repetition rate of the system to be doubled to 10 Hz in Phase II using the existing high voltage power supplies. The Phase I wavemeter will be replaced with a Phase II wavemeter with much higher spectral resolution (0.3 pm) and increased absolute frequency accuracy (0.06 pm). The receiver system module including the detectors, analog signal processing electronics, and optics (except the telescope) will be replaced to provide increased accuracy, sensitivity, and altitude resolution, as well as greater dynamic range.

A detailed description of the LASE Phase II proposed activity is provided in this chapter. The scientific objectives are described and are used to define the measurement requirements in terms of accuracy and horizontal and vertical resolution. Phase II technical objectives are also discussed. The differential absorption lidar method is described for temperature and pressure measurements. The feasibility study described, together with the measurement requirements as determined from the scientific objectives, determines the characteristics of the lidar system to be developed. After a brief summary of the characteristics of the Phase I lidar system, the specific modifications to the transmitter, wavemeter, receiver, and data system required for Phase II are described.

LASE Phase II Program Objectives

Scientific Objectives

The scientific objectives of the LASE Phase II experiment relate to the study of mesoscale phenomena and can be advanced by the high flight altitude of the ER-2 aircraft and the capability of the lidar system to determine three-dimensional fields of temperature, pressure, and humidity. The objectives specifically involve troposphere-stratosphere interactions and boundary layer development. In the tropics, these processes include mesoscale cloud clusters, cumulo-nimbus deep convection, tropical storms, and easterly wave developments. In the extratropical regions, these include frontogenesis and cyclogenesis related to stratospheric-tropospheric exchange in response to tropospheric forcing. A detailed discussion of extratropical cyclogenesis using near simultaneous measurements of temperature, pressure, and moisture fields is included. This is of particular scientific importance and current interest because of the recent occurrence of major severe storms and the likelihood of major field programs which will provide detailed meteorological data to supplement the lidar measurements. In addition, a detailed examination of the scale of the processes involved allows the determination of the resolution and accuracy of the measurements required for coordinated observations from the ER-2 aircraft, including the LASE lidar instrument as well as various passive sensors.

Extratropical cyclogenesis has long been the topic of extensive research involving several approaches. This includes the pioneering work of the Norwegian school that formulated the "polar front" theory of cyclones (Bjerknes, 1919; Bjerknes and Solberg, 1923), the application of "Dines compensation" to surface cyclogenesis (Bjerknes and Holmboe, 1944; Bjerknes, 1951a; Reiter, 1963), instability theories of cyclone growth (*e.g.*, Charney, 1947; Eliassen, 1956), and quasi-geostrophic approaches to cyclogenesis and associated vertical motions (Sutcliffe, 1947; Sutcliffe and Forsdyke, 1950; Petterssen, 1955).

Several aspects of major cyclogenesis that have received increasing attention are the structure and evolution of upper tropospheric jet streaks, transverse circulations associated with the jets and attending frontal zones, and stratospheric extrusions associated with the jet/front system. These mesoscale features appear to play critical roles, not only in cyclogenesis but also in associated severe weather events (Danielsen, 1974; Uccellini, *et al.*, 1984 and 1985; Uccellini, 1986). Danielsen (1974) provides several examples of how strong descending jet streaks associated with intense upper level fronts influence the development of severe convective storm systems over the central United States. The indirect circulation found in the exit region of the upper level jet is linked to the veering of the wind with height, which destabilizes the preconvective environment through differential moisture and temperature advections (Uccellini and Johnson, 1979; Brill, *et al.*, 1985). Stratospheric extrusions associated with the jet/front systems [called a "tropopause fold" by Reed (1955)] also contribute to the severe weather outbreak. It appears that severe storms develop after stratospheric air is brought down toward a deep, well-mixed planetary boundary layer (PBL) near the mountains where it then accelerates toward the east and converges with the warm, moist air flowing northward from the Gulf of Mexico.

Eliassen and Kleinschmidt (1957), Danielsen (1966), and, more recently, Uccellini, *et al.* (1985) have also described the importance of stratospheric-tropospheric exchange processes in the explosive development of cyclones. Uccellini, *et al.* (1985) provide a detailed diagnostic study of the Presidents' Day cyclone which occurred 18-19 February 1979. They document the following sequence of events. Tropopause folding accompanying an amplifying polar jet trough system occurred along the axis of the intensifying polar jet in response to subsidence forced by geostrophic deformation patterns associated with the jet streak. The folding process extruded dry stratospheric air, marked by high values of potential vorticity down toward the 700 mb level, 1500 km upstream of the East Coast, and 12 to 24 hr prior to the explosive development phase of the

cyclone. This result differs from previous case studies which have emphasized the concurrent development of a folded tropopause and cyclogenesis. During the 12 hr preceding rapid cyclogenesis, the stratospheric air descended toward the 800 mb level and moved toward the East Coast to a position just upstream of the area in which rapid cyclogenesis occurred. Even though potential vorticity was not strictly conserved, the absolute vorticity increased in the lower to middle troposphere, in association with adiabatic mass convergence, vertical stretching, and the related decrease of static stability of the air mass originating in the stratosphere. As was inferred from the infrared and visible satellite imagery and the ozone measurements, the stratospheric air mass was nearly colocated with the storm center as explosive deepening and vortex development occurred, suggesting that the explosive development of the cyclone was likely influenced by the stratospheric air mass as it descended toward a deep oceanic PBL immediately off the East Coast.

Uccellini (1986) provides evidence that a similar process preceded and probably contributed to the explosive development of the QE II storm on 9-10 September 1978 off the northeastern coast of the United States (Figure 13-1). Gyakum (1983a,b) and Anthes, *et al.* (1983) show that diabatic processes, especially those that influence the structure of the oceanic boundary layer, contributed to the explosive development of the QE II storm. Uccellini (1986) shows that a short wave trough/jet system which propagated from southeastern Canada toward the New England coast (Figure 13-2) appears to also be important for the development of this storm. An intense front extending from 300 mb down to the surface (Figure 13-3a) and a polar jet streak with winds approaching 65 m/sec (Figure 13-3b) were associated with this system.

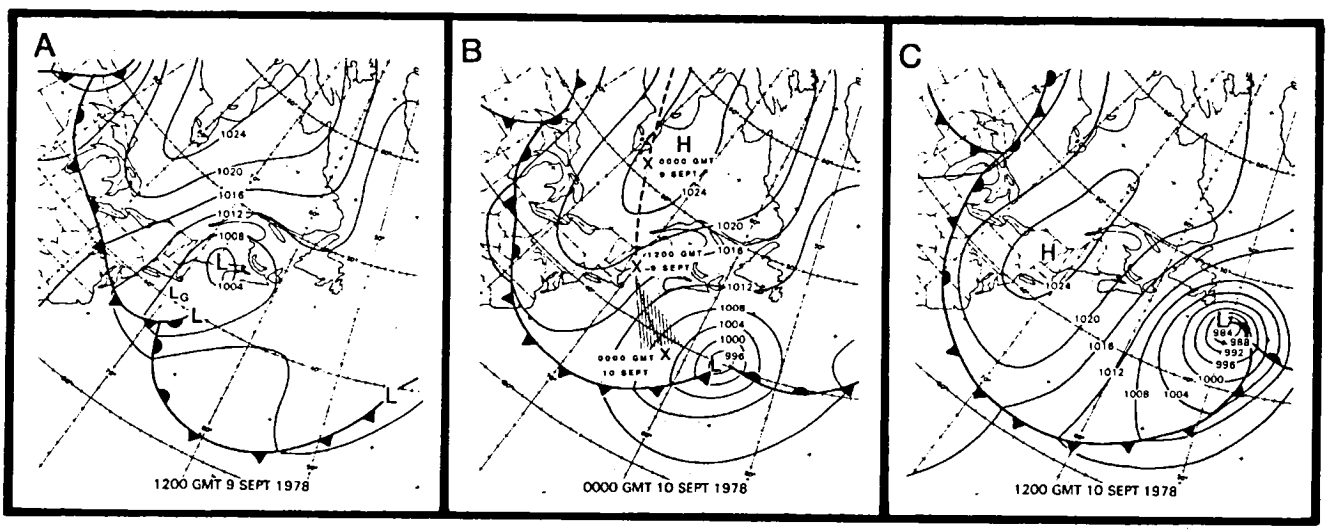

Figure 13-1. National Weather Service operational surface analyses for a) 1200 GMT 9 September, b) 0000 GMT 10 September, and c) 1200 GMT 10 September 1978. L_G on (a) is position of surface low analyzed by Gyakum (1983a) using Seasat wind analysis. Indicated central pressures for QE II cyclone are too high for 10 September analysis as emphasized by Gyakum (1983a). The x's on (b) show position of observed 500 mb height fall maximum for short wave for 12 hr periods ending at 0000 and 1200 GMT 9 September, while shaded region indicates extrapolated position for height fall maximum during 12 hr period between 0000 GMT 9 September and 0000 GMT 10 September.

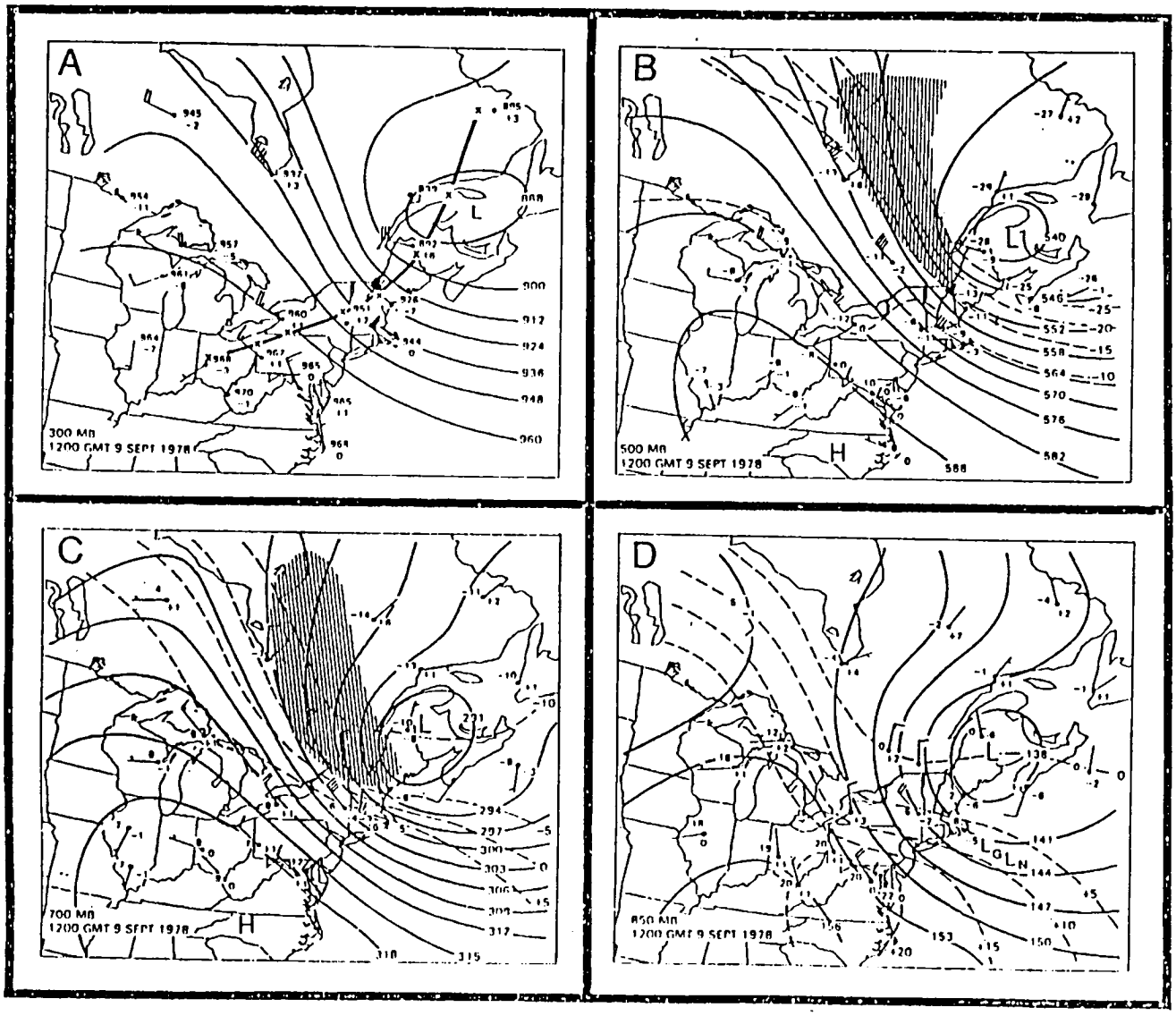

Figure 13-2. National Weather Service analysis for 1200 GMT 9 September 1978 for a) 300 mb, b) 500 mb, c) 700 mb, and d) 850 mb. In (a), geopotential heights (937=9370 m) and height tendency plotted at stations. Temperature (°C) is dashed; geopotential height (dam) is solid. Plotted data at stations include temperature (°C) at upper left and 12 h height tendency (dam) at lower right; wind barbs indicated by standard notation (m/sec). Thick solid line on 300 mb map indicates position of cross section shown in Figure 13-3. Shading in 500 and 700 mb analysis indicates approximate region in which cold air advection coincides with area of cyclonic geostrophic wind shear, a contributing factor to a frontogenetic ageostrophic circulation.

The upper level frontogenesis over New England at 1200 GMT 9 September 1978 was probably linked to the distribution of vertical motion across the front, as simulated by Keyser and Pecnick (1985a,b) for idealized flow situations that include both the confluence and horizontal shear and diagnosed for the Presidents' Day cyclone by Uccellini, *et al.* (1985). The subsidence along the frontal zone, combined with the intensity and depth of the front (as displayed in the cross section in Figure 13-3), indicates that tropopause folding likely extruded stratospheric air down toward the 700 mb level by 1200 GMT 9 September immediately upstream of the region where the QE II storm underwent explosive deepening. The dry air extending down from the

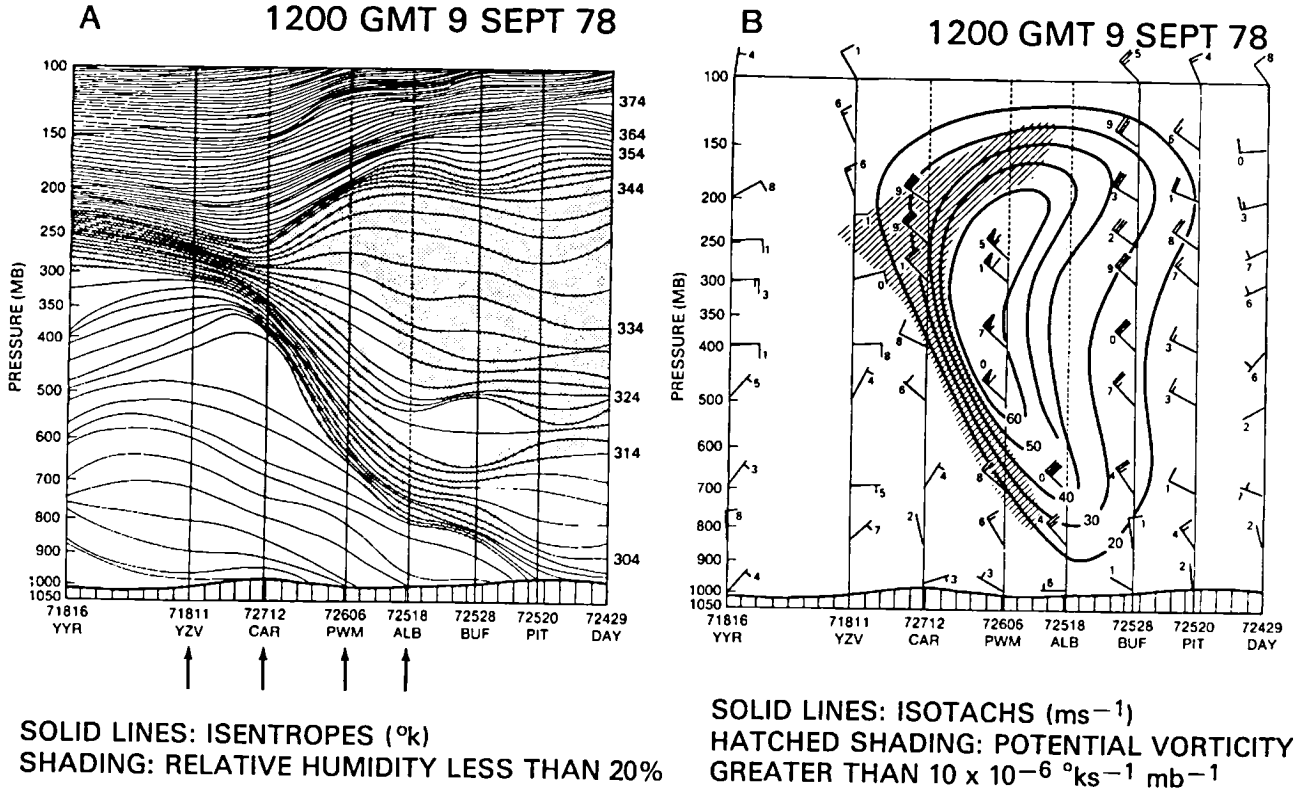

Figure 13-3. Vertical cross section from Goose Bay, Newfoundland (YYR) to Dayton, Ohio (DAY) for 1200 GMT 9 September 1978 (see thick solid line in Figure 13-2a for position of cross section). Dashed portions of vertical lines at CAR, PWM, and ALB indicate levels at which wind data were not available. a) Isentropes (K, solid); shading represents area where relative humidity is less than 20%. b) Subjective isotach analysis for total wind speed (solid, m/sec); wind barbs plotted with last digit of wind speed observation. Wind analysis over ALB derived from cross-checking with NWS analyses on 200, 300, 500, and 700 mb surfaces. Shading indicates region 1) where potential vorticity was computed from selected points using data restricted to plane of cross section and the expression $[-(\partial u/\partial y_\theta + f)(\partial\theta/\partial p)]$, *and 2) where the potential vorticity has values exceeding 10 x 10⁻⁶ K/sec-mb which are typical of stratospheric air.*

400 mb level at CAR to below 800 mb at BUF within the frontal zone (Figure 13-3a) is one sign of a stratospheric extrusion within a narrow region 300 km wide. Another indication of tropopause folding is the large static stability ($\partial\theta/\partial p$) in the frontal zone (Figure 13-3a), which, combined with the large cyclonic wind shears, would yield large values of potential vorticity (Figure 13-3b). The use of static stability and cyclonic wind shears in the plane of the cross section yields potential vorticity values exceeding 10^{-5} K/sec-mb down toward the 800 mb level within the front (illustrated by the shading in Figure 13-3b).[7] The stratospheric air moved through the folded tropopause toward the position of the surface low, and appeared to influence the explosive development phase of the QE II storm, as discussed for the Presidents' Day cyclone by Uccellini, *et al.* (1985).

[7] Reed and Danielsen (1959) define the 1 x 10^{-5} K/sec-mb contour as a value for potential vorticity that separates stratospheric and tropospheric air masses near upper level fronts. The potential vorticity computations showing large values in the shaded region in Figure 13-3b likely underestimate the actual magnitude near the front, given the poor resolution of the data set and the exclusion of curvature vorticity by use of only the data in the plane of the cross section.

Common features of the analyses provided by Danielsen (1974) for severe storm outbreaks and by Uccellini *et al.* (1985), Anthes, *et al.* (1983), and Uccellini (1986) for coastal cyclogenesis are the juxtaposition of stratospheric air [extruded downward from a normal tropopause level toward the lower troposphere through a narrow (300 km wide) frontal zone] and a deep PBL (in which the static stability is weakened over a 200 to 300 mb layer due to sensible heating near the Earth's surface). It appears that the severe weather and explosive oceanic cyclogenesis commence as the stratospheric air descends toward the deep PBL. Although these previous diagnostic studies have suffered from data bases which are inadequate to totally resolve the means by which the stratospheric air interacts with the PBL, these studies point to the need for simultaneous detailed measurements of the stratospheric-tropospheric exchange process and the diabatically influenced PBL to resolve the evolution of these features and their contribution to severe weather events.

The LASE lidar instrument to be developed during Phase II will perform measurements of temperature, pressure, moisture, aerosol distribution, and cloud top heights. Flown aboard the ER-2 aircraft, it will allow observations of the evolving meteorological pattern at various times, leading to new insights into these mesoscale processes. These include direct observations of descending stratospheric air marked by distinct signatures in the static stability fields, direct measurements of evolving PBL structures, and the interaction of these air masses during storm events. From the detailed study of such particular events, one can determine the required spatial (horizontal and vertical) resolution and measurement accuracies as in Table 13-1. These parameters are compatible with the various scales of motion and meteorological processes related to tropospheric-stratospheric exchange processes, frontogenesis and cyclogenesis, and boundary layer development.

During Phase II missions, the lidar will measure one of the atmospheric state variables (temperature, pressure, or water vapor) at a given time, and will simultaneously measure aerosol distributions and cloud top or boundary layer heights. To maximize the scientific return, complementary instruments will also be flown on the ER-2 aircraft. These will include advanced passive microwave and infrared sounders, which will be used to retrieve temperature and water vapor profiles. Passive visible and infrared radiometers will be used for radiative transfer studies, and a nadir-looking camera will provide images of the flight track.

Table 13-1. Requirements for LASE Phase II scientific objectives.

Measurement Parameter	Altitude Range (km)	Vertical Resolution (km)	Horizontal Resolution (km)	Accuracy
Temperature	0 - 15	0.5	10	1 K
Surface or cloud top pressure	0 - Tropopause	0.005	10	1 mb
Pressure	0 - 15	0.5	10	0.3%
Water vapor	0 - Tropopause	0.5	10	5%
Cloud top height	0 - Tropopause	0.05	0.5	0.05
Aerosol/Boundary layer	0 - 15	0.05	0.5	——

In situ measurements on the aircraft will include aerosol size distribution, ice and liquid water content, and ozone concentration, in addition to standard housekeeping parameters.

Technical Objectives

The temperature and pressure measurements are a new capability which will be added to the ER-2 during Phase II. The measurement objectives for temperature presented in Table 13-1 are more than an order of magnitude better than the current or anticipated future capability of passive temperature sounders. The measurement of the atmospheric pressure profile (pressure versus altitude) is a fundamentally new remote sensing capability.

The measurement objectives require that substantial improvements be made to the Phase I system. The LASE Phase II program involves advanced technology from various fields to provide: (1) a high performance dual-wavelength alexandrite solid state laser transmitter with an ultranarrow emission line, (2) a very high resolution wavemeter, and (3) a high spectral resolution receiver system. The technical approach followed both by GSFC and CNES/CNRS in the design of these advanced subsystems will meet the requirements for the development of an autonomous and fully automatic lidar system, which is a first step toward a future spaceborne lidar.

Differential Absorption Lidar Temperature and Pressure Measurement Simulations

High vertical resolution measurements of the atmospheric temperature, pressure, and humidity profile will allow significant improvement in the understanding of mesoscale phenomena such as extratropical cyclogenesis. A differential absorption lidar technique forms the basis for the proposed high accuracy measurements of temperature, pressure, and humidity. The technique uses two pulsed lasers, one located on a resonant absorption line of the species to be measured and a second at a nearby reference frequency. The energy backscattered at each frequency by aerosols and molecules in the atmosphere is measured as a function of time using a range gated receiver, which allows the atmospheric absorption of a particular species to be measured over a known path. The absorption is then used to determine the species concentration. Since LaRC has considered water vapor measurements in the Phase I portion of this program, water vapor will not be discussed in detail here. Alternatively, if measurements are made using a species which is uniformly mixed in the atmosphere, such as oxygen, then the mixing ratio is known *a priori*, and the measurements can be structured to determine either the temperature or pressure profile. The following sections describe simulations of the expected performance from the ER-2 aircraft, and a brief description of the experiment requirements.

Figure 13-4 gives the results of a simulation of the effects of noise due to photon fluctuations on temperature measurements from a 20 km ER-2 platform. The simulations use a high resolution multilayer atmospheric radiative transfer program, which includes the effects of laser finite bandwidth, elastic and inelastic scattering processes (Korb and Weng, 1982), and background radiation. The simulations were done for the the following conditions: a 0.1 m^2 collector, an overall collection and detection efficiency of 0.084, a laser energy of 0.15 J per shot, a laser bandwidth of 0.02 cm^{-1}, a receiver field of view of 1.4 mrad, a receiver bandwidth of 0.24 cm^{-1}, and daylight backgrounds with a 30% ground albedo. As shown in Figure 13-4, temperature measurements with accuracies better than 1 K can be obtained, with vertical resolution as high as 500 m with 10 km spatial averaging. For measurements in the lower and middle troposphere, the ^{P}P29 line of oxygen at 12999.95 cm^{-1} yields measurements with the highest accuracy. On the other hand, for measurements above 7 km altitude, the stronger absorption associated with the ^{P}P27 line of oxygen yields the best results.

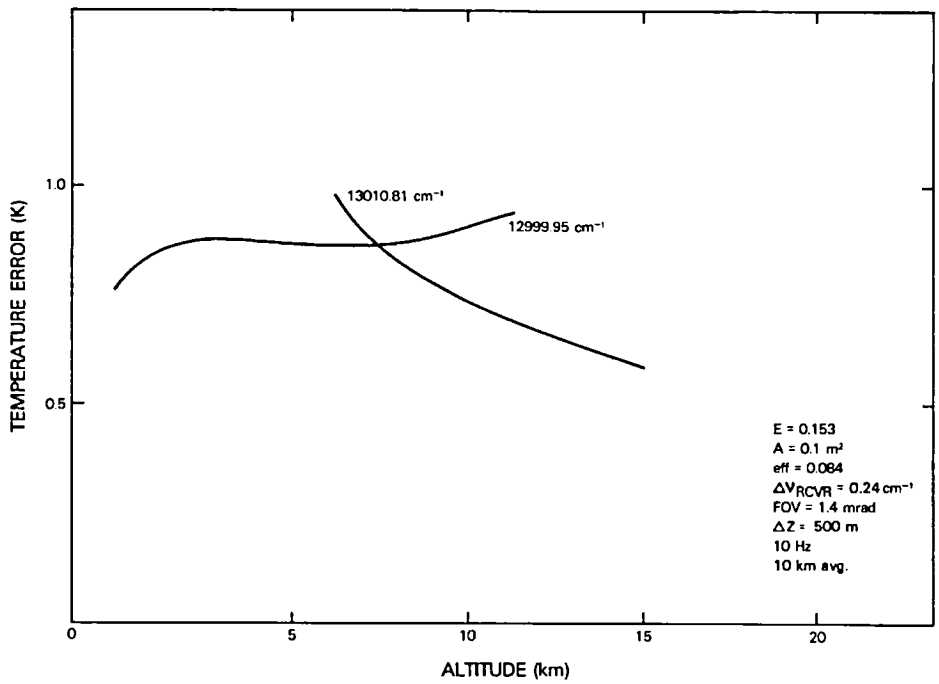

Figure 13-4. Simulated accuracy of the ER-2-based temperature experiment at 20 km altitude for daylight backgrounds using oxygen A *band absorption lines at 12999.95 or 13010.81 cm^{-1}.*

The results of simulations of the errors due to photon fluctuations on pressure profiling experiments from an ER-2 altitude of 20 km are shown in Figure 13-5, using the absorption troughs at 13152.49, 13150.86, and 13153.79 cm^{-1}. The results are given for 250 m vertical resolution, 5 km spatial averaging, and a 0.12 cm^{-1} receiver spectral bandwidth. The other system parameters, including daylight background conditions with 30% Earth albedo, are the same as those previously given for temperature. As shown, the troughs at either 13150.86 or 13153.79 cm^{-1} can be used to obtain measurements with accuracy better than 0.3% over the altitude range from 0.5 to 10 km. In addition, the results for surface pressure (not displayed in Figure 13-5) show that the effects of noise are less than 0.1% for 1 km spatial averaging and an Earth albedo as low as 3%.

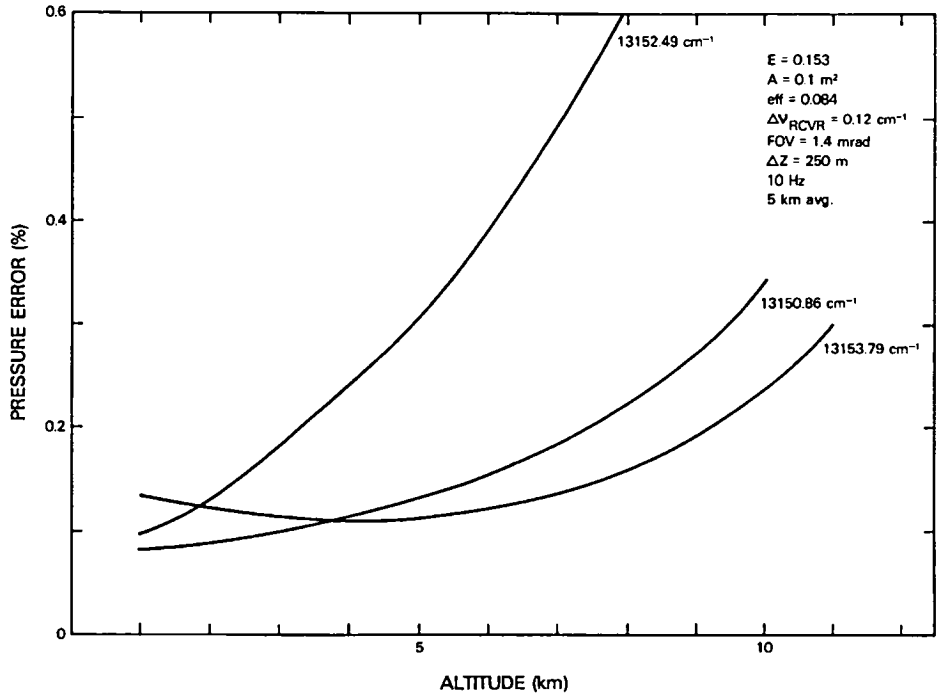

Figure 13-5. Simulated accuracy of the ER-2-based lidar pressure experiment at 20 km altitude for three trough locations in the 13150 cm^{-1} region for daylight backgrounds.

Experiment Requirements

The simulations in the preceding section show that the temperature experiments can produce measurement accuracies better than 1 K for 0.5 km vertical resolution and 10 km spatial averaging over the altitude range 0 to 15 km. The pressure profile simulations show accuracies better than 0.3% for 0.25 km vertical resolution and 5 km spatial averaging, for the altitude range from 0.5 to 11 km. For surface pressure, we found accuracies (random noise component) better than 0.1% for 1 km spatial averaging.

These accuracies generally meet or exceed the requirements for the science objectives. The system parameters needed to achieve these accuracies are: a laser energy of 0.15 J, a 0.1 m^2 aperture telescope, a receiver field of view <1.4 mrad, a receiver sampling interval of 15 m, a receiver spectral bandwidth of 0.12 to 0.24 cm^{-1}, an overall efficiency <0.084, which includes the use of a photomultiplier detector with a quantum efficiency of 0.2. The signal measurement accuracy required is better than 1%, which affects the dynamic range and digitization accuracy, and the systematic error level needed is less than 0.2% in the signal measurement, which affects considerations of system linearity and the system electrical frequency response.

We have also conducted a number of other studies to evaluate various detailed aspects of the experiment requirements, which significantly impact the experiment design and configuration. In particular, we found that the accuracy requirements for setting the laser frequency are a dominant factor in achieving good temperature accuracy. Our studies show that to obtain temperature accuracies <1 K, the on-line laser frequency must be centered and then remain on the temperature sensitive absorption line to an accuracy of <0.002 cm^{-1}. Since passive stabilization of the laser to this accuracy is not practical, this requires that a separate frequency measuring device, a wavemeter, be included as part of the experiment package. The wavemeter, which is described later in this chapter, must measure the centroid of the laser frequency on a per

shot basis and must be capable of an accuracy <0.001 cm^{-1}. The measured centroid will be compared with the pre-set frequency and the difference signal, after averaging, will be used to control the laser frequency. The laser, in turn, must be continuously tunable on a scale of 0.001 cm^{-1}.

Other studies of importance to the overall experiment are the selection of the laser spectral bandwidth and the required accuracy of the wavemeter measurements of the laser spectral energy distribution. We found that while a laser bandwidth of 0.02 cm^{-1} was quite adequate for high accuracy science measurements, this would impose severe requirements on the wavemeter measurements of the laser spectral energy distribution. An initial tradeoff study indicates that a laser bandwidth of 0.005 cm^{-1} (0.3 pm) is achievable. At this resolution, the laser energy distribution is only a weak factor in the temperature and pressure measurements and can be well corrected using the wavemeter data. These system studies will continue in the first year of this program.

LASE Phase I Description[8]

The tunable dual wavelength lidar system to be developed for the LASE Phase I mission is designed primarily for water vapor measurements in the lower and mid-troposphere.

The differential absorption technique used to measure water vapor requires a sequential emission of two narrow laser lines at two different wavelengths within a few hundred microseconds. In addition to humidity, other meteorological parameters, such as tropospheric aerosol profiles, low altitude cloud top height, and high altitude subvisible clouds, will be studied. These experiments, which are conducted simultaneously, will provide a consistent and unique set of meteorological data which will meet the science objectives of the LASE Phase I missions.

The lidar system characteristics are dictated primarily by the water vapor experiment: a powerful dual wavelength transmitter with an associated wavemeter, and high sensitivity detection, followed by high rate data storage of the backscattered signals. The lidar characteristics for Phase I were presented at a Conceptual Design Review held at NASA/Langley Research Center in January 1985.

The lidar system will be installed in the ER-2 Q-bay (Figure 13-6). The volume available is 2.1 m^3 (1.7 m by 1.42 m by 0.86 m) and the maximum weight and power allocations are 590 kg and 3.7 kW (28 VDC), respectively. The Q-bay environmental conditions are temperatures between 15 to 40°C, pressures from sea level to 4.5 psi, and mechanical loads in flight equal to +0.5 *g* 100 Hz sine vibrations and +2.0 *g* acceleration.

The lidar system is modular to easily accommodate any major improvements at the subsystem level. Figure 13-7 is a block diagram of the LASE instrument. The transmitter and receiver telescope are in a nadir-looking mode, in a side-by-side configuration. The transmitter and receiver fields of view are 0.73 and 1.23 mrad, respectively, to minimize sky background noise for daytime missions. To avoid saturation of the detector, the minimum distance for complete overlap of the transmitted and received beams is 6 km.

The laser transmitter requirements for water vapor measurements (Table 13-2) are met or exceeded by a dual wavelength alexandrite laser being developed for the Phase I program by NASA/GSFC. Each laser cavity is a stable resonator with an internal telescope. Tuning and narrow line emission capabilities are provided by a birefringent filter and two etalons with 13 and 1 pm fringe widths, respectively. The lasers are designed to

[8] Commercial names and models are used for identification purposes only; no endorsement of any product is intended.

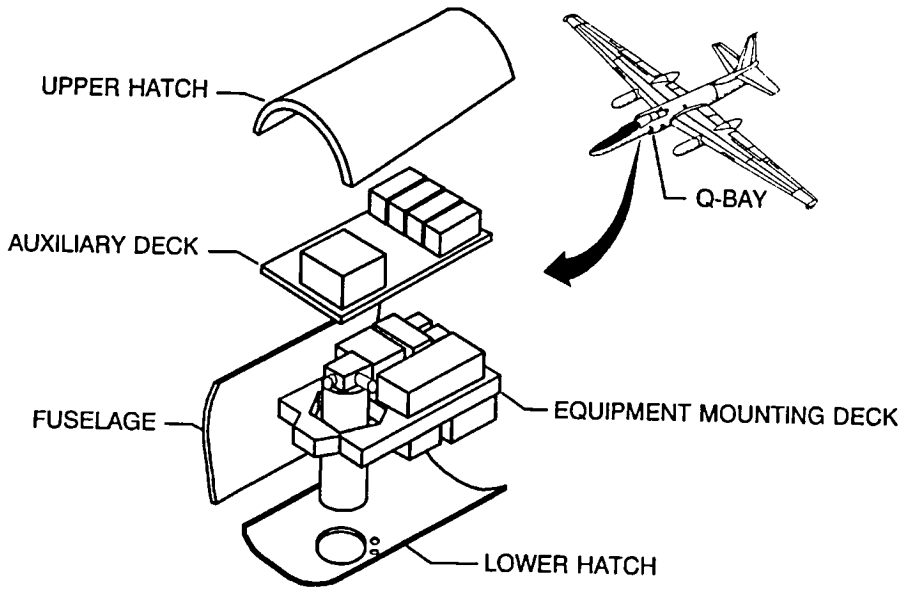

Figure 13-6. LASE ER-2 installation. The LASE instrument is installed in the ER-2 Q-Bay, leaving the wing pods available for corroborative instruments. The instrument is mounted on two decks, one containing the laser, telescope, optics, and detectors, and an auxiliary deck containing the data system electronics.

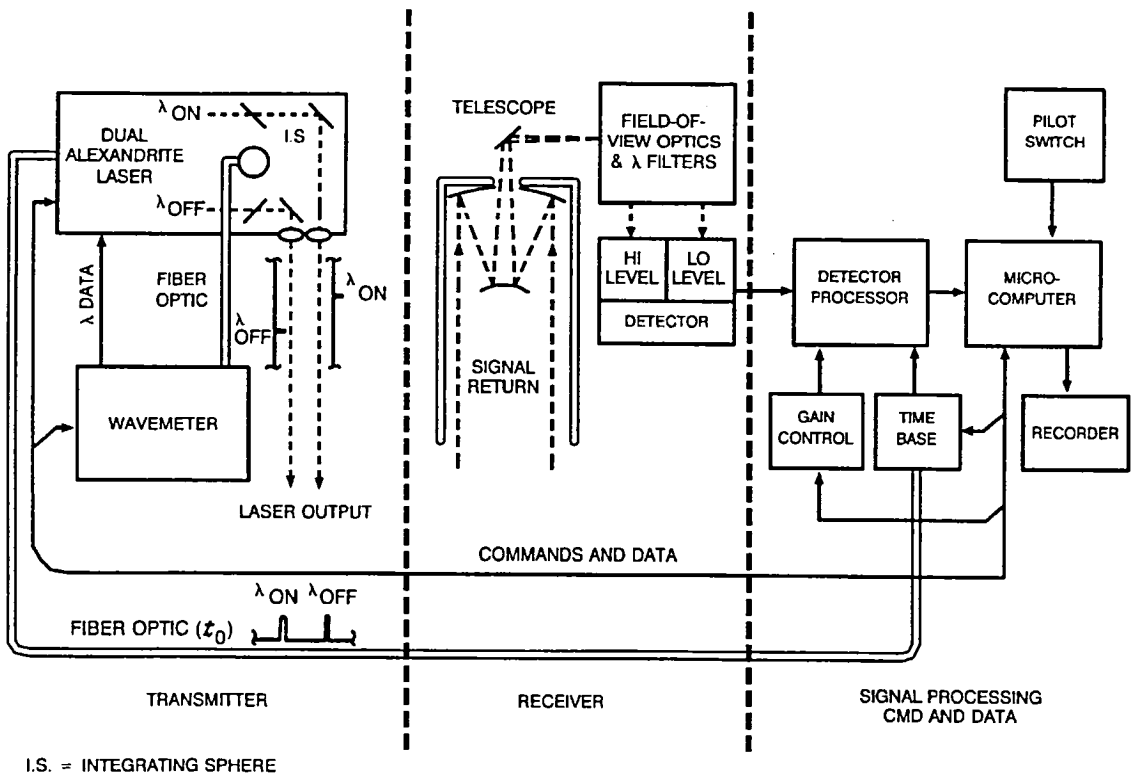

Figure 13-7. LASE system block diagram.

Table 13-2. Transmitter requirements for water vapor measurements.

Tuning range	726.5 to 732.0 nm for each laser
Laser linewidth	1 pm
Wavelength separation	70 pm
Energy per pulse	150 mJ
Energy variation	15% (1σ)
Repetition rate	5 Hz
Pulse separation	200 to 400 μsec
Pulse length	<500 nsec (100% of energy)
Spectral purity	99% of the total energy within a spectral interval ≤1.06 pm
Wavelength mismatch between desired and actual position	0.5 pm (1σ) for on-line and ≤2.0 pm for off-line
Laser divergence	(minimum acceptable to meet eye safety requirements)
Number of pulse pairs	$\geq 10^6$ (or 55 hr at 5 Hz)

provide an open loop wavelength tuning accuracy to better than 170 pm. The spectral characteristics of the laser outputs are measured on a shot-to-shot basis by a wavemeter and provide real time information on the laser centroid wavelengths for active, closed loop wavelength stabilization of the dual alexandrite lasers.

The wavemeter requirements are:

1. to measure the spectral characteristics of each output pulse at λ_{ON} and λ_{OFF},
2. uncertainty of centroid wavelength <0.25 pm (1σ) for λ_{ON} and <1.0 pm (1σ) for λ_{OFF},
3. to measure the amplitude of all array elements,
4. spectral resolution (FWHM) of the laser energy <0.5 pm for λ_{ON}, and
5. spectral distribution <2.0 pm for λ_{OFF}.

An integrating sphere in each laser will provide uniform illumination of the wavemeter, so that the measured intensity versus wavelength distribution represents the output of the lasers. Commercial multimode fiber optics will provide the coupling between the integrating sphere and the wavemeter.

The requirements are to be met with a three-stage Fabry-Perot wavemeter to be developed by NASA/Langley Research Center. A stable helium-neon laser provides a self-calibration of a thick spherical Fabry-Perot (5.3 pm free spectral range [FSR]) and two flat Fabry-Perots (40 and 500 pm FSR, respectively).

The receiver telescope (Ritchey-Chretien) and detector package optics have a collection area of 0.11 m^2 (38 cm diameter), and the capability to select between two narrow bandwidth (<0.3 nm) filters and a broadband (20.0 nm) filter. A beam splitter which divides the return signal into 10% and 90% portions allows simultaneous measurement of both low intensity (atmospheric) and high intensity (cloud and ground) returns. The receiver total transmission is 0.23 for daylight operation and 0.64 for night missions. The relative pointing accuracy between the transmitter and receiver is 134 μrad (2σ).

The detector and data systems are designed to measure the returns with 150 m resolution from 6 km below the aircraft to the ground with a systematic measurement uncertainty <2%, a random uncertainty <10%, and an uncertainty in the time phasing for digitization of the return signals <10 nsec. The detectors and pre-amplifiers to be used for the Phase I mission are a cooled (-20°C) silicon avalanche photodiode (SiAPD) with

a high gain 0.5 MHz bandwidth (150 m range resolution) pre-amplifier and a second, uncooled SiAPD with a lower gain 1.5 MHz bandwidth (50 m range resolution) pre-amplifier. A programmable gain control amplifier with either a 0.5 MHz or 1.5 MHz presample filter and a 5 MHz, 12-bit transient recorder (8 K memory) are also included in each channel.

The entire lidar system is controlled by a 16-bit microcomputer (LSI 11/23). The transient recorders and other analog-to-digital electronic instrumentation are contained in a CAMAC standard (IEEE 583) instrument crate. Digital data are read out from the instrument modules by the system computer and recorded on a high density flight-qualified tape recorder (MARS 2000) for post-flight data analysis. The system data rate is 17.3 kilosamples/sec (12-bit samples), which is well below the recorder's maximum rate of 51.5 kilowords/sec (16-bit words). The tape capacity is ~1.8 gigawords.

LASE Phase II

The following describes the required changes to three major subsystems in order to add the capability of measuring atmospheric temperature and pressure profiles to accuracies and resolutions consistent with the Phase II science objectives. The system capability to measure water vapor is not compromised. In the interest of minimizing costs, the experimental approach is to measure only one atmospheric state variable (temperature, pressure, or humidity) on a single pass of a flight line, with the capability of changing to a different measurement between passes to achieve the science objectives.

The Phase I transmitter will be improved to provide narrower laser linewidth and better frequency stability. The Phase I wavemeter will be replaced with a wavemeter with much higher spectral resolution and increased absolute frequency accuracy. The receiver system detectors, analog signal processing electronics, and optics (except for the telescope) will be replaced to provide increased accuracy, sensitivity, and altitude resolution, as well as greater dynamic range. We expect that some minor modifications to the Phase I instrument software will be required, but since this software has not yet been specified, the details of software modifications are not discussed herein.

Phase II Laser Transmitter

Modifications to Phase I Specifications. The pressure and temperature measurement simulations described previously in this chapter indicate that an upgrade of the laser transmitter will be required. The changes in the relevant transmitter specifications are primarily driven by the temperature profiling requirements and are indicated in Table 13-3.

Table 13-3. Phase I and Phase II transmitter specifications.

Specification	Phase I	Phase II
Laser tuning range	726-732 nm	726-732 and 760-770 nm
Laser linewidth	1.2 pm (0.02 cm^{-1})	0.3 pm (0.005 cm^{-1})
Wavelength control	0.25 pm (0.004 cm^{-1})	0.06 pm (0.001 cm^{-1})
Repetition rate	5 pulses/sec	5 and 10 pulses/sec

Impact on Transmitter Design. As can be seen from the block diagram in Figure 13-8, the Phase I transmitter consists of several subsystems. These include: (l) a dual wavelength laser head, (2) two lamp driver units ("A" and "B" PFN/PS), (3) a microprocessor-based laser control unit, (4) a low temperature flashlamp cooling loop, (5) a high temperature heating loop for controlling the alexandrite rod temperature, and (6) transmit optics for controlling beam magnification and divergence. Based on our current understanding, no hardware modifications will be required to achieve the Phase II specifications, with the exception of the laser head. Some reprogramming of software in the laser control unit (Subsystem 3) will be required to allow for the increased repetition rate, to change power supply voltage settings in the lamp drivers (Subsystem 2), and to change the rod temperature set point in the high temperature loop (Subsystem 5) to achieve optimum efficiency and avoid optical damage. The principal impact of the upgraded specifications will be felt in Subsystem l as described below.

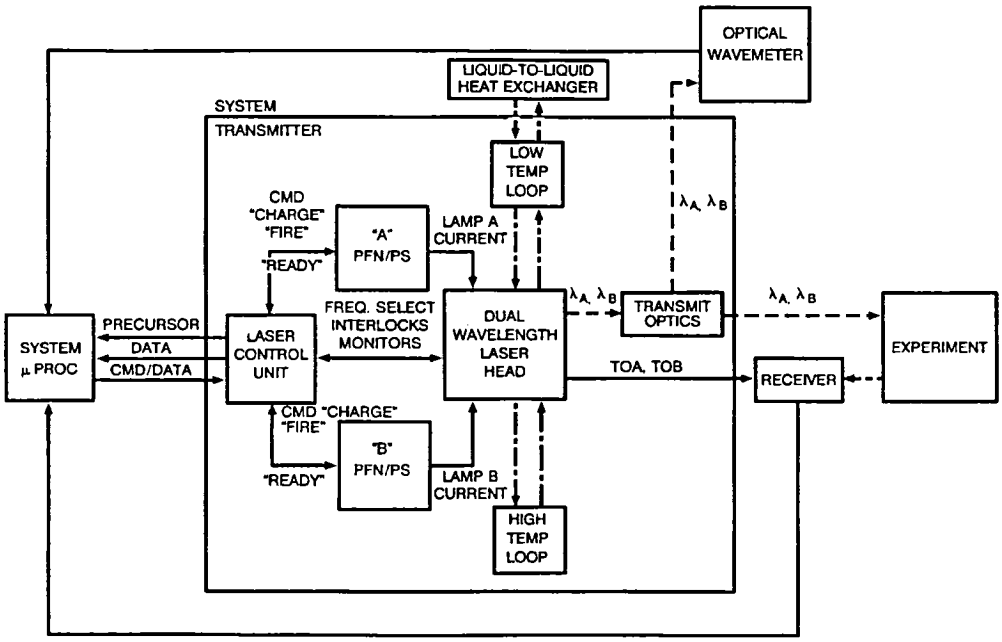

Figure 13-8. Laser transmitter block diagram showing system interfaces.

As illustrated in Figure 13-9, the alexandrite laser gain peaks in the 750 nm wavelength region. In order to force the laser to operate in the relatively low gain region near 727 nm for the Phase I water vapor measurements, it will be necessary to include in the Phase I transmitter a coarse tuning element, such as a birefringent filter, with a free spectral range spanning the wavelength interval from 720 to 780 nm. In addition, the Phase I design allows for two line-narrowing etalons which, with modification, should be adequate to meet the Phase II linewidth specification. Thus, the basic automated tuning elements required to operate in the 760 to 770 nm band will be available in the Phase I transmitter.

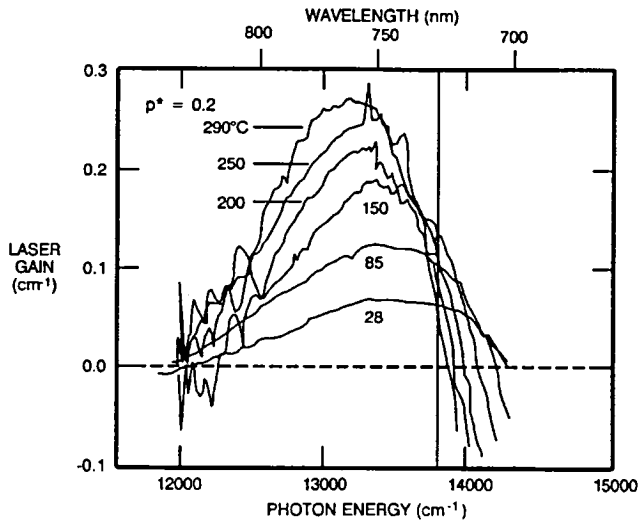

Figure 13-9. Laser gain in alexandrite at various temperatures for a 20% excitation level.

The higher gain at Phase II wavelengths between 760 and 770 nm also implies that the flashlamp energy loadings per pulse can be substantially reduced relative to 727 nm. Thus, the repetition rate can probably be increased to the desired 10 pulses/sec rate using the existing high voltage charging power supplies with little or no increase in consumption of aircraft prime power.

The largest potential hardware impact is due to the reduction in the laser linewidth and wavelength control specifications by a factor of 4 relative to Phase I. The wavelength-selecting air gap etalons in the Phase I transmitter are being designed to have a short term stability on the order of 0.1 pm. This is achieved through the use of low expansion spacer materials, thermal regulation to 0.1 K, and pressurization of the laser head. To achieve the 0.06 pm Phase II control specifications with the existing air gap design, the thermal controller must be upgraded to maintain temperature within a range of 0.03 K. Furthermore, pressure variations within the etalon due, for example, to passing sound waves, cannot exceed about 0.25 mbar (0.025% of atmospheric pressure), implying that extensive sound baffling might be required. An alternative approach might be to substitute vacuum etalons with ultrahigh stability spacers, such as Corning ULE Quartz or Schott Zerodur. Long term drifts would be removed by the wavemeter.

In the Phase I conceptual design, the resonant modes of the laser cavity are allowed to "float" freely through the narrow bandpass transmission curve of the fine tuning etalon, as in Figure 13-10. This approach is taken to avoid the need for active control of the laser resonator length, and it relies on the condition that a sufficient number of resonator modes (three or more) lies within the net gain bandwidth of the laser. Thus, as a resonance mode moves out of the net gain bandwidth, another enters to take its place, and the energy output and wavelength position of the centroid are not changed significantly. Different longitudinal resonances of a given spatial mode (*e.g.*, TEM_{00}, TEM_{01}, etc.) are separated in frequency by $c/2l$, where c is the speed of light in vacuum and l is the effective optical length of the laser resonator. Thus, a given spatial mode will always have a resonance within $c/4l$ of the etalon transmission peak. In a longer cavity, the modes are spaced more closely. For an effective resonator length of 1 m (the approximate length proposed for the Phase I transmitter), the longitudinal modes are separated by ~0.25 pm, which insures that a resonance occurs within 0.125 pm of the etalon transmission peak. To be certain that a mode lies within 0.06 pm of the etalon peak as required by Phase II, the resonator length would have to be slightly >2 m. Given the size constraints of the

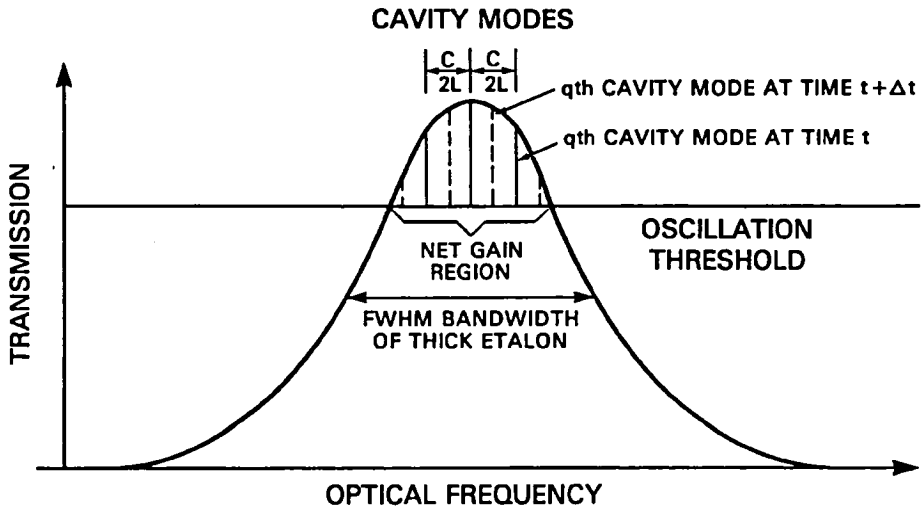

Figure 13-10. Superposition of free-running laser cavity modes on fixed etalon transmission curve.

ER-2 Q-bay and the LASE experiment, the longest cavity that can be achieved is 1 m without resorting to folded geometries, a major and expensive design change. The above considerations leave two alternatives for achieving the Phase II control specifications.

The first alternative is to provide active control of the laser cavity length. In this approach, the laser control microprocessor receives wavelength information from the wavemeter on previous pulses and applies a correction voltage to a piezoelectric translator (PZT) stack on one of the resonator mirrors. This, in turn, adjusts the laser resonator length to keep the mode centered in the etalon passband. This approach assumes that the effective optical length is stable from pulse to pulse. The effective length will be affected by localized thermal fluctuations in the flashlamp-pumped rod, laser induced heating and thermal fluctuations in the optical components and intervening air, thermally induced length changes in the aluminum honeycomb baseplate and optical mounts, and local pressure fluctuations and microphonics created by sound waves generated in or transmitted by the housing. This alternative appears to have a fair amount of associated risk.

A second, and potentially much simpler, alternative is the use of highly degenerate cavity configurations. In this approach, the spatial modes of the resonator are split into N subsets, where N is a small integer. Longitudinal modes of a given spatial type, such as TEM_{00}, are still separated by $c/2l$, but individual subsets of modes are separated by $c/2Nl$. A common example is the confocal resonator ($N = 2$), where the modes split into even and odd numbered subsets separated by $c/4l$. To achieve the Phase II control specifications, a value of N equal to 2 or 3 would be adequate. The cavity modes would again float freely through the etalon passband, as in the Phase I design. The conversion to a N-degenerate cavity could probably be accomplished by substituting new mirrors and internal lenses in the Phase I transmitter. For a value of $N = 3$, the resulting mode spacing would be ~0.08 pm, insuring that resonant modes would occur within 0.04 pm of the center of the etalon passband, and that a complete set of TEM_{mn} spatial modes would fall within the 0.3 pm linewidth specification. As the cavity length changed, a different linear combination of spatial modes would oscillate, but a lower order mode ($<TEM_{02}$) would always lie within 0.04 pm of the center of the etalon passband. To validate this approach, we will perform extensive analysis and testing on the Phase II brassboard, as well as on our current alexandrite laser used in conjunction with our current high resolution wavemeter.

The wavemeter is designed to measure the spectral characteristics of the laser beams for each emitted pulse. The values of the two centroid wavelengths, λ_{ON} and λ_{OFF}, are computed by the wavemeter in real time, and are used in a servo-loop to provide active control of the laser frequency. Complete information on the measured spectral profiles is sent to the LASE computer for storage on magnetic tape. The true spectral energy distribution is computed during post-analysis.

Performance Specifications. The laser input to the wavemeter will have characteristics as shown in Table 13-4.

Table 13-4. Wavemeter characteristics.

Wavelength range	725 to 770 nm
Linewidth (FWHM)	$\delta\lambda$ <0.3 pm (0.005 cm^{-1})
Pulse pair repetition rate	5 Hz and 10 Hz
λ_{ON}, λ_{OFF} temporal separation	200 to 400 μsec
Emitted wavelength position from tuning elements	$\Delta\lambda = \pm 170$ pm

The wavelength of each output pulse is measured in real time. For the wavelength measurement, the absolute accuracy required for Phase II is $\Delta\lambda = \pm 0.06$ pm ($\Delta\nu = \pm 0.001$ cm^{-1}). The value of the wavelength is defined as the centroid of the spectral energy distribution for the laser pulse. The absolute wavelength is an experimental value defined with reference to an absorption line. The spectral energy distribution will be measured for each output pulse. Raw data will be stored on tape, and the computations necessary to obtain the true spectral energy distribution will be made in the post-flight data analysis. The energy distribution is computed at spectral intervals of 0.06 pm (0.001 cm^{-1}) with a relative amplitude accuracy ≤20%.

Principle of the Wavelength Measurement. The absolute wavelength can, in principle, be fully determined from the position of interference fringes provided by Fizeau interferometers. A rough value can be computed first from the measured interval between two successive fringes produced by a low order interferometer. This value is then more accurately determined from the position of the fringes obtained using successive Fizeau interferometers of increasing thickness. For the LASE experiment, the approximate wavelength of the laser is known from the position of the laser tuning elements, which allows the final wavelength determination to be accomplished using only two Fizeau interferometers.

Measurement of the absolute emission wavelength requires laboratory calibration and determination of the geometrical characteristics of the Fizeau interferometers, and real-time (in-flight) processing to calculate the centroid wavelength. The various steps in these processes are described below.

The optical diagram is shown in Figure 13-11 for one Fizeau wedge. The important parameters are given below, where ε is the angle of the wedge, $e = e_0 + \varepsilon x$ is the thickness of the wedge at a point with coordinate x, and $R = f(\lambda)$ is the reflectivity of the coated surface.

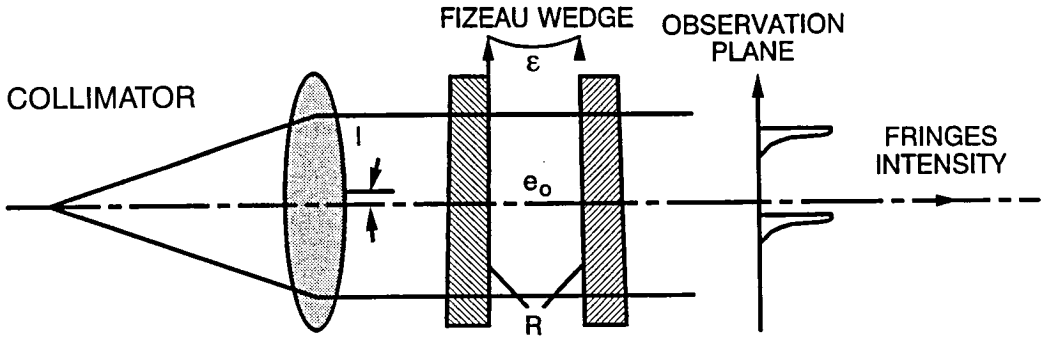

Figure 13-11. Fizeau wedge optical diagram indicating plate spacing e_0, *wedge angle* ε, *reflectively coated surfaces* R, *distance from optic axis* I, *and the fringe intensity pattern in the plane of observation in a direction* x, *perpendicular to the straight-line fringes.*

Interfringe spacing: $i = \dfrac{\lambda}{2\varepsilon}$,

Interference order: $k = \dfrac{2e}{\lambda}$,

Free spectral range: $\Delta\lambda_{FSR} = \dfrac{\lambda^2}{2e}$,

Apparatus function (FWHM): $\delta\lambda = \dfrac{\lambda^2}{2Fe}$, and

Finesse: $F = f(R, e_0, \varepsilon, I)$.

The light sources input successively to the wavemeter are the λ_{ON} and the λ_{OFF} alexandrite laser wavelengths and a reference wavelength from a stabilized He-Ne laser. The fringes obtained from the He-Ne laser allow an in-flight determination of the optical thickness of the Fizeau wedge at each point x. The interference order of the laser wavelength can then be computed. Then, from the position of the λ_{ON} (or λ_{OFF}) fringes, the value of the wavelength is determined.

Due to induced mechanical or thermal variations in the optical system, the position of the fringes will drift, so that the He-Ne laser fringes corresponding to the interference order k_0 may vary within a zone of width Z_0 (Figure 13-12). However, the stability of the system is such that Z_0 is much smaller than the interfringe spacing i, so that the interference order numbers remain unambiguous.

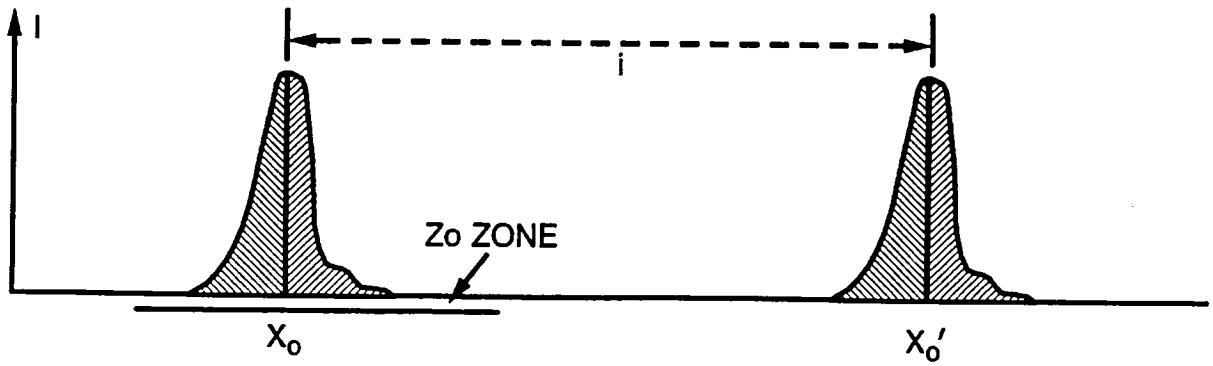

Figure 13-12. Fizeau interferometric fringe intensity pattern, generated with a single frequency stabilized He-Ne laser showing two orders of the interferometer located at X_0 and X_0', spaced at a distance i. *The Z_0 zone is the region within which the k_0th order He-Ne fringe will fall due to instabilities in the instrument.*

The thickness of the Fizeau wedge at point x is then given by

$$e(x) = \frac{\lambda_0}{2}\left(k_0 + \frac{x - X_0}{X_0' - X_0}\right), \tag{13-1}$$

where λ_0 is the He-Ne wavelength, and X_0, X_0' are the fringe positions. In the derivation of this equation, it is assumed that:

1. the stability of the system allows Z_0 to be smaller than the He-Ne interfringe spacing,
2. the measurement of the interference order k_0 and the determination of the Z_0 zone are accomplished in the laboratory,
3. the thickness of the wedge at λ_{ON} (λ_{OFF}) is equal to the thickness measured at λ_0 (or can be inferred from it),
4. the wavelength variation of the phase dispersion is known from laboratory calibration, and
5. λ_0 is known with an accuracy of $\Delta\lambda_0/\lambda_0 \sim 2 \times 10^{-8}$ (stability of the He-Ne laser).

The interference order for a given wavelength λ is

$$k = \frac{2e(X)}{\lambda}, \tag{13-2}$$

where λ is an approximate value of the wavelength known with an accuracy of $\pm\Delta\lambda$. The interference order is an integer k, which is thus known exactly, if the accuracy of k is $\Delta k < 0.5$. This is obtained if λ is known with an accuracy of $\Delta\lambda$, such that $\Delta\lambda < \Delta\lambda_{FSR}/2$, where $\Delta\lambda_{FSR}$ is the free spectral range of the Fizeau wedge. The wavelength λ is determined from the knowledge of the thickness of the Fizeau wedge and from the interference order as

$$\lambda = \frac{2e(X)}{k}, \tag{13-3}$$

where the accuracy of the wavelength determination is

$$\frac{\Delta\lambda}{\lambda} = \frac{\Delta e(X)}{e(X)}. \tag{13-4}$$

If the wavelength is known with an accuracy of $\pm\Delta\lambda_L$ from the alexandrite laser tuning element positions, then the free spectral range of the first Fizeau interferometer must satisfy the condition that $\Delta\lambda_{FSR} > 2\Delta\lambda_L$. The thickness of the Fizeau wedge is then computed from the position of the He-Ne fringes (Eq. 13-1). The interference order of λ_{ON} (λ_{OFF}) is computed from the position of a given λ_{ON} (λ_{OFF}) fringe (Eq. 13-2), and the value of λ_{ON} (λ_{OFF}) is then obtained with an accuracy of $\pm\Delta\lambda_{F_1}$ (Eq. 13-4).

The same operations are then performed with a second Fizeau interferometer satisfying the condition that $\Delta\lambda_{FSR} > 2\Delta\lambda_1$. The values of the wavelengths are then obtained with an increased accuracy $\pm\Delta\lambda_{F_2}$.

Conceptual Design of the Wavemeter. A schematic diagram of the wavemeter system is given in Figure 13-13. All the light routing is done using fiber optics. Since the interferometers are successively illuminated by the He-Ne laser and the alexandrite laser (λ_{ON}, λ_{OFF}), optical couplers are used to mix the light coming from the various sources. The light emitted by the He-Ne laser is injected into a monomode fiber optic by means of a focusing lens. Due to the small diameter of a monomode fiber, the same injection process cannot be used with the alexandrite laser, because it will result in spatial filtering and, due to the inhomogeneities in the laser beam itself, in spectral filtering. Special injection optics will be designed in order to conserve the emission spectral characteristics of the alexandrite lasers. Characteristics of both Fizeau interferometers are provided in Table 13-5.

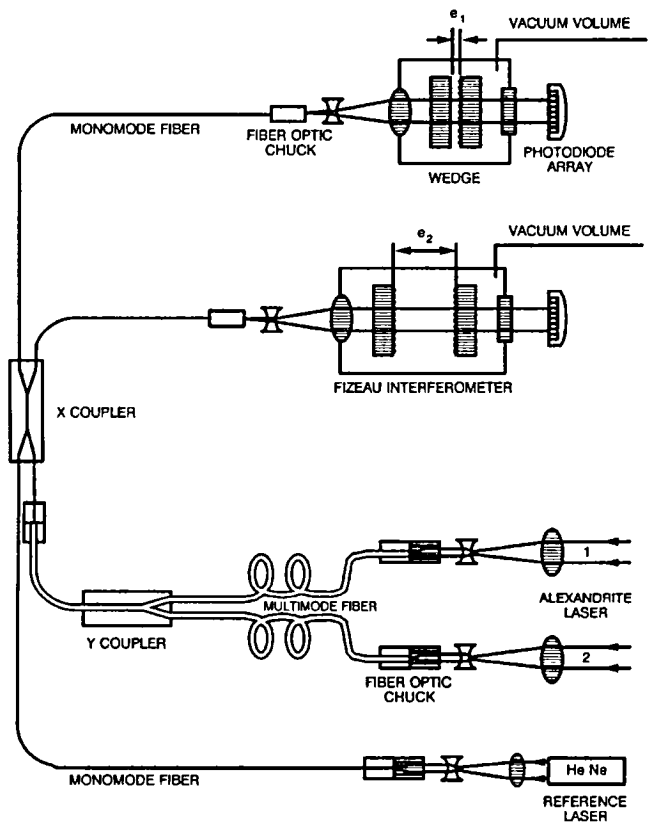

Figure 13-13. Wavemeter optical design.

Table 13-5. Fizeau interferometer characteristics.

Parameters	F_1	F_2
e	0.750 mm	50 mm
ε	5×10^{-5} rad	5.35×10^{-5} rad
R	97%	92%
$\Delta\lambda_{FSR}$	375 pm (for λ = 750 nm)	5.6 pm
Apparatus function	7.5 pm (finesse 50)	0.25 pm (finesse 22)

Given a knowledge of the emitted wavelength (from the position of the laser cavity tuning elements) with a maximum error of 170 pm, the use of F_1 ($\Delta\lambda_{FSR} > 2 \times 170$ pm) leads to the determination of λ with an accuracy of $\Delta\lambda_{F_1} = \pm 2$ pm.

Since the free spectral range is larger than $2\Delta\lambda_{F_1}$, the use of F_2 allows the determination of the emitted wavelength λ to an accuracy of ± 0.06 pm. Furthermore, the spectral profile of the emitted line is determined by deconvolution of the observed fringe pattern from F_2.

Fringe Pattern Detection and Analysis. The fringe detection is done using a 1024-element CCD diode array. Each diode has a width of 13 μm, resulting in a single diode spectral width of 0.65 pm for F_1 and 0.01 pm for F_2. The diodes are successively illuminated by the alexandrite laser λ_{ON} and λ_{OFF} wavelengths (200 to 400 μsec time interval), and by the He-Ne laser light, which is integrated over a time interval Δt. The three signals are digitized and sent to the microprocessor which is used to compute the centroid wavelength in real time, control the diode electronics and housekeeping parameters, and interact with the LASE computer by transmitting all data required for further analysis.

Operation Modes. The wavemeter has several modes of operation, as follows. In the laboratory, the wavemeter is used for system alignment, calibration of the thickness of the Fizeau interferometer using the fractional excess orders method, calibration of the measured wavelengths with reference to the species absorption spectra (multipath cell), and operation tests in conditions similar to field conditions. In the field, the wavemeter is used for operation tests and calibration of the measured wavelengths with reference to absorption spectra.

Receiver Data System. Differences between the Phase I and Phase II receiver and data systems are due to the higher accuracy needed to make differential absorption lidar (DIAL) temperature and pressure measurements as opposed to DIAL water vapor measurements. The following modifications will be made in Phase II.

Optical Filtering. Phase II utilizes different wavelengths and requires strong rejection of daytime background light. Background light not only adds a random noise component to the measured signals, but it also decreases the available dynamic range of the system, since large changes in the DC background component must be accommodated. It can also severely impact the measurement accuracy, since when a large background is subtracted from a small signal, even small errors in the measured background will introduce large errors into the resultant signal. Since the laser divergence and hence the receiver field of view are constrained by eye safety requirements, greater background rejection can only be achieved by utilizing spectrally narrowband optical filtering techniques.

Our studies indicate that spectral detection bandwidths of 0.1 to 0.2 cm^{-1} are required to achieve the desired degree of daytime background rejection for Phase II. This is higher by a factor of 20 to 40 than that available from commercial interference filters. These stringent requirements can be met by utilizing a combination of two Fabry-Perot etalons and one interference filter for a given lidar measurement. The interference filter is used to limit the overall detection bandpass of the system to a given wavelength region ~15 cm^{-1} wide. A single etalon with a finesse of 20 and a FSR of ~4 cm^{-1} is then used to further restrict the bandpass within the 15 cm^{-1} region to five equally spaced regions, each with a width of 0.2 cm^{-1}. A second etalon with a slightly different FSR can then be utilized to select two of the above narrow regions for detection, *viz.*, for the on- and off-line laser wavelengths. The Fabry-Perot and interference filter package will have integral temperature control to within 0.1 K. The post-telescope receiver optics will be modified to provide the required wavelength planarity.

Detectors. The signal levels from the on-line laser returns from low altitudes are expected to be on the order of a few hundred photons per microsecond. Since the signal level and the associated statistical (shot) noise are low, other sources of noise must be carefully treated to prevent degrading the signal-to-noise ratio. Our calculations show that the use of a high quantum efficiency photomultiplier with a GaAs photocathode will give better signal-to-noise ratios than a SiAPD for strongly absorbed lidar return signals.

Table 13-6 is a comparison of the noise as a percentage of the measured signal for several noise sources for each detection scheme and two levels of return signal. We note that the smaller of these signal levels corresponds to a digitized value of about 2 counts in the current Phase I system. The total random noise in any measured signal is the root mean square (RMS) sum of all the random noise components. It is clear that for the high gain channel of the receiver, which is used to recover weak lidar return signals, the photomultiplier gives lower noise due to its low dark current and Johnson noise-free intrinsic high gain.

Table 13-6. Noise as a percentage of signal for a single shot.

	PMT[a]		SiAPD[b]	
Photon Arrival Rate (per μsec)	1000	100	1000	100
Noise source[c]				
Signal shot noise	12	39	9	29
Background shot noise[d]	4	45	3	35
Dark current noise	2	17	40	400
Amplifier Johnson noise[e]	——	3	130	1300
Total noise (%)	13	61	136	1361

[a]Gain = 10^5, quantum efficiency = 20%, and temperature = 27°C.
[b]Gain = 75, quantum efficiency = 85%, and temperature = -20°C.
[c]Electronic bandwidth = 2 MHz, and optical throughput = 23%.
[d]Daytime background = 10^{11} photons/m^2-ster-nm-μsec, and optical bandwidth = 0.2 cm^{-1}.
[e]PMT amplifier gain = 100, and SiAPD amplifier gain = 3.3 x 10^4.

The Phase II receiver system will utilize high efficiency photomultiplier detection. We have measured the quantum efficiency of an RCA C-31034A photomultiplier to be 20% at 760 nm, even after >10 years at room temperature. The PMT's will be selected for good linearity, low after-pulsing, and low signal induced noise.

Electronics. In order to correct the lidar data for the effects of vertical nonhomogeneities in the atmospheric backscattered signal (Korb and Weng, 1980), we will increase the receiver bandwidth to obtain the fine scale structure of the backscattered return signals. These effects are particularly important where the data are most interesting, because enhanced aerosol structure is often associated with temperature inversions and moisture layers. The altitudes of the pressure heights of cloud layers and surface pressure are limited by the altitude resolution of the return signals. We will increase the resolution of the low gain channel sufficiently to resolve 15 m altitude intervals. The low and high gain channels will have bandwidths of 5 and 2 MHz, respectively. The digitizer sample rates will be 10 and 5 MHz, respectively.

The increased number of samples and increased system repetition rate (10 Hz) will bring the total data rate to 49,310 samples/sec. With data packing, this becomes about 37 kilowords/sec, which is ~72% of the tape recorder's maximum record rate. The data transfer time, assuming block mode data transfer from the CAMAC crate, will be ~27 msec. The data transfer rate of the Phase I LASE system is not yet known. We anticipate that some modifications to the computer system may be needed to augment the data transfer rate.

We are considering the use of a logarithmic amplifier in place of the linear amplifier in one or more of the receiver channels to increase the system dynamic range and to reduce digitization errors. Log amps have been used with success on the NASA/GSFC ER-2 lidar and are currently being used and extensively evaluated in two other lidar programs.

LASE Phase II Update[9]

This update provides a discussion of improvements in our approach as a result of comments and critiques received from reviews of the original proposal. The update covers the following subjects, each of which will be discussed separately.

1. Laser transmitter development: To preserve the modular integrity of the LASE concept, it is now our intent to develop a separate laser for LASE Phase II. A baseline configuration derived from the LASE Phase I design which fully meets the Phase II requirements is described and other possible design approaches are also mentioned.

2. Receiver filters and detectors: The approach to the design of high resolution receiver filters is described. We also comment on the selection of an optimum detector for our application (photomultipliers versus silicon avalanche photodiodes).

3. Wavemeter development: Significant progress, both theoretical and experimental, in the design and testing of an advanced wavemeter by CNRS is discussed. Our plans continue to be focused on the Fizeau wedge interferometer with monomode optical fiber coupling, which is expected to eliminate the speckle problem.

4. Systems analysis: An analysis of the LASE Phase II system is presented. Recent airborne measurements of pressure profiles using alexandrite lasers are also discussed. These results demonstrate the feasibility of

[9] This section is excerpted from an update of the proposal entitled, "Advanced ER-2 Lidar for Mesoscale Meteorological Studies - LASE II."

DIAL pressure measurements and confirm the results of previous theoretical system analysis. They also constitute the basis for establishing the LASE Phase II system performance.

5. Simultaneous determination of multiple meteorological parameters: The ability to measure the major atmospheric state variables (pressure, temperature, and water vapor) simultaneously is discussed in terms of the use of other sensors in conjunction with the LASE Phase II instrument. In addition, we address the possibility of designing the LASE Phase II system so that it will be capable of measuring pressure and/or temperature and moisture during a single flight mission.

6. Test, evaluation, and ground support equipment: A brief description is provided.

Phase II Laser Transmitter

Transmitter Design Constraints and Considerations. In proposing a transmitter for the LASE Phase II program, we must consider constraints imposed by the ER-2 aircraft, existing laser technology and that being developed under the Phase I program, and potential programmatic risks and benefits associated with more advanced technological approaches. Principally, the ER-2 aircraft imposes restrictions on size, weight, and, to a lesser extent, prime power. The Phase I transmitter effort will result in major reductions in these areas relative to current commercial alexandrite laser hardware. In addition, the Phase I transmitter will presumably demonstrate reliable autonomous operation under a wide range of environmental conditions. Demonstration of the Phase I performance requirements with respect to laser energy and linewidth have already been made with an existing alexandrite laser at GSFC. Material presented at the LaRC Preliminary Design Review strongly indicates that a transmitter, meeting the Phase I performance specifications with acceptable size, weight, and prime power margins, can be developed.

In our original LASE Phase II proposal, it was assumed that only minor modifications could be made to the existing Phase I transmitter in an attempt to meet the more rigorous Phase II laser linewidth and wavelength control requirements. While this approach had a favorable impact on Phase II development costs and schedules, it greatly restricted the technological options for the Phase II laser design. The recommendation by NASA Headquarters and various reviewers, for scientific and programmatic reasons, that a totally new Phase II transmitter be built opens up several new options not previously considered. Nevertheless, the engineering decisions made in arriving at the Phase I baseline transmitter design are relevant to the Phase II effort as well. Furthermore, development costs and schedule changes for the Phase II transmitter will be minimized by utilizing as much of the Phase I technology as possible. For this reason, our baseline design is a straightforward extrapolation of the Phase I approach. The baseline design, as well as other design options to be investigated further during the early phases of the Phase II program, are described below.

Baseline Transmitter Approach: *Long Folded Resonator.* The most straightforward approach to achieving the Phase II goals is to develop a longer resonator. Because of space limitations on the Equipment Mounting Deck (EMD) in the ER-2 Q-bay, this would require the use of a folded geometry for each of the two alexandrite lasers. Folded geometries can be very stable mechanically and are commonly used in military lasers where size constraints often dictate the geometry of the laser. In this application, the longer resonator offers two advantages, *viz.*, larger spot sizes in the resonator and, more importantly, a smaller longitudinal mode spacing. The latter is given by $c/2L$, where c is the speed of light and L is the effective optical length of the cavity. With the longer cavity, operation of the Phase II transmitter would be completely analogous to the Phase I system, where 3 to 5 longitudinal or "temporal" laser cavity modes are free-running with respect to the transmission bandpass of the thick etalon, as in Figure 13-10. This approach has two important practical advantages. First of all, no control of the overall laser resonator length is required. The practical difficulties

associated with achieving adequate active control are discussed in our original proposal. A second advantage of our baseline approach is that multimode operation is most efficient and leads to greater stability in both the output energy and the wavelength centroid. This is illustrated in Tables 13-7 through 13-11, which show the effect on linewidth and energy as the cavity modes move randomly through the bandpass of a thick etalon with a varying finesse-thickness product. The tables were generated using a sophisticated alexandrite laser modelling program developed by GSFC in support of the Phase I laser development. In the calculations presented here, we have optimized a number of laser parameters (*e.g.*, lamp input energy, output coupler reflectivity, and rod temperature) to obtain a nominal output energy of 150 mJ at an operating wavelength of 760 nm. It is assumed in the calculations that individual temporal modes build up from spontaneous emission, and that the spontaneous emission rates are equal for all modes lying within the narrow bandpass of the thick etalon.

The mode phase shift at the top of each column in Tables 13-7 through 13-11 is defined as the frequency difference between the center of the etalon passband and the central laser mode, expressed as a fraction of the laser resonator free spectral range (FSR), *i.e.*, $c/2L$. In the calculations presented here, a resonator length of 160 cm is assumed, resulting in a temporal mode spacing or FSR (in wavelength units) of 0.1805 pm. A mode phase shift equal to 0 implies that the central resonator mode is resonant with the peak of the etalon passband. A mode phase shift of 0.5 represents the maximum possible deviation of the central mode from the peak of the etalon transmission. The rows in the tables give the total energy contained in all of the modes, the wavelength centroid in picometers relative to the center of the etalon passband, the 1σ linewidth of the laser, the wavelength intervals containing 99% and 100% of the laser energy, and the fractional energies contained in the central mode q and its 4 nearest neighbors (q-2, q-1, q+1, and q+2).

Table 13-7 shows the effect of an etalon with a low finesse-thickness product of 2 cm. Because of the relatively wide passband, 15 temporal modes initially have gain and compete for the available population inversion. Energy is fairly well distributed among all the modes with 87% contained in the central 5 modes. As a result, the output energy and wavelength centroid are very insensitive to the positioning of the resonator modes within the etalon passband. On the other hand, the laser linewidth is relatively large with 99% of the laser energy contained within 1.444 pm, and 100% within 2.166 pm.

Table 13-8 represents the opposite extreme of an etalon with a relatively high finesse-thickness product of 13 cm. With this etalon, only 3 temporal modes have gain, and the central mode extracts 99.83% of the total energy when it is in resonance with the peak of the etalon passband. Since the central mode dominates the oscillation, the position of the wavelength centroid largely follows the movement of this mode until the (q-1) mode achieves comparable gain and drives the centroid back toward the peak of the etalon bandpass. At the maximum mode phase shift of 0.5, the (q-1) and q modes are on opposite sides of the etalon bandpass, and therefore have equal losses, resulting in equal energies and zero shift in the wavelength centroid. As the central mode moves down the steep slope of the etalon transmission curve, it sees significantly smaller net gain, which is not totally compensated by the increasing gain of the (q-1) mode. This results in a significant decrease in the laser output energy. In this example, the free-running laser energy would be expected to vary over a range of 129 to 160 mJ. On the other hand, the laser linewidth is narrow, since all of the energy is contained in 2 to 3 modes. Clearly, a tradeoff exists between laser linewidth, and wavelength centroid and output energy stability.

Table 13-7. Mode competition for etalon with a low finesse-thickness product of 2 cm.

Mode Phase Shift	0	0.1	0.2	0.3	0.4	0.5
Mode total energy (mJ)	152.7912	152.7912	152.7912	152.7912	152.7911	152.7913
Mode centroid (pm)	0.0000	0.0000	0.0000	0.0000	0.0000	0.0000
Mode sigma (pm)	0.3030	0.3030	0.3030	0.3030	0.3030	0.3030
Mode linewidth 99% (pm)	1.4440	1.4440	1.4440	1.4440	1.4440	1.4440
Mode linewidth 100% (pm)	2.1660	2.1660	2.1660	2.1660	2.1660	2.1660
Mode fractional energy (q-2)	0.1158	0.1243	0.1328	0.1415	0.1502	0.1589
Mode fractional energy (q-1)	0.1995	0.2065	0.2130	0.2189	0.2242	0.2287
Mode fractional energy (q)	0.2394	0.2390	0.2377	0.2355	0.2325	0.2287
Mode fractional energy (q+1)	0.1995	0.1920	0.1841	0.1759	0.1675	0.1589
Mode fractional energy (q+2)	0.1158	0.1076	0.0996	0.0919	0.0845	0.0774

Etalon finesse = 2
Etalon thickness = 1.00 cm
Active modes = 15
Lamp input energy = 51.0 J
Resonator length = 160 cm
Wavelength = 760 nm

Table 13-8. Mode competition for etalon with a relatively high finesse-thickness product of 13 cm.

Mode Phase Shift	0	0.1	0.2	0.3	0.4	0.5
Mode total energy (mJ)	160.7068	159.3010	155.1810	147.2915	136.8923	129.3327
Mode centroid (pm)	0.0000	-0.0175	-0.0340	-0.0462	-0.0426	0.0000
Mode sigma (pm)	0.0074	0.0106	0.0197	0.0371	0.0669	0.0903
Mode linewidth 99% (pm)	0.0000	0.0000	0.1805	0.1805	0.1805	0.1805
Mode linewidth 100% (pm)	0.3610	0.1805	0.1805	0.1805	0.1805	0.1805
Mode fractional energy (q-2)	0.0000	0.0000	0.0000	0.0000	0.0000	0.0000
Mode fractional energy (q-1)	0.0008	0.0033	0.0120	0.0441	0.1642	0.5000
Mode fractional energy (q)	0.9983	0.9965	0.9880	0.9559	0.8357	0.5000
Mode fractional energy (q+1)	0.0008	0.0002	0.0001	0.0001	0.0001	0.0001
Mode fractional energy (q+2)	0.0000	0.0000	0.0000	0.0000	0.0000	0.0000

Etalon finesse = 13
Etalon thickness = 1.00 cm
Active modes = 3
Lamp input energy = 51.0 J
Resonator length = 160 cm
Wavelength = 760 nm

Tables 13-9 and 13-10 represent intermediate cases, having etalon finesse-thickness products of 6 and 8 cm, respectively. In particular, the 8 cm example appears to approach the Phase II linewidth requirements. Disadvantages of high finesse etalons include greater optical throughput losses and greater susceptibility to optical damage. Some advantage can be gained by increasing the thickness of the etalon (within limits

Table 13-9. Mode competition for etalon with an intermediate finesse-thickness product of 6 cm.

Mode Phase Shift	0	0.1	0.2	0.3	0.4	0.5
Mode total energy (mJ)	153.3171	153.2120	152.9663	152.6162	152.3360	152.2309
Mode centroid (pm)	0.0000	0.0000	-0.0018	-0.0018	-0.0011	0.0000
Mode sigma (pm)	0.0980	0.0986	0.1000	0.1019	0.1034	0.1040
Mode linewidth 99% (pm)	0.3610	0.3610	0.3610	0.3610	0.5415	0.5415
Mode linewidth 100% (pm)	0.7220	0.7220	0.7220	0.7220	0.5415	0.5415
Mode fractional energy (q-2)	0.0014	0.0026	0.0045	0.0076	0.0126	0.0204
Mode fractional energy (q-1)	0.1416	0.1920	0.2529	0.3234	0.4005	0.4796
Mode fractional energy (q)	0.7139	0.7030	0.6713	0.6206	0.5550	0.4796
Mode fractional energy (q+1)	0.1416	0.1016	0.0709	0.0318	0.0318	0.0204
Mode fractional energy (q+2)	0.0014	0.0008	0.0004	0.0002	0.0001	0.0001

Etalon finesse = 6
Etalon thickness = 1.00 cm
Active modes = 5
Lamp input energy = 51.0 J
Resonator length = 160 cm
Wavelength = 760 nm

Table 13-10. Mode competition for etalon with an intermediate finesse-thickness product of 8 cm.

Mode Phase Shift	0	0.1	0.2	0.3	0.4	0.5
Mode total energy (mJ)	155.8151	155.2865	154.0889	151.6358	149.4983	148.6234
Mode centroid (pm)	0.0000	-0.0069	-0.0124	-0.0131	-0.0085	0.0000
Mode sigma (pm)	0.0601	0.0629	0.0689	0.7920	0.0880	0.0916
Mode linewidth 99% (pm)	0.3610	0.3610	0.3610	0.1805	0.1805	0.1805
Mode linewidth 100% (pm)	0.3610	0.3610	0.3610	0.5415	0.5415	0.5415
Mode fractional energy (q-2)	0.0000	0.0000	0.0001	0.0003	0.0007	0.0018
Mode fractional energy (q-1)	0.0554	0.0935	0.1469	0.2349	0.3552	0.4982
Mode fractional energy (q)	0.8893	0.8747	0.8375	0.7568	0.6402	0.4982
Mode fractional energy (q+1)	0.0554	0.0317	0.0155	0.0080	0.0039	0.0018
Mode fractional energy (q+2)	0.0000	0.0000	0.0000	0.0000	0.0000	0.0000

Etalon finesse = 8
Etalon thickness = 1.00 cm
Active modes = 5
Lamp input energy = 51.0 J
Resonator length = 160 cm
Wavelength = 760 nm

imposed by the FSR of the thin etalon) and reducing the finesse proportionally to maintain the same finesse-thickness product. A 2 cm thick etalon with a finesse of 4 would be an appropriate choice for the Phase II transmitter.

By increasing the effective resonator length to 192 cm, one can reduce the intermode spacing to 0.15 pm, which collapses the 99% linewidth to the 0.3 pm Phase II specification for all values of the mode phase shift, as in Table 13-11. The predicted output energy variations of <1% and centroid variations <0.004 pm due to the free-running movement of modes within the thick etalon bandpass are negligible and easily meet the Phase II specifications.

The analysis presented here effectively compares the competition effects between different temporal modes for the inverted population accessible to a given spatial or transverse mode, TEM_{mn}. Different spatial modes can also compete for the excited atoms within their respective mode diameters in the laser rod. The relative spacing between the resonant frequencies of different spatial modes varies with the precise resonator geometry, so that the phase shift (relative to the etalon peak) for each set of spatial modes is a function of the transverse mode quantum numbers, m and n. Although the presence of high order spatial modes can result in new frequencies lying between the modes presented here, it can be justifiably argued that competition between spatial modes will not appreciably alter the qualitative results on laser linewidth and centroid stability presented here, since, as a subset, each set of temporal modes associated with a given spatial mode should behave in a manner consistent with the calculations presented here.

Table 13-11. Mode competition for etalon with an intermediate finesse-thickness product of 8 cm and an increased effective resonator length.

Mode Phase Shift	0	0.1	0.2	0.3	0.4	0.5
Mode total energy (mJ)	154.0894	153.8782	153.2470	152.4064	151.7403	151.4605
Mode centroid (pm)	0.0000	-0.0022	-0.0035	-0.0036	-0.0023	0.0000
Mode sigma (pm)	0.0699	0.0710	0.0737	0.0771	0.0799	0.0810
Mode linewidth 99% (pm)	0.3008	0.3008	0.3008	0.3008	0.3008	0.3008
Mode linewidth 100% (pm)	0.6017	0.4513	0.4513	0.4513	0.4513	0.4513
Mode fractional energy (q-2)	0.0004	0.0008	0.0015	0.0029	0.0055	0.0099
Mode fractional energy (q-1)	0.1066	0.1554	0.2193	0.2988	0.3911	0.4901
Mode fractional energy (q)	0.7860	0.7728	0.7334	0.6698	0.5863	0.4901
Mode fractional energy (q+1)	0.1066	0.0709	0.0457	0.0285	0.0171	0.0099
Mode fractional energy (q+2)	0.0004	0.0002	0.0001	0.0000	0.0000	0.0000

Etalon finesse = 4
Etalon thickness = 2.00 cm
Active modes = 5
Mode intervals = 5000
Lamp input energy = 51.0 J
Resonator length = 192 cm
Wavelength = 760 nm

Alternate Approaches: Degenerate Resonators. These geometries were discussed in our original proposal as the preferred choice when we were constrained to consider only minor modifications of the Phase I transmitter. In this technique, the spatial modes of the laser resonator can be split into subsets such that the frequency spacings between subsets mimic the effect of a longer resonator with smaller temporal mode spacings. The principal advantage of this approach is that it represents the minimum deviation from the Phase I design. It is therefore potentially the least expensive option to implement. Breadboard studies of this approach will be carried out at GSFC during the first year of the Phase II program using a laboratory alexandrite laser. Ramsay and Degnan (1970) provided the basic theory of degenerate resonators and experimental demonstrations of degeneracy effects on the optical throughput of passive interferometers and the output power of a hole-coupled CO_2 laser.

Injection-locked Oscillator/Amplifiers. The use of injection locking to meet the Phase II requirements has been suggested. GSFC and CNRS have conducted research with respect to injection-locked Nd:YAG regenerative amplifiers for ultrashort pulse satellite laser ranging and injection-locked travelling wave Rhodamine 6G dye laser amplifiers for narrowband tunable atmospheric lidars. In this technique, the output of a low power oscillator having desirable characteristics (*e.g.*, ultrashort pulsewidth in ranging or ultranarrow linewidth in lidars) is injected into a power amplifier with the result that the high energy output retains the characteristics of the input pulse. Since the high energy amplifier does not require the inclusion of lossy and damage-prone optical elements such as etalons, the overall system efficiency and reliability can potentially be improved. A coarse tuning element, such as a birefringent tuner, is generally required in the power amplifier to prevent buildup at the peak of the alexandrite gain curve when operating at off-peak wavelengths. Use of a ring amplifier configuration can sometimes eliminate the potential problem of high power feedback from the amplifier to the oscillator. Thus, injection locking of an alexandrite amplifier can be advantagous if (1) optical damage to the etalons prevents operation of the oscillator at the desired output energies, or (2) the narrow bandwidth oscillator can be pumped with such low powers that the overall system efficiency greatly improves.

The material properties which make alexandrite a highly tunable laser medium also make it a relatively low gain medium. Most of the lamp energy input to the laser rod is required to raise the gain to the oscillation threshold, *i.e.*, to the level where the gain equals the losses introduced by the internal optical elements. Above the threshold, the output energy climbs rapidly with additional lamp energy. For a nominal 150 mJ output, the laser is operated at about 1.2 times threshold. Thus, a flashlamp-pumped alexandrite amplifier injection locked by a flashlamp-pumped low power alexandrite oscillator is wasteful of prime power and offers no advantage for these output energy levels. If, however, a small volume of the alexandrite oscillator rod were pumped longitudinally by an efficient external laser (*e.g.*, doubled Nd:YAG) or if the master oscillator were a well-stabilized, narrowband AlGaAs diode laser emitting at the desired wavelength, some considerable prime power savings and output energy increases might be realized in an injection-locked master oscillator/ flashlamp-pumped alexandrite power amplifier configuration. These are active research areas which are being explored at GSFC, LaRC, and other institutions outside NASA, such as CNRS and Allied Corporation. Experimental data on diode injection-locked alexandrite lasers are still too preliminary to propose such a device as a baseline transmitter. Recent experimental data from Allied Corporation indicate that the amplified energy typically appears in two adjacent temporal modes on either side of the injected signal. This result would again imply a need for either an actively controlled resonator length or a longer resonator geometry to meet the Phase II linewidth requirements. Important technical issues include: (1) the commercial availability of narrowband (0.3 pm) frequency-stabilized diodes (0.06 pm) operating with sufficient power at the desired lidar wavelengths, (2) the potential need for active tracking of the oscillator frequency by the power amplifier cavity in pulsed narrow linewidth (0.3 pm) applications, and (3) optical and electrical isolation of the laser

diode master oscillator from the flashlamp-pumped alexandrite power amplifier. Although we believe that the Phase II experiment requirements can be met by the baseline folded resonator geometry described previously, we propose to investigate the use of laser diodes as injection locking oscillators because (1) they offer the potential of rapid wavelength switching between the "on" and "off" line wavelengths in multiple parameter measurements (*i.e.*, water vapor, temperature, and pressure), and (2) they may permit sizeable reductions in prime power due to the elimination of the etalons from the alexandrite cavity. An experimental study will be carried out under contract to Allied Corporation during the first year of the Phase II program. This will eliminate any interference with the Phase I transmitter development at GSFC.

Self-Injection-Locked Oscillators. A variation on the injection-locked theme, which is sometimes more energy efficient, is the self-injection-locked oscillator, in which a single active medium is used first to generate the desirable characteristic (*i.e.*, narrow pulsewidth or linewidth) and then serve as a power amplifier to increase the output energy. For example, one state of an electro-optic Q-switch will permit operation of the laser at a very low level, while internal optical elements (modelocker for pulsewidth or etalons for line narrowing) develop the appropriate pulse characteristics over the long pulse buildup time. At the completion of this low power "prelasing" cycle, the Q-switch changes state, thereby causing the laser to enter a "high-Q" or low loss energy amplification state. This energy amplification can take place within the same resonator or in an alternate high power leg, if optical damage is a consideration.

The alternate leg approach was recently used at Allied Corporation to achieve single mode operation of a narrowband alexandrite laser. Two etalons and a birefringent tuner were placed in an oscillator leg to narrow the linewidth. An electro-optic Q-switch then switched the radiation to a low loss amplifier leg via an internal polarizer. Large energy fluctuations were observed due to the drift between resonance frequencies of the two legs and drift of the oscillator resonance relative to the passband peak of the thick etalon. In addition, operation at wavelengths far from the peak of the gain curve was hampered by competition from buildup of radiation in the high gain regions during amplification. Although inclusion of a weakly dispersive element in the amplifier leg would eliminate this competition, the single mode system suffers from many of the same problems as the high finesse-thickness product case discussed previously. The additional size and weight impact and minimal gains offered by this approach make it presently unattractive for the Phase II transmitter.

Receiver System

The LASE Phase II detector and focal plane optics module will replace the corresponding module in the LASE Phase I system. The general requirements are to reduce daytime background radiation by a factor of 10^8, to detect lidar return signals with a noise level of 1% after averaging over a specific number of lidar returns, and to maintain relative systematic errors to <0.2%.

Optical Filtering. Expected daytime background spectral radiance is ~3 x 10^{-2} watts/m^2/ster/nm at the receiver telescope aperture, assuming a ground albedo of 0.3, clear atmosphere aerosol loading, and no molecular resonant absorption. The background shot noise can be reduced only by narrowing the field of view of the receiver telescope (until it is equal to the laser divergence) or by spectrally filtering the returns with narrowband optical filters. Laser divergence is constrained by eye safety requirements to 0.7 mrad, and the receiver aperture is kept to 1.2 mrad as a practical matter of keeping the laser beam completely in the receiver field of view, accounting for uncertainties in either laser or receiver pointing. Since the field of view is constrained, additional background light rejection is achieved by limiting the optical filter bandwidth to ~0.24 cm^{-1} for pressure measurements and ~0.48 cm^{-1} for temperature measurements. Since the on- and off-line laser separations are greater than these values, the optical filter will have a double bandpass, each with half the

indicated bandwidth and centered on each of the laser frequencies. For these parameters, the number of background photons incident on the entrance window will be ~200 photons/μsec. In fact, the level of background flux in the on-line bandpass is small compared to that in the off-line bandpass because of the strong oxygen absorption at the on-line wavelength, particularly for the pressure measurement wavelength of 760 nm, and the resultant background is about half this level. The following values are used for receiver throughput computations. The transmission T and reflectivity R for the various components are: two anti-reflection coated windows (T = 0.995 for each surface) are followed by two overcoated silver mirrors (R = 0.98), a collimating lens (anti-reflection coated; T = 0.995 for each surface), a turning mirror (R = 0.986), a beamsplitter (T = 0.995 for each surface), a total filter transmission of 0.5, a beamsplitter which transmits 90% of the light to the PMT, and a detector quantum efficiency of 20%. Using these values, it can be shown that 8% of the photons incident on the instrument bay window will be detected by the PMT.

The random fluctuations on the background level will be ~3 photoelectrons/μsec, compared to an expected on-line signal level of ~175 photoelectrons/μsec for an altitude of 0.5 km. This gives a S/N of 8.2 (background noise and signal fluctuations) for a single shot, which will increase to 130 after averaging over 250 lidar returns.

The design of the optical filter is based on techniques used in the PEPSIOS instrument (Mack, *et al.*, 1963) and the University of Wisconsin High Spectral Resolution Lidar (Shipley, *et al.*, 1983). Two Fabry-Perot etalons in series are used in conjunction with a conventional interference filter which selects only two of the narrow pass bands of the double etalon (Figure 13-14). The etalon mirror spacings are chosen so that the resultant transmission peaks are spaced by the desired on-line, off-line wavelength spacing. Wavelength tuning to position the filter bandpasses to the exact laser wavelengths is accomplished by controlling the pressure of the gas inside the etalon housings. The etalons will be optically contacted and temperature controlled for mechanical and thermal stability. To maintain ±0.01 cm^{-1} stability, the temperature of the filter must be controlled to ±0.1°C and the pressure controlled to 1 mb. In order to achieve the necessary spectral resolution, the light rays must be collimated to <6 mrad.

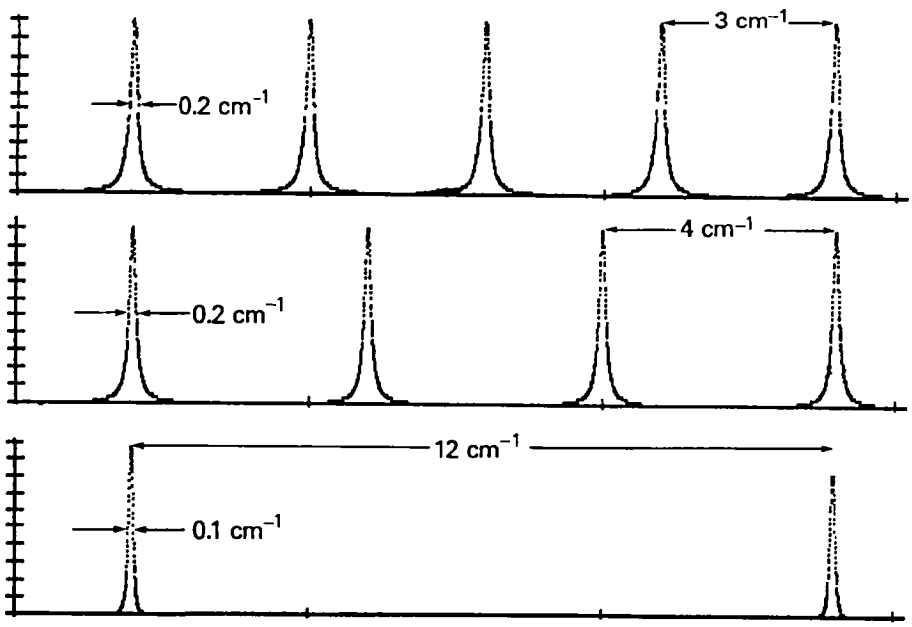

Figure 13-14. Optical filtering conceptual design: The transmission curves of two Fabry-Perot etalons (top and middle) and the transmission of both in tandem (bottom).

Given the 1.2 mrad field of view and 38 cm aperture of the LASE telescope, this requires a 7.6 cm diameter beam in the filter. The etalons must be tested for proper finesse, plate spacing, and low scattered light levels in order to perform satisfactorily. These specifications will be determined during the conceptual design phase of the program.

The above approach to optical filtering involves low to moderate risk, with little or no research required for development. It utilizes proven technology and is an order of magnitude lower in resolution than previously built instruments. There is substantial experience within NASA of building space-qualified interferometer instruments.

Detectors and Electronics. The LASE Phase II detector module baseline design contains two detectors: 1) a high sensitivity RCA C31034 photomultiplier tube with a gallium arsenide photocathode, and 2) a silicon avalanche photodiode. Our analyses to date have shown that we need the higher sensitivity and lower noise characteristics of the photomultiplier for sufficient signal-to-noise in the lower troposphere. We can save weight and volume in the receiver package by utilizing a SiAPD to recover the much stronger cloud and ground reflection signals. During the initial research and development phase of the program, additional modeling and analysis will be performed. Various components, including detectors, electronic filters, and amplifiers will be characterized and evaluated in the laboratory in order to optimize the design of the detection system. Alternate components, such as logarithmic amplifiers and high-voltage modulators, will be evaluated to augment performance. We are also following closely the current studies performed by the LASE program. We will draw on the extensive experience of the lidar programs at GSFC and CNES/CNRS in the use of photomultipliers to identify, minimize, and correct or compensate for systematic effects in the detection process, such as signal-induced dark current, after-pulsing, and other transient effects. For example, the PMT will be gated off electronically during the ground reflections to minimize effects of this transient. Final flight hardware will be subjected to environmental tests and calibrated under expected flight conditions to derive linearity and response functions. These may be necessary for lidar data processing in order to achieve the 0.2% relative systematic accuracy required to derive atmospheric temperature and pressure profiles from the measured lidar return signals. It is important to note that PMT's have been used successfully and have performed satisfactorily in the Goddard Pressure and Temperature Lidar System, as evidenced by the successful flight data presented in Chapters 10 and 11. The requirements for the detector for the low altitude instrument are similar to those needed for the ER-2 system, except for the lower signal levels and automated operation in the ER-2.

Wavemeter

The wavemeter proposed for LASE Phase II is based on a breadboard developed for water vapor measurements. Theoretical and experimental studies have been performed in the laboratory to demonstrate the feasibility of the system and to define the various components. A LASE Phase II operating breadboard will be identical except for the Fizeau interferometer thickness. The LASE Phase II spectral resolution has to be higher by a factor of two than the breadboard already developed and in use in the laboratory. The thickness of the LASE Phase II Fizeau interferometer will be twice that of the breadboard. Figure 13-14 gives the optical design, and Figure 13-15 gives the wavemeter block diagram.

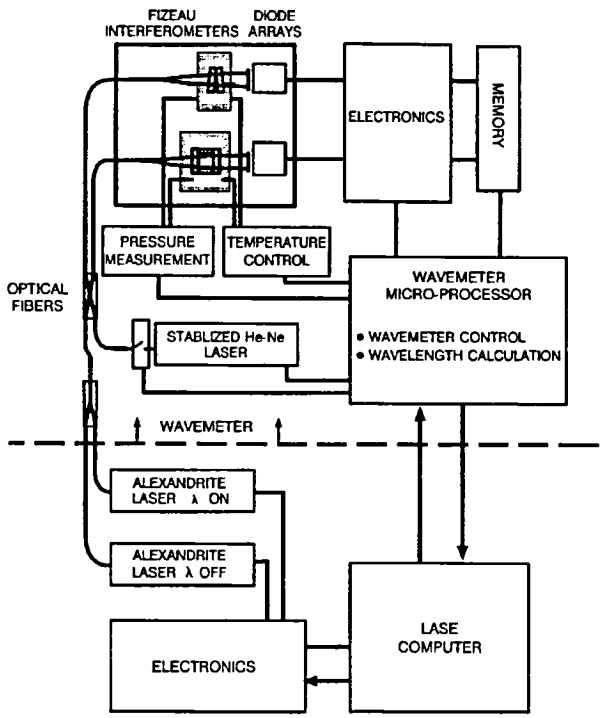

Figure 13-15. Wavemeter block diagram.

Speckle

The laser beams are transferred to the wavemeter using optical fibers. An experimental study of the impact of speckle by multimode fibers on the system measurements shows speckle noise to be unacceptable. As a result, we have chosen to use monomode fibers with the advantages of no speckle at the output and a Gaussian beam. A Selfoc lens is used to inject the laser beam into the fiber optic. The monomode fiber core is only 5 μm in diameter. The laser pulse energy gives a high energy density into the fiber. Destructive tests we performed in order to measure the damage threshold of the fibers and the energy needed to illuminate the breadboard detector show that the pulse energy needed for the LASE Phase II wavemeter will be <0.1 of the damage threshold value.

Fizeau Apparatus Function

The feasibility study performed for our system first developed a model to simulate the apparatus function. The characteristics of this function are the half-width, asymmetry in shape, sidebands which vary with wavelength, interferometer thickness, coating reflectivity, wedge angle, and beam divergence. We have conducted various experimental studies in the laboratory to check theoretical studies, and to define the Fizeau specifications and assess the required accuracy. The reflectivity is carefully chosen in order to reduce the amplitude of the sidebands. This choice increases the half-width, but provides better accuracy on the fringe centroid determination and deconvolution. Once the Fizeau interferometer is available, proper adjustment of the beam incidence angle allows the optimum apparatus function shape to be selected.

Accuracy

The apparatus function of a 50 mm Fizeau interferometer identical to the one described has been measured in the laboratory in order to evaluate the wavemeter performance. The proposed concept and design is within the LASE Phase II specifications.

The deconvolution used to retrieve the spectral shape was studied using a simulation program. This program simulates a spectral profile for the laser line and the Fizeau apparatus function, and computes the detector output reading using a convolution and random noise simulation. It computes the wavelength centroid and the spectral profile shape by deconvolution using the apparatus function. The pulsed laser line is assumed to be completely unknown before computation. The deconvolution provides very good results when the alexandrite laser line is broad (1 pm). In the case of a narrow line, preliminary results indicate that the wavemeter just meets the specifications. One way to improve the spectral profile determination is to increase the thickness of the interferometer. Another way is to provide the program with additional information about the laser line, such as the number of peaks, the relative spectral position of the peaks, and the width of each peak. Once the laser is available and tested, all this information will be available.

Tolerances

The already available breadboard has allowed us to determine the tolerances and sensitivity of the wavemeter. A critical parameter, the geometrical thickness, must be very stable. With optically contacted interferometers, this requirement is easily met. Other tolerances are not too severe and would easily be satisfied for a flight system.

Detection, Electronics, and Microprocessor

The concept and feasibility have been demonstrated. The microprocessor controls the wavemeter and computes the wavelength at the on- and off-lines. A schematic of the algorithm is given in Figure 13-16.

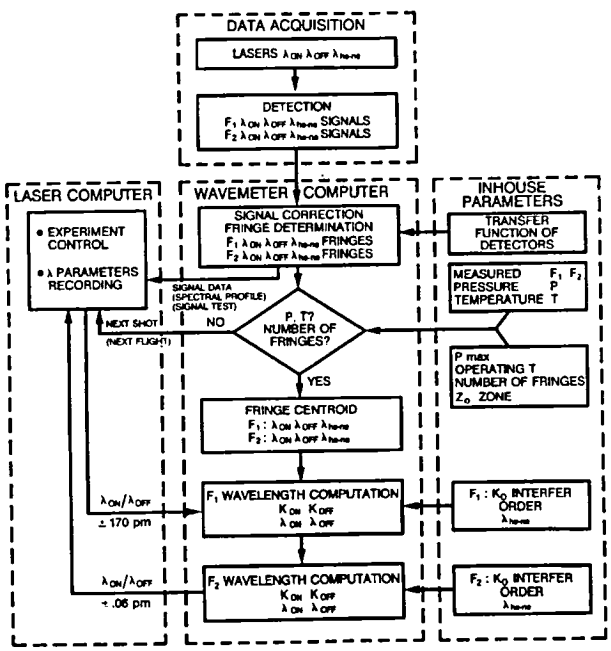

Figure 13-16. Wavemeter algorithm.

Systems Analysis

In lidar measurement of pressure and temperature, various error sources contribute to the total systems error. The largest source of error is the effect of random noise in the signal detection process. This may be reduced to very low levels using a photomultiplier detector and suitable averaging. Important systematic error sources include the accuracy and stability of setting the laser frequency and the interrelationship between the effects of laser line shape and bandwidth in the measurement process. Other error sources, such as timing and range gate width effects on altitude determination, digitization, differential spectral backscatter, temporal effects including advection and aircraft motion, and speckle effects in the scattering scene, can be reduced to <0.05% (Chapter 1) with a properly designed LASE Phase II system.

Our studies show that the accuracy and stability of setting the laser frequency have important effects for lidar temperature measurements. We found that to obtain accuracies <l K, it is necessary to set and maintain the laser frequency to <0.002 cm^{-1}. This result was derived for a laser bandwidth of 0.02 cm^{-1}, but is relatively insensitive to bandwidths in the range of 0 to 0.03 cm^{-1}. For a laser with three spectral modes and a bandwidth of 0.02 cm^{-1}, we also found that measurement accuracy was strongly dependent upon knowledge of the detailed shape of the laser spectral energy distribution. For example, a 0.0005 cm^{-1} change in the relative position of either outlying spectral mode is sufficient to produce a temperature uncertainty of 1 K. This provides the basic motivation for narrowing the laser bandwidth, which greatly desensitizes the measurements to laser line shape effects. We further note that most (80 to 90%) of the residual error due to laser line shape spectral information can be removed using the line shape measured by the wavemeter.

We can use the measurement results of Chapters 10 to 12 to estimate the performance of the LASE Phase II system from the ER-2 aircraft. The principal parameter changes from the Electra to an ER-2 system are the following: an increase in vertical averaging from 30 to 250 m, an increase in laser energy from 75 to 150 mJ per pulse, and an increase in photomultiplier quantum efficiency from 4 to 20% in going from a multi-alkali to a GaAs photo tube. We have measured 20% quantum efficiency in a ten-year-old GaAs photomultiplier tube in our laboratory. These photomultipler tubes are commercially available from RCA. The net increase in detected laser energy per range cell by a factor of 80 is slightly larger than the 60-fold loss in signal that occurs due to an increase in range from ~2.5 to 20 km. Thus, the LASE Phase II system should produce accuracies similar to those achieved from the Electra, namely, 1.5 mb for measurements in the lower troposphere for a 100-shot average, which corresponds to 2 km spatial resolution. For a 5 km spatial average, as was discussed in Figure 13-5 of the original LASE Phase II proposal, the accuracy of the measurements will improve to <1 mb.

We will continue to investigate the properties of high resolution laser systems. Our early studies show that at a laser spectral resolution of 0.005 cm^{-1} (0.3 pm), the effects of laser spectral line shape and energy distribution on temperature measurements are small (<0.7 K). This is important, since it reduces the criticality of the wavemeter measurement of the laser spectral line shape. We will also complete a full assessment of the effects of mixed aerosol and Rayleigh scattering. Initial studies indicate that the effects should be compensated in the data analysis using the off-line backscatter information and measurements of temperature or pressure to reduce the net effect to <0.4 K.

Simultaneous Determination of Multiple Meteorological Parameters

We understand that, at a meeting of the Science Advisory Committee (12 April 1986), it was strongly recommended that multiple meteorological parameters be measured simultaneously, or nearly so, in order to define the dynamical and thermodynamical state of the atmosphere. Obviously, the desirable parameters

include profiles of pressure, temperature, moisture, winds, and cloud structure. It is not possible to consider all of these measurements in the context of this experimental program. However, some measurement options are as follows:

1. High vertical resolution (500 m) and horizontal resolution (5 km) measurements of temperature (±1 K) or pressure (±2 mb) from the ER-2, using the LASE Phase II instrument with passive microwave and/or infrared sounders for lower vertical resolution (2 to 8 km) measurements of temperature and moisture.

   We also anticipate utilizing the cloud-top lidar to provide an independent measure of cloud-top structure and the thermodynamic phase (water/ice discrimination) of cloud-top hydrometeors. Also included in the ER-2 instrument complement would be a cloud imager to estimate cloud winds and an infrared radiometer for the determination of cloud-top and surface temperature.

2. The development, as an advanced goal of the program, of a LASE Phase II system which can simultaneously or alternately measure pressure and/or temperature along with moisture profiles. We anticipate that the complement of other instruments onboard the ER-2 and their measurement capabilities would be identical to those described in the first option above.

A brief description of a candidate passive infrared instrument (*i.e.*, High Resolution Interferometer or HIS) and a candidate passive microwave instrument (*i.e.*, Microwave Temperature Sounder or MTS) is given below.

The HIS is basically a Michelson interferometer measuring the Earth-emitted radiance with high spectral resolution to obtain fine scale vertical structure of temperature, water vapor, and other gases. It has a spectral range of 3.7 to 16.7 μm, resolving power >2000, resolution up to 0.35 cm^{-1}, and noise levels <0.1 K. From an altitude of 20 km, water vapor and temperature data can be provided at ~2 km altitude invervals. Weighting functions cause measurements to be correlated over 4 to 8 km altitude. The MTS instrument provides temperature profiles without cloud interference. It has ten channels symmetrically spaced about 118.75 GHz and one channel at 60 GHz. It is a scanning instrument; therefore, resolution is a function of integration time. Temperature can be determined with noise levels of ~0.25 to 1 K, depending upon integration time.

Test, Evaluation, and Ground Support Equipment

It will be necessary to have the capability of testing the LASE Phase II instrument, including interfaces, totally separate from the LASE facility, not only during instrument development for subsystem integration and system tests, but also during pre-integration testing to prove independently that instrument performance and interface requirements are satisfied. To this end, a test facility will be developed for LASE Phase II which will simulate electrical and optical interfaces with the LASE facility (which provides necessary power sources and signal processing), will record and process output data, and will provide the capability of near-real time evaluation of the results. As part of the LASE Phase II evaluation program, test flights on the NASA Electra and/or DC-8 aircraft are envisioned. For these flights, the LASE Phase II system components will be integrated with the Goddard Airborne Lidar facility, which consists of a telescope, optical bench, and LSI 11/23 data system. The computer will be upgraded to an 11/73, and will be made compatible with the LASE facility data system.

Each major subsystem will have unique ground support equipment (GSE) sufficient to evaluate the performance of the subsystem and will be usable in the field for trouble-shooting and retesting. For the laser subsystem, some of this support instrumentation should be available from the LASE Phase I effort. Presently envisioned are the following items:

Wavemeter

1. CW krypton-pumped dye laser system to generate calibration wavelengths
2. High resolution spectrometer
3. Multipath gas cell
4. Computer for data processing
5. Subsystem auxiliary power supplies
6. 220/208 volt supply/plug-in
7. Vacuum pump (0.5 hectopascals)
8. Special tool kit and spare parts

Laser

1. Ground chiller and fill-and-purge system
2. Energy meter
3. 400 Hz, 208 VAC, three-phase power supply
4. 28 VDC power supply
5. 100 MHz oscilloscope
6. PC for on-site diagnostics
7. Multimeter
8. Photo detector with bias supply
9. Special tool kit and spare parts

Detector/Receiver Optics Subsystem

1. Lidar return and background simulator
2. Multipath gas cell with mirrors
3. Telescope/laser mirror equipment
4. Vacuum pump (nitrogen fill system)
5. A/D-formatter-computer-record system for data processing and filter tuning control.

CHAPTER 14 CONCEPTS FOR FUTURE WEATHER AND CLIMATE LIDAR OBSERVATIONS FROM SPACE

INTRODUCTION

This chapter will focus on the need for and potential applications of lidar observations to research and operations in the weather and climate area. These are a representative subset of the most important problems within the broader realm of the environmental sciences. While the focus will be on space-based observing systems, a host of significant lidar studies and applications are better accomplished from the ground, aircraft, or balloon. Measurements from space will frequently have to be supported by such ancillary observing systems, and the logical development cycle often will involve a progression from ground to aircraft to space-based experiments. Although this chapter is concerned primarily with lidar, the need for other systems will also be considered, since a combination of sensors will be required. Indeed, we show how lidar can be combined with other remote sensors to provide hybrid measurement capabilities.

Recent conferences and literature reviews give a sense of the exceedingly broad range of potential applications of lidar to the atmospheric sciences, from the lowest levels of the troposphere to the outer magnetosphere. NASA (1979) has conducted an in-depth survey of the scientific problems and the feasibility of conducting lidar experiments from the space shuttle. The present discussion will consider mainly weather and climate problems in the troposphere and stratosphere, with some elaboration on key problem areas such as winds and air-sea interactions. Another NASA survey report (1980) deals with tropospheric air quality and discusses requirements for lidar measurements of tropospheric trace gases and aerosols.

GENERAL REMARKS ON WEATHER AND CLIMATE

Weather prediction on both global and regional scales remains the dominant scientific and operational problem facing the meteorological community. Recently, concerns with societal impacts of climate variability on shorter time scales (*i.e.*, months to years) and climatic change over decades have greatly heightened activity in climate research, with much work on climate predictability.

The approach to both numerical weather prediction and climate prediction generally proceeds through the use of general circulation models (GCM's) and high speed computers. In global weather prediction, the concern is with detailed specification of weather on regional scales of ~1000 km and time scales of up to 10 days. Conversely, climate prediction investigates the statistical description (in terms of means and variances) of the weather over larger regions and for a month or more. In the case of climate, forcing parameters, which have longer time constants and are thought to give climate long term "memory", are observed. These parameters include surface properties such as sea surface temperature, snow and sea ice, albedo, and soil moisture, and the more slowly varying radiatively active gases and aerosols.

These basic differences in approach to weather and climate also have important implications for observing systems, in terms of accuracy, precision, and time and space resolution. Because climate research uses time and space averaging, sampling rates can generally be reduced; by the same token, precision and accuracy must be increased, because climate perturbations are averaged ensembles of weather fluctuations. However, where weather measurement systems are characterized by random errors, required climatic accuracies often can be obtained simply by averaging large observational sets. Thus, all basic measurements required for numerical weather prediction may also be used for climatic purposes. However, the long time scales of interest in climate research put a high premium on instrument stability and intercalibration, and also on the uniformity and accessibility of operational weather data.

Since both weather and climate prediction begin with basic hydrodynamic and thermodynamic equations and attempt to ascertain the future state of the environment from the present one, both are initial value problems which depend critically on the accurate specification of the state at time zero. Assuming the models incorporate all the relevant physics and the numerical computational schemes are accurate, future progress depends, in large part, upon the improved quality and quantity of observations. This view is generally shared by the numerical prediction community, which has made remarkable progress in model development, but requires better observations to initialize and test its models and diagnose deficiencies. Indeed, this was a primary motivation of the year-long Global Weather Experiment (GWE) completed December 1979. Another perspective on this subject was presented by McPherson (1980). Kreitzberg (1980) considered corresponding requirements for short range local and regional predictions.

OBSERVATIONAL REQUIREMENTS

A comprehensive list of observational requirements for the diagnosis and modeling of climate on monthly, seasonal, and interannual time scales is given in Table 14-1 (NASA, 1977). Requirements for studies of the climate on decadal and longer time scales have been omitted, mainly for reasons of brevity, although lidar is applicable to problems involving measurements and monitoring of long term trends in radiatively active trace gases and aerosols. The first set of parameters labeled "weather variables" includes requirements for global weather. It is not possible to review in this chapter the rationale by which these observational requirements were established (NASA, 1977; NASA, 1974; WMO-ICSU, 1973).

Table 14-1 includes a current subjective judgment as to whether the measurement requirement can be met or supported through the use of lidar. These assessments appear in the last column with the following code:

A - ready; feasibility studies completed and technology available.
B - probably feasible; experiments need to be conducted and/or technology needs some development.
C - reasonable lidar concept available, but full feasibility studies and experiments need to be conducted and/or major advances in technology required.
S - lidar applicable in a supporting role.
NA - not applicable.

While much development is required, it seems likely that lidar will ultimately be capable of measuring all basic state variables and wind within the base requirements for accuracy, both for climate and global weather. It is also clearly applicable to cloud measurements, including cloud-top height, cover, and cloud water phase. Lidar is at least as important in support of other passive and active sensors, and in this area is ready for near term applications. In the case of cloud track winds obtained by geosynchronous satellite (GEOS), cloud heights must be known in order to assign winds to proper levels. Until stereo heights are available from pairs of GEOS, this can be done by lidar. Cloud heights are also required in radiation budget studies, because the net effects of clouds are very dependent on their heights. Cloud heights, in turn, aid in deducing cloud liquid water content (LWC) in two ways: through estimates of the LWC released adiabatically between deduced cloud base and cloud top, and by determinations of the depth of the cloud layer contributing to the radiative brightness (or attenuation) of microwave sensors sensitive to cloud water.

Although aerosol profiles are not explicitly listed in Table 14-1, they are of obvious importance in the radiation budget, as well as in many other ways. For example, corrections for aerosols and absorbing gases (especially CO_2 and H_2O) must be made in virtually every measurement of surface properties, including sea surface

Table 14-1. Observational Requirements for Climate on Monthly, Seasonal, and Interannual Time Scales.

Parameter	Desired Accuracy	Base Requirement	Horizontal Resolution	Vertical Resolution	Temporal Resolution	Lidar Capability
Weather Variables						
•Temperature profile	1 K	2 K	500 km	200 mb	12-24 hr	B
•Surface pressure	1 mb	3 mb	500 km	——	12-24 hr	B
•Wind velocity	3 m/sec	3 m/sec	500 km	200 mb	12-24 hr	B/C
•Sea surface temp.	0.2 K	1 K	500 km	——	3 days	B/S
•Humidity	7%	30%	500 km	400 mb	12-24 hr	B
Precipitation	10%	25%	500 km	——	12-24 hr	NA
Clouds			100 km	——	1 day	
Cloud cover	5%	20%				A/B
Cloud-top temp.	2 K	4 K				A/B/S
Albedo	0.02	0.04				A/B/S
Total liq. H_2O	10 mg/cm^2	1.50 mg/cm^2				A/B/S
Ocean Parameters						
Sea surface temp.	0.2 K	1 K	500 km	——	1 month	B/S
Evaporation	10%	25%	500 km	——	1 month	NA
Surface sensible heat flux	10 W/m^2	25 W/m^2	500 km	——	1 month	NA
Wind stress	0.1 dyne/cm^2	0.3 dyne/cm^2	500 km	——	1 month	NA
Radiation Budget						
Clouds' effect on radiation			500 km	——	1 month	
Cloud cover	5%	20%				A/B
Cloud-top temp.	2 K	4 K				A/B/S
Albedo	0.02	0.04				A/B/S
Total liq. H_2O	10 mg/cm^2	50 mg/cm^2				A/B/S
Regional net radiation components	10 W/m^2	25 W/m^2	500 km	——	1 month	B/S
Eq.-Pole gradient	2 W/m^2	4 W/m^2	1000 km zones	——	1 month	B/S
Surface albedo	0.02	0.04	50 km	——	1 month	B/S
Surface rad. budget	10 W/m^2	25 W/m^2	500 km	——	1 month	B/S
Solar constant	1.5 W/m^2	1.5 W/m^2	——	——	1 day	NA
Solar UV flux	10% per 50 Å interval		——	——	1 day	NA

Land, Hydrology, Vegetation

Precipitation, surface albedo, soil moisture (surface, root zone), vegetation cover,evapotranspiration, plant water stress

Cryosphere

Sea ice (% open water), snow cover, snow water content

•Basic First GARP Global Experiment (FGGE) measurement.

temperature, one of the key climate variables. Unless infrared measurements can be corrected for water vapor absorption and emission, it is unlikely that the base accuracy of 1 K will ever be obtained, much less the desired accuracy of 0.2 K. Lidar measurements of water vapor profiles by differential absorption lidar (DIAL) methods should provide information for necessary corrections. Discontinuities in aerosol concentration mark both the tropopause and the boundary layer. If these heights are known from lidar observations, retrievals of temperature and moisture profiles by passive methods would be greatly improved by constraining them to fit the height measurements.

Measurements of the boundary layer height, either by scatter from aerosols or boundary layer clouds, would be of great value throughout the atmospheric sciences. These data are required especially in regional and global numerical models which carry the planetary boundary layer (PBL) height as a prognostic variable. In the area of air-sea interactions, included in Table 14-1 by evaporation, surface sensible heat flux, and ocean wind stress, physical interpretation of the time and space variability of the boundary layer height can provide very good estimates of the heat and moisture fluxes. This brief discussion indicates the wide variety of significant roles for space-based lidar in future weather and climate investigations.

TEMPERATURE, PRESSURE, AND MOISTURE PROFILING

Wind and the atmospheric state variables of temperature, pressure, and humidity are basic parameters required in all prediction methods. Indeed, these are fundamental to studies of virtually every meteorological phenomenon on all space and time scales. The large investment in the global network of radiosonde stations and space satellites for measurements over the oceans and unpopulated regions demonstrates the significance of these parameters.

The interest in improved space measurements of temperature and humidity derives from two factors. The accuracy of present passive remote temperature sensors, such as the High Resolution Infrared Spectrometer (HIRS), is now limited by root mean square (RMS) errors of ~1.5 to 3 K depending upon height, and to vertical resolution $\geq$5 km, with very little useful information in the surface layer. Humidity soundings have poor accuracy and resolution and provide very little useful information in the lower layers. The situation would improve with the proposed new Advanced Meteorological Temperature Sounder (AMTS). A comparison of the simulated temperature accuracies of the AMTS and the HIRS is shown in Figure 14-1. While the AMTS nearly satisfies the temperature accuracy requirement (RMS) of $\pm$1 K, its vertical resolution is inherently limited to ~4 km. Also, as in passive temperature sounders, its weighting functions extend over the entire atmosphere, and data must be inverted to retrieve the temperature profile. As a result, data obtained depend heavily on the shape of the initial approximate profile, and the presence of unknown temperature structure (*e.g.*, inversions) can cause large errors. By contrast, simulations of the accuracies and resolutions achievable by a lidar temperature sounder in the troposphere (see below) indicate RMS errors of <1 K and vertical resolution of 2 km. The combination of higher accuracies and resolutions is expected to be of considerable value. Moreover, a lidar temperature sounder provides relatively direct measurements of temperature at known heights without the need for inversion. Indeed, the accuracy and resolution of a lidar sounder is currently limited only by the energy available for a measurement.

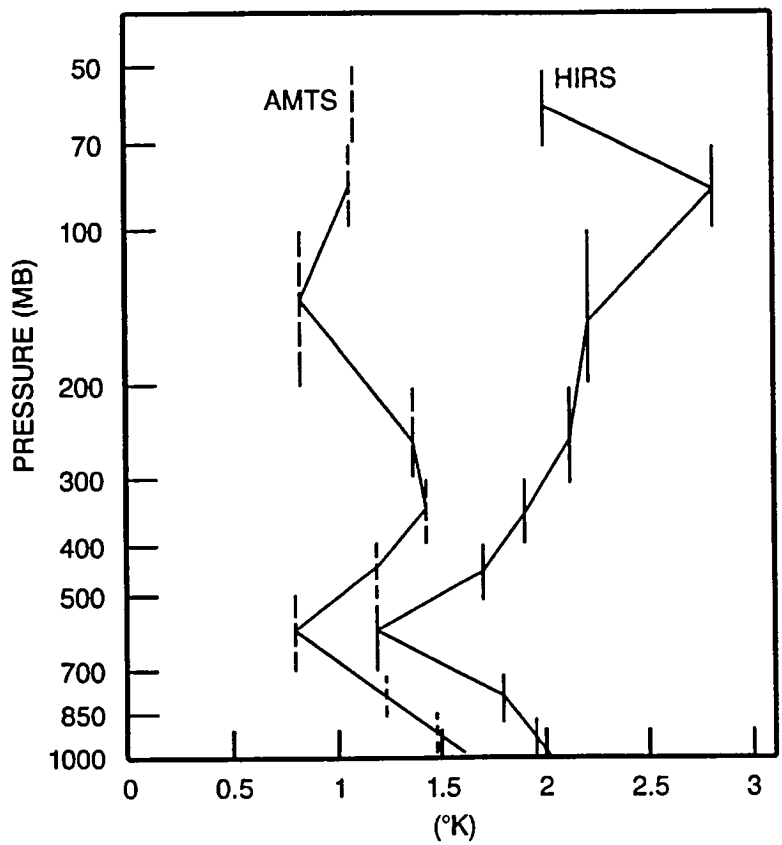

Figure 14-1. Simulated RMS temperature errors of the AMTS and HIRS passive temperature sounders as a function of height. Dashed (AMTS) and solid (HIRS) vertical bars indicate layer over which the mean layer temperature is obtained using 800 global soundings.

LIDAR ATMOSPHERIC SOUNDER AND ALTIMETER[10]

The Lidar Atmospheric Sounder and Altimeter (LASA) Panel was organized to develop the scientific objectives and corresponding engineering requirements for a lidar instrument as part of NASA's Earth Observing System (EOS) study. The initial concept of LASA was described in Volume I of the Earth Observing System Reports (Butler, *et al.*, 1984).

Atmospheric Pressure Observations

The pressure field is one of the fundamental variables used for weather prediction and atmospheric circulation studies. Surface pressure and 500 mb heights are used by meteorologists and other atmospheric scientists to describe the state of the atmosphere, to define frontal characteristics, and to determine mass movement. The three-dimensional pressure field is also a principal variable used in general circulation models for mid-range and long range forecasting. The pressure profile can be used directly to specify both the temperature profile

[10] This section consists of excerpts from Curran (1987).

and the balanced wind. In contrast, the derivation of a pressure profile from a temperature profile is not possible without specifying pressure at a reference height. Lidar provides the only remote sensing technique for the direct measurement of the pressure profile. In addition, it also provides the only remote sensing technique for measuring surface pressure over both land and ocean surfaces. Moreover, the lack of an accurate pressure reference level hinders the derivation of pressure profiles from radiometrically sensed temperature profiles. As a result, measurements of the pressure profile are available only at radiosonde locations and where satellite temperature profiles and a surface pressure measurement coincide.

Measurement Simulations for Surface Pressure

This experiment will accurately determine surface pressure over land and ocean regions of the globe for both day and night operation. In areas with low-lying clouds, the pressure and altitude of the clouds will be measured; this measurement can be used to derive surface pressure.

The surface pressure experiment is a variation of the two wavelength DIAL measurement described in Chapter 1, utilizing the backscattered energy from the Earth's surface or from low-lying clouds. The measurements can be made in either a crosstrack-scanning or nadir-viewing mode, depending upon availability of a scanning configuration.

A two wavelength solid-state alexandrite laser tunable over the 0.76 μm region is assumed. It has a spectral resolution ≤ 0.02 cm^{-1}, and a pulse length of <100 nsec, and an energy of 0.1 to 0.5 J per pulse is used for the measurement.

The atmospheric model used for the simulations is a one-dimensional model with up to 50 homogeneous vertical layers. The temperature and pressure data are taken from the mid-latitude January U.S. Standard Atmosphere model, and the aerosol composition data are taken from the Elterman model (Elterman, 1968). The simulations were performed using a high spectral resolution atmospheric transmission code. The transmission at a given frequency is calculated using the Voigt line profile and integrated vertically over the layers from space to altitude z. The simulations include detailed calculations of laser finite bandwidth. The effects of background radiation on the simulations have been considered. These include surface reflectance, aerosol scattering, and Rayleigh scattering.

The simulations used the following parameters for measurements from a 700 km EOS platform: a 0.5 J alexandrite laser transmitter with a repetition rate of up to 10 Hz, a three-mode spectral output with a bandwidth of 0.02 cm^{-1}, a telescope diameter of 1.25 m, a receiver field-of-view (FOV) of 0.15 or 0.5 mrad for daytime or nighttime experiments, respectively, and a surface reflectance of 0.1. An optical efficiency of 0.59 was used for nighttime simulations, which includes the transmission of a wide-band 2 nm spectral detection filter. An optical efficiency of 0.38 was used for daytime simulations, which includes the additional narrow-band (1.6 or 5 cm^{-1}) filters required. A quantum efficiency of 0.15 is assumed for the detector. The detailed parameters for nighttime and daytime experiments are given on the figures with the overall efficiency for each experiment. Figures 14-2 and 14-3 give the results of simulations for a crosstrack-scanning experiment to measure surface pressure using the pressure-sensitive trough absorption at 13150.86 cm^{-1}. The figures give the number of shots required to achieve 0.2% surface pressure accuracy versus scan angle for nighttime and daytime measurements with a 250 km grid. As shown, a repetition rate of 2.9 Hz is sufficient for nighttime measurements, and 4.5 Hz is sufficient for daytime measurements. For a nadir experiment, the required laser energy could be reduced by a factor of four and still achieve these accuracies. We note that for cloud-top pressure altitude measurements, an accuracy of $\leq 0.2\%$ could be obtained with ~0.2 the laser power factor.

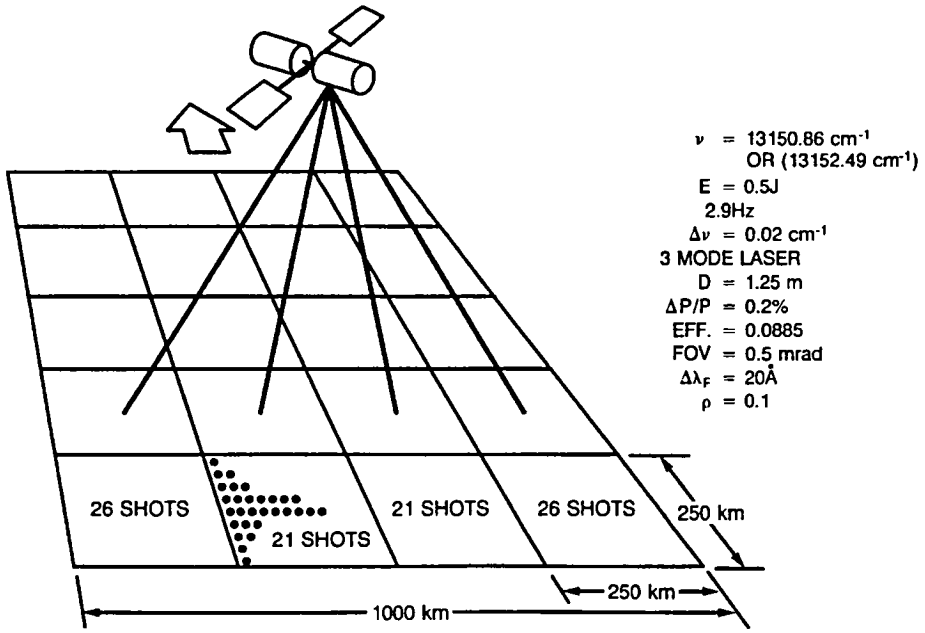

Figure 14-2. Surface pressure scanning lidar simulated for EOS nighttime experiment at 700 km.

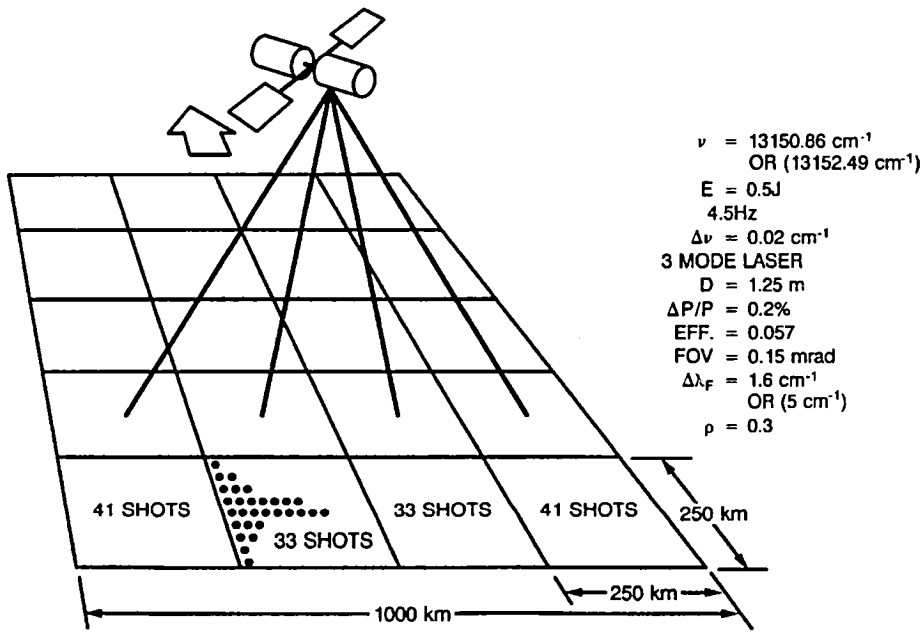

Figure 14-3. Surface pressure scanning lidar simulated for EOS daytime experiment at 700 km.

Measurement Simulations for the Pressure Profile

LASA can also accurately determine the pressure profile, *viz.*, the pressure and altitude structure of the atmosphere over land and ocean regions of the globe for both day and night operation. The instrument characteristics required are similar to those given for surface pressure, again using a two wavelength tunable solid-state laser. Higher energy, 0.5 J per pulse, is needed for the profiling measurement. The profiling measurements, however, do not require an energy monitor measurement.

The basic atmospheric model used for these simulations is similar to that used for surface pressure. The laser transmitter assumed for the simulations is an alexandrite laser with a three-mode spectral pattern with a bandwidth of 0.02 cm^{-1}. The simulations include detailed calculations of laser finite bandwidth. The effects of background radiation on the simulations have been considered. These include the effects of surface albedo, aerosol scattering, and Rayleigh scattering.

The pressure profile simulations used almost the same parameters as those for surface pressure. Differences were the use of a wide-band 1 nm spectral detection filter for nighttime and a narrowband 0.12 cm^{-1} filter for daytime simulations. Also, a quantum efficiency of 0.2 is assumed for the detector. The detailed parameters for nighttime and daytime experiments are given on the figures with the overall efficiency for each experiment.

Figures 14-4 and 14-5 show the results of simulations of pressure profiling for a nadir-viewing experiment. As shown, for 1 km vertical and 250 km horizontal resolution, good accuracy (<0.4%) can be obtained over a large portion of the troposphere using the pressure-sensitive absorption troughs located at either 13150.86 or 13153.79 cm^{-1}. We note that the use of a 0.15 mrad FOV and a 0.12 cm^{-1} spectral detection filter minimizes the effects of background radiation and allows high accuracy daytime measurements.

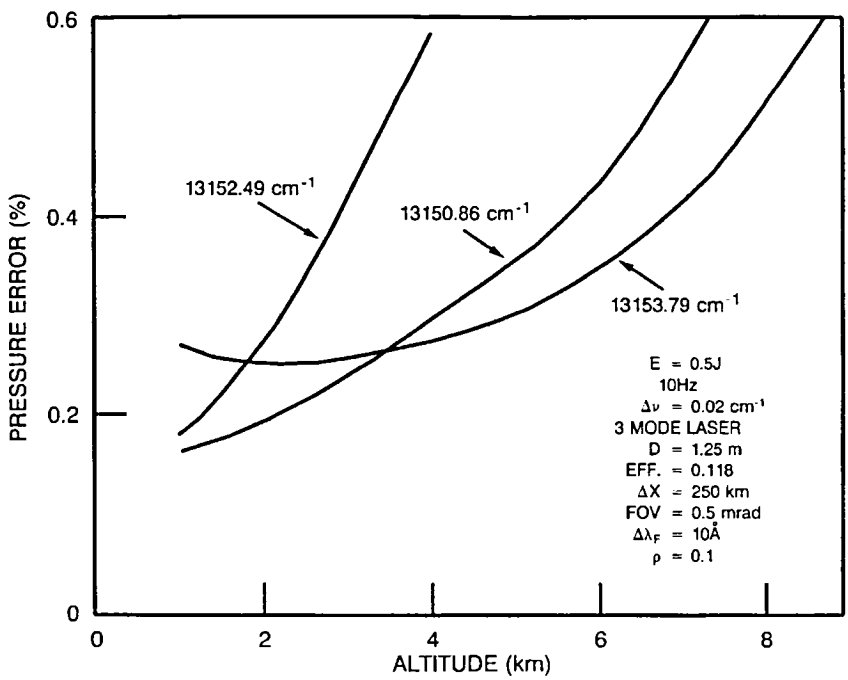

Figure 14-4. Pressure profiling accuracy for simulated EOS nighttime experiment at 700 km.

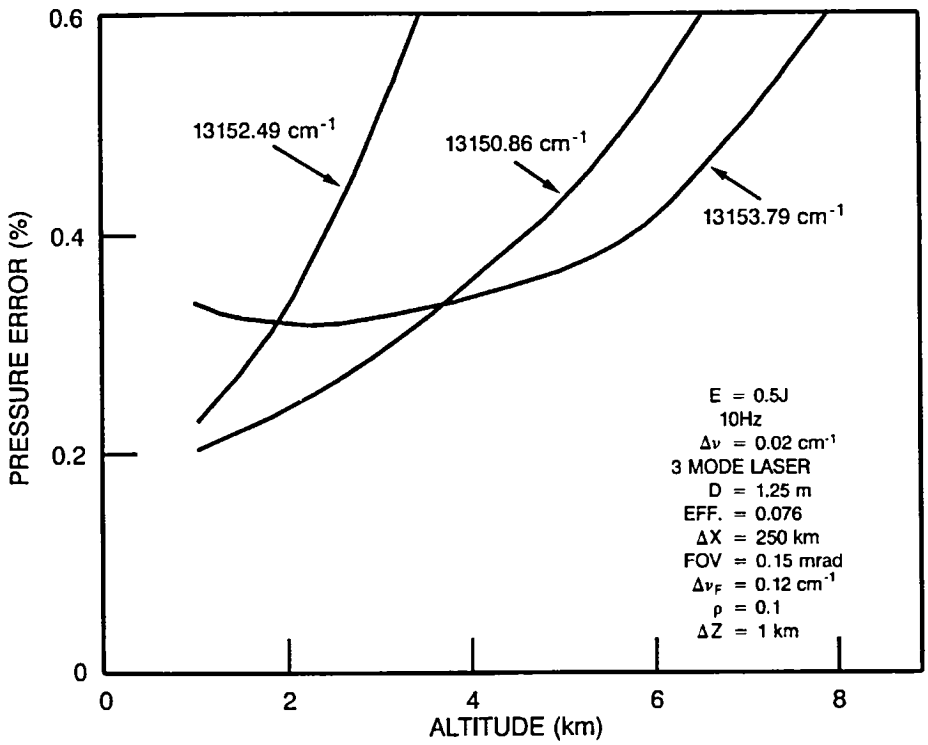

Figure 14-5. Pressure profiling accuracy for simulated EOS daytime experiment at 700 km.

Atmospheric Temperature Profile Observations

The temperature field is of fundamental importance in meteorology, climate, and for initializing global circulation models for all scales of weather forecasting. Temperature profiles are required for determining tropopause height, tropopause breaks, the depth and structure of the planetary boundary layer, and frontal and air mass characteristics, as well as numerous other meteorological phenomena. In the mid- and high latitudes, temperatures are of added importance, since, over oceanic areas in these latitudes, wind fields are derived from temperature fields using balance relationships.

General circulation models have now developed to the point where data at as many as seven independent tropospheric levels are required. The most advanced passive sounders currently under study cannot accurately provide vertical resolution at this scale.

Lidar differential absorption measurements can provide direct measurements of the temperature profile with extremely high vertical resolution. The use of the lidar technique will allow the temperature to be measured in a direct manner, rather than requiring the use of inversion techniques, as must currently be done in order to use data from passive profilers. The simulations as described below indicate that a lidar temperature profile experiment could achieve 1 K temperature accuracy while simultaneously obtaining 1.25 to 2.5 km vertical resolution.

LASA can accurately determine the atmospheric temperature profile over land and ocean regions of the globe for both day and night operation. The temperature profile measurement uses the two wavelength DIAL technique described in Chapter 2.

The instrument characteristics for temperature profiling are the same as those given for pressure profiling. The return signals are measured with a nominal 100 m range cell. The atmospheric model and the laser transmitter used for these simulations are the same as those used for the surface pressure and pressure profile experiment.

The simulations use the same parameters as those used for pressure profiling: a 0.5 J alexandrite laser transmitter with a repetition rate of 10 Hz, a three-mode spectral output with a bandwidth of 0.02 cm^{-1}, a telescope diameter of 1.25 m, and a receiver FOV of 0.15 or 0.5 mrad for daytime or nighttime experiments, respectively. An optical efficiency of 0.59 was used for nighttime simulations, which includes a wide-band 1 nm spectral detection filter. An optical efficiency of 0.38 was used for daytime simulations, which includes a narrow-band 0.12 cm^{-1} filter. A quantum efficiency of 0.2 is assumed for the detector. The detailed parameters for nighttime and daytime experiments are given on the figures with the overall efficiency for each experiment.

Figures 14-6 to 14-8 show the results of simulations of temperature profiling for a nadir-viewing experiment. As shown for the line at 12999.95 cm^{-1}, 2.5 km vertical resolution allows high accuracy measurements with <1 K error for altitudes ≤10 km. In addition, the use of the stronger absorption line at 13010.81 cm^{-1} with 3 km resolution allows high accuracy measurements to be extended to 15 km altitude. The horizontal resolution is 175 km for nighttime and 250 km for daytime measurements. The effects of background on the measurement are small for the 12999.95 cm^{-1} line, but become significant for the 13010.81 cm^{-1} line.

Figures 14-9 to 14-11 show the results of temperature profiling accuracy simulations for a 1.25 km vertical resolution nadir-viewing experiment. As shown, high temperature accuracy and high vertical resolution can be obtained in the lower portion of the troposphere.

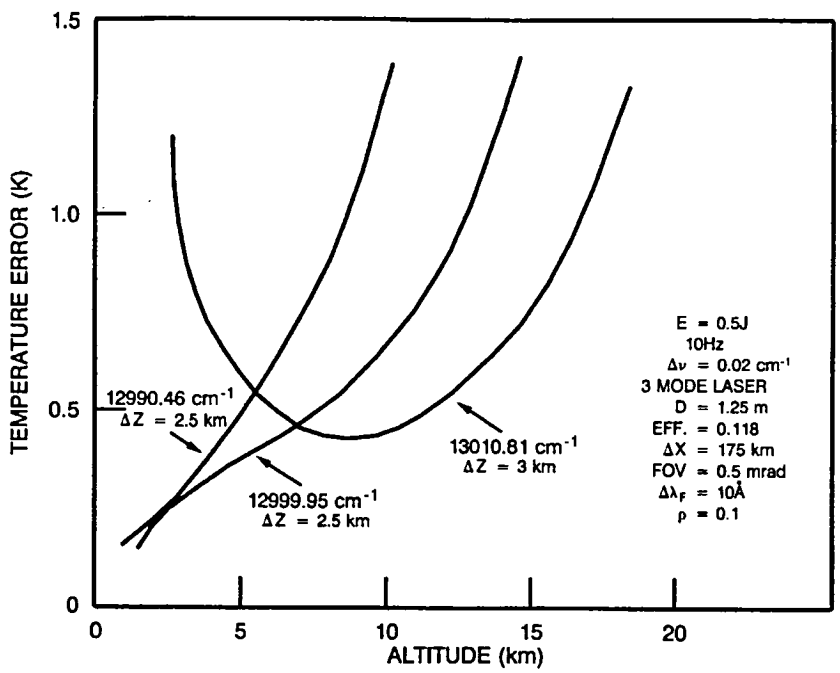

Figure 14-6. Temperature accuracy for simulated EOS nighttime experiment at 700 km. Calculations performed for Δx = 175 km. Other parameters as in Figure 14-4.

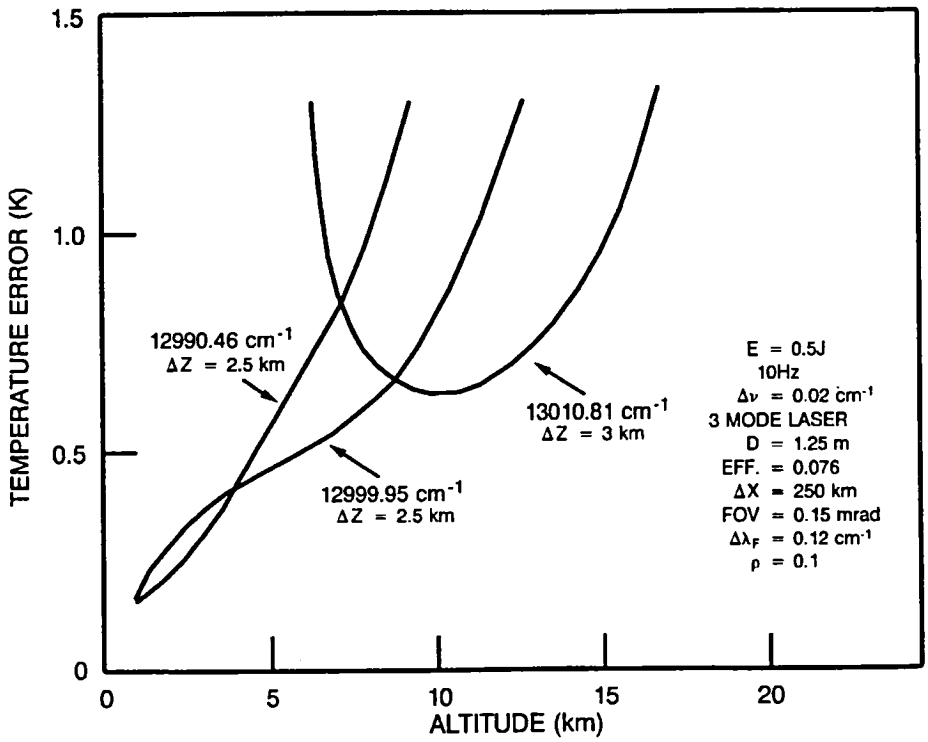

Figure 14-7. Temperature accuracy for simulated EOS daytime experiment at 700 km. Parameters as in Figure 14-5.

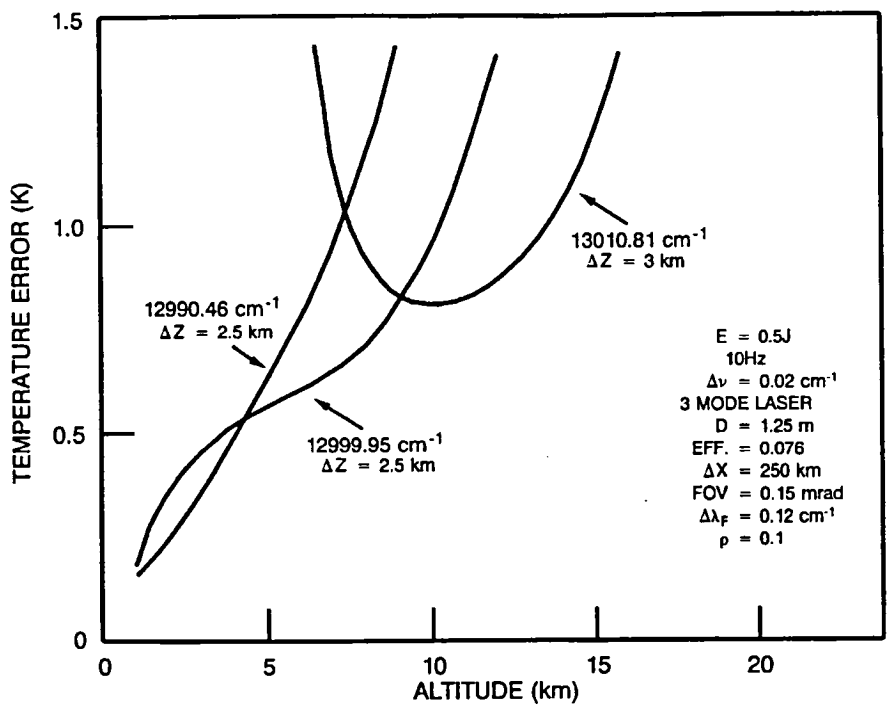

Figure 14-8. Temperature accuracy for simulated EOS daytime experiment at 700 km. Calculations performed for $\rho = 0.3$. Other parameters as in Figure 14-5.

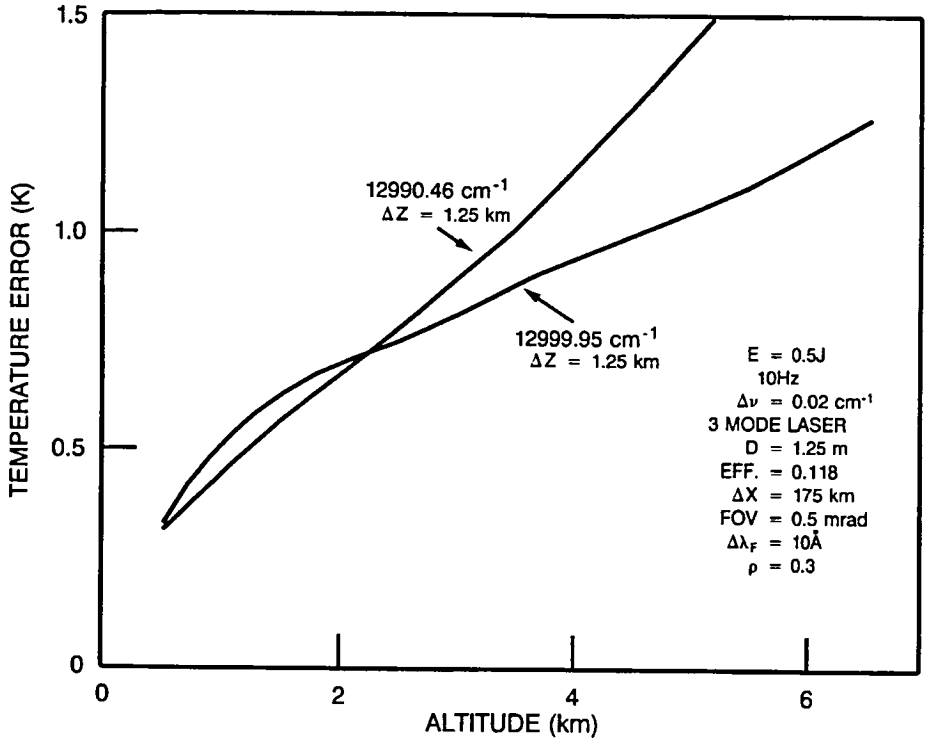

Figure 14-9. Temperature accuracy for simulated EOS nighttime experiment at 700 km. Calculations performed for $\rho = 0.3$. Other parameters as in Figure 14-6.

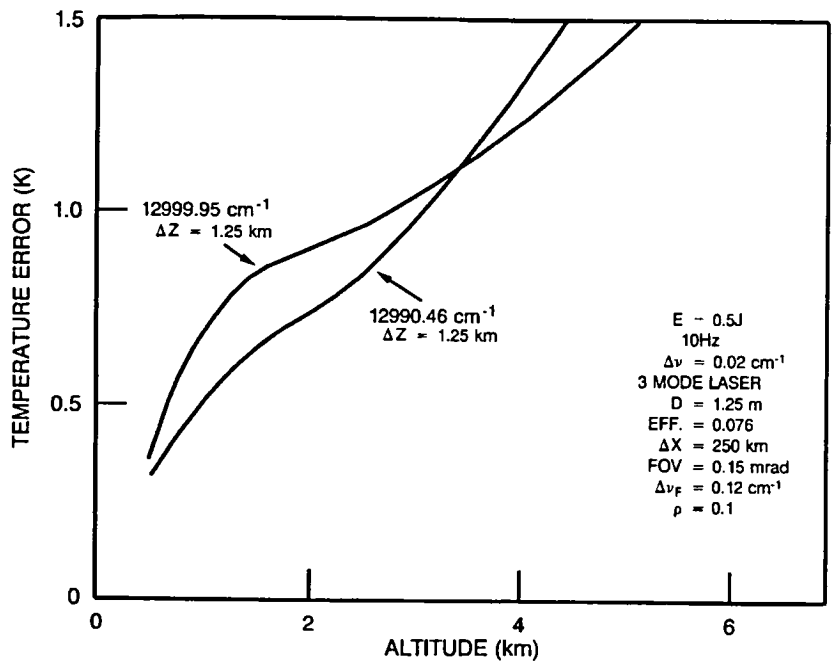

Figure 14-10. Temperature accuracy for simulated EOS daytime experiment at 700 km. Parameters as in Figure 14-5.

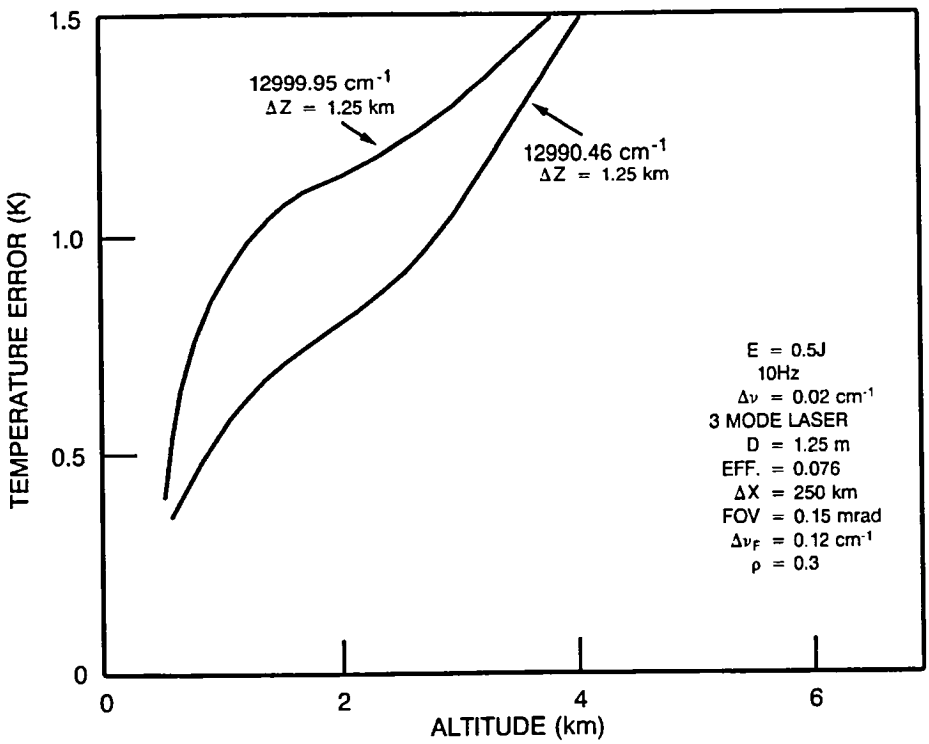

Figure 14-11. Temperature accuracy for simulated EOS daytime experiment at 700 km. Calculations performed for $\rho = 0.3$. Other parameters as in Figure 14-5.

ACKNOWLEDGEMENTS

This work was supported by the NASA Office of Space Science and Applications (and previous incarnations) under the direction of Dr. Ramesh Kakar, Dr. John Theon, and Dr. Robert Curran. Significant scientific and/or technical contributions to the work were made by Dr. Chi Weng, Mark Dombrowski, Dr. David O'C. Starr, Dr. H. Sang Lee, Leonid Roytblat, James C. Smith, Jeffry Milrod, Dr. Robert H. Kagann, Dr. S. Harvey Melfi, Bert Johnson, Dr. John Degnan, Dr. Gerard Megie, Dr. Pierre Flamant, Dr. Jacques Pelon, Mireille Bourdet, Dr. Louis Uccellini, Dr. James E. Kalshoven, Dr. Tom Wilkerson, Leo Cotnoir, and Dr. David Atlas. In addition, engineering contributions were made by Ray DiSilvestre, Jr., Ken Kirks, Pete Leone, Dave Carter, Tom Ashton, Fred Huegel, Bob Farmer, Gunner Sundstrom, Max Strange, and John Semyan.

BIBLIOGRAPHY

PATENTS

Korb, C. L., and J. E. Kalshoven, 1985, "Method and Apparatus for Measuring Temperature and Pressure," U.S. Patent No. 4,494,533.

Schwemmer, G. K., 1993, "Doppler Shift Compensation System for Laser Transmitters and Receivers," U.S. Patent No. 5,184,241.

JOURNAL AND BOOK ARTICLES

Atlas, D., and C. L. Korb, 1981, "Weather and Climate Needs for Lidar Observations from Space and Concepts for Their Utilization," *Bull. Am. Meteor. Soc.*, **62**, p. 1270.

Kalshoven, J. E., C. L. Korb, G. K. Schwemmer, and M. Dombrowski, 1981, "Laser Remote Sensing of Atmospheric Temperature by Observing Resonant Absorption of Oxygen," *Appl. Opt.*, **20**, p. 1967.

Korb, C. L., and C. Y. Weng, 1982, "A Theoretical Study of a Two Wavelength Lidar Technique for the Measurement of Atmospheric Temperature Profiles," *J. Appl. Meteor.*, **21**, p. 1346.

Korb, C. L., and C. Y. Weng, 1983, "Differential Absorption Lidar Technique for Measurement of the Atmospheric Pressure Profile," *Appl. Opt.*, **22**, p. 3759.

Korb, C. L., and C. Y. Weng, 1983, "Reply to the Comments on the Paper, A Theoretical Study of a Two Wavelength Lidar Technique for the Measurement of Atmospheric Temperature Profiles," *J. Climate and Appl. Meteor.*, **22**, p. 1137.

Korb, C. L., G. K. Schwemmer, M. Dombrowski, and C. Y. Weng, 1983, "Atmospheric Pressure and Temperature Profile Measurements Using Near IR Lidar Systems," Chapter 3.1, *Optical and Laser Remote Sensing*, Springer-Verlag.

Korb, C. L., G. K. Schwemmer, M. Dombrowski, and C. Y. Weng, 1989, "Airborne and Ground-Based Lidar Measurements of the Atmospheric Pressure Profile," *Appl. Opt.*, **28**, pp. 3015-3020.

Korb, C. L., G. K. Schwemmer, M. Dombrowski, and R. H. Kagann, 1986, "Remote Sensing with a Tunable Alexandrite Laser Transmitter," in *Tunable Solid State Lasers for Remote Sensing*, R. L. Byer, E. K. Gustafson, and R. Trebino, eds., Springer-Verlag, p. 35.

Lee, H. S., G. K. Schwemmer, C. L. Korb, M. Dombrowski, and C. Prasad, 1990, "Gated Photomultiplier Response Characterizations for DIAL Measurements," *Appl. Opt.*, **29**, pp. 3303-3315.

Ritter, K. J., and T. D. Wilkerson, 1987, "High-Resolution Spectroscopy of the Oxygen A Band," *J. Molec. Spec.*, **121**, pp. 1-19.

Schwemmer, G. K., M. Dombrowski, C. L. Korb, J. Milrod, H. Walden, and R. H. Kagann, 1987, "A Lidar System for Measuring Atmospheric Pressure and Temperature Profiles," *Rev. Sci. Instru.*, **58**, p. 2226.

Starr, D. O'C., C. L. Korb, G. K. Schwemmer, 1992, "Observations of Height-Dependent Pressure Perturbation Structure of a Strong Mesoscale Gravity Wave," *Mon. Wea. Rev.*, **120**, pp. 2808-2820.

REPORTS AND CONFERENCE PROCEEDINGS

Atlas, D., and C. L. Korb, 1980, "Weather and Climate Needs for Lidar Observations from Space and Concepts for Their Realization," NASA TM 82006, 48 pp.

Cotnoir, L. J., 1984, "Laser Wavemeter/Spectometer," *Proc. 12th International Laser Radar Conference*, pp. 323-325, Aix-en-Provence, France, August 13-17.

Cotnoir, L. J., T. D. Wilkerson, M. Dombrowski, R. H. Kagann, C. L. Korb, G. K. Schwemmer, and H. Walden, 1985, "Wavemeter for Use with a Line-Narrowed Alexandrite Laser in Differential Absorption Lidar," Technical Digest, *Topical Meeting on Tunable Solid-State Lasers*, pp. FC5-1-4, Arlington, Virginia, May 16-17.

Curran, R. J., 1987, *Earth Observing System Instrument Panel Report*, "LASA - Lidar Atmospheric Sounder and Altimeter," Vol. IId, R. J. Curran, Chairman, LASA Instrument Panel, NASA, pp. 28-33.

Dombrowski, M., G. K. Schwemmer, and C. L. Korb, 1990, "A Lidar System for Measuring Atmospheric Pressure and Temperature," *Proc. of the SPIE*, pp. 388-391.

Dombrowski, M., H. Walden, G. K. Schwemmer, and C. L. Korb, 1986, "Real Time Atmospheric Absorption Spectra for In-Flight Tuning of an Airborne DIAL System," *Proc. of 13th International Laser Radar Conference*, Toronto, Canada, August 11-15, p. 46.

Johnson, B. L., Jr., C. L. Korb, P. Flamant, M. Bourdet, J. Degnan, G. Megie, S. H. Melfi, G. Schwemmer, and L. Uccellini, 1987, "Overview of an Advanced Lidar for an Atmospheric Temperature Profile Measurements Program," *Topical Meeting on Laser and Optical Remote Sensing: Instrumentation and Techniques, Technical Digest Series*, Vol. **18**, Optical Society of America, pp. 313-315, Washington, DC.

Kalshoven, J. E., and C. L. Korb, 1978, "Engineering a Laser Remote Sensor for Atmospheric Pressure and Temperature," NASA TM 79538.

Kalshoven, J. E., and C. L. Korb, 1982, "Atmospheric Pressure Determination from Laser Absorption Measurements," Annual Meeting, *Proc. of Optical Society of America*, Tucson, Arizona, October.

Kalshoven, J. E., C. L. Korb, G. K. Schwemmer, and M. Dombrowski, 1980, "CW Laser Measurements of Atmospheric Temperature," *Proc. of 10th International Laser Radar Conference*, Silver Spring, Maryland, October 6-9, p. 68.

Korb, C. L., 1977, "Laser Measurement of Atmospheric Pressure Profiles," *Proc. of the 32nd Symposium on Molecular Spectroscopy*, Ohio State University, Columbus, Ohio.

Korb, C. L., 1977, "A Laser Technique for the Remote Measurement of Pressure in the Troposphere," *Proc. of 8th International Laser Radar Conference*, Drexel University, Philadelphia, Pennsylvania.

Korb, C. L., 1979, "Surface Pressure and Cloud Top Pressure and Height Measurement," in *Shuttle Atmospheric Lidar Research Program*, NASA SP-433, p. 131.

Korb, C. L., 1979, "Temperature Profiles," in *Shuttle Atmospheric Lidar Research Program*, NASA SP-433, p. 137.

Korb, C. L., 1979, "Vertical Profiles of Atmospheric Pressure," in *Shuttle Atmospheric Lidar Research Program*, NASA SP-433, p. 134.

Korb, C. L., 1981, "Differential Absorption Lidar Measurements of Atmospheric Temperature and Pressure Profiles," invited paper, *Proc. of International Geoscience and Remote Sensing Symposium*, **I**, p. 23, Washington, D.C., June 8-10.

Korb, C. L., 1981, "Lidar Techniques for Differential Absorption Measurements of Atmospheric Temperature and Pressure Profiles," invited paper, *Proc. of Tri-Service Lidar Workshop*, Tucson, Arizona, February 3-5.

Korb, C. L., 1983, "Determination of Atmospheric Properties from Lidar Measurements," invited paper, *Proc. of International Soc. Opt. Eng.*, **410**, pp. 26-31, Washington, D.C., April 4-8.

Korb, C. L., and C. Y. Weng, 1979, "A Theoretical Approach to the Lidar Measurement of Differential Absorption for Non-Homogeneous Media," *Proc. of 9th International Laser Radar Conference*, Munich, Federal Republic. of Germany.

Korb, C. L., and C. Y. Weng, 1979, "A Two-Wavelength Lidar Technique for the Measurement of Atmospheric Temperature Profiles," *Proc. of 9th International Laser Radar Conference*, Munich, Federal Republic of Germany.

Korb, C. L., and C. Y. Weng, 1980, "The Formulation and Solution of Differential Absorption Lidar Equations for Non-Homogeneous Atmospheres," *Proc. of 10th International Laser Radar Conference*, p. 115, Silver Spring, Maryland, October 6-9.

Korb, C. L., and C. Y. Weng, 1982, "A Two Wavelength Lidar Technique for the Measurement of Atmospheric Density Profiles," *Proc. of Conference on Lasers and Electro-Optics*, Phoenix, Arizona, April 14-16.

Korb, C. L., and C. Y. Weng, 1982, "The Theory and Correction of Laser Finite Bandwidth Effects in DIAL Experiments," *Proc. of 11th International Laser Radar Conference*, pp. 78-81, University of Wisconsin, Madison, Wisconsin, June 21-25.

Korb, C. L., and C. Y. Weng, 1983, "Differential Absorption Lidar Measurement of the Pressure Profile with a Trough Technique," *Proc. of Topical Meeting on Optical Techniques for Remote Probing of the Atmosphere*, pp. TUC8-1-4, Incline Village, Nevada, January 10-12.

Korb, C. L., and C. Y. Weng, 1984, "An Effective Frequency Technique for Representing Finite Bandwidth Effects in DIAL Experiments," *Proc.12th International Laser Radar Conference*, pp. 177-180, Aix-en-Provence, France, August 13-17.

Korb, C. L., and C. Y. Weng, 1985, "An Effective Frequency Technique for Laser Measurements with Finite Spectral Bandwidth," *Topical Meeting on Optical Remote Sensing of the Atmosphere*, pp. TUC28-1-4, Incline Village, Nevada, January 15-18.

Korb, C. L., and C. Y. Weng, 1987, "Simulation of Lidar Pressure and Temperature Profile Measurements from the Earth Observing System (EOS) Satellite," *Topical Meeting on Laser and Optical Remote Sensing: Instrumentation and Techniques, Technical Digest Series*, **18**, Optical Society of America, pp. 55-58,Washington, DC.

Korb, C. L., and C. Y. Weng, 1988, "Simulation of Cross-Track Scanning Lidar Pressure and Temperature Profile Measurements from the Earth Observing System (EOS) Satellite," *Proc. of 14th International Laser Radar Conf.*, Innichen-San Candido, Italy, pp. 176-178.

Korb, C. L., E. J. Hurley, and C. Y. Weng, 1980, "The Theory and Technique of Differential Correlation Radiometry of Atmospheric Trace Species," invited paper, *Trans. of the Amer. Geophys. Union,* **61**, p. 965.

Korb, C. L., G. K. Schwemmer, C. Prasad, C. Y. Weng, J. Famiglietti, and C. N. Flamant, 1993, "Temperature Profile Measurements Using Oxygen DIAL," *Technical Digest on Optical Remote Sensing of the Atmosphere*, **5**, Salt Lake City, Utah, March 3, pp. 157-160.

Korb, C. L., G. K. Schwemmer, and B. M. Gentry, 1993, "Lidar Remote Sensing of Pressure, Temperature, and Wind," invited paper, *Annual Meeting of the Optical Society of America and the 9th Interdisciplinary Laser Science Conference*, Toronto, Canada, Oct. 3-8, paper FN1.

Korb, C. L., G. K. Schwemmer, D. O'C. Starr, C. R. Prasad, H. Walden, H. S. Lee, and C. Y. Weng, 1991, "Airborne Lidar Observations of the Atmospheric Pressure Field," *Proc. 5th International Conference on Multiple Scattering*, (MUSCLE 5), Philadelphia, Pennsylvania, Nov. 13-15.

Korb, C. L., G. K. Schwemmer, D. O'C. Starr, C. R. Prasad, H. Walden, H. S. Lee, and C. Y. Weng, 1991, "Structure in the Atmospheric Pressure Field Observed with an Airborne Lidar," *Proc. Atmospheric Volume and Surface Scattering and Propagation*, Florence, Italy, Aug. 27-30.

Korb, C. L., G. K. Schwemmer, D. O'C. Starr, M. Dombrowski, C. R. Prasad, H. Walden, H. S. Lee, C. Y. Weng, and L. Roytblat, 1990, "Airborne Lidar Observations of Gravity Waves from Measurements of the Two-Dimensional Pressure Profile," invited paper, *Proc. 15th International Laser Radar Conference*, pp. 30-33, Tomsk, USSR, July 23-27.

Korb, C. L., G. K. Schwemmer, J. Famiglietti, D. O'C. Starr, C. R. Prasad, C. Y. Weng, 1992, "Lidar Remote Sensing of Atmospheric Temperature and Pressure Fields," Proposal submitted to the NASA Office of Space Sciences and Applications by the Laboratory for Atmospheres, Goddard Space Flight Center, 41 pp., July 16.

Korb, C. L., G. K. Schwemmer, M. Dombrowski, and C. Y. Weng, 1983, "Atmospheric Pressure and Temperature Profile Measurements Using Near IR Lidar Systems," invited paper, *Proc. of Workshop on Optical and Laser Remote Sensing*, pp. E1-1-9, Monterey, California, February 9-11.

Korb, C. L., G. K. Schwemmer, M. Dombrowski, and C. Y. Weng, 1987, "Alexandrite Lidar Measurement of the Atmospheric Pressure Profile," invited paper, International Conference on Lasers '87, *Technical Digest*, Incline Village, Nevada, invited paper HF.3, December 7-11.

Korb, C. L., G. K. Schwemmer, M. Dombrowski, and R. H. Kagann, 1984, "Remote Sensing with a Tunable Alexandrite Laser Transmitter," invited paper, *NASA Workshop on Tunable Solid State Lasers for Remote Sensing*, Stanford University, Stanford, California.

Korb, C. L., G. K. Schwemmer, M. Dombrowski, C. R. Prasad, H. Walden, H. S. Lee, C. Y. Weng, and L. Roytblat, 1990, "Airborne Lidar Measurements of the Two-Dimensional Atmospheric Pressure Profile," Optical Remote Sensing of the Atmosphere, *Technical Digest*, **4**, pp. 347-350, Incline Village, Nevada, Feb. 12-15.

Korb, C. L., G. K. Schwemmer, M. Dombrowski, J. Milrod, and C. Y. Weng, 1985, "Atmospheric Pressure and Temperature Measurements with Tunable Alexandrite Lasers," invited paper, *International Conference on Lasers '85*, Las Vegas, Nevada, December 2-6.

Korb, C. L., G. K. Schwemmer, M. Dombrowski, J. Milrod, and H. Walden, 1985, "Lidar Measurements of Atmospheric Pressure and Temperature Profiles with Tunable Alexandrite Lasers," invited paper, *First International DIAL Data Collection and Analysis Workshop*, pp. 46-49, Virginia Beach, Virginia, November 18-21.

Korb, C. L., G. K. Schwemmer, M. Dombrowski, J. Milrod, and H. Walden, 1986, "Airborne Lidar Measurements of the Atmospheric Pressure Profile with Tunable Alexandrite Lasers," *Proc. of 13th International Laser Radar Conference*, Toronto, Canada, August 11-15, p. 52.

Korb, C. L., G. K. Schwemmer, M. Dombrowski, J. Milrod, H. Walden, and C. Y. Weng, 1986, "Ground-Based Lidar Measurements of Atmospheric Pressure and Temperature Profile," invited paper, *Alfred-Wegener-Konferenz on Ground-Based Remote Sensing Techniques for the Troposphere*, Hamburg, Germany, August 25-28, pp. 51-60.

Korb, C. L., J. E. Kalshoven, and C. Y. Weng, 1979, "A Lidar Technique for the Measurement of Atmospheric Pressure Profiles," *Trans. of the Amer. Geophys. Union.*, **60**, Washington, D.C., p. 333.

Korb, C. L., J. E. Kalshoven, G. K. Schwemmer, and M. Dombrowski, 1980, "Atmospheric Temperature Determination from High Resolution Laser Absorption Measurements," *Proc. of Topical Meeting on Spectroscopy in Support of Atmospheric Measurements*, Sarasota, Florida, November 10-12, p. TuP20.

Korb, C. L., P. Flamant, M. Bourdet, J. Degnan, G. Megie, G. Schwemmer, and L. Uccellini, 1985, "Advanced ER-2 Lidar for Mesoscale Meteorological Studies, LASE II," Joint Proposal Submitted to the NASA Office of Space Science and Applications and the Centre National D'Etudes Spatiale by the NASA/Goddard Space Flight Center and Centre National de la Recherche Scientifique, 84 pp.

Korb, C. L., P. Flamant, M. Bourdet, J. Degnan, G. Megie, G. Schwemmer, and L. Uccellini, 1986, "Advanced ER-2 Lidar for Mesoscale Meteorological Studies, LASE II: Proposal Update," Joint Proposal Submitted to the NASA Office of Space Science and Applications and the Centre National D'Etudes Spatiale by the NASA/Goddard Space Flight Center and Centre National de la Recherche Scientifique, 47 pp.

Lee, H. S., G. K. Schwemmer, and C. L. Korb, 1987, "Detector Response Characterization for DIAL Application," *Topical Meeting on Laser and Optical Remote Sensing: Instrumentation and Techniques, Technical Digest Series*, **18**, Optical Society of America, Washington, D.C., pp. 290-292.

Lee, H. S., G. K. Schwemmer, and C. L. Korb, 1988, "Detector Characterization for DIAL Measurements," *Proc. of 14th International Laser Radar Conference*, Innichen-San Candido, Italy, pp. 216-219.

Melfi, S. H., 1988, "Spaceborne Rawinsonde (SPAR)," Joint proposal from Goddard Space Flight Center and Centre National de la Recherche Scientifique in response to the Earth Observing System (EOS) Announcement of Opportunity No. OSSA-1-88, 40 pp.

Prasad, C. R., C. L. Korb, and G. K. Schwemmer, 1987, "Speckle Effects on Laser Wavelength Measurements with a Fizeau Wavemeter," *Topical Meeting on Laser and Optical Remote Sensing: Instrumentation and Techniques, Technical Digest Series*, **18**, Optical Society of America, Washington, D.C., pp. 293-296.

Prasad, C. R., C. L. Korb, and G. K. Schwemmer, 1988, "Laser Wavelength Measurement in Presence of Speckle," *Proc. of 14th International Laser Radar Conference*, Innichen-San Candido, Italy, pp. 253-256.

Prasad, C. R., C. L. Korb, and G. K. Schwemmer, 1990, "Active Frequency Stabilization of an Alexandrite Laser with a Wavemeter for Pressure and Lidar Measurements," *Proc. 15th International Laser Radar Conference*, July 23-27, Tomsk, USSR.

Prasad, C. R., C. L. Korb, and G. K. Schwemmer, 1990, "Frequency Stabilization of an Alexandrite Laser for Pressure-Temperature Lidar Measurements," Optical Remote Sensing of the Atmosphere, *Technical Digest*, **4**, pp. 344-346, Incline Village, Nevada, Feb. 12-15.

Prasad, C. R., G. K. Schwemmer, and C. L. Korb, 1992, "Wavemeter Measurement of Frequency Stability of an Injection Seeded Alexandrite Laser for Pressure and Temperature Lidar," *Proc. 16th International Laser Radar Conference*, NASA Conf. Pub. 3158, Part 2, pp. 517-520.

Ritter, K. J., 1986, "A High Resolution Spectroscopic Study of Absorption Line Profiles in the *A* Band of Molecular Oxygen," Ph.D Dissertation, University of Maryland, 210 pp.

Schwemmer, G. K., 1988, "Frequency Stabilized Diode Laser System for Active Control of DIAL Lasers, Wavemeters, and Receiver Filters," *Proc of 14th International Laser Radar Conference*, Innichen-San Candido, Italy, June 20-24, pp. 274-277.

Schwemmer, G. K., and M. Dombrowski, 1984, "A Lidar System for Measuring Atmospheric Pressure and Temperature: Ground Based System Design and Operation," X-913-83-18, NASA Goddard Space Flight Center.

Schwemmer, G. K., C. L. Korb, C. R. Prasad, H. Walden, H. S. Lee, and C. Y. Weng, 1991, "Lidar Measures Atmospheric Pressure Fields with High Resolution," invited paper, *29th Aerospace Sciences Meeting*, American Institute of Aeronautics and Astronautics, January 7-10, Reno, Nevada.

Schwemmer, G. K., C. L. Korb, M. Dombrowski, and C. Y. Weng, 1986, "Measurements of the Effect of Horizontal Variability of Atmospheric Backscatter on DIAL Measurements," *Proc. of 13th International Laser Radar Conference*, Toronto, Canada, August 11-15, p. 55.

Schwemmer, G. K., C. L. Korb, M. Dombrowski, and R. H. Kagann, 1985, "Atmospheric Pressure Profiles Measured Using an Alexandrite Laser Differential Absorption Lidar," *Topical Meeting on Optical Remote Sensing of the Atmosphere*, pp. TUC29-1-4, Incline Village, Nevada, January 15-18.

Schwemmer, G. K., C. L. Korb, M. Dombrowski, and R. Kagann, 1984, "Atmospheric Pressure Profile Measured with a Differential Absorption Lidar," *Proc. 12th International Laser Radar Conference*, Aix-en-Provence, France, August 13-17, pp. 157-159.

Schwemmer, G. K., H. S. Lee, C. Prasad, 1991, "Narrowband Alexandrite Laser Injection Seeded with Frequency Dithered Diode Laser," *Proc. of SPIE*, **1492**, Earth and Atmosphere Remote Sensing, Orlando, Florida, April 2-4, pp. 52-62.

Schwemmer, G., M. Dombrowski, and C. L. Korb, 1982, "Advanced Near IR Lidar for Meteorological Remote Sensing," *Proc. of 11th International Laser Radar Conference*, pp. 26-29, University of Wisconsin, Madison, Wisconsin, June 21-25.

Smith, J. C., and G. K. Schwemmer, 1988, "Tuning and Scanning Control System for High Resolution Alexandrite Lasers," *Proc. of SPIE*, **924**, Recent Advances in Sensors, Radiometry, and Data Processing for Remote Sensing, Orlando, Florida, April 1-8, pp. 57-64.

REFERENCES

Akopdzhanov, G. A., A. V. Inyakin, and P. S. Shuvalov, 1979, "Photomultiplier Short-term Instability," *Nucl. Instrum. and Meth.*, **161**, pp. 247-257.

Anthes, R. A., Y. H. Kuo, and J. R. Gyakum, 1983, "Numerical Simulations of a Case of Explosive Marine Cyclogenesis," *Mon. Wea. Rev.*, **111**, pp. 1174-1188.

Armstrong, B. H., 1967, "Spectrum Line Profiles: The Voigt Function," *J. Quant. Spectrosc. Radiat. Transfer*, **7**, pp. 61-88.

Arshinov, Y. F., S. M. Bobrovnikov, V. E. Zuev, and V. M. Mitev, 1983, "Atmospheric Temperature Measurements Using a Pure Rotational Raman Lidar," *Appl. Opt.*, **22**, pp. 2984-2990.

Atlas, D., and C. L. Korb, 1981 "Weather and Climate Needs for Lidar Observations from Space and Concepts for their Realization", *Bull. Amer. Meteor. Soc.*, **62**, pp. 1270-1285.

Baker, W. E., 1991, "Wind Measurements Expected with the Laser Atmospheric Wind Sounder," *7th Symp. on Meteorological Observations and Instrumentation*, New Orleans, Louisiana, American Meteorological Society, pp. 169-174.

Barrick, J. D. W., 1986, "Gating Characteristics of Photomultiplier Tubes for Lidar Application," NASA TM 87699.

Baumeister P. W., and F. A. Jenkins, 1957, "Dispersion of the Phase Change for Dielectric Multilayers, Application to the Interference Filter," *JOSA*, **47**, pp. 57-61.

Bjerknes, J., 1919, "On the Structure of Moving Cyclones," Reprinted in *Selected Papers of J. A. B. Bjerknes*, Western Periodicals Co., North Hollywood, California, 1975, pp. 21-28.

Bjerknes, J., and H. Solberg, 1923, "Life Cycle of Cyclones and the Polar Front Theory of Atmospheric Circulation," Reprinted in *Selected Papers of J. A. B Bjerknes*, Western Periodicals Co., North Hollywood, California, 1975, pp. 30-45.

Bjerknes, J., and J. Holmboe, 1944, "On the Theory of Cyclones," *J. Meteor.*, **1**, pp. 1-22.

Bjerknes, J., 1951, "Extratropical Cyclones," *Compendium of Meteorology*, American Meteorological Society, pp. 577-598.

Bosart, L. F., and A. Seimon, 1988, "A Case Study of an Unusually Intense Atmospheric Gravity Wave," *Mon. Wea. Rev.*, **116**, pp. 1857-1886.

Brill, K. F., L. W. Uccellini, R. P. Burkhart, T. T. Warner, and R. A. Anthes, 1985, "Numerical Simulations of a Transverse Indirect Circulation and Low-Level Jet in the Exit Region of an Upper-Level Jet," *J. Atmos. Sci.*, **42**, pp. 1306-1320.

Browell, E. V., T. D. Wilkerson, and T. J. McIlrath, 1979, "Water Vapor Differential Absorption Lidar Development and Evaluation," *Appl. Optics*, **18**, pp. 3474-3483.

Browell, E. V., A. F. Carter, and T. D. Wilkerson, 1981, "Airborne Differential Absorption Lidar System for Water Vapor Investigations," *Optical Eng.*, **20**, pp. 84-90.

Browell, E. V., N. S. Higdon, C. F. Butler, M. A. Fenn, B. E. Grossmann, P. Ponsardin, W. B. Grant, and A. S. Bachmeier, 1991, "Tropospheric Water Vapor Measurements with an Airborne Lidar System," *7th Symp. on Meteorological Observations and Instrumentation*, New Orleans, Louisiana, American Meteorological Society, pp. 250-251.

Brown, E. H., and F. F. Hall, 1978, "Advances in Atmospheric Acoustics," *Rev. Geophys. Space Phys.*, **16**, p. 47-110.

Buck, R. C., and E. F. Buck, 1965, *Advanced Calculus*, McGraw-Hill, New York, p. 106.

Burch, D. E., and D. A. Gryvnak, 1969, "Strengths, Widths and Shapes of the Oxygen Lines Near 13100 cm^{-1}," *Appl. Opt.*, **8**, pp. 1493-1497.

Burlbaw, E. J., and R. L. Armstrong, 1983, "Rotational Raman Interferometric Measurements of Flame Temperatures," *Appl. Opt.*, **22**, pp. 2860-2866.

Butler, D. M., *et al.*, 1984, "Earth Observing System: Science and Mission Requirements Working Group Report," NASA TM 86129.

Cahen C., and G. Megie, 1981, "A Spectral Limitation of the Range Resolved Differential Absorption Lidar Technique," *J. Quant. Spect. Rad. Trans.*, **25**, pp. 151-157.

Canavero, F. G., F. Einaudi, E. R. Westwater, M. J. Falls, J. A. Schroeder, and A. J. Bedard, 1990, "Interpretation of Ground-Based Radiometric Observations in Terms of a Gravity Wave Model," *J. Geophys. Res.*, **95**, pp. 7637-7652.

Candy, B. H., 1985, "Photomultiplier Characteristics and Practice Relevant to Photon Counting," *Rev. Sci. Instrum.*, **56**, pp. 183-193.

Carrabba, M. M., K. M. Spencer, C. Rich, and D. Rauh, 1990, "The Utilization of a Holographic Bragg Diffraction Filter for Rayleigh Line Rejection in Raman Spectroscopy," *Appl. Spectros.*, **44**, pp. 1558-1561.

Chanin, M. L., A. Hauchecorne, and D. Nedeljkovic, 1992, "Temperature Measurement by Rotational Raman Lidar," *Lidar for Remote Sensing*, Society of Photo-Optical Instrumentation Engineers, **1714**, pp. 242-250.

Charney, J. G., 1947, "The Dynamics of Long Waves in a Baroclinic Westerly Current," *J. Meteor.*, **4**,pp. 135-162.

Cheung, T. K., and C. G. Little, 1990, "Meteorological Tower, Microbarograph Array, and Solar Observations of Solitary-Like Waves in the Nocturnal Boundary Layer," *J. Atmos. Sci.*, **47**, pp. 2516-2536.

Chimonas, G., and J. R. Grant, 1984, "Shear Exitation of Gravity Waves. Part 2: Upscale Scattering from Kelvin-Helmholtz Waves," *J. Atmos. Sci.*, **41**, pp. 2278-2288.

Clark, R. H., R. K. Smith, and D. G. Reid, 1981, "The Morning Glory of the Gulf of Carpentaria: An Atmospheric Undular Bore," *Mon. Wea. Rev.*, **109**, pp. 1726-1750.

Coates, P. B., 1973a, "The Origin of Afterpulses in Photomultipliers," *J. Phys. D: Appl. Phys.*, **6**, pp. 1159-1166.

Coates, P. B., 1973b, "A Theory of Afterpulse Formation in Photomultipliers and the Pulse Height Distribution," *J. Phys. D: Appl. Phys.*, **6**, pp. 1862-1869.

Collis, R. T. H., 1969, "Lidar," *Advances in Geophysics*, **13**, Academic Press, New York, pp. 113-139.

Cotnoir, L. J., 1984, "Laser Wavemeter/Spectrometer," *Proc.12th International Laser Radar Conference*, Aix-en-Provence, France, August 13-17, pp. 323-325.

Curran, R. J., 1987, *LASA Instrument Panel Report of the Earth Observing System Report*, **IId**, 91 pp.

Danielsen, E. F., 1966, "Research in Four-Dimensional Diagnosis of Cyclonic Storm Cloud Systems," Rep. No. 66-30, Air Force Cambridge Res. Lab., Bedford, Massachusetts, 53 pp., (NTIS AD-632668).

Danielsen, E. F., 1974, "The Relationship Between Severe Weather, Major Dust Storm and Rapid Large-Scale Cyclogenesis," *Proc. Subsynoptic: Extratropical Weather System Conf.*, Notes from ASP-SSAP Colloquium, NCAR, Boulder, Colorado, **2**, pp. 215-241.

Doviak, R. J., and R. Ge, 1984, "An Atmospheric Solitary Gust Observed with a Doppler Radar, a Tall Tower and a Surface Network," *J. Atmos. Sci.*, **41**, pp. 2559-2573.

Doviak, R. J., S. S. Chen, and D. R. Cristie, 1991, "A Thunderstorm-Generated Solitary Wave Observation Compared with Theory for Non-Linear Waves in a Sheared Atmosphere," *J. Atmos. Sci.*, **48**, pp. 87-111.

Driedger, K. P., W. Krouse, and H. Weber, 1986, "Average Refractive Power of an Alexandrite Laser Rod," *Opt. Comm.*, **57**, pp. 403-406.

Ehret G., C. Kiemle, W. Renger, and G. Simmet, 1993, "Airborne Remote Sensing of Tropospheric Water Vapor with a Near-IR Differential Absorption Lidar System," *Appl. Opt.*, **32**, p. 4534.

Einaudi, F., D. P. Lalas, and G. E. Perona, 1978-79, "The Role of Gravity Waves in Tropospheric Processes," *Pure Appl. Geophys.*, **117**, pp. 627-663.

Einaudi, F., W. L. Clark, D. Fua, J. L. Green, and T. E. VanZandt, 1987, "Gravity Waves and Convection in Colorado During July 1983," *J. Atmos. Sci.*, **44**, pp. 1534-1553.

Einaudi, F., A. J. Bedard, and J. J. Finnigan, 1989, "A Climatology of Gravity Waves and Other Coherent Disturbances at the Boulder Atmospheric Observatory During March-April 1984," *J. Atmos. Sci.*, **46**, pp. 303-329.

Elliassen, A., 1956, "Instability Theories of Cyclone Formation," Chapter 15, *Weather Analysis and Forecasting*, McGraw-Hill, New York, 428 pp.

Elliassen, A., and E. Kleinschmidt, 1957, "Dynamic Meteorology," *Handbuch der Physik*, **48**, Springer-Verlag, pp. 1-154.

Elterman, L., 1968, "Ultraviolet, Visible and Infrared Attenuation for Altitudes to 50 km," Environmental Research Paper 285, AFCRL-68-0153, Air Force Cambridge Research Laboratories, Bedford, Massachusetts, pp. 35-36.

Endemann, M., and R. L. Byer, 1980, "Remote Single-Ended Measurements of Atmospheric Temperature and Humidity at 1.77 μm Using a Continuously Tunable Source," *Opt. Lett.*, **5**, pp. 452-454.

Erickson, C. O., and L. F. Whitney, 1973, "Gravity Waves Following Severe Thunderstorms," *Mon. Wea. Rev.*, **101**, pp. 708-711.

Fenster, A., J. C. Leblanc, W. B. Taylor, and H. E. Johns, 1973, "Linearity and Fatigue in Photomultipliers," *Rev. Sci. Instrum.*, **44**, pp. 689-694.

Fulton, R., D. S. Zrnic, and R. J. Doviak, 1990, "Initiation of a Solitary Wave Family in the Demise of a Nocturnal Thunderstorm Density Current," *J. Atmos. Sci.*, **47**, pp. 319-337.

Gardner, C. S., 1979, *Appl. Opt.*, **18**, p. 3184.

Gedzelman, S. D., and R. A. Rilling, 1978, "Short Period Atmospheric Gravity Waves: A Study of Their Dynamic and Synoptic Features," *Mon. Wea. Rev.*, **106**, pp. 196-210.

Gedzelman, S. D., 1983, "Short-Period Atmospheric Gravity Waves: A Study of Their Statistical Properties and Source Mechanisms," *Mon. Wea. Rev.*, **111**, pp. 1293-1299.

Gill, R., K. Geller, J. Farina, J. Cooney, and A. Cohen, 1979, "Measurement of Atmospheric Temperature Profiles Using Raman Lidar," *J. Appl. Meteor.*, **18**, pp. 225-227.

Goodman, J. W., 1965, *Proc. IEEE*, **53**, p. 1688.

Gossard, E. E., and W. H. Hooke, 1975, *Waves in the Atmosphere*, Elsevier, 456 pp.

Grant, W. B., 1982, *Appl.Opt.*, **21**, p. 2390.

Gyakum, J. R., 1983a, "On the Evolution of the QE II Storm. I: Synoptic Aspects," *Mon. Wea. Rev.*, **111**, pp. 1137-1155.

Gyakum, J. R., 1983b, "On the Evolution of the QE II Storm. II: Dynamic and Thermodynamic Structure," *Mon. Wea. Rev.*, **111**, pp. 1156-1173.

Hartman, D. H., 1978, "Pulse Mode Saturation Properties of Photomultiplier Tubes," *Rev. Sci. Instrum.*, **49**, pp. 1130-1133.

Hertzberg, G., 1950, *Molecular Spectra and Molecular Structure — Part I: Spectra of Diatomic Molecules*, 2nd edition, D. Van Nostrand, Princeton, New Jersey.

Hori, H., Y. Kitayama, M. Kitano, T. Yabuzaki, and T. Ogawa, 1983, "Frequency Stabilization of GaAlAs Laser Using a Doppler-Free Spectrum of the Cs-D_2 Line," *IEEE J. Quantum Electr.*, **QE-19**, pp. 169-174.

Hunt, W. H., and S. K. Poultney, 1975, "Testing the Linearity of Response of Gated Photomultipliers in Wide Dynamic Range Laser Radar Systems," *IEEE Trans. Nucl. Sci.*, **NS22**, pp. 116-120.

Ismail, S., and E. V. Browell, 1989, "Airborne and Spaceborne Measurements of Water Vapor Profiles: A Sensitivity Analysis," *Appl. Opt.*, **28**, p. 3603.

Jansson, P. A., 1970, *J. Opt. Soc. Amer.*, **60**, p. 184.

Jones, D. P., and G. S. Kent, 1974, "Measurement of Overload Effect in a Photomultiplier," *J. Phys.*, **E7**, pp. 744-746.

Kalshoven, J. E., Jr., C. L. Korb, M. Dombrowski, and G. Schwemmer, 1981, "Laser Remote Sensing of Atmospheric Temperature by Observing Resonant Absorption of Oxygen," *Appl. Opt.*, **20**, pp. 1967-1971.

Kalshoven, J. E. and C. L. Korb, 1982, *J. Opt. Soc. Am.*, **72**, pp. 1801A.

Kaplan, L. D., M. T. Chahine, J. Susskind and J. E. Searl, 1977, "Spectral Band Passes for a High Precision Satellite Sounder," *Appl. Opt.*, **16**, pp. 322-325.

Keen, J. P., 1963, "Fatigue and Saturation in Photomultipliers," *Rev. Sci. Instrum.*, **34**, pp. 1220-1222.

Keliher, T. E., 1975, "The Occurrence of Microbarograph-Detected Gravity Waves Compared with the Existence of Dynamically Unstable Wind Shear Layers," *J. Geophys. Res.*, **80**, pp. 2967-2976.

Keyser, D., and M. J. Pecnick, 1985a, "A Two-Dimensional Primitive Equation Model of Frontogenesis Forced by Confluence and Horizontal Shear," *J. Atmos. Sci.*, **42**, 1259-1282.

Keyser, D., and M. J. Pecnick, 1985b, "Diagnosis of Ageostrophic Circulations in a Two-Dimensional Primitive Equation Model of Frontogenesis," *J. Atmos. Sci.*, **42**, 1283-1305.

King, R. A., 1976, *Multiplexed Fabry Perot Interferometers*, thesis, Princeton University, New Jersey.

Koch, S. E., and R. E. Golus, 1988, "A Mesoscale Gravity Wave Event Observed During CCOPE. Part 1: Multiscale Statistical Analysis of Wave Characteristics," *Mon. Wea. Rev.*, **116**, pp. 2527-2544.

Koch, S. E., R. E. Golus, and P. B. Dorian, 1988, "A Mesoscale Gravity Wave Event Observed During CCOPE. Part II: Interactions Between Mesoscale Convective Systems and Antecedent Waves," *Mon. Wea. Rev.*, **116**, pp. 2545-2569.

Koch, S. E., and P. B. Dorian, 1988, "A Mesoscale Gravity Wave Event Observed During CCOPE. Part III: Wave Environment and Probable Source Mechanisms," *Mon. Wea. Rev.*, **116**, pp. 2570-2592.

Koch, S. E., P. B. Dorian, R. Ferrare, S. H. Melfi, W. C. Skillman, and D.Whiteman, 1991, "Structure of an Internal Bore and Dissipating Gravity Current as Revealed by Raman Lidar," *Mon. Wea. Rev.*, **119**, pp. 857-887.

Kogelnik, H., 1964, "Coupling and Conversion coefficients for Optical Modes," *Proc. of Symp. on Quasi-Optics*, **XIV**, Polytechnic Press, Polytechnic Institute of Brooklyn, New York, June, pp. 333-347.

Korb, C. L., 1977, *Proc. of 8th Int. Laser Radar Conf.*, Philadelphia, Pennsylvania, American Meteorological Society, Boston.

Korb, C. L., J. E. Kalshoven, Jr., and C. Y. Weng, 1979, "A Lidar Technique for the Measurement of Atmospheric Pressure Profiles," *Trans. Am. Geophys Union,* **60**, Spring Meeting, Washington, D.C., p. 333.

Korb, C. L., and C. Y. Weng, 1979, "A Two Wavelength Lidar Technique for the Measurement of Atmospheric Temperature Profiles," *Proc. of 9th Int. Laser Radar Conf.*, Munich, American Meteorological Society, pp. 185-186.

Korb, C. L., J. E. Kalshoven, Jr., G. K. Schwemmer, and M. Dombrowski, 1980, "Atmospheric Temperature Determination from High Resolution Laser Absorption Measurements," *Tech. Dig.*, Topical Mtg. Spectroscopy in support of Atmospheric Measurements, Sarasota, Florida, Optical Society of America, TuP20-1-4.

Korb, C. L., and C. Y. Weng, 1980, "The Formulation and Solution of Differential Absorption Lidar Equations for Nonhomogeneous Atmospheres," *Proc. of 10th Int. Laser Radar Conf.*, Silver Spring, Maryland, American Meteorological Society, pp. 115-116.

Korb, C. L., and C. Y. Weng, 1982, "The Theory and Correction of Finite Laser Bandwidth Effects in DIAL Experiments," *Proc. of 11th Int. Laser Radar Conf.*, Madison, Wisconsin, American Meteorological Society, pp. 78-81.

Korb, C. L., G. K. Schwemmer, M. Dombrowski, and C. Y. Weng, 1983, in *Optical and Laser Remote Sensing*, Springer Series on Optical Sciences, **39**, edited by D. K. Killinger and A. Mooradian, Springer, Berlin, p. 120.

Korb, C. L., G. K. Schwemmer, M. Dombrowski, and R. Kagann, 1985, in *Tunable Solid State Lasers for Remote Sensing*, edited by R. L. Byer, E. K. Gustafson, and R. Trebino, Springer, New York, p. 35.

Korb, C. L., G. K. Schwemmer, M. Dombrowksi, J. Milrod, and H. Walden, 1986, *13th International Laser Radar Conference Abstracts*, Toronto, Ontario, Canada, NASA Conf. Publ., **52**, p. 2431.

Kostkowski, H. J., and A. M. Bass, 1956, *J. Opt. Soc. Amer.*, **46**, p. 1060.

Kreitzberg, C., 1980, *Conf. on Coherent Laser Radar for Atmospheric Sensing*, Optical Society of America, Aspen, Colorado, July 15-17.

LaChambre, J. L., P. LaVigne, G. Otis, and M. Noel, 1976, "Injection Locking and Mode Selection in TEA-CO_2 Laser Oscillators," *IEEE J. Quant. Electron.*, **QE-12**, pp. 756-764.

Lalas, D. P., and F. Einaudi, 1976, "On the Characteristics of Gravity Waves Generated by Atmospheric Shear Layers," *J. Atmos. Sci.*, **33**, pp. 1248-1259.

Land, P. L., 1971, "A Discussion of the Region of Linear Operation of Photomultipliers," *Rev. Sci. Instrum.*, **42**, pp. 420-425.

Lapp, M., C. M. Penney, and J. A. Asher, 1973, *Application of Light-Scattering Techniques for Measurements of Density, Temperature, and Velocity in Gas Dynamics*, Aerospace Research Laboratory, Wright-Patterson Air Force Base, Report No. ARL 73-0045.

Lapp, M., and C. M. Penney, 1974, *Laser Raman Gas Diagnostics*, Plenum, New York, Chap. 6.

Lindzen, R. S., and K. K. Tung, 1976, "Banded Convective Activity and Ducted Gravity Waves," *Mon. Wea. Rev.*, **104**, pp. 1602-1617.

Lu, D., T. E. VanZandt, and W. L. Clark, 1984, "VHF Doppler Radar Observations of Buoyancy Waves Associated with Thunderstorms," *J. Atmos. Sci.*, **41**, pp. 272-282.

Lush, H. J., 1965, "Photomultiplier Linearity," *J. Sci. Instrum.*, **42**, pp. 597-602.

Mack, J. E., McNutt, D. P., Roesler, F. L., and Chabbal, R., 1963, "The PEPSIOS Purely Interferometric High-Resolution Scanning Spectrometer. I: The Pilot Model," *Appl. Opt.*, **2**(9), pp. 873-87.

Malhotra, N. K., M. K. Ramamurthy, and R. M. Rauber, 1991,"A Comparative Study of Large Amplitude Atmospheric Gravity Waves," *First Int. Symp. on Winter Storms*, New Orleans, Amer. Meteor. Soc., pp. 280-282.

Mason, J. B., 1975, "Lidar Measurement of Temperature: A New Approach," *Appl. Opt.*, **14**, pp. 76-78.

Massey, H. S. W., and E. H. S. Burhop, 1969, *Electronic and Ionic Impact Phenomena*, **1**, Clarendon, Oxford, U.K., Chap. 3.

Maxworthy, T., 1980, "On the Formation of Nonlinear Internal Waves from Gravitational Collapse of Mixed Regions in Two and Three Dimensions," *J. Fluid Mech.*, **101**, pp. 321-348.

McClatchey, R. A., W. S. Benedict, S. A. Clough, D. E. Burch, R. F. Calfee, K. Fox, L. S. Rothman, and J. S. Garing, 1959, Environmental Research Paper 434, AFCRL-TR-73-0096, Air Force Cambridge Research Laboratories, Bedford, Massachusetts.

McPherson, 1980, *Conf. on Coherent Laser Radar for Atmospheric Sensing*, Optical Society of America, Aspen, Colorado, July 15-17.

Mead, M. L., 1981, "Instrumentation Aspects of Photon Counting Applied to Photometry," *J. Phys. E: Sci. Instrum.*, **14**, pp. 909-918.

Measures, R. M., 1984, *Laser Remote Sensing Fundamentals and Applications*, Wiley, New York.

Megie, G., 1980, "Mesure de la Pression et de la Temperature Atmospherique par Absorption Differentiel Lidar: Influence de la Largeur d'Emission Laser," *Appl. Opt.*, **19**, pp. 34-43.

Melfi, S. H., D. Whiteman, and R. Ferrare, 1989, "Observations of Atmospheric Fronts Using Raman Lidar Moisture Measurements," *J. Appl. Meteor.*, **28**, pp. 789-806.

Menyuk, N., D. K. Killinger, and C. R. Menyuk, 1985, *Appl. Opt.*, **24**, p. 118.

Miller, J. H., R. W. Boese, and L. P. Giver, 1969, "Intensity Measurements and Rotational Intensity Distribution for the Oxygen *A* Band," *J. Quant. Spectrosc. Radiat. Transfer*, **9**, pp. 1507-1517.

Morris, M. B., T. J. McIlrath, and J. J. Snyder, 1984, "Fizeau Wavemeter for Pulsed Laser Wavelength Measurement", *Appl. Opt.*, **23**, pp. 3862-3868.

Murray, E. R., D. D. Powell, and J. E. van der Laan, 1980, "Measurement of Average Atmospheric Temperature Using a CO_2 Laser Radar," *Appl. Opt.*, **19**, pp. 1794-1797.

Nagasawa, C., M. Abo, H. Yamamoto, and O. Uchino, 1990, "Random Modulation CW Lidar Using New Random Sequence," *Appl. Opt.*, **29**, pp. 1466-1469.

NASA, 1974, *U.S. Plan for Participation in FGGE*, NASA, Goddard Space Flight Center, Greenbelt, Maryland.

NASA, 1977, *Proposed NASA Contribution to the Climate Program*, Goddard Space Flight Center, Greenbelt, Maryland.

NASA, 1979, *Shuttle Atmospheric Lidar Research Program*, SP-433, Washington, D.C.

NASA, 1980, *NASA Tropospheric Program Plan (DRAFT)*, Working Group on Tropospheric Program Planning, Washington, D.C.

NBS-AM, 1954, *Tables of the Error Function and its Derivative*, Natl. Bur. of Stand. Appl. Math. Ser. 41, U.S. Government Printing Office, Washington, D.C.

Olivero J. J., and R. L. Longbothum, 1977, *J. Quant. Spectrosc. Radiat. Transfer*, **17**, p. 233.

Payne, S. A., L. L. Chase, H. W. Newkirk, L. K. Smith, and W. F. Krupke, 1988, "$LiCaAlF_6$: Cr^{3+} - A Promising New Solid-State Laser Material," *IEEE J. of Quant. Elect.*, **24**, pp. 2243-2252.

Peckham, G. E., and D. A. Flower, 1981, "A Microwave Pressure Sounder," in *Dig. Int. Geosci. Remote Sens. Symp.*, Washington, pp. 46-51.

Pecnick, M., and J. A. Young, 1984, "Mechanics of a Strong Subsynoptic Gravity Wave Deduced from Satellite and Surface Observations," *J. Atmos. Sci.*, **41**, pp. 1850-1862.

Penner, S. S., and R. W. Kavanagh, 1953, "Radiation from Isolated Spectral Lines with Combined Doppler and Lorentz Broadening," *J. Opt. Soc. Amer.*, **43**, pp. 385-388.

Penner, S. S., 1959, *Quantitative Molecular Spectroscopy and Gas Emissivities*, Addison-Wesley, Reading, Massachusetts, pp. 26-37.

Petheram, J. C., 1981, "Differential Backscattering from the Atmospheric Aerosol: the Implication for IR Differential Absorption Lidar," *Appl. Opt*, **20**, pp. 3941-3946.

Petterssen, S., 1955, "A General Survey of Factors Influencing Development at Sea-Level," *J. Meteor.*, **12**, pp. 36-42.

Pevtschin, V., and S. Ezekiel, 1987, "Investigation of Absolute Stability of Water-Vapor-Stabilized Semiconductor Laser," *Optics Lett.*, **12**, pp. 172-174.

Pitz, E., 1979, "Nonlinearity Measurements on Photometric Devices," *Appl. Opt.*, **18**, 1360-1362.

Plass, G. N., and D. I. Fivel, 1953, *Astrophys. J.*, **117**, p. 225.

Post, M. J., and W. D. Neff, 1986, "Doppler Lidar Measurements of Winds in a Narrow Mountain Valley," *Bull. Amer. Meteor. Soc.*, **67**, pp. 274-281.

Rahn. L. A., 1985, "Feedback Stabilization of an Injection Seeded Nd:YAG Laser," *Appl. Opt.*, **24**, p. 940.

Ramamurthy, M. K., B. P. Collins, R. M. Rauber, and P. C. Kennedy, 1990, "Evidence of Very-Large-Amplitude Solitary Waves in the Atmosphere," *Nature*, **348**, pp. 314-317.

Ramsay, I. A., and J. J. Degnan, 1970, "A Ray Analysis of Optical Resonators Formed by Two Spherical Mirrors," *Appl. Opt.*, **9**, p. 385.

Raymond, T. D., and A. V. Smith, 1991, "Injection-Seeded Titanium-Doped-Sapphire Laser," *Opt. Lett.*, **16**, pp. 33-35.

Reed, R. J., 1955, "A Study of a Characteristic Type of Upper-Level Frontogenesis," *J. Meteor.*, **12**, pp. 226-237.

Reed, R. J., and E. F. Danielsen, 1959, "Fronts in the Study of the Tropopause," *Arch. Meteor. Geophys. Bioclim.*, **A11**, pp. 1-17.

Reiter, E. R., 1963, *Jet Stream Meteorology*, The University of Chicago Press, Chicago, 515 pp.

Riley, R. J., and A. G. Wright, 1977, "The Effect of Photomultiplier Afterpulse in Coincidence Systems," *J. Phys. E*, **10**, pp. 873-874.

Rosenthal, A. J., and R. S. Lindzen, 1983, "Instabilities in a Stratified Fluid Having One Critical Level. Part II: Explanation of Gravity Wave Instabilities Using the Concept of Over-reflection," *J. Atmos. Sci.*, **40**, pp. 521-529.

Rothman, L. S., 1981, *Appl. Opt.*, **20**, p. 791.

Rottman, J. W., and J. E. Simpson, 1989, "The Formation of Internal Bores in the Atmosphere: A Laboratory Model," *Quart. J. Roy. Meteor. Soc.*, **115**, pp. 941-963.

Russell, P. B., and B. M. Morley, 1982, *Appl. Opt.*, **21**, p. 1554.

Sanders, C. L., 1972, "Accurate Measurements of and Correction for Nonlinearities in Radiometers," *J. Res. Nat. Bur. Stand.*, **76A**, pp. 437-453.

Sassen, K., D. O'C. Starr, and T. Uttal, 1989, "Mesoscale and Microscale Structure of Cirrus Clouds: Three Case Studies," *J. Atmos. Sci.*, **46**, pp. 371-396.

Schotland, R. M., 1974, "Errors in the Lidar Measurement of Atmospheric Gases by Differential Absorption," *J. Appl. Meteor.*, **13**, pp. 71-77.

Schwemmer, G. K., and T. D. Wilkerson, 1979, "Lidar Temperature Profiling: Performance Simulations of Mason's Method," *Appl. Opt.*, **18**, pp. 3539-3541.

Schwemmer, G., M. Dombrowski, and C. L. Korb, 1982, "Advanced Near IR Lidar for Meteorological Remote Sensing," *Proc. of 11th Int. Laser Radar Conf.*, Madison, Wisconsin, American Meteorological Society, p. 26.

Schwemmer, G. K., C. L. Korb, M. Dombrowski, and R. Kagann, 1984, *12th Int. Laser Radar Conf.*, Aix-en-Provence, France, Abstracts, Etablissement d'Etude et de Recherche Météorologique, Paris., p. 157.

Schwemmer, G. K., M. Dombrowski, C. L. Korb, J. Milrod, H. Walden, and R. H. Kagann, 1987, "A Lidar System for Measuring Atmospheric Pressure and Temperature Profiles," *Rev. Sci. Inst.*, **58**, pp. 2226-2237.

Schwemmer, G. K., 1988, "Frequency Stabilized Diode Laser System for Active Control of DIAL Lasers, Wavemeters, and Receiver Filters," *Proc. 14th Int. Laser Radar Conf.*, San Candido, Italy, June 20-24, pp. 274-277.

Schwemmer, G. K., 1993, "Doppler Shift Compensation System for Laser Transmitters and Receivers," U.S. Patent No. 5,184,241.

Shettle, E. P., and R. W. Fenn, 1975, "Model of the Atmospheric Aerosols and Their Optical Properties," *Proc. AGARD Conf: Optical Propagation in the Atmosphere*, **183**, pp. 2.1-2.9.

Shimizu, H., K. Noguchi, and C. Y. She, 1986, *Appl. Opt.*, **25**, p. 1460.

Shipley, S. T., D. H. Tracey, E. W. Eloranta, J. T. Trauger, S.T. Sroga, F. L. Roesler, and J. A. Weinmann, 1983, "High Spectral Resolution Lidar to Measure Optical Scattering Properties of Atmospheric Aerosols. 1: Theory and Instrumentation," *Appl. Opt.*, **22**, pp. 3716-3724.

Siegman, A. E., 1986, *Lasers*, University Science Books, Mill Valley, California.

Singer, S. F., 1968, *Appl. Opt.*, **7**, p. 1125.

Smith, James C., 1988a, "Interface for Digital Pots Directs Servomotor Positioning," *Electronic Design Magazine*, Design Ideas, March 3.

Smith, James C., 1988b, "Serial Data System Uses Three-Wire Distribution," *EDN Magazine*, Ideas for Design, March 31.

Smith, R. K., 1988c, "Travelling Waves and Bores in the Lower Atmosphere: The 'Morning Glory' and Related Phenomena," *Earth Sci. Rev.*, **25**, pp. 267-290.

Snyder, J. J., 1980, "Algorithm for Fast Digital Analysis of Interference Fringes," *Appl. Opt.*, **19**, p. 1228.

Staehr, W., W. Lahmann, and C. Weitkamp, 1985, *Appl. Opt.*, **24**, p. 1950.

Starr, D. O'C., and D. P. Wylie, 1990, "The 27-28 October 1986 FIRE Cirrus Case Study: Meteorology and Clouds," *Mon. Wea. Rev.*, **118**, pp. 2259-2287.

Stevens, D. E., P. E. Ciesielski, R. H. Johnson, and K. R. Dean, 1989, "Observational Evidence for Asymmetric Inertial Instability," *J. Atmos. Sci.*, **46**, pp. 817-831.

Stobie, J. G., F. Einaudi, and L. W. Uccellini, 1983, "A Case Study of Gravity Waves-Convective Storm Interaction: 9 May 1979," *J. Atmos. Sci.*, **40**, pp. 2804-2830.

Sutcliffe, R. C., 1947, "A Contribution to the Problem of Development," *Quart. J. Roy. Meteor. Soc*, **73**, pp. 370-383.

Sutcliffe, R. C., and A. G. Forsdyke, 1950, "The Theory and Use of Upper Air Thickness Patterns in Forecasting," *Quant. J. Roy. Meteor. Soc.*, **76**, pp. 189-217.

Takevchi, N., N. Sugimoto, H. Baba, and K. Sadurai, 1983, "Random Modulation CW Lidar," *Appl. Opt.*, **22**, pp. 1382-1386.

Theopold, F. A., and J. Bosenberg, 1993, "Differential Absorption Lidar Measurements of Atmospheric Temperature Profiles: Theory and Experiment," *J. Atmos. Ocean Technol.*, **10**, p. 165.

Thorpe, S. A., 1978, "On the Shape and Breaking of Finite Amplitude Internal Gravity Waves in a Shear Flow," *J. Fluid Mech.*, **85**, pp. 7-31.

Thorpe, S. A., 1979, "Instability and Waves," *Weather*, **34**, pp. 102-106.

Tsuchida, H., M. Ohtsu, T. Tako, N. Kuramochi, and N. Oura, 1982, "Frequency Stabilization of AlGaAs Semiconductor Laser Based on the ^{85}Rb-D_2 Line," *Jap. J. Appl. Phys.*, **21**, pp. L561-L563.

Uccellini, L. W., and D. R. Johnson, 1979, "The Coupling of Upper and Lower Tropospheric Jet Streaks and Implications for the Development of Severe Convective Storms," *Mon. Wea. Rev.*, **107**, pp. 682-703.

Uccellini, L. W., P. J. Kocin, R. A. Petersen, C. H. Wash, and K. F. Brill, 1984, "The Presidents' Day Cyclone of 18-19 February 1979: Synoptic Overview and Analysis of the Subtropical Jet Streak Influencing the Pre-Cyclogenetic Period," *Mon. Wea. Rev.*, **112**, pp. 31-55.

Uccellini, L. W., D. Keyser, C. H. Wash, and K. F. Brill, 1985, "The Presidents' Day Cyclone of 18-19 February 1979: Influence of a Tropopause Fold on Rapid Cyclogenesis," *Mon. Wea. Rev.*, **113**, pp. 962-988.

Uccellini, L. W., 1986, "On the Possible Influence of Upstream Upper-Level Baroclinic Processes on the Development of the QE-II Storm," *Mon. Wea. Rev.*, **114**, 1019-1027.

Uccellini, L. W., and S. E. Koch, 1987, "The Synoptic Setting and Possible Energy Sources for Mesoscale Wave Disturbances," *Mon. Wea. Rev.*, **115**, pp. 721-729.

Vaughan, J.M., 1989, *The Fabry-Perot Interferometer*, Adam Hilger, Philadelphia, Chap. 3.

Vaughan, G., D. P. Wareing, S. J. Pepler, L. Thomas, and V. Mitev, 1993, "Atmospheric Temperature Measurements Made by Rotational Raman Scattering," *Appl. Opt.*, **32**, pp. 2758-2764.

Walling, J. C., O. G. Peterson, H. P. Jenssen, R. C. Morris, and E. W. O'Dell, 1980, *IEEE, J. Quant. Elect.*, **QE-16**, p. 1302.

Walling, J. C., 1987, "Tunable Paramagnetic-ion Solid State Lasers," *Tunable Lasers*, Springer Verlag, Berlin.

Walls, F. L., 1987, "Errors in Determining the Center of a Resonance Line Using Sinusoidal Frequency (Phase) Modulation," *IEEE Trans. Ultrason. Ferroelec. Freq. Contr.*, **UFFC-34**, pp. 592-597.

Wark, D. Q., and D. M. Mercer, 1965, *Appl. Opt.*, **4**, p. 839.

WMO-ICSU Joint Organizing Committee, 1973, *The First GARP Global Experiment—Objectives and Plans*, GARP Publ. Ser. No. 11, World Meteorological Organization, International Council of Scientific Unions, Geneva, Switzerland, p. 11.

Yamamoto, G. and D. Q. Wark, 1961, *J. Geophys. Res.*, **66**, p. 3596.

Yamashita, M., O. Yure, and Y. Kawada, 1982, "Probability and Time Distribution of Afterpulses in GaP First Dynode Photomultiplier Tubes," *Nucl. Instrum. and Meth.*, **196**, pp. 199-202.

Yang, B., M. D. Morris, and H. Owen, 1991, "Holographic Notch Filter for Low-Wavenumber Stokes and Anti-Stokes Raman Spectroscopy," *Appl. Spectros.*, **45**, pp. 1533-1536.

Zeldovich, Ya. B., and Yu. P. Raizer, 1966, *Physics of Shock Waves and High-Temperature Hydrodynamic Phenomena*, Academic Press, New York.

REPORT DOCUMENTATION PAGE

Form Approved
OMB No. 0704-0188

1. AGENCY USE ONLY *(Leave blank)*	2. REPORT DATE	3. REPORT TYPE AND DATES COVERED
	November 1995	Technical Memorandum

4. TITLE AND SUBTITLE

Differential Absorption Lidars for Remote Sensing of Atmospheric Pressure and Temperature Profiles: Final Report

5. FUNDING NUMBERS

RTOP: UPN 460-28-40
Code 912

6. AUTHOR(S)

C. Laurence Korb, Geary K. Schwemmer, Joseph Famiglietti, Harvey Walden, and Coorg Prasad

7. PERFORMING ORGANIZATION NAME(S) AND ADDRESS (ES)

Laboratory for Atmospheres
Goddard Space Flight Center
Greenbelt, Maryland 20771

8. PEFORMING ORGANIZATION REPORT NUMBER

95B00061

9. SPONSORING / MONITORING AGENCY NAME(S) AND ADDRESS (ES)

National Aeronautics and Space Administration
Washington, DC 20546-0001

10. SPONSORING / MONITORING AGENCY REPORT NUMBER

NASA TM-104618

11. SUPPLEMENTARY NOTES

Korb, Schwemmer, Famiglietti, and Walden: Goddard Space Flight Center, Greenbelt, Maryland
Prasad: Science and Engineering Services, Inc., Burtonsville, Maryland

12a. DISTRIBUTION / AVAILABILITY STATEMENT

Unclassified - Unlimited
Subject Category 35

Availability: NASA CASI (301) 621-0390.

12b. DISTRIBUTION CODE

13. ABSTRACT *(Maximum 200 words)*

A near infrared differential absorption lidar technique is developed using atmospheric oxygen as a tracer for high resolution vertical profiles of pressure and temperature with high accuracy. Solid-state tunable lasers and high-resolution spectrum analyzers are developed to carry out ground-based and airborne measurement demonstrations and results of the measurements presented. Numerical error analysis of high-altitude airborne and spaceborne experiments is carried out, and system concepts developed for their implementation.

14. SUBJECT TERMS

Lidar, differential absorption, alexandrite laser, laser wavemeter, photomultiplier, pressure profile, temperature profile, gravity wave, raman scattering

15. NUMBER OF PAGES
257

16. PRICE CODE

17. SECURITY CLASSIFICATION OF REPORT	18. SECURITY CLASSIFICATION OF THIS PAGE	19. SECURITY CLASSIFICATION OF ABSTRACT	20. LIMITATION OF ABSTRACT
Unclassified	Unclassified	Unclassified	UL

National Aeronautics and
Space Administration
Goddard Space Flight Center
Greenbelt, Maryland 20771